Cell Reports
Physical Science

Review

Advancing wide-band-gap perovskite solar cells via vapor-phase deposition

Ziquan He,[1,2] Siqian Zhou,[1,2] Haozhen Zhu,[1,2] Junchao Han,[1] Ying Hu,[1] Chenxi Shen,[1] Yanjun Cheng,[1] Dicong Yang,[1] Mingjun Zhang,[1] Zihan Shao,[1] Qianpeng Zhang,[1,*] and Xiaoliang Mo[1,*]
[1]Institute of Optoelectronics, State Key Laboratory of Photovoltaic Science and Technology, Shanghai Frontiers Science Research Base of Intelligent Optoelectronics and Perception, Fudan University, Shanghai 200433, China
[2]These authors contributed equally
*Correspondence: zhang_qp@fudan.edu.cn (Q.Z.), xlmo@fudan.edu.cn (X.M.)
https://doi.org/10.1016/j.xcrp.2026.103346

SUMMARY

Wide-band-gap perovskite solar cells (WBG PSCs) hold significant optoelectronic potential, with applications spanning building-integrated photovoltaics, large-area modules, and tandem solar cells. Vapor-phase deposition, leveraging its unique solvent-free processing, provides an ideal platform to address critical WBG perovskite challenges, including halide segregation, phase instability, and defect control. This review critically assesses the vapor-phase technology landscape for WBG perovskites. It first dissects fundamental physicochemical challenges in vacuum environments: mixed-halide lattice thermodynamic metastability, precursor sublimation kinetic mismatch, and complex organic cation volatility. It then systematically evaluates advanced deposition methodologies, ranging from sequential evaporation to hybrid vapor-solution routes, alongside optimization strategies spanning nucleation thermodynamics, bulk defect management, and interface energy alignment. It further examines the translation of material innovations into functional devices, highlighting vapor deposition's advantages in semitransparent cells, scalable modules, and high-efficiency perovskite/silicon tandem cells, before outlining key challenges and future directions to guide both fundamental research and industrial-scale development.

INTRODUCTION

The urgent global demand for a low-cost, high-efficiency energy transition is the primary driver of research into perovskite solar cells (PSCs), which have now reached a power conversion efficiency (PCE) of 27% toward commercialization.[1–3] In this context, developing highly efficient and stable wide-band-gap (WBG) perovskite thin films ($Eg > 1.65$ eV) is a central challenge for next-generation tandem solar cells (TSCs). By integrating WBG top cells with crystalline silicon or narrow-band-gap (NBG) perovskites, TSCs can surpass the Shockley-Queisser limit of single-junction devices, as evidenced by the current record PCE approaching 35%.[1,4–8]

However, realizing high-performance WBG perovskites, particularly bromine-rich compositions, faces intrinsic material hurdles that are often poorly addressed by mainstream solution processing.[9,10] The most prominent issues include light-induced halide segregation[11–14]; high crystallization barriers, especially for all-inorganic systems such as $CsPbBr_3$[15–18]; and the complexity of maintaining compositional homogeneity in multi-cation frameworks.[19–21] These factors collectively lead to non-radiative recombination, phase instability, and uneven vertical distribution of components. While solution methods such as spin coating suffer from rapid, solvent-dependent crystallization and poor conformal coverage on textured substrates,[22–25] vapor-phase deposition has emerged as a robust alternative. As a solvent-free dry process, vapor deposition enables precise control over precursor transport and surface reaction physics, offering superior large-area uniformity, accurate stoichiometry control, and excellent conformality on complex morphologies.[26–29]

This review systematically examines the evolution of vapor-phase deposition for high-performance WBG perovskite photovoltaics (Figure 1). We first delineate the unique thermodynamic and kinetic challenges of solvent-free crystallization, followed by a comprehensive classification of vapor-based methodologies, ranging from traditional co-evaporation to emerging combinatorial and epitaxial techniques. We then categorize optimization strategies for defect mitigation and interface modulation and highlight the decisive advantages of these techniques in semitransparent cells and monolithic tandem devices. Finally, we provide a strategic outlook on overcoming the throughput-quality trade-offs to facilitate the gigawatt-scale implementation of perovskite-based tandem technologies.

THE INTRINSIC CHALLENGES OF VAPOR-DEPOSITED WBG PEROVSKITES

Metal halide perovskites, defined by the ABX_3 stoichiometry, feature a corner-sharing $[BX_6]$ octahedral framework where

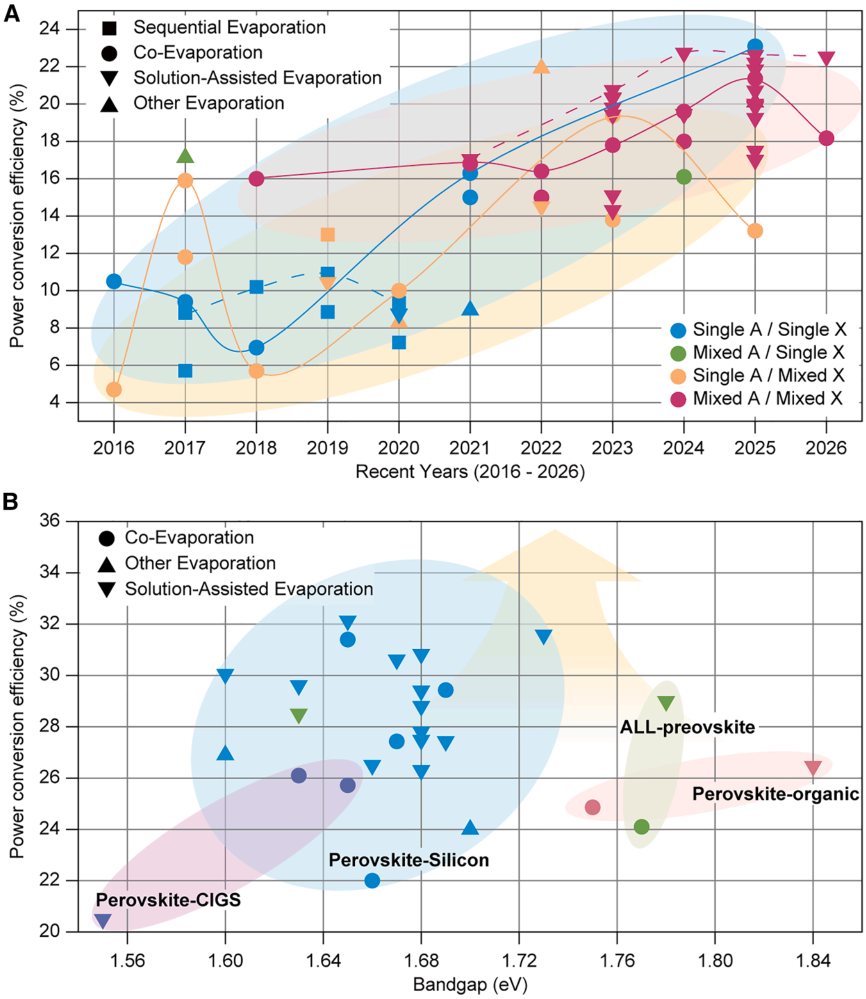

Figure 1. Summary of achieved power conversion efficiencies

(A) Wide-band-gap perovskite solar cells based on vapor process.

(B) Tandem solar cells based on vapor process.

exceptional optoelectronic properties emerge from a dynamically disordered soft lattice. While structural stability is classically approximated using geometric descriptors such as the Goldschmidt tolerance factor t and octahedral factor μ (Figure 2A),[30] the complexity of WBG compositions necessitates more refined predictors. Bartel et al. proposed a new tolerance factor τ, where $\tau < 4.18$ serves as the threshold for stable perovskite formation.[31] Critically, the incorporation of high bromine content and mixed cations (e.g., Cs^+ and FA^+) in WBG systems introduces significant local lattice strain and steric frustration, pushing these materials to their thermodynamic stability limit. Unlike stable binary semiconductors, WBG perovskites exist in a delicate energetic equilibrium in which entropy-driven mixing competes with enthalpy-driven segregation, making their final phase purity highly dependent on the initial nucleation and the underlying substrate template.

Such structural fragility extends to the electronic structure where the band gap arises from the antibonding overlap between Pb *6s* and halide *n*p orbitals (Figure 2B).[32] Although this configuration ensures a direct band gap and high absorption coefficient (Figure 2C),[31] the weak ionic-covalent nature of the Pb–X bond renders the lattice highly susceptible to thermal vibrations. Consequently, the crystal undergoes polymorphic transitions traversing cubic α, tetragonal β, and orthorhombic γ phases, which are sensitive to temperature and stoichiometry (Figure 2D).[26,33] The primary metastability challenge for WBG systems involves preventing collapse into the photo-inactive δ phase, which functions as a thermodynamic sink at room temperature (Figure 2E).[26] This intrinsic tendency toward phase degradation dictates that the device environment—specifically the contact interfaces—must provide a stabilizing influence during film growth.

Device architecture selection is thus not merely a matter of charge extraction but a critical factor in structural stabilization. Conventional n-i-p devices utilizing doped hole transport layers (HTLs) such as Spiro-OMeTAD have historically set efficiency benchmarks but suffer from processing complexities and instability. Conversely, the inverted p-i-n architecture shown in Figure 2F has emerged as the definitive platform for tandem applications due to negligible hysteresis and scalability.[34] The recent adoption of self-assembled monolayers (SAMs) such as Me-4PACz has further solidified this dominance, as these monolayers minimize interfacial non-radiative recombination and provide a more compatible chemical surface for the high-energy growth of WBG crystals.

Within this framework of material and interfacial sensitivity, vapor deposition introduces unique challenges. The absence of coordination buffering by solvent molecules allows highly reactive vapor-phase precursors to adsorb directly onto the substrate and trigger rapid solid-state reactions. This necessitates that the interface layer assume a dual function: providing selective carrier extraction through energy alignment and serving as a nucleation template via chemical surface energy modification. Such template-guided growth is required to circumvent the uncontrolled and disordered crystallization characteristic of solvent-free environments. Consequently, the stability and quality of the resulting WBG films are intrinsically tied to how vapor-phase dynamics are managed at the interface, a theme that underpins the optimization strategies discussed in the following sections.

Intrinsic thermodynamic fragilities of WBG perovskites

WBG perovskites exhibit intrinsic thermodynamic fragilities that stem from a multi-level hierarchy of instability. We

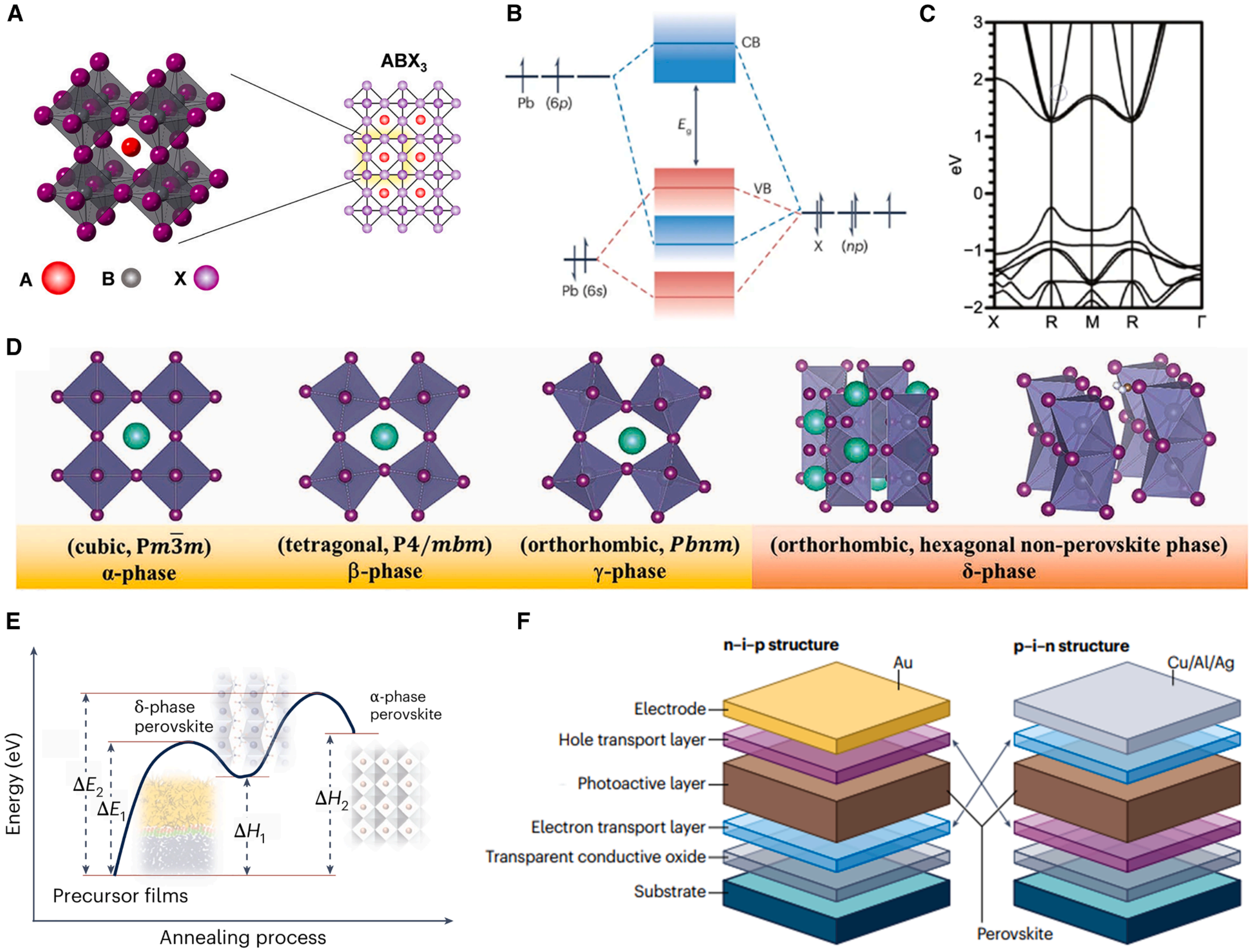

Figure 2. Metal halide perovskite

(A) Schematic diagram of the perovskite lattice. Reproduced with permission.[30] Copyright 2018, American Chemical Society.

(B) Schematic diagram of the formation of the perovskite energy band. Reproduced with permission.[32] Copyright 2025, Springer Nature.

(C) Energy band structure of perovskite. Reproduced with permission.[31] Copyright 2014, AIP Publishing.

(D) Schematic diagram of the cubic phase, tetragonal phase, orthorhombic phase, and non-perovskite phase of perovskite. Reproduced with permission.[33] Copyright 2022, Wiley-VCH.

(E) Phase-transformation process of perovskite. Reproduced with permission.[26] Copyright 2025, Springer Nature.

(F) Normal (n-i-p)-type and inverted (p-i-n)-type perovskite solar cell devices. Reproduced with permission.[34] Copyright 2025, Springer Nature.

propose a three-level correlation: lattice strain serves as the thermodynamic root, defect migration acts as the kinetic conduit, and phase segregation is the observable manifestation.

Lattice strain is the most critical factor in thermodynamics. Mixed-halide alloys possess a positive enthalpy of mixing due to the size mismatch between iodide and bromide ions.[35] Without this strain-induced energetic penalty, the system would remain a stable solid solution regardless of ion mobility. Defect migration represents the rate-limiting step. Even in unstable regimes, segregation cannot occur if ion transport is kinetically frozen.[36] Phase segregation is merely the cumulative result when the previous two safeguards fail. Table 1 compares the variation trends in thermodynamic and kinetic parameters under different strain conditions.

The Hoke effect and thermodynamic driving forces

The primary challenge lies in photoinduced phase segregation, commonly termed the Hoke effect. First reported by Hoke et al., this reversible phenomenon involves the demixing of mixed-halide perovskites into low-band-gap iodide-rich traps and bromide-rich domains under illumination, revealing a thermodynamically driven metastable behavior. Stability in these alloys depends on the competition between the stabilizing entropy of mixing and the destabilizing internal lattice energy.[37] Currently, hypotheses explaining the microscopic origin of photoinduced phase segregation fall into three primary dimensions.

The polaron-induced strain model emphasizes the role of electron-phonon coupling. Bischak et al. proposed that photocarriers funnel into iodide-rich domains. Due to the soft nature of

Table 1. The influence of lattice strain properties on key parameters of wide-band-gap perovskite stability

Parameter	Tensile strain	Compressive strain	Logical implications/impact
Enthalpy of mixing (ΔH_{mix})	increases	decreases	determines the thermodynamic stability limit
Migration activation energy (E_a)	decreases	increases	determines the rate of phase segregation
Defect formation energy	decreases	medium: limited by solution step uniformity; batch annealing process.	determines the density of ion migration channels
Phase segregation tendency	enhanced	inhibited	determines the long-term stability of the final device

the perovskite lattice, these accumulated carriers induce polaronic distortions, forming large polarons. The resulting local strain field creates an elastic potential gradient, driving larger iodide ions toward the strain center (Figure 3A).[38] This hypothesis is supported by Zhao et al., who identified a strain-composition threshold. They demonstrated that segregation in films with less than 50% Br is strain activated and sensitive to external pressure, whereas higher Br contents trigger a spinodal decomposition regime (Figure 3B).[39] Limmer and Ginsberg pointed out that a key challenge for this model is whether the strain energy induced by polarons is sufficient to overcome the high activation barrier for ion diffusion.[40]

In contrast to dynamic mechanisms, Brivio et al. consider phase segregation an intrinsic thermodynamic behavior. Calculations show that mixed-halide systems sit within a miscibility gap at room temperature, favoring spinodal decomposition.[35] Under this framework, illumination acts by providing energy to help ions overcome diffusion barriers or reshaping the free energy landscape via photocarrier occupancy.[44] The miscibility gap hypothesis struggles to fully explain why the process is reversible in the dark; if the system is thermodynamically biased toward segregation, it should theoretically remain segregated after removing illumination.

Another emerging view is the electrochemical and defect-mediated model. This model examines photoinduced phase segregation from an electrochemical perspective. Belisle et al. suggested that photo-generated holes are trapped at defects and oxidize I^- to neutral I^0, breaking local electroneutrality and significantly reducing migration resistance.[45] Furthermore, the counterflow of halide vacancies and ions driven by surface electric fields is considered key to compositional segregation.[46] The current debate focuses on whether this is an intrinsic physical process or an early manifestation of chemical degradation. These models together form a comprehensive understanding of the Hoke effect from electronic, structural, and electrochemical perspectives. The debate essentially centers on whether the light factor acts to alter the energy landscape or lower migration barriers.

Defect-mediated ion migration channels

Thermodynamics provides the drive, but defect-mediated migration determines the kinetics. Eames et al. combined density functional theory calculations and experiments to identify iodide vacancies as the primary vehicle for halide transport, given their exceptionally low activation energy of approximately 0.58 eV (Figures 3C and 3D).[41] Kinetic tracking studies by Yoon et al. further confirmed that segregated domain formation rates correlate strictly with halide defect concentrations, as films with fewer defects exhibit significantly retarded segregation kinetics.[47] Furthermore, Sabino et al. proposed a light-induced Frenkel defect pair theory offering a quantum mechanical explanation. They posit that hole localization weakens Pb–X bonds and expels halide atoms into interstitial sites to form vacancy-interstitial pairs, thereby unlocking rapid migration channels (Figure 3E).[42] This is experimentally corroborated by Ren et al., who showed that mobile iodine and vacancies act as both recombination centers and triggers for self-accelerating degradation. Capturing these mobile species via interfacial materials proved effective in suppressing this process.[48]

Consequently, intrinsic instability can be mitigated by kinetically freezing ion migration channels. Whether utilizing the steric hindrance effect of thiocyanate filling vacancies as reported by Zhang et al.[49] or increasing the segregation activation energy via chloride doping as observed by Cho et al.,[50] the underlying logic is universally based on defect engineering.

Correlation between structural distortion and V_{OC} loss

Beyond phase segregation, WBG perovskites suffer from substantial open-circuit voltage (V_{OC}) deficits. Phase segregation leads to severe V_{OC} loss through a triple-coupling mechanism. First, the carrier-anchoring effect plays a decisive role: once iodide-rich clusters form, their lower band gap creates energetic pits within the film, causing photocarriers to rapidly funnel into these micro-domains. This localized charge accumulation restricts the overall quasi-Fermi level splitting of the device to the range of the low-band-gap phase, thereby fundamentally pinning the upper limit of V_{OC}.

Simultaneously, strain-induced non-radiative recombination further exacerbates energy loss. The lattice mismatch between iodide-rich domains and the parent matrix generates massive local strain, which not only lowers defect formation energies but also induces a high density of deep-level traps, significantly accelerating non-radiative recombination rates.[51,52] Furthermore, this spatial compositional heterogeneity leads to band bending and transport barriers, distorting the built-in electric field and creating local extraction barriers that result in severe interfacial charge accumulation.[53,54]

Such multidimensional degradation is often rooted in local octahedral tilting and energetic disorder induced by I/Br alloying. Yin et al. demonstrated that while A-site doping-induced tilting can stabilize the structure, it alters electron-phonon coupling and impacts carrier lifetimes.[55] To address this challenge, Zhang et al. emphasized that homogenizing halide distribution and inducing vertical orientation via ligand engineering, specifically using MeOPEA at the buried interface, is critical for minimizing

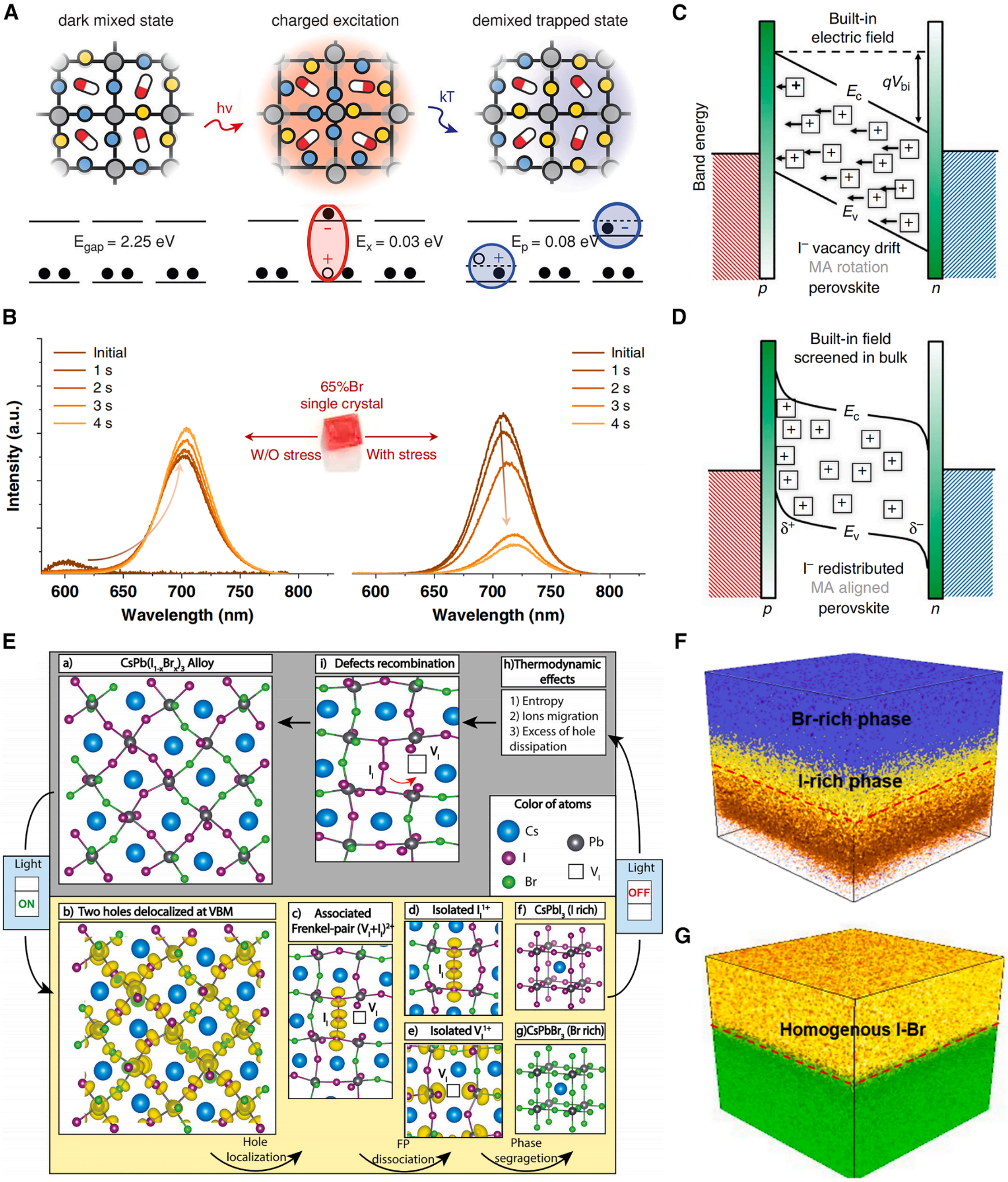

Figure 3. Intrinsic thermodynamic fragilities of wide-band-gap perovskites

(A) Photoinduced polaron trapping and associated energy scales associated with phase separation. Reproduced with permission.[38] Copyright 2017, American Chemical Society.

(B) The evolution of photoluminescence (PL) spectra for 65% Br single crystal under illumination without (left) and with (right) external uniaxial pressure. Reproduced with permission.[39] Copyright 2020, Springer Nature.

(C and D) Schematic diagrams indicating the influence of vacancy drift on the band energies of a p-i-n device at short circuit. EC is the conduction band energy, E_V is the valence band energy, and V_{bi} is the built-in potential. Iodide ion vacancies are represented by the squares with "plus" symbols. Reproduced with permission.[41] Copyright 2015, Springer Nature.

(E) Mechanism for phase segregation. Reproduced with permission.[42] Copyright 2023, Wiley-VCH.

(F and G) Time-of-flight secondary ion mass spectrometry (ToF-SIMS) 3D render overlay images of I-Br distribution. Reproduced with permission.[43] Copyright 2024, American Chemical Society.

Table 2. The core differences in precursor mixing kinetics between solution and vacuum methods

Property	Solution method	Vacuum method	Kinetic impact
Transport mechanism	diffusion and convection	ballistic transport	interaction-free in vacuum
Modulation medium	solvent complexes	none	lack of energy buffers in vacuum
Homogenization time	pre-crystallization equilibrium	none; instant freezing	propensity for non-equilibrium gradients

deep-level traps.[43] Their work indicates that 3-MeOPEA$^+$ ligands assist in forming homogeneous Br-I mixed-halide WBG perovskites (Figures 3F and 3G).

However, a critical disparity exists regarding implementation. Most successful stabilization strategies, such as bulky organic ligands or Lewis base additives, are readily compatible with solution processing but pose significant challenges in the high-vacuum environment of vapor deposition. Introducing these stabilizers at the atomic scale without disrupting the crystallization kinetics of vapor growth remains a formidable technical hurdle.

The halide segregation dilemma in vacuum

While the intrinsic thermodynamic instability of WBG perovskites establishes the baseline for phase segregation, as discussed in intrinsic thermodynamic fragilities of WBG perovskites, the specific kinetic environment of vapor deposition amplifies this vulnerability through a distinct mechanism involving vertical compositional heterogeneity. Unlike solution processing, where precursor distribution can be homogenized via chemical manipulation, vacuum deposition introduces a fundamental kinetic mismatch that facilitates the Hoke effect.

Absence of solvent modulation

In solution-based protocols, solvent molecules act as critical chemical buffers, forming intermediate complexes such as $PbI_2 \cdot xDMSO$ that lower nucleation barriers and enable ionic reorganization prior to crystallization.[56,57] This solvent cage effect establishes a homogeneous chemical potential field promoting uniform iodide and bromide distribution. Conversely, vacuum deposition operates in a regime governed by ballistic transport where precursor molecules travel linearly from source to substrate with negligible collisions. Consequently, I and Br precursors lack opportunities for pre-mixing or chemical interaction before reaching the substrate surface.[58]

Upon impact, adatoms follow a hit-and-stick mechanism.[59] In the absence of solvent assistance, surface diffusion lengths of organic cations such as formamidinium iodide (FAI) and heavy metal halides remain relatively short. Rapid burial by subsequent flux arrivals freezes local stoichiometry in a non-equilibrium state. Therefore, temporal fluctuations in evaporation flux or spatial inhomogeneity in adsorption are permanently recorded in the vertical structure, rendering the film susceptible to compositional gradients absent in optimized solution-processed films.

Table 2 summarizes the core differences in precursor mixing kinetics between solution and vacuum methods.

Thermodynamic and kinetic disparities of precursors

The formation of these gradients stems from inherent physical property disparities between iodide and bromide precursors, which are amplified in the vacuum environment. Iizuka et al. established that $PbBr_2$ exhibits a distinct vapor pressure curve and high thermal stability, whereas PbI_2 is prone to thermal decomposition into metallic Pb and I_2 during sublimation.[60–62] This difference in sublimation enthalpy implies that PbI_2 and $PbBr_2$ respond asynchronously to source temperature fluctuations. In the co-evaporation processes, even minor thermal instabilities lead to mismatched flux oscillations, causing the Br/I ratio reaching the substrate to drift over time.

Furthermore, deposition kinetics are complicated by the sticking coefficient (S), which Gil-Escrig et al. highlighted is strongly dependent on substrate temperature.[63] Due to differing binding energies, Br species and I species possess distinct residence times on heated substrates, leading to selective re-evaporation. Rodkey et al. noted that in techniques such as close-space sublimation (CSS), this effect results in severe fractionation where deposited film composition deviates significantly from the source material, establishing vertical non-uniformity.[64]

This disparity in sticking kinetics can be described by the Arrhenius equation. The expression is

$$S = S_0 \exp\left(-E_{act} / k_B T\right). \qquad \text{(Equation 1)}$$

Here, E_{act} is the adsorption activation energy. For organic components such as FAI, the E_{act} is low. Therefore, the sticking coefficient drops rapidly with increasing temperature. For inorganic components such as PbI_2, the sticking coefficient is relatively stable. This mismatch leads to severe organic cation deficiency or Br/I ratio imbalances during high-temperature deposition.

Phase separation induced by vertical composition gradients

This process-induced vertical compositional heterogeneity precipitates photoinduced phase segregation. Fundamentally, a graded halide stoichiometry creates a graded band-gap profile. This generates a built-in energy funnel that directs photo-generated carriers toward local potential minima, typically iodide-rich strata.[65] Localized carrier accumulation occurs even under uniform illumination. According to polaron theory supported by Barker et al., high local carrier density induces severe lattice distortion via polaron formation, which destabilizes the lattice.[66] Consequently, the activation energy for halide demixing decreases exponentially in these iodide-rich regions.

Concurrently, continuous variation in lattice constants along the vertical axis generates coherent strain. Unlike porous solution-processed counterparts, vacuum-deposited films are characteristically dense and lack stress-relaxation channels such as pores or grain boundaries. This unrelaxed coherent strain creates an additional thermodynamic driving force where halide ions migrate to relieve elastic potential energy, thereby accelerating segregation.[67] Empirical evidence underscores this instability mechanism. Nasi et al. demonstrated that incongruent

Table 3. The transport behaviors of different precursors in the horizontal direction

Precursor type	Evaporation mode	Horizontal distribution	Impact on uniformity
Inorganic halides	quasi-collimated beam	highly dependent on geometric line of sight	pronounced lateral shadowing effects
Organic halides	diffusive cloud	pronounced non-directional character	sensor crosstalk and lateral spillover

evaporation rates in single-source deposition yield vertical-phase impurities such as $CsPb_2Br_5$.[68] Furthermore, Ghosh et al. revealed via depth-profiling hard X-ray photoelectron spectroscopy (HAXPES) that such vertical heterogeneity fosters deep-level metallic lead defects that act as precursors for device failure.[69]

Phase separation induced by horizontal composition gradients

Horizontal heterogeneity is prominent in multi-source co-evaporation systems. This phenomenon is especially prominent in multi-source co-evaporation systems. Horizontal compositional deviations primarily originate from the geometric layout of evaporation sources. The flux density generated by each source on the substrate plane follows the cosine distribution law. Iodide and bromide sources are located at different spatial coordinates. The superposition ratio of their flux at the substrate edges differs significantly from the central position.[70] This geometric mismatch establishes an inherent lateral stoichiometry gradient. For WBG perovskites, this mismatch directly leads to macroscopic band-gap non-uniformity.

A key kinetic factor is the difference in transport modes of precursor molecules. Inorganic precursors such as PbI_2 and $PbBr_2$ typically exhibit quasi-collimated directional beams. In contrast, organic precursors such as FAI or methylammonium iodide (MAI) form a diffusive cloud-like distribution when heated.[71] This cloud distribution leads to crosstalk between sensors. This interference makes it difficult for quartz crystal microbalances (QCMs) to precisely monitor local I/Br ratios.[70] This asymmetry in lateral diffusion implies that the substrate edges may remain in a Br-rich or I-rich state even if stoichiometry is achieved at the center. This initial horizontal deviation provides starting sites for subsequent photoinduced segregation.

Table 3 compares the transport behaviors of different precursors in the horizontal direction.

Substrate-induced lateral compositional deviation and chemical affinity disparities

Substrate surface chemical properties play a leading role in horizontal kinetics. Surface energy of different charge transport layers exhibits lateral fluctuations. These fluctuations alter the initial adhesion distribution of precursor atoms. Research by Abzieher et al. revealed vast differences in the sticking coefficients of FAI on various underlying layers.[72] For example, FAI adsorption is significantly higher on MeO-2PACz surfaces than on PTAA surfaces. MeO-2PACz surfaces are rich in phosphonic acid groups. If the underlying layer has horizontal unevenness or chemical degradation, this affinity disparity translates directly into lateral compositional heterogeneity.[70,73]

This horizontal chemical mismatch establishes lateral chemical potential barriers. These barriers promote the lateral diffusion of ions. The adatom diffusion distance on the substrate is limited by interface interactions during the early stages of co-evaporation. A specific halide component will preferentially nucleate in a micro-region if its binding energy is stronger there. This process leads to a relative enrichment of the other component in the surrounding areas.[74] This horizontal micro-scale segregation disrupts lattice continuity. It generates high-density defects at grain boundaries. These defects serve as fast channels for halide ion migration. They greatly accelerate the occurrence of the Hoke effect.[71,75,76]

Impact of substrate temperature field non-uniformity on horizontal kinetics

Horizontal gradients in substrate temperature are non-negligible factors in vacuum deposition. Temperature differences of several degrees often exist between the center and edges of the substrate during heating. Minor temperature gradients generate significant compositional fluctuations because the sticking coefficient of organic precursors such as FAI is extremely sensitive to temperature.[63] Temperature differences between the center and edges alter local adhesion kinetics. Hotter regions tend to form iodide-deficient phases.[74] This lateral thermal non-uniformity induces a non-uniform stress distribution.

Vacuum-deposited films generate thermal stress during cooling. Horizontal temperature gradients lead to mismatches in thermal expansion coefficients. This mismatch generates shear stress inside the film. This shear stress lowers the activation energy for ion exchange.[77] It prompts iodide ions to aggregate in low-stress regions. This migration triggers larger-scale horizontal phase segregation. Furthermore, the presence of temperature gradients leads to lateral variations in grain size. This disparity further exacerbates the transport asymmetry of photo-generated carriers in the horizontal direction.

Coupling mechanism of lateral carrier migration and phase segregation

Horizontal heterogeneity manifests its impact on photoinduced phase segregation through lateral carrier dynamics. Lateral compositional fluctuations lead to local band-gap ripples. These ripples form lateral potential wells within the film plane.[76] Under illumination, photo-generated carriers diffuse vertically and aggregate toward lateral potential minima.[71] This lateral charge accumulation effect is similar to the vertical energy funnel. It generates extremely high charge density within horizontal micro-regions. The model by Barker et al. indicates that carrier-induced lattice polarization greatly weakens local Pb–X bonds.[66] This weakening provides the driving force for the lateral rearrangement of halide ions.

Experimentally, conductive atomic force microscopy (AFM) and cathodoluminescence (CL) mapping have confirmed the existence of this lateral heterogeneity.[71,75] Grains with different orientations exhibit different surface potentials in WBG perovskites.[71] This difference drives lateral ion drift across grain boundaries. This lateral migration is often irreversible. It leads to the continuous growth of iodide-rich phases in specific horizontal micro-regions.[75,76] The evolution cycle of this lateral

Table 4. The synergistic contributions of vertical and horizontal kinetics to phase segregation

Dimension	Kinetic driving force	Segregation manifestation	Impact on device
Vertical	depth-dependent chemical potential gradient[76]	layered phase segregation[76]	FF drop and built-in field distortion[63,76]
Horizontal	lateral potential ripples and strain gradients[71,77]	spot-like local segregation[75]	significant V_{OC} loss and stability failure[71,76]

instability is longer than the vertical one.[76] Therefore, suppressing horizontal heterogeneity is a core goal for optimizing vacuum deposition processes.

Table 4 summarizes the synergistic contributions of vertical and horizontal kinetics to phase segregation.

Notably, these compositional gradients result primarily from non-ideal kinetic control. Gil-Escrig et al. demonstrated that precise regulation of the partial pressures of PbI_2 and $PbBr_2$, achieved by independently controlling four evaporation sources, effectively counterbalances thermodynamic disparities to yield homogeneous films.[78] This confirms that kinetic-induced phase instability can be suppressed through refined process engineering without compromising the inherent advantages of vacuum deposition.

The challenge of organic precursor volatility

While inorganic halide segregation stems from subtle kinetic disparities, challenges posed by organic precursors such as MAI and FAI are fundamentally more severe. Unlike inorganic salts such as PbI_2 and CsI, which exhibit sublimation behavior governed by classical kinetics, organic ammonium halides in vacuum undergo complex decomposition, non-linear vapor-pressure evolution, and surface-sensitive adsorption. These anomalies constitute the physical origin of the poor reproducibility frequently observed in vapor-deposited perovskites. Table 5 summarizes the thermal decomposition products, mechanisms, and impacts of organic precursors (FAI/MAI) under vacuum conditions.

Thermal decomposition of FAI

As research pivots toward the thermally robust $FAPbI_3$ system, the unique degradation chemistry of FAI warrants scrutiny.[79] Juarez-Perez et al. utilized coupled thermogravimetry-mass spectrometry to reveal that FAI does not simply sublime as molecular clusters (Figure 4A). Instead, it preferentially undergoes a deammoniation-polymerization reaction at temperatures as low as 95°C, yielding sym-triazine as the dominant thermodynamic product.[80]

This mechanism involves the condensation of three formamidine molecules, releasing ammonia. Since sym-triazine is a volatile, stable aromatic heterocycle unable to incorporate into the perovskite lattice, its formation represents a net loss of effective FA cations, leading to lead-rich non-stoichiometry. Furthermore, Thampy et al. confirmed that this decomposition pathway is catalytic on metal oxide surfaces such as NiO_x and TiO_2, implying that transport layer selection can inadvertently trigger precursor degradation during initial deposition stages.[85]

However, this degradation is not thermodynamically irreversible. Sahli et al. introduced the concept of degradation inversion, demonstrating that introducing an atmosphere rich in degradation products such as ammonia shifts chemical equilibrium back toward FAI formation. They showed that ammonia-assisted vapor transport actively cleaves the triazine ring to regenerate FA cations.[86] Most recently, Kuba et al. advanced this paradigm by establishing a dynamic equilibrium where the volatile decomposition products sym-triazine, ammonia, and HI serve as feedstock. They successfully synthesized phase-pure $FAPbI_3$ via this route, conclusively proving that thermal degradation of FAI is a reversible chemical feature (Figures 4B and 4C).[81] This thermodynamic insight provides a rationale for common empirical observations where systems operating at rough vacuum or with carrier gas assistance yield superior FAI film quality compared to high-vacuum counterparts. In these environments, elevated background pressure and reactive atmospheres actively promote the reverse reaction, thereby suppressing net decomposition.

Dissociative sublimation of MAI

MAI presents distinct kinetic complexities. Bækbo et al. established that MAI sublimes via proton transfer dissociation into neutral methylamine and hydrogen iodide gases (Figure 4D).[82] These low-molecular-weight gases possess high diffusion coefficients, creating a non-directional vapor cloud rather than a focused molecular beam, resulting in poor material utilization and severe chamber contamination.

Borchert et al. uncovered a counterintuitive phenomenon where high-purity MAI is often harder to control than industrial-grade material. Impurities such as hypophosphorous acid induce a sintering effect in MAI powder, preventing spitting and promoting stable evaporation flux. Pure MAI lacks this sintering aid and behaves erratically with rapid dissociation, leading to unstable rates.[87] Roβ et al. further elucidated that these impurities alter sublimation kinetics, transitioning the process from rapid dissociation to more controlled sublimation-like behavior, thereby enhancing process reproducibility (Figures 4E and 4F).[83]

Geometric effects of crucible shape and particle size

Beyond chemical factors, evaporation source geometry governs flux uniformity. Diercks et al. quantified the coupling between crucible geometry and particle size. Conical crucibles designed to maximize load induce a beam-focusing effect where vapor flux concentrates into a narrow forward lobe, leading to severe non-uniformity across large substrates.[84]

Furthermore, granular convection drives size segregation within precursor powder during heating. Since fine particles pack densely and increase tortuosity for escaping vapor, flux angular distribution drifts as the powder bed rearranges. Diercks et al. demonstrated that cylindrical crucibles and controlled particle-size distributions, such as pressed pellets, are essential for mitigating geometric artifacts and achieving Lambertian-like emission profiles suitable for large-area

Table 5. Thermal decomposition products and characteristics of organic precursors (FAI/MAI) in vacuum

Precursor	Product	Formula	Formation mechanism	Impact on film growth	Reference
FAI	formamidine	$CH(NH)NH_2$	proton transfer dissociation: $HC(NH_2)_2 + I^- \rightleftharpoons HC(NH)NH_2\uparrow + HI\uparrow$	the active ingredients that form $FAPbI_3$	Juarez-Perez et al.[80] and Thampy et al.[85]
	sym-triazine	$C_3H_3N_3$	condensation: $3CH(NH_2)_2^+ \rightarrow C_3H_3N_3 + 3NH_3 + 3H^+$	unable to embed into the perovskite lattice, resulting in severe loss of FA cations in the film and residual PbI_2	Stoumpos et al.,[79] Juarez-Perez et al.,[80] and Kroll et al.[88]
	hydrogen cyanide	HCN	fragmentation: $CH(NH)NH_2 \rightarrow HCN + NH_3$	thoroughly destroying the framework, causing irreversible loss of components; the high toxicity poses a challenge to safety	Juarez-Perez et al.[80] and Thampy et al.[85]
	ammonia	NH_3	byproduct	introducing excessive NH_3 atmosphere to suppress decomposition equilibrium and even cracking the triazine ring to regenerate FA cation	Sahli et al.[86] and Kuba et al.[81]
MAI	methylamine	CH_3NH_2	disproportionation: $CH_3NH_3I \rightarrow CH_3NH_2\uparrow + HI\uparrow$	forming a "gas cloud" instead of a molecular beam leads to low material utilization efficiency; the extremely low adhesion coefficient on the QCM gold electrode leads to the failure of rate monitoring	Baekbo et al.[82] and Roß et al.[83]
	hydrogen iodide	HI	disproportionation	need to react with methylamine again on the substrate surface to generate MAI	Baekbo et al.[82] and Kim et al.[89]
	MAI clusters	$(CH_3NH_3I)_n$	impurity-induced sublimation: assisted by phosphorus-containing impurities, liquid-phase sintering is used to suppress decomposition and achieve quasi-molecular beam sublimation	significantly improve the stability of QCM monitoring and the controllability of sedimentation rate, reducing splashing	Borchert et al.[87] and Roß et al.[83]

deposition (Figures 4G–4I).[84] This distribution pattern allows vapor to cover larger solid angles, facilitating uniform film deposition through substrate rotation and multi-source superposition.

Metrological limitations of QCM monitoring

Standard rate monitoring via QCM encounters significant limitations regarding sticking coefficient mismatch when applied to organic precursors. Although the Sauerbrey equation assumes a unity sticking coefficient in which every molecule striking the sensor adheres, the reality for organic ammonium halides is complex.[63] Kim et al. and Kroll et al. revealed that on standard inert gold electrodes, species such as MAI and FAI exhibit near-zero sticking coefficients, an issue that is exacerbated when sensor temperatures rise due to source radiation.[88,89] This thermal effect triggers rapid re-evaporation from the sensor surface, causing flux readings to be drastically underestimated despite high vapor densities. The result is a destabilized feedback loop manifesting as erratic rate oscillations and poor batch-to-batch reproducibility.

Crucially, this thermal artifact extends beyond re-evaporation to active material degradation. Given the low thermal conductivity of organic layers, incidental thermal radiation from the evaporation source accumulates on the sensor, triggering the *in situ* decomposition of thermally labile precursors such as FAI into volatile sym-triazine. This mass loss results in the QCM registering negative rates or severe drift.[80] Bhowmik et al. demonstrated that this radiative heating constitutes a systemic hazard where thermal radiation generated during overlayer evaporation is sufficient to induce degradation in the underlying perovskite film itself, such as surface iodide loss, confirming that source radiation poses a dual threat to metrological accuracy and device integrity.[90]

This metrological error is compounded by surface-chemical disparities between the sensor and substrate. Adsorption of organic precursors is governed by a dipole-induced mechanism, meaning MAI adsorbs far more efficiently on reactive lead halide surfaces than on clean metal electrodes.[89] Consequently, a clean QCM sensor fails to capture the accelerated growth rate occurring on the device substrate where perovskite formation is active. Operators relying on skewed QCM readings inevitably overdose the organic component, driving film composition away from the desired stoichiometry. This confirms that traditional physical metering is ill-equipped to monitor what is essentially a reactive chemical process.

To circumvent these metrological limitations, recent strategies shifted toward indirect referencing and high-pressure

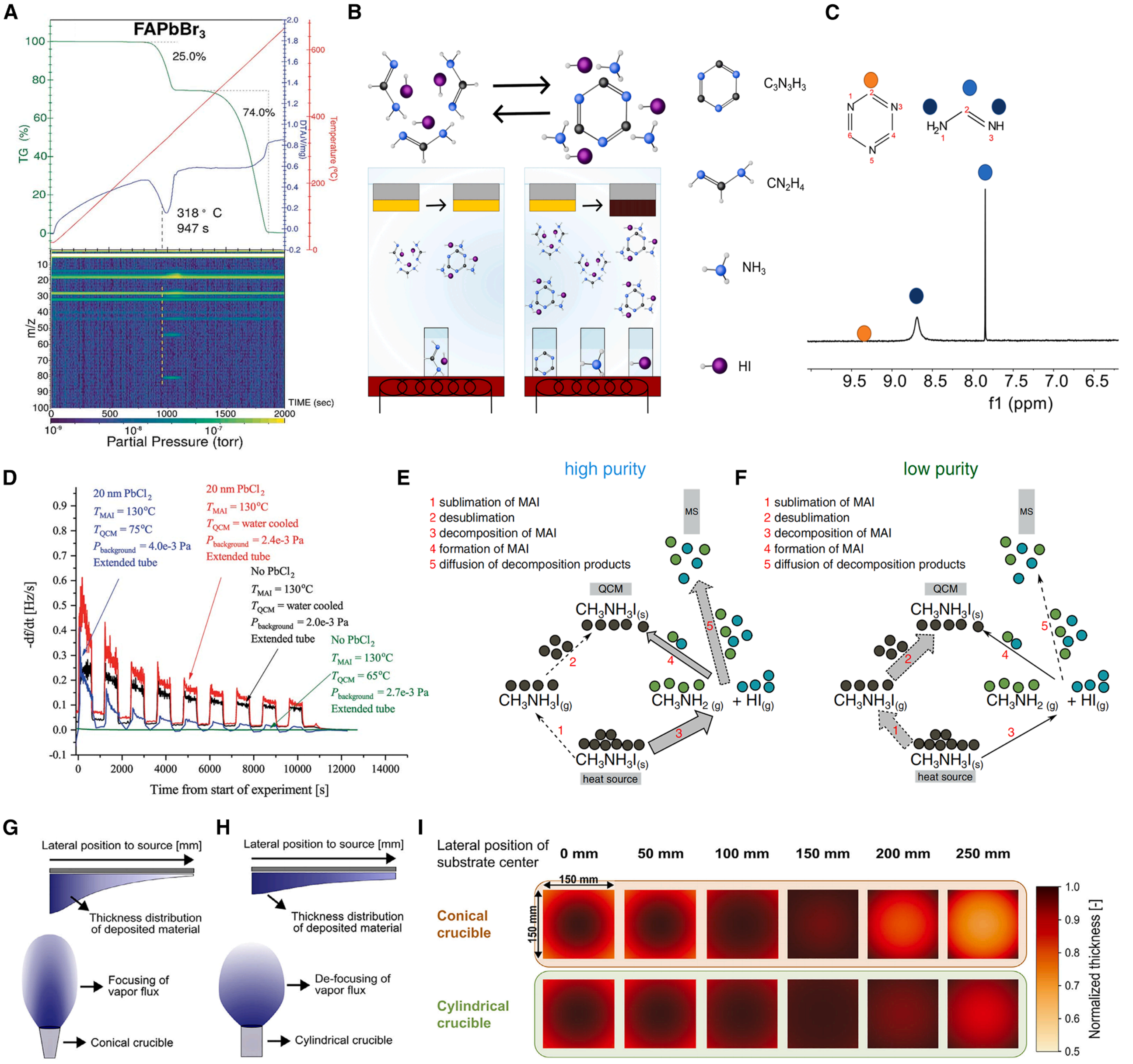

Figure 4. The challenge of organic precursor volatility

(A) Tandem thermogravimetry-differential thermal analysis/mass spectrometry (TG-DTA/MS) coupled experiments for the FAPbBr$_3$ hybrid halide perovskites. The top images show the archetypal two-step-type mass-loss thermogravimetry (TG) pattern (green line) for hybrid perovskites. The bottom images show the MS traces simultaneously recorded (1–100 amu) during the experiment. The gray dashed line indicates the initial temperature (time) of the first detection of released gases during the high-temperature thermal degradation. Reproduced with permission.[80] Copyright 2019, The Royal Society of Chemistry.

(B) Schematic depiction of the reaction scheme. When using FAI as a precursor, the partial pressure is low, and the FAI decomposes to components such as s-triazine, ammonia, and hydrogen iodide (HI), hindering the reaction. When using s-triazine, ammonia, and HI, the components can be completely evaporated above the boiling point at room temperature, and the components react to form FAI, resulting in film conversion.

(C) ^{1}H NMR of six perovskite films dissolved in DMSO-d$_6$ showing FA incorporation with undetectable levels of s-triazine and ammonia.

(B and C) Reproduced with permission.[81] Copyright 2025, American Chemical Society.

(D) The observed rates of the MAI sticking experiments using the forward-facing QCM, where TMAI is the MAI source temperature, TQCM is the QCM temperature, and Pbackground is the background pressure. Extended tube means that the distance from the source to the sensor was 19.5 cm. The black curve shows the rate measured when the QCM crystal is water cooled and blank. The red curve shows the rate when the QCM crystal is water cooled and has 20 nm of PbCl$_2$ deposited on it. Finally, the blue curve shows the rate when the QCM crystal is heated to 75°C and has 20 nm of PbCl$_2$, while the green curve shows the rate when a blank crystal heated to 65°C is used. In all cases, the signal was chopped using 10-min intervals. Reproduced with permission.[82] Copyright 2018, The Royal Society of Chemistry.

(legend continued on next page)

confinement. Zanoni et al. proposed a relative mass approach in which organic flux is inferred by monitoring total perovskite mass formed on a secondary sensor pre-coated with PbI_2, thereby matching sensor chemistry to the substrate.[91] Alternatively, Rodkey et al. demonstrated that transitioning to CSS effectively bypasses long-distance flux monitoring needs. In CSS, high local vapor pressure establishes a self-regulating dynamic equilibrium between source and substrate, rendering the process robust against fluctuations that plague high-vacuum physical vapor deposition.[64] These advances suggest that future industrial tools must integrate surface-sensitive or pressure-based metrology to achieve the precision required for perovskite manufacturing.

The volatility of organic precursors is thus a multifaceted challenge spanning thermal decomposition chemistry, non-ideal gas dynamics, and metrology limitations. Mastering these variables requires a departure from simple thermal evaporation toward reactive vapor transport, such as ammonia-assisted, and advanced source designs, such as cylindrical, pelletized sources.

The solid-state growth constraints in solvent-free environments

While the challenge of organic precursor volatility highlights the chemical volatility of precursors, fundamental physical hurdles emerge upon their arrival at the substrate. In solution processing, the wet environment allows for solvent-assisted reorganization, which heals defects via dissolution-recrystallization. Conversely, vacuum deposition operates as a dry physics process. This absence of a fluid medium exposes crystallization physics to thermodynamic and geometric constraints and chemical adsorption kinetics.

Physical principles and growth kinetics

High-quality fabrication of WBG perovskite films via thermal evaporation requires moving beyond empirical trial and error to a rigorous understanding of the underlying physics. Unlike solution processing, which is governed by fluid dynamics and solvent evaporation, vacuum deposition is a kinetic process dictated by phase transitions, ballistic transport, and surface adatom dynamics.

The physical abstraction of thermal evaporation comprises four distinct kinetic stages: precursor vaporization, vacuum transport, condensation, and film growth (Figures 5A and 5B). The process of vaporization initiates at the source, where thermal energy overcomes the cohesive energy of the solid precursor. For multi-component perovskites, the challenge lies in the exponential dependence of vapor pressure on temperature. Minor thermal fluctuations can lead to significant deviations in the flux ratio between CsI and PbI_2, necessitating precise temperature control rather than simple current regulation.

In a high-vacuum environment ($<10^{-3}$ Pa), the mean free path of vapor molecules exceeds the source-to-substrate distance, ensuring a collision-free ballistic transport regime. This linearity preserves the kinetic energy of the molecules but imposes strict geometric requirements to prevent shadowing effects, particularly on textured substrates used in TSCs. Upon reaching the substrate, deposition efficiency is governed by the sticking coefficient (S). For inorganic halides such as PbI_2, S is typically unity. However, for volatile organic precursors, S is non-unity and highly sensitive to substrate temperature (T_{sub}) and surface coverage, creating a dynamic equilibrium between adsorption and re-evaporation that dictates the final stoichiometry.

Achieving large-area uniformity relies on understanding the spatial emission characteristics of the evaporation source. While an idealized point source emits isotropically ($1/r^2$ decay), practical sources (e.g., crucibles) function as small surface sources where flux emission follows Knudsen's cosine law (Figure 4C).

$$J_{inc}(l) = \frac{\dot{m}}{\pi r^2} \cdot \cos\phi \cos\theta \qquad \text{(Equation 2)}$$

This physical model reveals that the flux density is proportional to the cosine of the emission angle ($cos\phi$) and the incidence angle ($cos\theta$), and $\dot{m}$ is the total mass evaporated per unit time from the source (unit: $kg \cdot s^{-1}$). Consequently, the deposition rate forms a lobe-shaped distribution, peaking at normal incidence and dropping significantly at the periphery. This intrinsic non-uniformity constitutes the theoretical basis necessitating planetary substrate rotation and optimized source-to-substrate distances (r) in perovskite co-evaporation systems.

The microstructural evolution of the film is determined by the thermodynamic competition between adatom-substrate interaction and adatom-adatom interaction. Thin-film growth generally follows three modes (Figure 5B). When $\gamma_f + \gamma_i > \gamma_s$, island growth (Volmer-Weber) occurs. When $\gamma_f + \gamma_i < \gamma_s$, layer-by-layer growth (Frank-van der Merwe) occurs. For perovskites deposited on heterogeneous transport layers (e.g., organic polymers or metal oxides), Volmer-Weber island growth is typically the dominant mechanism due to a high surface energy mismatch. This explains the common experimental observation of pinholes and shunting pathways in ultra-thin evaporated perovskite layers. To promote continuous film formation, kinetic control strategies, such as increasing the deposition rate to boost nucleation density or optimizing T_{sub} to enhance adatom surface diffusion, must be employed to facilitate the coalescence of islands into a compact, pinhole-free film. Evaporation methods can be primarily categorized as follows: sequential evaporation (Figure 5D), co-evaporation (Figure 5E), solution-assisted evaporation (Figure 5F), and other evaporation processes.

(E and F) Schematic illustration of sublimation and decomposition processes occurring when MAI is heated in vacuum. For high-purity MAI: (E) the main path (indicated by thick arrows) is the decomposition into methylamine and hydrogen iodide. For low purity, (F) is the main path for the sublimation and desublimation. Reproduced with permission.[83] Copyright 2022, Wiley-VCH.

(G and H) Schematic of the FAI vapor flux and deposition on the substrate from a conical and cylindrical crucible, respectively.

(I) Heatmaps of calculated thickness distribution (normalized) over a rotating substrate holder at different lateral positions to source (0, 50, 100, 150, 200, and 250 mm).

(G–I) Reproduced with permission.[84] Copyright 2025, Wiley-VCH.

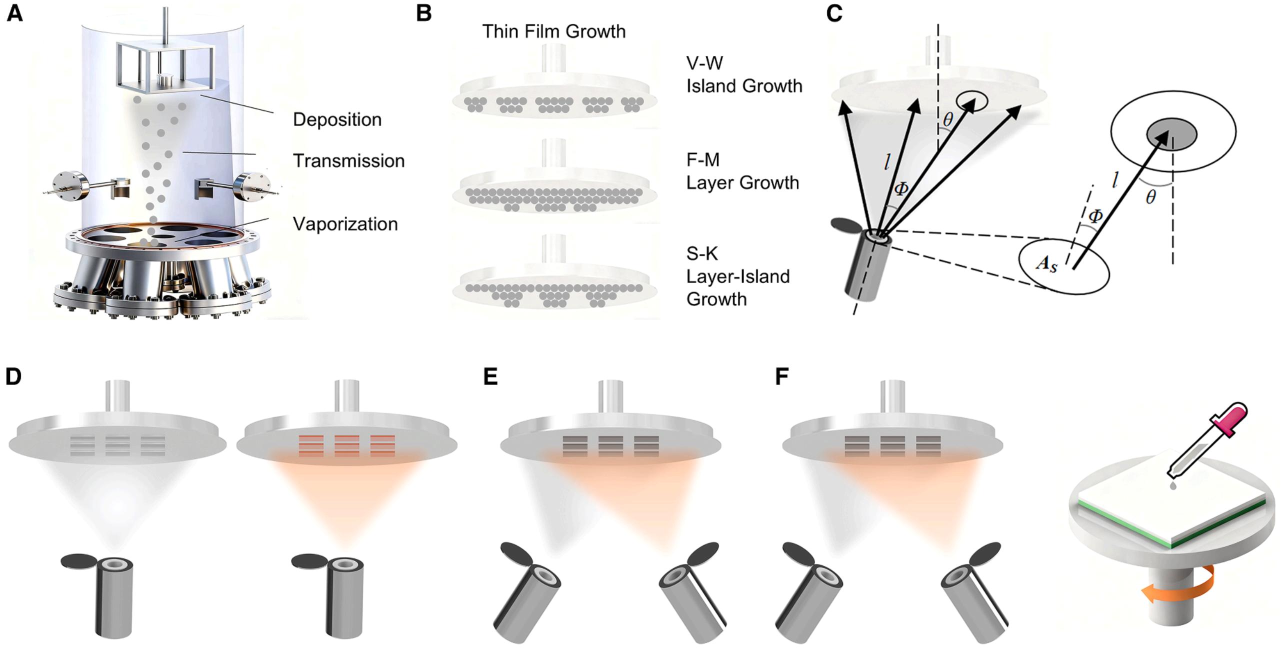

Figure 5. Schematic diagram of the evaporation principle

(A) The physical process of thermal evaporation thin-film deposition.
(B) Three different thin-film growth modes.
(C) The physical abstraction of the evaporation source model.
(D) Sequential evaporation.
(E) Co-evaporation.
(F) Solution assisted evaporation.

The contradiction between the thin-film growth mode and compactness

A central conflict in vapor deposition exists between the thermodynamic drive for island formation and the kinetic necessity for continuous coverage. According to the Bauer criterion, growth modes are dictated by the balance of surface energies. For perovskites depositing on common transport layers, the sum of film and interface energy typically exceeds substrate surface energy, thermodynamically mandating a Volmer-Weber island growth mode.[92] Parrott et al. provided conclusive evidence for this mechanism in co-evaporated $MAPbI_3$, revealing that films initiate as isolated 8-nm-high crystallites. These islands must grow and coalesce to cover the substrate. However, due to limited mass transport, deep voids between islands often persist as pinholes in ultra-thin layers.[93]

This islanding is exacerbated by hit-and-stick kinetics. At low substrate temperatures required to protect organic interlayers, adatoms lack sufficient thermal energy to diffuse across the surface and fill voids between nuclei. Recent work by Wang et al. confirmed the severity of this issue by demonstrating that a continuous film could be achieved only by artificially altering surface energy via a pre-deposited SnI_2 layer to force a transition to Frank-van der Merwe layer-by-layer growth.[94] This underscores that without intervention, the intrinsic tendency of vacuum deposition yields rough, defect-rich interfaces.

Residual thermal stress and lattice strain

In exploring the mechanical integrity of vapor-deposited WBG perovskite thin films, it is essential to precisely define the influence of thermal history on the lattice state. Current typical vapor processes generally involve precursor deposition on room temperature substrates, followed by controlled thermal annealing to achieve crystallization. Research by Gil-Escrig et al. indicates that vacuum co-evaporation exhibits extreme sensitivity to the kinetic equilibrium of organic cations.[63] To ensure the stoichiometry of the film, maintaining a low substrate temperature is critical. Roβ et al. further confirm that tuning the substrate temperature between −25°C and 60°C can optimize nucleation kinetics, whereas excessively high substrate temperatures lead to the thermal desorption of organic components, thereby inducing non-stoichiometric defects such as lead iodide.[74] Findings from Gil-Escrig et al. also demonstrate that by leveraging the solvent-free nature of vapor methods, phase-pure cubic perovskites can be obtained without the need for extreme high-temperature environments.[95]

Although vapor deposition and solution-based methods differ in their initial film formation mechanisms, they exhibit highly convergent mechanical responses during thermal annealing and subsequent cooling to room temperature. The root of this phenomenon lies in the significant mismatch of the coefficient of thermal expansion (CTE) between the perovskite and the rigid substrate. Zhao et al. provides a deep analysis of this physical logic, noting that because the CTE of soft perovskite materials is much larger than that of glass or conductive glass substrates, the cooling process inevitably generates intense in-plane tensile stress within the perovskite lattice.[96] The Volmer-Weber growth model established by Coppeta et al. reveals the intrinsic evolutionary path of stress transitioning from compression to tension.[92] This thermal-history-driven residual stress is universal across different deposition methods, thereby diminishing the purported unique advantages of vapor deposition in reducing mechanical strain.

For WBG perovskites, this residual lattice strain not only compromises mechanical durability but also acts as a chemical catalyst for inducing halide phase segregation. In bromide-rich systems, tensile strain lowers the energy barrier for ion migration, making halide vacancies more mobile under illumination. Quantitative research by Kong et al. suggests that the strain field directly alters the physical properties of the material by distorting the octahedral structure.[97] Observations from Wang et al. show that this strain is more concentrated on the film surface.[98] The tensile state accelerates the formation of iodide-rich domains, leading to a significant deterioration in the photostability of WBG perovskites. Rijal et al. posit that if this residual strain deposited by thermal history is not mitigated at its source, the long-term operational stability of the device will be difficult to guarantee through external encapsulation alone.[99]

To overcome this challenge, strain engineering has become a research hotspot in the field of WBG perovskites. Yang et al. demonstrate the significant effect of utilizing surface molecular modulation techniques to release residual tensile strain, where the introduction of long-chain organic salts successfully establishes a compressive strain field, effectively suppressing phase segregation and enhancing efficiency.[100] Kapil et al. explore the role of compositional tuning in stress relief, while research by Yuan et al. further proves that devices fabricated via all-vacuum methods can achieve fundamental improvements in intrinsic thermal stability under high-temperature environments if strain evolution is effectively managed during initial film formation.[73,101] These advancements suggest that future research should focus on precise thermal history management to enhance the intrinsic chemical potential stability of WBG perovskites by regulating microscopic stress fields.

Even if a continuous film forms, it is mechanically compromised by the thermal history of the vacuum process. Vacuum deposition typically requires elevated substrate temperatures of 100°C–200°C to promote crystallinity. Upon cooling to room temperature, the significant mismatch in the CTE between soft perovskites and rigid substrates creates substantial tensile stress. Coppeta et al. modeled this stress evolution during the coalescence of Volmer-Weber islands, identifying a transition from compressive to tensile stress capable of inducing cracking.[92]

Pandey et al. highlighted that this residual lattice strain constitutes a chemical issue rather than merely a mechanical one. Tensile strain lowers the activation energy for ion migration, effectively catalyzing phase segregation, as discussed in the halide segregation dilemma in vacuum. Thus, the thermal processing inherent to vacuum deposition inadvertently predisposes the lattice to subsequent degradation.[102]

Geometric shadowing on textured substrates

For tandem applications, a geometric limitation emerges. While vapor deposition is recognized for its ability to coat textured substrates, the reality is constrained by line-of-sight transport. As analyzed by Abzieher et al., vapor flux travels linearly. On micron-scale pyramidal textures of silicon bottom cells, this leads to geometric shadowing, where windward facets receive heavy deposition while leeward facets remain starved. This microscopic thickness inhomogeneity results in local shunting paths and varying current densities.[103]

To counter shadowing, multi-axis substrate rotation is employed. However, this creates a trade-off where rotation drastically reduces effective deposition rates and material utilization efficiency. Abzieher et al. argue that this geometric constraint challenges the high-throughput potential of vacuum technology, forcing a compromise between conformal coverage and manufacturing speed.[103]

Chemical adsorption kinetics on textured substrates

In exploring the film formation mechanisms of vapor-deposited PSCs, while geometric constraints at the physical dimensions dominate at the macroscopic level, chemical adsorption effects on the substrate surface exert a far more profound influence on film quality during atomic-scale nucleation and growth processes. Traditional geometric shadowing models, primarily based on line-of-sight transport theory, explain the uneven flux distribution on the sidewalls of micrometer-scale pyramids caused by the rectilinear propagation of precursor vapor molecules.[104]

However, when the research focus shifts to the deposition of WBG perovskites on industrial-standard textured silicon substrates, this singular physical model fails to account for the significant chemical composition drifts observed during deposition. Precursor molecules do not immediately become fixed upon contacting the substrate; instead, they undergo a complex process of adsorption, desorption, and surface diffusion, all of which are highly dependent on the chemical characteristics of the species and the thermodynamic state of the substrate surface.

Chemical adsorption in the vapor deposition environment is essentially determined by the overlapping of electronic orbitals or electrostatic interactions between precursor molecules and substrate surface atoms. For multi-component systems involved in WBG perovskites, such as FAI, CsI, and PbI_2, the adsorption energies of different species on silicon substrates or HTL surfaces vary by orders of magnitude.[105] This discrepancy leads to the phenomenon of non-equilibrium adsorption; even in regions that geometrically receive precursor flux, a significant reduction in effective deposition rates occurs if the chemical adsorption energy is insufficient to balance the thermal motion of the molecules.[104] Table 6 summarizes the adsorption kinetic parameters of key precursors during the co-evaporation process.

At the moment precursor molecules arrive at the substrate surface, their conversion efficiency is primarily limited by the sticking coefficient. The sticking coefficient, defined as the ratio of adsorbed atoms to the total number of incident atoms, directly dictates the final stoichiometry of the thin film during the co-evaporation process.[104] For organic cation precursors, the low sticking coefficient stems from their complex molecular structures and weak surface interaction forces. Given the high vapor pressure of these molecules in a vacuum, their residence time on the substrate surface is extremely short, often leading to desorption before nucleation occurs.

Table 6. Adsorption kinetic parameters of perovskite precursors during vapor deposition

Precursor species	Adsorption type	Sticking coefficient (*S*) range	Adsorption kinetic characteristics
PbI_2	strong chemisorption	0.85–1.00	high adsorption stability; acts as a structural scaffold; *S* is nearly independent of moderate substrate temperature fluctuations
$PbBr_2$	strong chemisorption	0.80–0.95	similar to PbI_2; exhibits competitive occupancy with other halides during co-evaporation
$PbCl_2$	chemisorption	0.75–0.90	high thermal stability; often used as a seed layer to enhance the adsorption probability of subsequent organic components
CsI	moderate-to-strong chemisorption	0.60–0.85	strong electrostatic coupling with polar substrates (e.g., NiO_x); significantly more stable than organic salts
CsBr	moderate-to-strong chemisorption	0.55–0.80	reliable Cs^+ source for wide-band-gap perovskites; S decreases slightly as substrate temperature (T_{sub}) increases
CsCl	mixed physisorption/chemisorption	0.50–0.75	frequently used for seed-layer engineering; modifies surface wetting to regulate the nucleation of FAI
FAI	weak chemisorption	0.05–0.25	highly volatile; relies on hydrogen bonding; extremely sensitive to T_{sub}; *S* drops sharply above 60°C
MAI	physisorption/weak chemisorption	0.01–0.15	high saturation vapor pressure; low residence time on surface; requires significant over-stoichiometric flux
MACl	transient physisorption	<0.01	sacrificial additive; assists in grain growth but almost completely desorbs from the final film due to high volatility

In contrast, inorganic precursors, which possess stronger chemical affinity, undergo a film formation process that more closely resembles classical condensation growth modes.[106] On textured substrates, this chemical heterogeneity of sticking coefficients triggers a complex vapor-partitioning effect. When different precursors are deposited simultaneously, inorganic components with high sticking coefficients tend to adsorb completely upon the first collision, whereas organic components with low sticking coefficients undergo multiple scatterings between the pyramidal slopes. This coupling of physical motion and chemical capture leads to a compositional imbalance, with a propensity for excessive lead iodide phases on the sidewalls and organic enrichment in the pyramid valleys.[104] This compositional partitioning represents a primary source of non-radiative recombination and spatial band-gap heterogeneity in WBG devices, manifesting as a V_{OC} deficit.[107]

The micrometer-scale pyramids of textured silicon substrates are predominantly composed of (111) crystal facets, implying that the growth of perovskite thin films proceeds on an anisotropic surface with well-defined chemical characteristics.[108] The chemical adsorption energies of different precursor molecules vary significantly between the (111) and (100) facets, an effect that influences not only the compositional distribution but also determines the preferred orientation of the thin film.[109] Studies indicate that the (111) facet of the perovskite lattice features denser atomic packing and lower surface energy, providing enhanced resistance to phase transitions induced by environmental stressors.[109] During vapor deposition, introducing functional molecules such as 4-fluorobenzylamine hydroiodide (4-FBA) allows for preferential adsorption on specific surfaces of the perovskite nuclei, thereby altering growth rate ratios and enabling preferred orientation control.[110] Table 7 compares the adsorption characteristics across different interface regions and their impact on growth.

To address mismatched chemical adsorption, researchers have developed interface-engineering techniques to reshape kinetic processes on textured substrates. Introducing specific seed layers, such as pre-depositing ultra-thin CsI or CsCl on the HTL, provides a high density of active sites, enhancing the chemical adsorption strength of subsequent precursor vapors.[112,113] The work by Li et al. established a stable adsorption platform by introducing 3,3,3-trifluoropropyl-trimethoxysilane, effectively increasing the sticking coefficient of organic cations on the pyramidal sidewalls.[104] This strategy balances film formation rates across different facets through chemical means, yielding perovskite films with uniform composition and high phase purity. Furthermore, competitive adsorption among multiple components necessitates precise adjustment of evaporation flux ratios and substrate temperature to maintain dynamic equilibrium. This equilibrium requires not only physical flux matching but also chemical matching of adsorption rates to overcome the phase segregation issues common in WBG systems.[114,115]

Table 7. Facet-dependent adsorption characteristics on textured substrates

Facet features	Surface energy	Primary adsorption preference	Impact on film growth	Reference
Si(111) pyramid sidewalls	higher	preferential inorganic adsorption: strong adsorbates (e.g., PbI_2) are captured upon first impact	induces vertical grain growth; prone to local organic deficiency due to high capture rate on sidewalls	Sukow et al.[108]
Si(100) pyramid valleys	lower	organic enrichment via secondary scattering: weak adsorbates (e.g., FAI/MAI) accumulate in valleys after reflecting off sidewalls	prone to interface voids or local phase segregation (organic-rich); increases carrier recombination risks	Wang et al.[111]
Perovskite (111) facet	lowest	stable halogen-terminated adsorption: thermodynamically stable; facilitates continuous and uniform coverage	enhances thermal stability and charge carrier transport efficiency; suppresses ion migration	Gao et al.[109]

Polymorph competition in solvent-free environments

Finally, the absence of solvent intermediates complicates photoactive phase stabilization. In solution processing, intermediate complexes lower the energy barrier for forming the black α-phase. In vacuum, precursors must react directly in the solid state. Susic et al. demonstrated this difficulty in $CsPbI_3$, where the thermodynamically stable yellow δ-phase dominates at room temperature. Without chemical additives to modify formation energy, obtaining pure black-phase $CsPbI_3$ via vacuum deposition proves exceptionally difficult.[116]

To overcome this, Gil-Escrig et al. and Susic et al. showed that compositional engineering is strictly required to kinetically trap the black phase. However, this reintroduces multi-source control complexity discussed in the halide segregation dilemma in vacuum, creating a recursive challenge where solving phase purity exacerbates compositional heterogeneity.[78,116]

The intrinsic challenges outlined in the intrinsic challenges of vapor-deposited WBG perovskites, spanning thermodynamic instability, kinetic volatility, and microstructural constraints, indicate that vacuum deposition of WBG perovskites is a complex technology. Addressing these fundamental limitations requires developing specialized process methodologies, which are reviewed in the subsequent section.

VAPOR-PHASE METHODOLOGIES FOR WBG PEROVSKITE THIN FILMS AND APPLICABILITY ASSESSMENT

Thermal evaporation

Sequential evaporation

While Volmer-Weber kinetics predispose vacuum-deposited films to pinhole formation, sequential evaporation offers a kinetic pathway to counteract this tendency. By fundamentally decoupling precursor mass transport from the phase-transformation reaction, this method introduces a volume expansion mechanism absent in co-evaporation.

The fundamental rationale involves depositing a templating inorganic framework, typically layered PbI_2, followed by the intercalation of organic or alkali cations such as FAI and CsBr. Crucially, the transformation from hexagonal PbI_2 to cubic perovskite accompanies an approximate 2-fold unit cell volume expansion.[117] This expansion exerts an intrinsic squeezing effect where growing perovskite crystallites fill the free volume and close voids left by initial island growth. This mechanism transforms a porous inorganic template into a compact, pinhole-free absorber, significantly enhancing shunt resistance.[117,118]

However, this volume expansion presents inherent trade-offs regarding process scalability. Rapid surface expansion creates a dense perovskite crust acting as a blocking layer that retards organic vapor infiltration into the buried PbI_2 interface.[119] Consequently, reaction kinetics shift from fast pore diffusion to sluggish solid-state lattice diffusion. As observed by Kim et al. and Du et al., this phenomenon often leaves unreacted PbI_2 residues at grain boundaries near the substrate, forming insulating barriers that impede charge extraction.[118,120] This surface crystallization renders sequential evaporation problematic for fabricating thick absorbers exceeding 500 nm.

More critically, volume expansion confined by rigid substrates induces significant internal stress.[121] Bush et al. utilized *in situ* wafer curvature measurements to reveal that the conversion process generates substantial biaxial in-plane compressive stress.[122] While moderate stress densifies the film, excessive accumulation exceeds critical buckling loads, triggering strain-release mechanisms such as surface wrinkling or delamination. Wu et al. and Nath et al. further noted that this residual stress constitutes a stability hazard, as it lowers the activation energy for ion migration and accelerates fatigue degradation under operational conditions.[123,124]

Consequently, diffusion constraints directly impair microstructural integrity. Figure 6A depicts a schematic diagram of the traditional sequential evaporation preparation process. Xiang et al. provided evidence that conventional one-step annealing of sequentially deposited $CsBr/PbBr_2$ stacks resulted in films containing visible voids and small micron-sized grains. This porosity arises because the rigid perovskite lattice forms at the interface before bulk precursors fully merge.[125] To overcome this, Xiang et al. introduced a two-step annealing strategy utilizing pre-melting $PbBr_2$ to facilitate liquid-phase assisted diffusion, which successfully densified the film and increased grain size (Figure 6B).[125] Similarly, Hua et al. employed pressure-assisted annealing to mechanically drive interdiffusion while suppressing volatile component loss.[126]

While annealing optimization alleviates symptoms, layer-by-layer architectures address the root cause by shortening the diffusion path. Lin et al. pioneered a thousand-layer alternating deposition for $CsPbI_2Br$ by slicing precursors into atomic-scale sub-layers. This created a pseudo-mixed state, minimizing the reaction distance (Figure 6C) and enabling the rapid formation

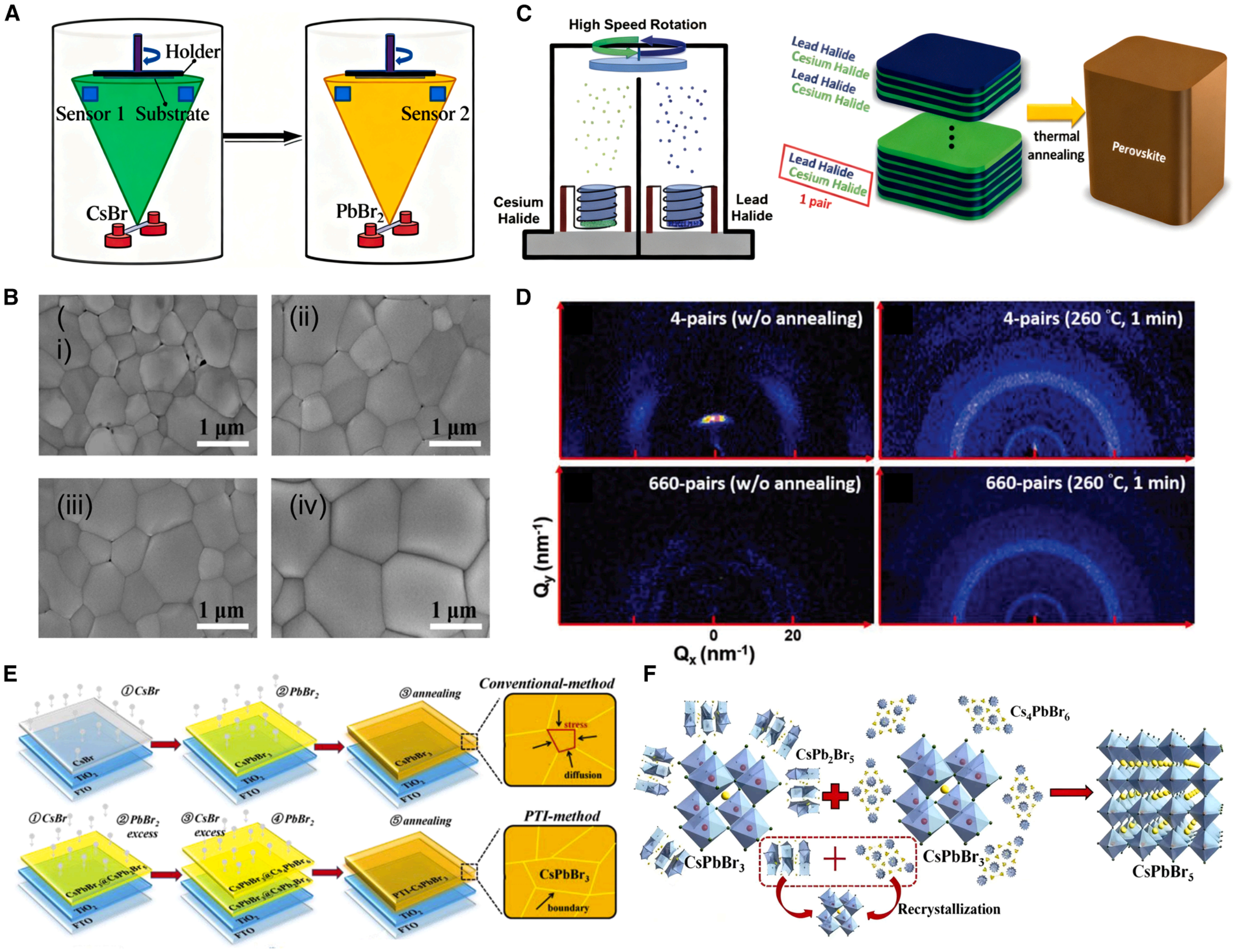

Figure 6. Sequential evaporation

(A) Schematic diagram of the conventional sequential evaporation preparation process.

(B) Surface scanning electron microscopy (SEM) images of (i) one-step sintering (OSS), (ii) two-step sintering (TSS) at 200°C, (iii) TSS at 250°C, and (iv) TSS at 300°C of $CsPbBr_3$ films. Reproduced with permission.[125] Copyright 2019, Elsevier.

(C) Schematic of the Cs-based perovskite alternative deposition process.

(D) 2D grazing-incidence wide-angle X-ray scattering (GIWAXS) patterns of a 4-pair as-deposited film, with films annealed at 260°C for 1 min; and a 660-pair as-deposited film, with films annealed at 260°C for 1 min.

(C and D) Reproduced with permission.[127] Copyright 2019, Wiley-VCH.

(E) The conventional and phase-transition-induced (PTI) methods for the $CsPbBr_3$ thin film.

(F) The formation from the derivative phase ($CsPb_2Br_5$/Cs_4PbBr_6) to the $CsPbBr_3$ inorganic perovskite phase.

(E and F) Reproduced with permission.[128] Copyright 2019, Elsevier.

of isotropic, defect-poor crystals without requiring deep diffusion (Figure 6D).[127] Hutter et al. validated this approach in $CsPbI_3$ and achieved microsecond-scale lifetimes.[129]

Beyond physical stacking, manipulating chemical reaction pathways offers control. Tong et al. proposed an excess deposition strategy involving excess $PbBr_2$ to form a Cs-deficient derivative phase, $CsPb_2Br_5$ (Figure 6E). Upon annealing, this core-shell intermediate undergoes controlled recrystallization, releasing excess $PbBr_2$ and converting into the pure perovskite phase. This phase-transition-mediated growth retards crystallization rates, significantly reducing trap density (Figure 6F).[128]

Sequential evaporation fundamentally trades process complexity for stoichiometric precision. While it resolves pinhole issues via volume expansion, its scalability to thick films is restricted by intrinsic self-limiting diffusion and induced stress. This limitation naturally motivates the industry toward a faster alternative: co-evaporation.

Co-evaporation

While sequential evaporation circumvents hit-and-stick issues via diffusion-mediated expansion, its reliance on solid-state transport inherently creates a vertical diffusion gradient, limiting applicability to complex, thick, or multi-cation absorbers. To

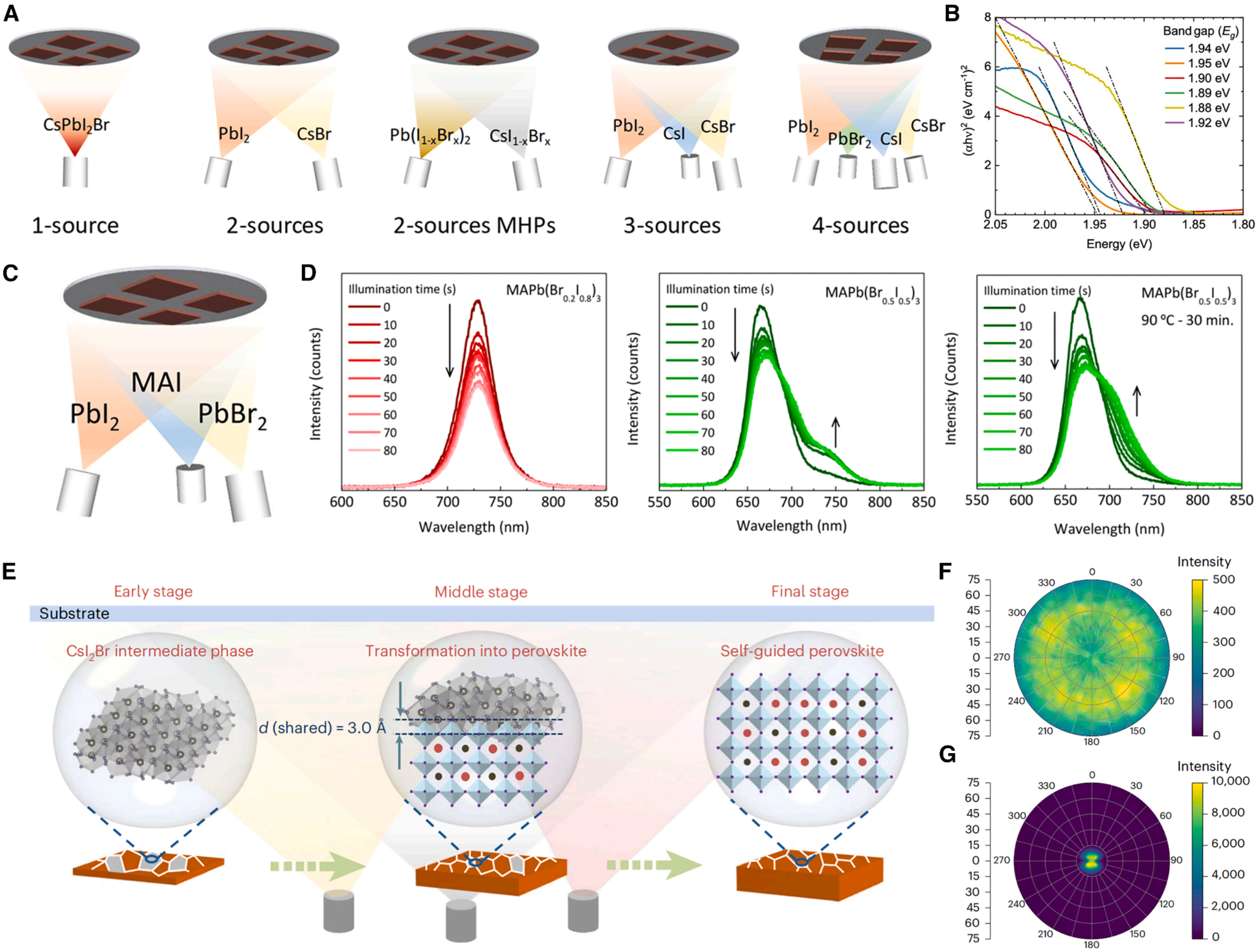

Figure 7. Co-evaporation

(A) Schematics of the type of thermal vacuum deposition methods investigated in the preparation of $CsPbI_2Br$ thin films.

(B) The corresponding Tauc plots (with the estimated band-gap energy) spectra for $CsPbI_2Br$ thin films deposited on glass with several different vacuum deposition techniques. The thickness for all films is 250 nm.

(A and B) Reproduced with permission.[132] Copyright 2020, American Chemical Society.

(C) Schematic diagram of the three-source co-evaporation preparation process.

(D) Evolution of the PL spectra under continuous illumination for as-deposited $MAPb(Br_{0.2}I_{0.8})_3$ and $MAPb(Br_{0.5}I_{0.5})_3$ and for $MAPb(Br_{0.5}I_{0.5})_3$ films after annealing. All spectra were collected with a 10-s delay under continuous excitation with a continuous wave (CW) laser at 515 nm with an irradiance of 300 mW/cm^2.

(C and D) Reproduced with permission.[133] Copyright 2017, American Chemical Society.

(E) Schematic of CsI_2Br-induced self-guided crystal growth (SCG) of perovskite during the deposition process.

(F) Pole figures of perovskite thin films from the (100) facet without SCG.

(G) Pole figures of perovskite thin films from the (100) facet with SCG.

(E–G) Reproduced with permission.[134] Copyright 2025, Springer Nature.

achieve the compositionally homogeneous bulk phases required for high-efficiency WBG devices, the field requires a transition to co-evaporation, a methodology that allows simultaneous arrival and crystallization of all constituents, thereby eliminating post-deposition diffusion bottlenecks.

Co-evaporation proves particularly advantageous for all-inorganic WBG perovskites such as $CsPbI_2Br$ and $CsPbBr_3$, where the high thermal stability of precursors aligns with vacuum sublimation requirements. In a simplified dual-source configuration, Cs halides and Pb halides are sublimated simultaneously. Ma et al. and Chen et al. established the feasibility of this route, revealing that precise flux control enables the fabrication of pinhole-free films with efficiencies >11%.[130,131]

However, managing the I/Br ratio introduces complexity. As illustrated in Figure 7A, a streamlined strategy involves using a mixed-halide source, typically $Pb(I_{1-x}Br_x)_2$, alongside CsBr. This reduces the degrees of freedom from three to two, effectively stabilizing reaction kinetics.[132] The resulting films exhibit uniform halide distribution and a sharp optical absorption edge at 1.90 eV (Figure 7B), confirming that source simplification offers a viable pathway to suppress phase segregation in WBG perovskites.

To rival solution-processed cells, vacuum deposition must accommodate complex compositions. Longo et al. systematically mapped the deposition parameter space for $MAPb(Br_xI_{1-x})_3$ using a triple-source setup (Figure 7C). Their work elucidated a critical thermodynamic constraint: while co-evaporation enables precise band-gap tuning across the visible spectrum, intrinsic immiscibility of high-Br phases renders them thermodynamically unstable. Without rigorous post-annealing to relax lattice strain, these films undergo rapid photoinduced phase segregation (Figure 7D), indicating that kinetic assembly alone is insufficient to counteract thermodynamic driving forces.[133]

Pushing complexity further, Gil-Escrig et al. validated the efficacy of four-source co-evaporation for triple-cation systems. They demonstrated a distinct advantage of the vacuum environment: the ability to kinetically lock the photoactive black phase of FAI-rich perovskites. Unlike solution processing, where solvent interactions favor formation of the non-perovskite δ-phase, the solvent-free vacuum environment facilitates direct crystallization of the metastable α-phase at moderate temperatures, achieving efficiencies of 16%–19% with superior thermal stability.[135]

Despite the capability to fabricate complex lattices, co-evaporation amplifies kinetic instabilities identified in the halide segregation dilemma in vacuum and the challenge of organic precursor volatility. In multi-source regimes, these microscopic physical limitations manifest as macroscopic process control challenges.

While thermodynamic and kinetic disparities of precursors highlighted the flux drift caused by the I/Br vapor-pressure mismatch, co-evaporation of hybrid perovskites faces a far more extreme thermal disparity. The sublimation temperatures of organic (FAI $\approx 150^\circ C$) and inorganic (CsI $> 450^\circ C$) precursors exhibit a substantial offset of several hundred degrees. This exacerbates the stoichiometry drift: slight thermal crosstalk or surface-area evolution in the sources leads to non-linear flux deviations. As noted by Igual-Muñoz et al., this imbalance forces the system into thermodynamic dead ends, precipitating distinct secondary phases: organic deficiency leads to the formation of laminar PbI_2, while inorganic excess or organic overshoot promotes the crystallization of the zero-dimensional Cs_4PbX_6 phase. These impurities act as non-radiative recombination centers, fundamentally compromising phase purity.[132]

The sticking coefficient mismatch detailed in metrological limitations of QCM monitoring creates specific operational hazards. Since cooled QCM sensors cannot mimic hot substrate surfaces where organic re-evaporation is active, operators rely on empirical excess ratios without real-time feedback. This not only wastes material but also contaminates vacuum chambers, rendering reproducible rate control difficult.[136]

Recognizing these instabilities, recent breakthroughs shifted focus toward intermediate-phase engineering. Dong et al. demonstrated that co-evaporation kinetics can be modulated. By precisely manipulating early-stage Cs, FA, and Pb fluxes, they induced the formation of a specific CsI_2Br intermediate phase. This intermediate acts as a crystallographic seed guiding oriented growth of subsequent perovskite grains (Figure 7E). A comparison of pole figures in Figure 7F shows that this self-guided crystal growth strategy changes crystal orientation from random to highly aligned. This growth mode achieved a record efficiency of 21.4% for 1.7 eV WBG cells, challenging the dominance of solution processing.[134]

Co-evaporation offers unique capabilities to construct complex, multi-component lattices via simultaneous crystallization. However, process precision is compromised by inherent volatility mismatches and sticking coefficient disparities. The applicability of these traditional evaporation methods to WBG perovskites is analyzed in the subsequent section.

Applicability analysis of thermal evaporation for WBG perovskite

Determining the optimal methodology between sequential evaporation and co-evaporation for specific WBG compositions depends on the interplay between precursor physicochemical properties, such as solubility and volatility, and target film crystallization habits, including nucleation density and strain state.

The primary challenge for hybrid FA-rich WBG perovskites lies in achieving dense coverage on charge transport layers. While co-evaporation theoretically allows for simultaneous film formation, it is inherently sensitive to substrate surface energy. Roβ et al. revealed that on hydrophobic HTLs such as PTAA or PACz, co-evaporated molecules exhibit severe dewetting behavior due to low nucleation density. This leads to Volmer-Weber island growth, resulting in discontinuous films with shunting paths. To enforce compactness, lowering substrate temperature increases supersaturation.[74] However, elevated temperatures are required to promote grain growth as adatoms obtain sufficient thermal energy to diffuse across the surface and fill voids between nuclei. Consequently, achieving high-quality films requires establishing a precise thermal equilibrium to balance these opposing kinetic factors.

Conversely, sequential evaporation offers a robust solution via intrinsic volume expansion. Even if the initial inorganic template is porous, subsequent organic intercalation triggers a unit-cell expansion that physically fills voids. Li et al. demonstrated that a Cl-alloy-mediated sequential process achieves pinhole-free films with efficiencies exceeding 24%, proving that diffusion-driven expansion is structurally more forgiving than stochastic nucleation of co-evaporation.[137]

As WBG formulations evolve toward complex double-cation and double-halide systems, such as $Cs_xFA_{1-x}Pb(I_yBr_{1-y})_3$, the applicability of co-evaporation warrants re-evaluation. Mahmoud et al. offered a critical assessment arguing that co-evaporation might not be optimal for industrial scaling of mixed-cation perovskites. They noted that disparate volatilities of FA, Cs, I, and Br precursors lead to uncontrollable interference and rate drifts during extended deposition. Furthermore, film composition becomes critically dependent on substrate type, making process transferability a formidable challenge.[70] Feeney et al. further highlighted that maintaining stoichiometry often limits deposition rates in FA-based systems to less than 5 Å/s, creating a throughput bottleneck contradicting gigawatt-scale manufacturing requirements.[138]

For all-inorganic WBG candidates such as $CsPbBr_3$ and $CsPbI_2Br$, sequential evaporation dominates fabrication strategies. Gordillo et al. compared various routes and concluded that sequential deposition of CsBr and $PbBr_2$ yields the highest reproducibility. Separating high-melting-point CsBr from lead halide allows for independent, precise control of the inorganic framework thickness, bypassing the stoichiometry drift inherent to co-evaporation.[139]

In conclusion, sequential evaporation represents the dominant strategy for all-inorganic WBG perovskites, offering superior stoichiometry control and dense morphology via template expansion. For complex hybrid quaternary or quinary systems, the diffusion kinetics of sequential evaporation are too intricate to ensure a uniform distribution of FA, Cs, I, and Br throughout the film thickness. While co-evaporation holds the theoretical efficiency ceiling by achieving uniform mixing in a single step, it remains hindered by low deposition rates and crosstalk instabilities. Unless the self-guided growth paradigms discussed in applicability analysis of thermal evaporation for WBG perovskite are fully realized, sequential evaporation remains the more scalable and pragmatic choice for industry.

Solution-assisted evaporation

Process of solution deposition followed by evaporation deposition

While pure thermal evaporation ensures solvent-free purity, it encounters limitations regarding slow deposition rates of high-melting-point inorganic precursors. Conversely, solution processing faces solubility limits for cesium salts. The hybrid strategy of solution deposition followed by evaporation emerges as a pragmatic compromise combining the rapid throughput of spin coating with the kinetic precision of vapor reaction.

The fundamental rationale involves decoupling film formation into two steps: using solution processing to construct the metal halide skeleton, such as $PbBr_2$, followed by vapor deposition to infuse organic or alkali cations, such as Cs and FA. This approach proves particularly advantageous for all-inorganic WBG perovskites such as $CsPbBr_3$, where the poor solubility of CsBr restricts one-step solution methods.

Li et al. demonstrated the precision of this method in $CsPbBr_3$ fabrication (Figure 8A). By evaporating CsBr onto a spin-coated $PbBr_2$ layer, they established that phase composition is strictly governed by vapor dosage. Insufficient CsBr leads to the lead-rich phase $CsPb_2Br_5$, while excessive CsBr produces the cesium-rich phase Cs_4PbBr_6 (Figure 8B). Precise control of evaporation thickness successfully locked the pure perovskite phase, effectively eliminating impurities.[140]

However, final film quality remains fundamentally anchored to the initial template. Liu et al. identified that conventional spin coating of $PbBr_2$ often yields porous structures that propagate defects into the final perovskite lattice. Addressing this, they introduced an anti-solvent engineering step during $PbBr_2$ deposition (Figure 8C). This induced rapid supersaturation, creating a dense and uniform $PbBr_2$ framework. Subsequent reaction with evaporated CsI vapor produced $CsPbIBr_2$ films exhibiting superior coverage and minimized recombination losses.[141] This underscores that while the vapor step drives phase conversion in hybrid methods, it cannot repair morphological defects inheriting from poor solution templates.

While this hybrid method resolves solubility issues for Cs-based perovskites, it encounters a critical geometric limitation for TSCs. Reliance on spin coating renders this method incompatible with rough surfaces. In silicon TSCs, bottom cells often feature micron-sized pyramids for light trapping. Solution coating tends to fill valleys and expose peaks, causing electrical short circuits. To preserve the chemical advantages of solution processing while overcoming the geometric limitations of spin coating, reversing the deposition sequence provides a compelling alternative solution.

Process of evaporation deposition followed by solution deposition

The fundamental rationale of this method is to utilize thermal evaporation to construct a rigid, conformal inorganic framework, such as $CsBr/PbI_2$, followed by infiltration of an organic salt solution to drive conversion. This sequence leverages directional line-of-sight evaporation transport to ensure uniform coverage on rough textures, while the subsequent solution step facilitates rapid mass transport via liquid-phase diffusion channels.

The microstructure of the evaporated framework dictates subsequent reaction thermodynamics. Zhou et al. conducted a kinetic analysis on $PbI_2/CsBr$ template formation, identifying a critical competition between nucleation and vertical growth. Extremely low evaporation rates yield dense, compact films, impeding organic salt infiltration. Conversely, excessively high rates induce kinetic roughening, resulting in unstable dendritic structures.

An optimized medium rate imparts the requisite porosity to the framework functioning as a nanoporous host, enabling complete reaction stoichiometry. This optimized porosity yields perovskite films with expansive grains and uniform halogen distribution (Figure 8D). Deviations from this rate window lead to residual precursors and structural defects manifesting as severe non-radiative recombination and diminished photoluminescence (PL) (Figure 8E).[142] Furthermore, Zhang et al. utilized response surface methodology to elucidate that elevated substrate temperatures during evaporation tailor pore size distribution, enhancing the organic solution diffusion coefficient deep into the framework.[144]

A persistent bottleneck in WBG films involves iodine and bromine segregation due to asynchronous crystallization. The evaporation-first method offers a solution via inorganic pre-alloying. By co-evaporating PbI_2 and CsBr or using single-source $CsPbI_2Br$ powder as demonstrated by Guesnay et al.,[145] the I/Br ratio is locked within the rigid inorganic lattice prior to triggering the organic reaction. This establishes a homogeneous compositional baseline activated rather than constructed by the subsequent solution step.[29,146] Shi et al. advanced this concept by co-evaporating a PbIBr eutectic precursor with CsCl. This strategy alters nucleation energy distribution, narrowing the disparity in crystallization rates between iodide and bromide components (Figure 8F). Consequently, it minimizes the driving force for vertical phase separation during annealing (Figure 8G), addressing the halide gradient problem at its source.

To further facilitate infiltration kinetics, Dewi et al. proposed introducing organic components early by co-evaporating MAI with PbI_2. This creates a hybrid framework with reduced structural rigidity compared to pure metal halides. Pre-existing organic cations expand the lattice spacing, reducing steric hindrance for subsequent MABr solution infiltration. This ensures uniform and complete phase transformation, eliminating the common issue of unreacted inorganic cores.[147]

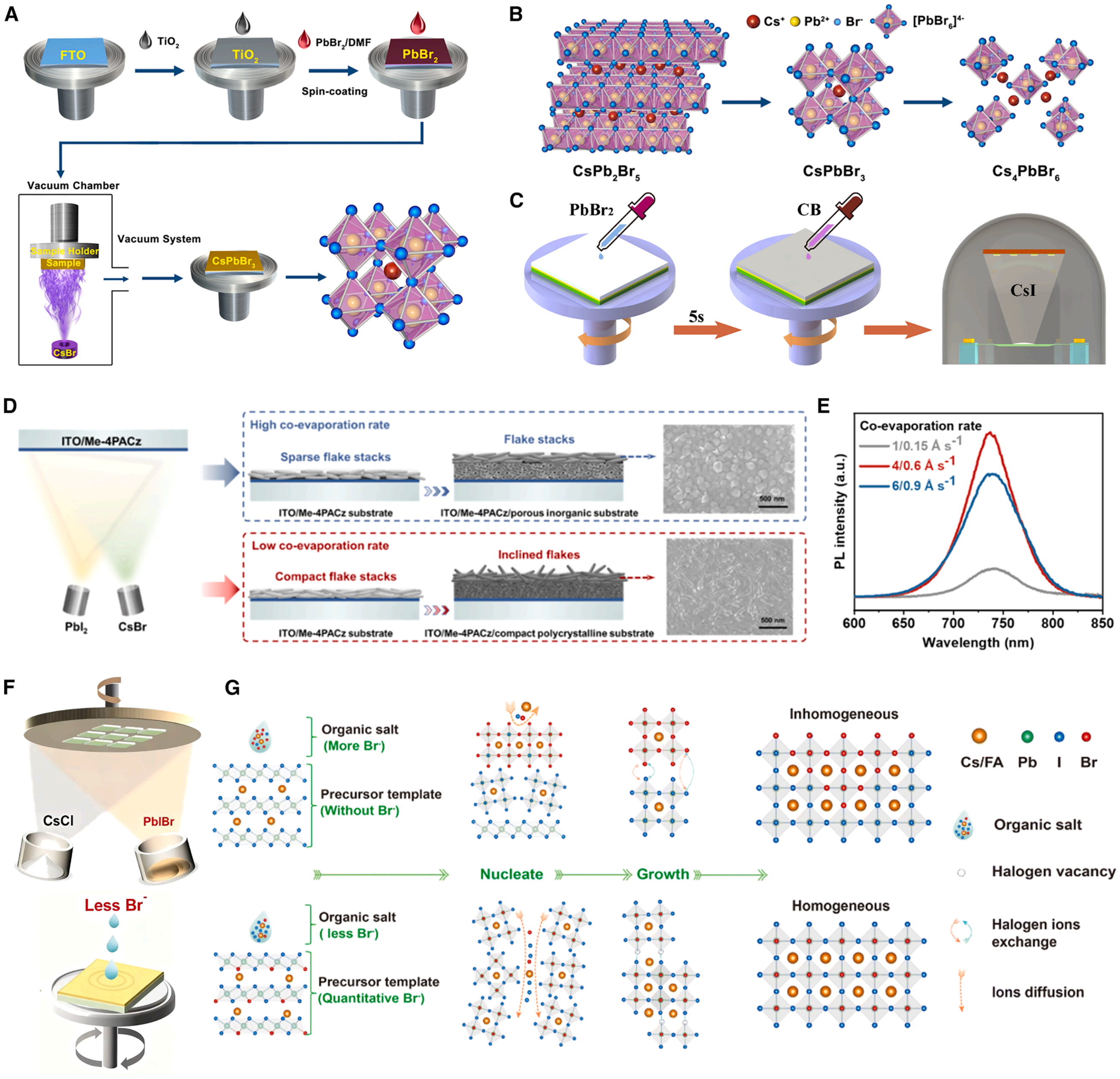

Figure 8. Solution-assisted evaporation

(A) Schematic illustration of the solution-assisted evaporation method (SAE) to fabricate a $CsPbBr_3$ thin film.

(B) 3D crystal models of $CsPb_2Br_5$, $CsPbBr_3$, and Cs_4PbBr_6 structures.

(A and B) Reproduced with permission.[140] Copyright 2019, American Chemical Society.

(C) Schematic illustration of the solution-assisted deposition process of the $CsPbIBr_2$ films in which the $PbBr_2$ layer is firstly spin coated via an anti-solvent technique and the CsI film is subsequently vacuum evaporated onto the $PbBr_2$ layer. Reproduced with permission.[141] Copyright 2019, Elsevier.

(D) A schematic diagram of the substrate characteristics transformation during the co-evaporation process of PbI_2/CsBr templates at high and low co-evaporation rates.

(E) Steady-state PL spectra of the pFBPA-alone perovskite films at co-evaporation rates of 1/0.15, 4/0.6, and 6/0.9 Å s^{-1}, respectively.

(D and E) Reproduced with permission.[142] Copyright 2025, American Chemical Society.

(F) Schematic diagram of evaporation-solution sequentially deposited wide-band-gap perovskite of pre-homogenizing (pre-H) method.

(G) Schematic diagram of the control and pre-H perovskite film crystallization processes.

(F and G) Reproduced with permission.[143] Copyright 2025, The Royal Society of Chemistry.

A distinct advantage of this method lies in its compatibility with textured silicon. Evaporation ensures conformal deposition of the inorganic template over micron-sized pyramids, circumventing shunting caused by solution leveling. Crucially, as highlighted by Er-raji et al., the porous framework acts as a capillary host, retaining the organic solution on pyramid facets against gravity, thereby ensuring uniform reaction across the entire texture.[29,148]

However, reintroducing a liquid step imposes a thickness constraint. For thick absorbers required for current matching, infiltration of the organic solution into the bottom of the framework becomes diffusion limited. This frequently results in a vertical reaction gradient leaving unreacted inorganic residues at the buried interface acting as extraction barriers, a limitation that pure solution or pure vapor methods do not necessarily encounter.[149]

While the evaporation-first protocol addresses geometric challenges of textured substrates, the current implementation relies heavily on spin coating. This technique, characterized by high material wastage and batch-processing limits, represents a significant bottleneck for industrial upscaling. To bridge the translational gap, the liquid infiltration step must evolve from centrifugal spreading to scalable, meniscus-guided, or droplet-based fluid dynamics. This necessitates extending the hybrid logic to scalable solution methodologies such as blade coating, slot-die coating, and inkjet printing to realize the true manufacturing potential of the evaporation-solution route.

Further extensions of evaporation followed by solution deposition

In blade and slot-die coating, film formation is governed by the interaction between external shear forces and internal capillary pressure within the porous framework. For textured silicon TSCs, achieving conformal coverage without centrifugal force presents a challenge. Er-raji et al. elucidated that the evaporated porous inorganic framework functions as a super-wick. High capillary pressure generated by nanopores spontaneously draws blade-coated organic ink into pyramid valleys, effectively overcoming gravity-induced leveling phenomena typical of solution processing.[150]

However, the slower solvent evaporation rates in blade coating (seconds compared to milliseconds in spin coating) can induce Ostwald ripening, leading to disconnected grains. To mitigate this, Luo et al. developed a framework heat treatment strategy coupled with ternary co-evaporation of PbI_2, $PbCl_2$, and CsBr. This produces a quasi-2D layered $CsPb_2X_5$ intermediate structure (Figure 9A). Crucially, this stratiform structure expands interlayer spacing and promotes organic salt infiltration. This structural engineering significantly enhanced PL intensity and suppressed non-radiative recombination (Figure 9B), enabling high-efficiency large-area modules.[151]

Spray coating is often compromised by the coffee-ring effect caused by capillary flow during drying. Chen et al. demonstrated that evaporated frameworks fundamentally alter drying behavior. The porous inorganic matrix rapidly absorbs impinging micro-droplets and immobilizes the solute. This prevents the fluid flow responsible for segregation and increases the average grain size from 488 to 712 nm.[155] Further optimization by Zhang et al. utilizing a BAI surfactant (Figure 9C) enhanced wettability, ensuring that droplets spread conformally rather than dewetting, leading to superior charge transport (Figure 9D).[152]

In slot-die coating, air entrapment within pyramid valleys constitutes a critical defect mechanism. Li et al. addressed this by introducing 2,5-NaDPA into the organic ink. This additive adjusts the nucleation free energy barrier and retards the crystallization rate. This delay provides a critical time window for liquid to displace trapped air bubbles and fully infiltrate the porous PbI_2 framework before solidification begins (Figure 9E). The result is a void-free interface essential for module reliability.[156]

Inkjet printing introduces digital lithography capabilities. Pesch et al. demonstrated a hybrid inkjet approach where picoliter droplets of organic cations are deposited onto a uniform inorganic template (Figure 9F). Remarkably, the porous framework limits lateral ink spreading and acts as a physical barrier, confining the reaction to the printed voxel. This capability enables high-resolution patterning of monolithic interconnections without destructive laser ablation while preserving the underlying layer integrity.[154]

Applicability analysis of solution-assisted evaporation for WBG perovskite

Hybrid methods address WBG perovskite degradation issues, including phase segregation strain and defects, through a complex interplay of thermodynamics and kinetics. The evaporation-first route relies on constructing a rigid inorganic framework such as nanorod-like PbI_2. Xu et al. demonstrated that this framework serves a dual purpose by acting as a capillary host that utilizes capillary pressure to absorb the organic solution into deep textures, ensuring conformal coverage superior to solution-only methods.[157] From a thermodynamic perspective, Huang et al. highlighted that this framework enables the pre-locking of the I/Br ratio within the rigid lattice before the organic reaction occurs. This pre-defined homogeneity establishes a robust halide backbone that raises the activation energy for the photoinduced Hoke effect and prevents the segregation observed in co-crystallized films.[158]

Conversely, the solution-first route relies on a chemical sintering mechanism. Zhou et al. and Sutter-Fella et al. elucidated that organic vapor permeates the initial disordered inorganic film and triggers a dissolution-recrystallization reaction. This reaction is driven by a significant volume expansion that consumes small grains and fills voids to achieve high density without high-temperature annealing.[159,160] Kim et al. further revealed that this expansion is mechanical rather than merely morphological, as it induces a beneficial compressive stress field. Unlike the tensile strain typical of solution-processed films that drives cracking, this chemically induced compression enhances mechanical toughness under thermal cycling.[161]

However, this hybrid advantage presents a trade-off. While evaporation ensures a clean starting point, reintroducing solvents such as DMF or DMSO in the liquid infiltration step poses a risk of solvent trapping. Residual solvents can coordinate with Pb^{2+} to form intermediate phases that degrade into defects under heat. Consequently, while hybrid methods offer superior morphology and strain management, they necessitate rigorous post-annealing protocols to match the defect purity of fully vapor-deposited films.[162]

For all-inorganic WBG perovskites, the evaporation-first method struggles to infiltrate cesium into the framework using standard solvents due to the limited solubility of cesium salts.

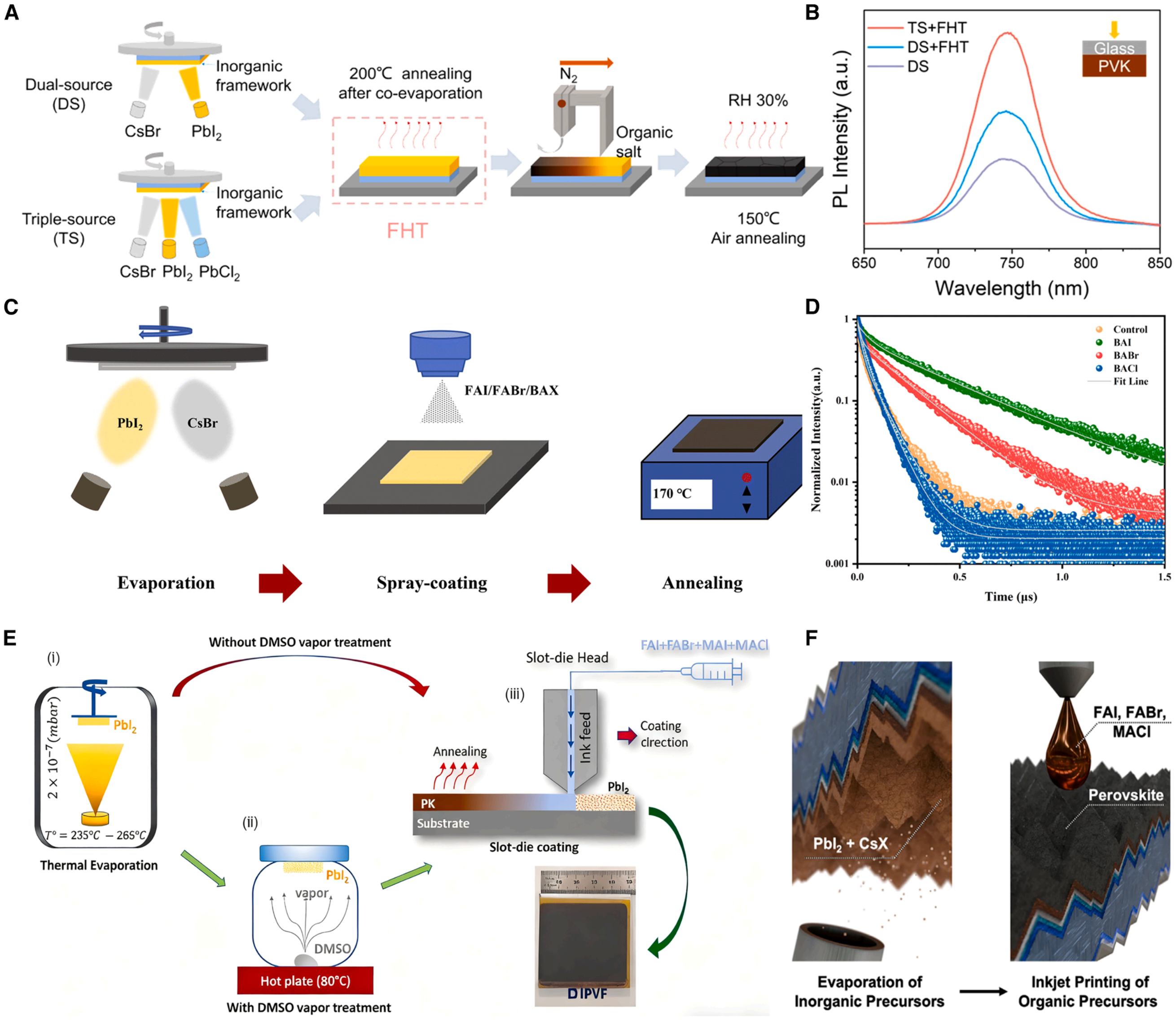

Figure 9. Solution-assisted evaporation

(A) Schematic of the hybrid two-step deposition method.

(B) Steady-state PL (inset illustrates the laser incident direction).

(A and B) Reproduced with permission.[151] Copyright 2023, American Chemical Society.

(C) Schematic illustration of the evaporation-spray process for the fabrication of perovskite films.

(D) Time-resolved photoluminescence (TRPL) curves of the control, BAI, BABr, and BACl thin-film samples deposited on FTO glass.

(C and D) Reproduced with permission.[152] Copyright 2025, The Royal Society of Chemistry.

(E) Schematic illustration of perovskite (PVK) film fabrication with and without DMSO vapor treatment. At the bottom right, a photograph of a 5 cm × 5 cm PVK film fabricated by the hybrid evaporation/slot-die method is presented. Reproduced with permission.[153] Copyright 2023, Elsevier.

(F) Fabrication process of perovskite/silicon tandem solar cells (PSTs) using a hybrid two-step deposition method that combines evaporation and inkjet printing. Reproduced with permission.[154] Copyright 2025, Wiley-VCH.

The solution-first method avoids this limitation by introducing cesium via vapor or aqueous spray steps, thereby bypassing the solubility bottleneck inherent to one-step methods. This enables the formation of thick and phase-pure inorganic films that are difficult to achieve otherwise.[159]

For complex compositions such as FA/Cs or I/Br mixtures on textured silicon, the evaporation-first protocol combined with blade or slot-die coating is superior. As analyzed in further extensions of evaporation followed by solution deposition, the evaporated framework provides geometric conformity, while the scalable liquid step delivers organic cations deep into the valleys. Er-raji et al. highlighted that humidity control during this infiltration is critical to synchronizing reaction kinetics and preventing the formation of unreacted zones at the interface.[162]

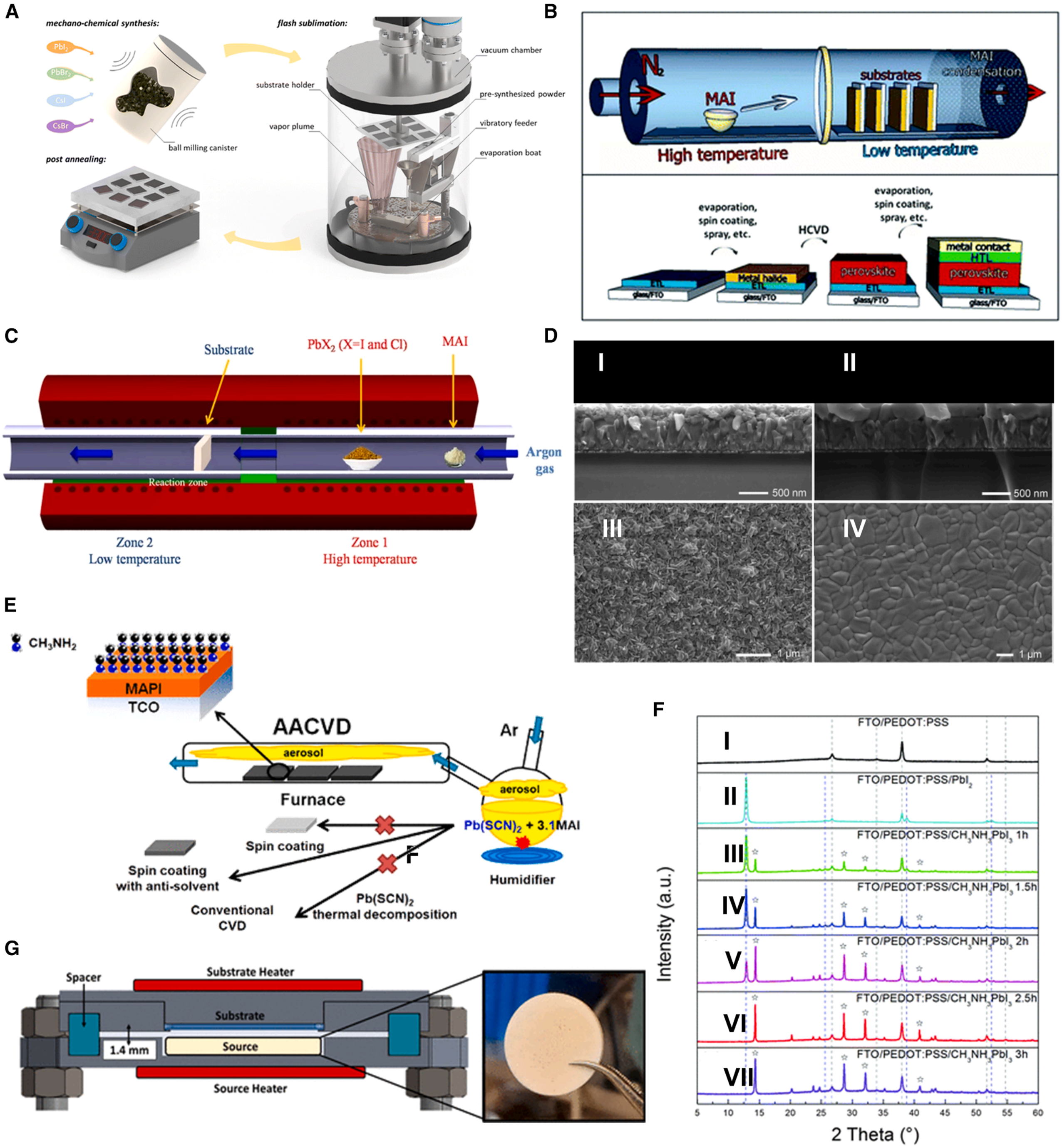

Figure 10. Continuous flash sublimation evaporation, chemical vapor deposition, and close-space sublimation routes for perovskite thin-film fabrication

(A) Schematic of the continuous flash sublimation evaporation system. Reproduced with permission.[166] Copyright 2024, The Royal Society of Chemistry.

(B) Hybrid chemical-vapor-deposition-based perovskite synthesis. Reproduced with permission.[167] Copyright 2014, The Royal Society of Chemistry.

(C) Schematics of the perovskite film fabrication using MAI and PbX_2 sources deposited onto a c-TiO_2-coated FTO glass substrate, which was performed in a CVD furnace. Reproduced with permission.[168] Copyright 2015, Springer Nature.

(D) Microstructure of PbI_2/CsBr before and after HCVD. Cross-section SEM image of (I) PbI_2/CsBr and (II) $Cs_{0.1}FA_{0.9}PbI_{2.9}Br_{0.1}$ perovskite films. Surface SEM image of (III) PbI_2/CsBr and (IV) $Cs_{0.1}FA_{0.9}PbI_{2.9}Br_{0.1}$ perovskite films. Reproduced with permission.[169] Copyright 2019, The Royal Society of Chemistry.

(legend continued on next page)

When module interconnection is required, inkjet printing on an evaporated framework offers pixel-level precision. Pesch et al. showed that the porous framework limits lateral ink spreading, enabling the definition of active areas without laser scribing damage, a capability unique to this hybrid pairing.[163] Furthermore, Fan et al. proposed a reverse hybrid logic involving solution deposition of the bulk followed by vacuum evaporation of a 2D capping layer. This strategy specifically addresses surface pinholes left by solution processing by utilizing the conformality of evaporation to heal defects and form a robust 2D/3D junction, achieving certified efficiencies exceeding 22%.[164]

The selection of an optimal solution-assisted evaporation strategy is strictly dictated by the interplay between compositional solubility and substrate topography. For all-inorganic WBG perovskites, the solution-first or aqueous-spray routes are indispensable for overcoming the intrinsic solubility limits of cesium salts. However, for hybrid TSCs on textured silicon, the evaporation-first protocol coupled with scalable blade or slot-die coating stands as the optimal industrial solution, as it effectively resolves the geometric conflict of conformal coverage without the material waste associated with spin coating.

Flash deposition and continuous manufacturing

Continuous flash sublimation

Continuous flash sublimation (CFS) addresses the fractionation problem inherent in conventional co-evaporation: components with different vapor pressures evaporate at disparate rates. It circumvents this issue by feeding small quantities of pre-mixed powder onto a heater set at a very high temperature. The powder sublimates instantly upon contact, ensuring that the vapor composition mirrors the source composition.

Longo et al. provided early proof of this concept by demonstrating that flash evaporation could deposit stoichiometric hybrid films without complex rate monitoring.[165] Abzieher et al. advanced this technique into a scalable industrial process by developing a continuous feed system capable of high-flux deposition (Figure 10A). This system is particularly critical for inorganic WBG absorbers such as $CsPbI_2Br$. CFS enables the deposition of these complex stoichiometries without the fractionation associated with slow evaporation. Abzieher et al. achieved efficiencies of approximately 15% with band gaps ranging from 1.8 to 1.94 eV. Crucially, the process alleviates rate bottlenecks in conventional vacuum methods and brings vacuum deposition speeds closer to production-line requirements.[166]

Applicability analysis of flash deposition for WBG perovskite

CFS resolves the conflict between rapid coverage and high crystallinity by compressing the crystallization timeline. It employs specific physical driving forces to bypass the porous Volmer-Weber growth mode and mitigates phase segregation via kinetic locking. By completing crystallization in seconds, iodine and bromine ions are frozen into the lattice before thermodynamic segregation can occur.

In CFS, films are deposited at high temperatures. Upon cooling, the thermal expansion mismatch with the substrate may induce tensile strain and potentially accelerate degradation. This suggests that CFS requires careful substrate temperature management or post-annealing strain-relaxation strategies.[161]

While this method eliminates solvent-related defects entirely, it introduces the risk of thermal defects such as halide vacancies if impinging molecules carry excessive kinetic energy. Therefore, CFS films often require a specific healing step in a mild vapor atmosphere to recover stoichiometry.[166]

For mixed-cation WBG films containing volatile organics, fast CFS risks thermal degradation of organic salts due to the high source temperatures required for sublimation.[172]

However, for $CsPbX_3$ systems, CFS is the definitive solution. Inorganic precursors possess thermal stability that allows for high-temperature flash sublimation without decomposition. Rapid thermal processing is essential for crystallizing the metastable black phase of inorganic perovskites, which often degrades under slow processing.[173]

CFS stands as the benchmark for inorganic systems by offering solvent-free purity and precise stoichiometry. It validates that the key to circumventing thermodynamic miscibility gaps in WBG perovskites lies in the kinetic compression of the crystallization timeline rather than chemical equilibrium alone.

Multi-field-driven vapor deposition

Flash deposition utilizes temporal control to freeze non-equilibrium phases, whereas multi-field-driven deposition exploits spatial fields, including gas flow dynamics and thermal gradients, to regulate crystal growth. By transitioning from the high-vacuum regime of thermal evaporation to viscous or transition flow regimes, techniques such as chemical vapor deposition (CVD) and CSS introduce mass transport regulation as a control dimension. This enables conformal coating of complex topographies and efficient precursor utilization, which addresses the material waste and coverage limitations inherent to line-of-sight physical vapor deposition.

CVD

CVD relies on chemical reactions at the gas-solid interface rather than simple condensation. The earliest literature report on CVD-fabricated PSCs can be traced back to 2014, when Leyden et al. first proposed a two-step gas-solid reaction paradigm based on hybrid CVD (HCVD) (Figure 10B): an inorganic precursor (such as PbI_2/CsBr) is first deposited, followed by gas-solid conversion using organic or inorganic ammonium halide vapors (FAI/MAI/MABr), yielding high-coverage films and demonstrating the first CVD-processed PSCs.[167] On this basis, Leyden et al. established the HCVD protocol. Exposing a pre-deposited metal halide template, such as lead chloride or lead iodide, to organic halide vapor enables conversion to perovskite via a gas-solid

---

(E) Aerosol-assisted chemical vapor deposition of air-stable $CH_3NH_3PbI_3$ films using a $Pb(SCN)_2$/MAI solution precursor. Reproduced with permission.[170] Copyright 2019, American Chemical Society.

(F) XRD patterns of (I) FTO/PEDOT:PSS substrate, (II) PbI_2, and perovskite films deposited on the FTO/PEDOT:PSS substrate reacted for (III) 1, (IV) 1.5, (V) 2, (VI) 2.5, and (VII) 3 h with a 0.2-mm sublimation distance. Reproduced with permission.[171] Copyright 2016, The Royal Society of Chemistry.

(G) Close-space sublimation reactor for scalable perovskite thin-film deposition. Reproduced with permission.[64] Copyright 2024, American Chemical Society.

interdiffusion mechanism. This method demonstrates intrinsic scalability and batch reproducibility by fundamentally separating inorganic framework formation from the organic intercalation step.[174]

A kinetic bottleneck exists regarding organic vapor diffusion into the inorganic lattice. Tavakoli et al. attempted a one-step CVD approach by co-evaporating precursors to form large-grained films (Figure 10C).[168] From a mechanistic perspective, a typical modified CVD (mCVD)/HCVD route couples a solid metal halide precursor layer (such as PbI_2, $PbCl_2$, mixed-halide $Pb(I,Br)_2$, or PbO) with gaseous organic/inorganic halide precursors (MAI, FAI, MABr, etc.). Under controlled temperature and halide vapor partial pressure, halogen/organic cation exchange first occurs at the precursor surface, followed by bulk diffusion to complete the *in situ* reconstruction of the ABX_3 lattice. However, competition between surface reaction rates and bulk diffusion rates determines film quality. Excessive surface reaction rates form a dense crust that blocks further infiltration. To resolve this, Qiu et al. developed a decoupling strategy by optimizing gas-phase supply pressure independently of diffusion temperature to achieve uniform mixed-cation films over large areas, as depicted in Figure 10D.[169] Their rapid HCVD process compressed reaction times to minutes while maintaining operational stability for over 800 h, demonstrating that diffusion kinetics can be accelerated without sacrificing order.[169,175]

Expanding precursor versatility, aerosol-assisted CVD and mist CVD introduce solution precursors into the vapor stream. Ke et al. utilized aerosol-assisted CVD with a pseudohalide precursor to fabricate air-stable films (Figure 10E). This technique leverages the Leidenfrost effect and micro-droplet transport to deposit dense films at moderate temperatures, effectively bypassing the high thermal budget of conventional CVD.[170] Similarly, Kim et al. applied mist CVD to inorganic $CsPbI_2Br$ and showed that carrier gas ratio control allows fine-tuning of the WBG grain structure, providing a pathway to deposit inorganic films without the solubility limits inherent to pure solution methods.[176]

CSS

CSS minimizes the source-substrate distance to a length comparable to the molecular mean free path. Guo et al. developed a simplified CSS configuration for perovskites to achieve pinhole-free $MAPbI_3$ under low-vacuum conditions (Figure 10F). This geometry creates a semi-closed equilibrium zone that ensures high mass transfer efficiency and nearly 100% material utilization, representing a significant improvement over the low utilization typical of long-throw thermal evaporation.[171]

High thermal flux in CSS enables rapid growth rates. Zhang et al. advanced this to a super-CSS configuration with a 200 μm distance to achieve ultrafast growth of mixed-halide films.[177] Crucially, Rodkey et al. and Gomar-Fernández et al. scaled this process to large-area modules under coarse vacuum conditions ranging from 1 to 10 mbar. Their work, as illustrated in Figure 10G, proved that CSS maintains compositional fidelity across large substrates without requiring ultra-high vacuum equipment, thereby significantly reducing capital expenditure. The inherent hot-wall nature of CSS promotes high crystallinity, yielding devices with excellent stability under thermal stress.[64,178]

CSS is particularly effective for all-inorganic WBG perovskites such as $CsPbBr_3$. Ihrenberger et al. showed that solvent-free CSS growth avoids intermediate solvate phases common in solution processing. High substrate temperatures typical of CSS facilitate crystallization of high-symmetry inorganic perovskite phases, leading to dense and phase-pure films suitable for tandem top cells.[179]

Applicability analysis of multi-field-driven vapor deposition for WBG perovskite

CVD relies on surface diffusion, in which the continuous supply of reactants via carrier gas facilitates grain-boundary healing during growth. Lee et al. demonstrated that this gas-phase conformality allows CVD to coat textured silicon pyramids without the shadowing effects observed in physical vapor deposition or surface tension issues associated with solution processing. Consequently, CVD effectively resolves morphological density issues on 3D substrates.[180] Furthermore, CVD offers a vapor-exchange mechanism in which continuous halide vapor flow establishes a dynamic equilibrium. This homogenizes halide distribution in mixed films and suppresses local segregation, which is often trapped during rapid solution crystallization.

CSS relies on high supersaturation, in which short distances create a dense vapor cloud, forcing rapid nucleation. While effective for planar films, the lack of carrier gas flow presents challenges for deep penetration into micron-scale textures compared to flow-driven CVD processes.

Both methods are solvent-free or low solvent in aerosol-assisted CVD, which inherently avoids tensile stress caused by solvent evaporation shrinkage. Du et al. showed that aerosol-assisted crystallization at low temperatures releases residual tensile strain and stabilizes the α-phase. This confirms that vapor-phase annealing facilitates strain relaxation and enhances WBG absorber durability against environmental stressors.[181]

The high thermal stability of inorganic precursors matches the high source and substrate temperatures of CSS, efficiently producing highly crystalline and defect-poor films.[179] In contrast, organic cations are thermally sensitive. Precise temperature zones in CVD reactors allow independent control of sublimation and reaction temperatures, minimizing organic degradation, whereas CSS carries a risk of radiative heating, which can decompose the organic surface.[181]

Multi-field-driven deposition bridges the gap between lab-scale quality and industrial scalability. CVD excels in conformality and hybrid composition control, making it indispensable for textured silicon TSCs, while CSS dominates the inorganic WBG sector due to high throughput and material efficiency.

Emerging paradigms and monitoring technologies

Conventional vapor deposition methods prioritize uniformity and throughput for industrial production. However, two critical bottlenecks remain in fundamental WBG perovskite research. The first involves the inefficiency of material discovery and the low repeatability of device fabrication within the vast multidimensional compositional space. The second concerns inherent polycrystalline disorder, which limits stability and photoelectric properties. To address these fundamental challenges, the field is diversifying into specialized emerging technologies, and this section assesses these frontiers.

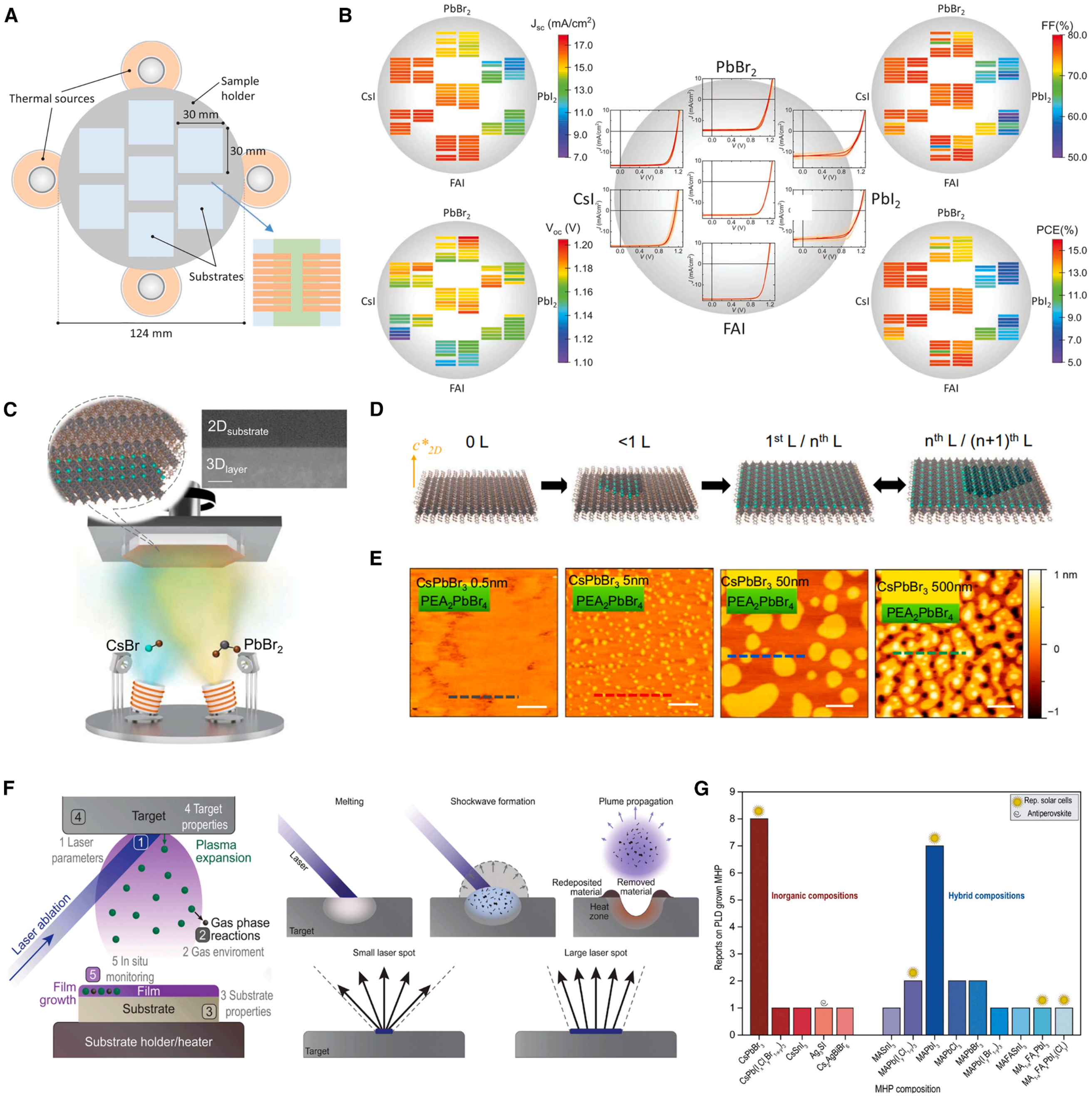

Figure 11. Emerging paradigms and monitoring technologies

(A) Top view of the substrate holder, position of the thermal sources, dimensions, and layout of a single substrate. Without sample rotation, a gradient of each precursor is deposited on the substrate, resulting in a CCS library of thin-film perovskites.

(B) Results of combinatorial deposition of wide-bandgap perovskite solar cells. 112 points color maps for J_{SC}, V_{OC}, (top) fill factor (FF), and PCE (bottom) are shown together with the J-V curves for each substrate (the mathematical average of all J-V curves for each substrate is shown as a thick red line). Reproduced with permission.[182] Copyright 2022, Wiley-VCH.

(C) Schematic illustration of vapor-phase co-evaporation of $CsPbBr_3$ onto single-crystal PEA_2PbBr_4 substrates. The top-left inset shows a schematic illustration of heteroepitaxial $CsPbBr_3$-PEA_2PbBr_4 growth.

(D) Schematic illustration of layer-by-layer (LbL) growth of $CsPbBr_3$ on PEA_2PbBr_4 (002) 2D surface.

(E) Surface morphology study by AFM of LbL growth of $CsPbBr_3$ on single-crystal PEA_2PbBr_4 from 0.5 (less than one Pb–Br octahedral layer), 5, and 50 nm through 500 nm.

(legend continued on next page)

Combinatorial vacuum deposition

Standard vacuum processes target absolute homogeneity, whereas combinatorial deposition exploits non-uniformity. Susic et al. developed a methodology utilizing a non-rotating substrate holder in a four-source co-evaporation system (Figure 11A). This configuration utilizes the cosine emission law of point sources to create a continuous compositional gradient across the substrate. Such an approach transforms a single deposition run into a library of over 100 distinct material compositions and enables simultaneous mapping of structural and optoelectronic properties against stoichiometric variations.[182]

This high-throughput capability is decisive for WBG perovskites. The phase stability of mixed-halide systems such as $Cs_xFA_{1-x}Pb(I_yBr_{1-y})_3$ is highly sensitive to the I/Br ratio and cesium content. Traditional iterative optimization employed in sequential evaporation studies requires laborious batch-by-batch fabrication to locate the optimal operating point.[185] In contrast, the combinatorial approach allows for rapid identification of specific compositional coordinates where high crystallinity intersects with the suppression of halide segregation. Susic et al. successfully pinpointed a narrow compositional window that yielded efficiencies over 14% while avoiding the formation of photo-inactive phases (Figure 11B). This demonstrates that combinatorial vacuum deposition serves as an effective method for navigating complex phase diagrams of multi-element WBG absorbers.[182]

Vapor-phase epitaxy

While combinatorial methods optimize composition, vapor-phase epitaxy targets the elimination of grain boundaries. Grain boundaries in polycrystalline WBG films accelerate halide segregation and non-radiative recombination. Borrowing from the semiconductor industry, vapor-phase epitaxy utilizes lattice-matched substrates to enforce oriented, single-crystalline growth.

Lu et al. demonstrated the precision of vapor-phase epitaxy by growing inorganic perovskites on 2D perovskite single-crystal templates (Figure 11C). Using vacuum-based layer-by-layer heteroepitaxy resulted in Angstrom-level thickness control of $CsPbBr_3$ on PEA_2PbBr_4 substrates. This process follows the crystallographic orientation of the template and eliminates random nucleation typical of solution processing. Consistent layer-by-layer growth behavior was observed among all thicknesses (Figure 11D). AFM characterization of $CsPbBr_3$ grown on PEA_2PbBr_4 single crystals revealed ultrasmooth surfaces at nominal deposition thicknesses of 0.5, 5, 50, and 500 nm, as evidenced in Figure 11E. This technique allows for band-offset tuning by manipulating interfacial termination chemistry, which enables the construction of precision heterojunctions and quantum wells unattainable by liquid methods.[183]

Addressing the challenge of lattice mismatch, Wang et al. introduced high-temperature ionic epitaxy utilizing alkali halide substrates such as NaCl and KCl, which share a similar ionic bonding character with perovskites. Performing deposition at elevated temperatures allows thermodynamic drivers to promote precursor reconstruction into a continuous and grain-boundary-free epitaxial film. This method effectively suppresses deep-level defects and reveals intrinsic carrier dynamics often masked in polycrystalline samples.[186]

Bridging the gap between solution simplicity and vapor quality, Sun et al. proposed contact transfer epitaxy. This method employs a donor-acceptor substrate configuration in which the perovskite is transferred and crystallized via a quasi-vapor transport mechanism across a microscopic gap. The acceptor substrate functionalized with self-assembled nanocubes directs film orientation. This dry transfer avoids solvent-incompatibility issues and enables the integration of high-quality WBG absorbers onto arbitrary substrates without the lattice constraints of traditional epitaxy.[187]

Pulsed laser deposition

While vapor-phase epitaxy relies on thermodynamic equilibrium to achieve crystal perfection, an alternative paradigm utilizes far-from-equilibrium synthesis to overcome volatility mismatches of complex precursors. This leads to high-energy kinetic deposition technologies, such as pulsed laser deposition and high-power impulse magnetron sputtering (HiPIMS). Unlike thermal evaporation, which is governed by the distinct vapor pressures of individual components, these methods utilize high-energy pulses to ablate targets and create a plasma plume that transfers materials stoichiometrically regardless of thermal properties.

The intrinsic challenge in depositing WBG perovskites, particularly mixed-cation and mixed-halide formulations, lies in the fractionation effect during thermal sublimation. Soto-Montero and Morales-Masis articulated that pulsed laser deposition fundamentally avoids this by using photon-matter interactions rather than thermal heating. The laser pulse induces non-thermal ejection of atoms, molecules, and clusters from a single target, ensuring that the complex stoichiometry of the target is congruently transferred to the substrate.[184]

This capability was experimentally verified by Soto-Montero et al., who successfully fabricated efficient p-i-n solar cells using a single-source pulsed laser deposition process for quaternary $MA_{1-x}FA_xPbI_3$ compositions (Figure 11F). The high kinetic energy of the ablated species facilitates the formation of dense and pinhole-free films without the need for multiple sources or complex rate monitoring, achieving efficiencies up to 19.7%. This confirms that pulsed laser deposition can decouple film composition from the disparate volatilities of organic and inorganic precursors (Figure 11G).[188]

However, the high energy of pulsed laser deposition introduces a new kinetic conflict. Kliner et al. conducted a systematic study on the growth dynamics of halide perovskites using *in situ* PL. Deposition rates exceeding 80 nm/min were achieved, more than 10-fold faster than conventional thermal evaporation. While the fundamental formation mechanism remains consistent

---

(C–E) Reproduced with permission.[183] Copyright 2025, The American Association for the Advancement of Science.

(F) Pulsed laser deposition principle.

(G) Overview of reported pulsed laser deposition-grown metal halide perovskite films classified by compositions. $CsPbBr_3$ is the most common composition reported by pulsed laser deposition, followed by $MAPbI_3$, the archetypal hybrid metal halide perovskite. Reproduced with permission.[184] Copyright 2024, American Chemical Society.

across rates, microstructural analysis revealed a critical trade-off: increasing deposition rates leads to randomly oriented crystallites and reduced charge carrier mobility. Rapid arrival of high-energy species overwhelms the surface diffusion time required for oriented growth, resulting in impact-induced disorder.[189]

Parallel to pulsed laser deposition, HiPIMS utilizes high-density plasma pulses to achieve film densification at low temperatures. Although primarily applied to charge transport layers such as Cu_2O, as demonstrated by Chuang et al., the underlying physics is highly relevant to WBG perovskites. High ionization rates in the plasma allow for the deposition of extremely compact films that can effectively passivate underlying defects without thermal damage. This suggests that plasma-assisted methods offer a unique route to resolving the conflict between island growth and compactness by substituting thermal energy with kinetic impact energy.[190]

For complex mixed-cation WBG perovskites, pulsed laser deposition demonstrates a unique stoichiometric locking capability. By congruently transferring the target composition to the substrate via a plasma plume, this method circumvents the thermodynamic fractionation inherent to thermal co-evaporation and ensures precise preservation of designed ratios. Simultaneously, both pulsed laser deposition and HiPIMS leverage the high kinetic energy of arriving species to achieve kinetic densification, suppressing void formation to yield films with near-theoretical density that outperform solution methods on rough textures.

However, this high-energy advantage presents a trade-off with crystallographic disorder. The hit-and-stick nature of the high flux hinders the thermodynamic reorganization required for preferred orientation. Consequently, the maturation of these technologies must rely on a hybrid strategy that couples high-energy deposition with post-deposition thermal or solvent annealing, thereby recovering crystalline order lost during energetic transfer.

Table 8 presents a comparative evaluation to determine the optimal processing scheme for specific WBG perovskite films, based on an in-depth analysis of three critical metrics: component reduction degree, process scalability, and the thermodynamic limitations of stoichiometric ratios.

The quality-throughput trade-off comparison of vapor-phase routes

In the vapor deposition of WBG perovskites, a profound physical antagonism exists between high deposition rates and film uniformity. According to the analysis in applicability analysis of thermal evaporation for WBG perovskite, conventional thermal co-evaporation typically maintains low rates of 1–5 Å/s at the laboratory scale, effectively trading throughput for precise compositional control. However, as rates scale to industrial requirements (>10 Å/s), the significant disparity in vapor pressures between CsI and PbI_2 in WBG formulations renders the system hypersensitive to thermal fluctuations, leading to severe lateral compositional inhomogeneity.

In contrast, CFS demonstrates immense throughput potential with instantaneous rates reaching hundreds of nanometers per second. Nevertheless, this high throughput often compromises spatial uniformity, with deviations exceeding 10% over a 15-cm scale. Consequently, this study defines the "effective deposition flux density" (Φ_{eff}) as the quintessential metric for evaluating WBG vapor routes. Φ_{eff} is rigorously defined as the maximum steady-state deposition rate achievable while maintaining thickness deviations <±5% and compositional variance <±1%. This metric shifts the evaluative framework from a singular focus on speed to a dual-constraint regime of precision and productivity.

The mathematical expression is defined as

$$\Phi_{eff} = \max\{\mathrm{R}|\sigma_T(R) \le \epsilon_T, \Delta C(R) \le \epsilon_C\}. \qquad \text{(Equation 3)}$$

The formal academic definitions of the physical variables are as follows: Φ_{eff} (deposition flux density) represents the maximum viable throughput of the system, typically measured in units of nm/s or μm/h; R (instantaneous deposition rate) is the real-time rate of material accumulation within the system; $\sigma_T(R)$ (thickness non-uniformity) is the spatial deviation in film thickness, expressed as a function of the deposition rate R; ϵ_T (thickness tolerance threshold) is the the critical limit for thickness variance, strictly maintained at $\le$5% for industrial-grade thin-film standards; $\Delta_C(R)$ (compositional variance) is the degree of stoichiometry deviation (e.g., the Cs/Pb atomic ratio) resulting from flux fluctuations at a given rate R; and ϵ_C (compositional tolerance threshold) is the maximum allowable variance in composition, typically set at $\le$1% to minimize the formation of non-radiative recombination centers.

From a quantitative perspective, the fabrication of WBG perovskites confronts a uniformity catastrophe. Given that WBG systems involve multiple ions with significantly different radii and diffusion coefficients, such as Cs^+ and Br^-, maintaining flux precision of <±1% during co-evaporation is a critical prerequisite for suppressing the formation of non-radiative recombination centers.

Quantitative comparisons reveal that while CSS excels in material utilization and thickness consistency, its narrow processing window renders the precise control of highly volatile organic components, as discussed in the challenge of organic precursor volatility, extremely challenging. The future breakthrough lies in developing closed-loop feedback systems with sub-second response times, such as tunable diode laser absorption spectroscopy (TDLAS), to reduce real-time flux fluctuations below 0.5%. This transition from qualitative commentary to quantitative metrics not only systematically addresses the demands of industrial production but also establishes the genuine physical barriers for the transition from laboratory prototypes to pilot production lines. As detailed in Table 9, each vapor-phase methodology exhibits distinct advantages and limitations in deposition rate, uniformity, and material utilization for WBG perovskites.

Innovation of equipment and monitoring technology

The vapor-phase fabrication of WBG perovskite thin films is in a critical transition from laboratory-based fundamental research to industrialized controlled production. Given that WBG materials involve complex mixed-cation and multi-halide compositions, their extreme sensitivity to stoichiometry requires equipment architectures with exceptional flux uniformity and transparency of process parameters.

At the hardware architecture level, the primary obstacle to large-area fabrication lies in transcending the spatial limitations

Table 8. Comparative assessment of vapor-phase methodologies for WBG perovskites

Methodology	Stoichiometric control	Scalability and throughput	WBG film quality	Major technical bottleneck	Target application
Sequential evaporation	diffusion limited: difficult to control precisely; reliant on self-limiting reaction depth	high: simple batch process; decoupled steps allow large-area uniformity	compact: volume expansion fills voids; risk: grading and incomplete conversion deep in film	blocking layer effect: surface densification retards deep infiltration; slow kinetics	planar heterojunctions; basic research
Co-evaporation	thermodynamic challenge: severe fractionation of organic/inorganic sources; requires complex rate monitoring	medium: crosstalk between sources limits large-area control; slow deposition rates (<1 Å/s)	high crystallinity: excellent phase purity; risk: porous films (Volmer-Weber growth) without substrate heating	rate control complexity: maintaining constant organic/inorganic ratio over long times	high-efficiency lab cells; planar tandem solar cells
Solution first	reconstructive: fixes metal halide ratio in solution; vapor drives conversion	medium: limited by solution step uniformity; batch annealing process	large grains: chemical sintering induces growth; risk: amorphous intermediates if P(vapor) is low	solubility limits: Cs salts hard to dissolve in first step; requires toxic solvents	all-inorganic ($CsPbX_3$); planar modules
Evaporation first	framework-defined: inorganic skeleton determines metal ratio; liquid infiltration is flexible	very high: compatible with roll-to-roll (R2R) slot-die/blade; high material utilization (>50%)	conformal: wicking effect ensures perfect coverage on textures; risk: solvent trapping	pore filling vs. drying: balancing deep infiltration with fast solvent removal	textured silicon tandem solar cells; industrial gigawatt scale
Vacuum flash	kinetic locking: rapid solvent removal freezes composition before segregation	high: fast processing; compatible with continuous coating lines	dense and smooth: explosive nucleation eliminates pinholes; risk: solvent-complex defects	process window: extremely narrow pressure/time window for phase purity	hybrid WBG modules; large-area crystallization
Flash sublimation	flash preserved: instant sublimation bypasses fractionation; high compositional fidelity	very high: high flux (>100 nm/min); minimal material waste; solvent-free	pinhole-free: flux saturation creates layer-by-layer growth; risk: tensile strain upon cooling	organic stability: thermal degradation of organics at high flash temperatures	all-inorganic WBG; high-speed manufacturing
Chemical vapor deposition	flow controlled: precise gas-phase stoichiometry via carrier gas and pressure control	high: linear sources/showerheads enable uniform large-area deposition	conformal: surface diffusion heals boundaries; risk: edge effects in flow field	equipment complexity: multi-zone temperature control and flow dynamics modeling required	textured/3D substrates; complex stoichiometry tuning
Close-space sublimation	equilibrium-driven: high mass transfer in semi-closed zone; self-regulating	high: very fast rates (>1 μm/min); near 100% material utilization	high crystallinity: large grains; risk: rough surface and thermal stress	thermal management: substrate overheating; lack of independent source control	thick inorganic absorbers; low-capital expenditure (CapEx) production
Vapor-phase epitaxy	atomic precision: layer-by-layer control; tunable band offsets	low: substrate-limited; slow growth rates; high cost	ultimate: single-crystal-like; grain-boundary-free; lowest defect density	lattice matching: requires specific substrates; hard to integrate on Si/glass	fundamental physics; high-end optoelectronics
Pulsed laser deposition	stoichiometric transfer: plasma plume transfers target composition congruently (non-thermal)	medium: target scanning limits area; particulate generation issues	dense but disordered: kinetic densification; risk: impact-induced crystallographic disorder	disorder-recovery: requires post-annealing to restore crystallinity; particulates	complex multi-cation WBG; compositional discovery

Table 9. Quantitative comparisons of vapor-phase methodologies for WBG perovskites

Vapor-phase route	Typical deposition rate (R, nm/s)	Thickness uniformity (σ,%)	Material utilization (U,%)	Flux precision control	Effective deposition flux density (Φ_{eff})	WBG applicability and physical limitations
Sequential evaporation	0.5–2.0	<±3	15–25	moderate	low	risk of residual PbI_2 at the interface; severely restricts V_{oc} in tandem devices
Co-evaporation	1.0–5.0	<±2	10–20	high	medium	most precise stoichiometry control; currently the benchmark for high-performance WBG devices
Flash sublimation	50–200	>±10	60–80	low	low	exceptional throughput potential; however, WBG phase purity and lateral homogeneity are critically compromised
Close-space sublimation	10–50	<±5	>90	high	high	superior material economy; yet narrow processing windows risk thermal decomposition of organic cations
Chemical vapor deposition/vapor-phase epitaxy	0.1–1.0	<±1	5–15	atomic precision	minimal	ideal for high-quality epitaxial growth; production tact time is incompatible with scalable manufacturing
Hybrid processes	5.0–20	<±5	30–50	precursor dependent	medium to high	bridges morphological stability of vapor phase with compositional flexibility of solution phase

of point-source evaporation in flux distribution. Petry et al. proposed a dynamic linear sublimation source architecture that utilizes a precisely arranged linear nozzle array to generate a uniform vapor flow, thereby achieving functional separation between the control logic of deposition width and flux uniformity.[191] This design minimizes thickness fluctuations over large areas while maintaining high throughput.

To address the control instability of organic precursors in CVD caused by high vapor pressure, Sanders et al. developed an equipment scheme based on a showerhead manifold.[192] Their study utilizes a micro-holed distribution plate to eliminate concentration gradients within the deposition chamber, ensuring spatial consistency of the organic vapor chemical potential across the substrate surface. Sahli et al. further optimized this process using a vapor transport deposition system, which physically isolates the organic precursor evaporation zone from the deposition zone and uses carrier gases for precise vapor delivery, achieving high-quality conformal growth on textured substrates.[193] This holds decisive engineering value for the fabrication of high-performance perovskite/silicon TSCs.

The limitation of monitoring technology is a central factor restricting the reproducibility of vapor deposition. Borchert et al. utilized residual gas analysis to achieve real-time tracking of volatile impurities and decomposition fragments of organic precursors within the deposition environment.[87] Their research demonstrates that even extremely low concentrations of impurities alter film-forming kinetics, and by monitoring the decomposition signals of organic components, researchers can establish a quantitative correlation between vapor composition and film quality.

In the dimension of optical diagnostics, spectroscopic ellipsometry is widely used to resolve the optical constants of complex compositions. Werner et al. systematically investigated the complex refractive indices of mixed-halide perovskites with band gaps ranging from 1.5 to 1.8 eV using variable-angle spectroscopic ellipsometry.[194] Their study established the dielectric function as a quantitative descriptor for evaluating the I/Br ratio. Wang et al. utilized *in situ* spectroscopic ellipsometry to monitor the thermal degradation kinetics of the films in real time, precisely capturing the physical critical points of material failure by analyzing the dynamic evolution of extinction coefficients.[195] Furthermore, Ermolaev et al. revealed a giant excitonic optical anisotropy in single-crystal perovskites.[196] This deep characterization based on physical properties provides necessary parameters for understanding the evolution of crystal orientation during the deposition of WBG materials.

Establishing absolute standards for compositional analysis is the foundation for achieving closed-loop control. Roβ et al. proposed an analytical framework combining nuclear magnetic resonance and total reflection X-ray fluorescence spectroscopy.[197] This method addresses the non-linear deviation between the precursor evaporation rate and the final film stoichiometry in vapor deposition. The study emphasizes that the cross-contamination effects of cations in WBG perovskites make it impossible to ensure compositional precision by relying solely on rate monitoring. By establishing this high-fidelity compositional validation system, researchers can provide an ultimate calibration standard for the optimization of deposition parameters.

Even sophisticated vapor deposition processes can result in residual vacancy defects and surface imperfections. Therefore, vapor-phase optimization strategies for WBG perovskite thin films explores overall optimization strategies with a focus on how additive engineering and gas-phase strategies, such as interface passivation, collaborate with gas-phase deposition processes to push WBG perovskite materials toward the theoretical efficiency limit.

VAPOR-PHASE OPTIMIZATION STRATEGIES FOR WBG PEROVSKITE THIN FILMS

WBG perovskites face intrinsic challenges, as detailed in the intrinsic challenges of vapor-deposited WBG perovskites, while vapor-phase methodologies for WBG perovskite thin films and applicability assessment introduces vapor-phase techniques as viable solutions. This section initially examines substrate surface energy and nucleation engineering before expanding to other critical strategies. The discussion culminates in a summary of the current research landscape for small-area single-junction solar cells fabricated via these methods.

Substrate surface energy engineering

In a solvent-free vacuum environment, the formation of perovskite films is entirely decoupled from solvent-mediated coordination processes and is instead governed by energy exchange and momentum transfer between incident vapor molecules and the solid substrate. This fundamental difference in the growth environment amplifies the control exerted by substrate surface properties over nucleation kinetics compared to solution-based methods. Particularly for WBG perovskites with high bromide and cesium content, the higher crystallization activation energy and lattice strain tendency make the physicochemical properties of the substrate interface the decisive factors for phase purity and structural integrity.

The core parameter in vacuum deposition is the sticking coefficient, which represents the probability that precursor molecules will reside on a specific substrate surface. Research indicates that organic precursors such as MAI or FAI exhibit significant kinetic disparities depending on the substrate chemistry.[198] These disparities are particularly critical in all-vacuum-processed WBG devices. Insufficient substrate surface energy triggers excessive surface diffusion of precursor adatoms, leading to severe Volmer-Weber island growth. This growth mode results in persistent pinholes within WBG films, directly causing shunting failures. By implementing advanced triarylamine-based oligomers such as the TAA-tetramer as the HTL, researchers can leverage their well-defined molecular structures and strong intermolecular π-π stacking to reduce energetic disorder at the interface, thereby providing uniform sites for perovskite nucleation during vacuum deposition.[199]

The substrate influence further extends to the structural templating of inorganic templates. In sequential vacuum deposition, the properties of the HTL significantly alter the crystallographic orientation of the initially deposited lead iodide layer. It has been observed that the orientation of lead iodide planes directly dictates the intercalation efficiency of organic cations and the subsequent perovskite conversion kinetics.[200] This templating effect is paramount for WBG perovskites, where high concentrations of cesium and bromide often trigger the formation of non-perovskite phases. Precise control over substrate temperature and chemical modification can induce preferential crystal orientation, optimizing charge transport and suppressing photoinduced phase segregation.[63,201]

The vertical compositional inhomogeneity frequently observed in co-evaporated WBG films, characterized by a cesium-rich layer at the buried interface due to the vapor-pressure difference between CsI and FAI, can be effectively mitigated by reordering the precursor contact sequence on the substrate. The reverse layer-by-layer process proposed by Xu et al., which involves pre-depositing an FAI layer before inorganic precursors, provides a novel kinetic pathway for WBG perovskite growth. In this configuration, the pre-deposited organic layer acts as a diffusion reservoir. As inorganic species land, they react downwards, fundamentally preventing the accumulation of inactive cesium-rich phases at the interface. Such enhancement in vertical phase homogeneity is decisive for maximizing the fill factor (FF) in WBG solar cells.[26]

Advanced insights suggest that simple physical wetting improvement is insufficient to address the stability challenges of WBG perovskites, necessitating the introduction of chemical anchoring mechanisms with strong coordination. Vacuum-deposited SAMs, particularly those featuring phosphonic acid groups, can firmly bind to oxide electrode surfaces via P–O bonds while coordinating with lead ions in the perovskite lattice.[114,123] This atomic-scale interfacial engineering enhances precursor adhesion and, more crucially, immobilizes halide ions at the buried interface. By increasing the activation energy for ion migration, this approach thermodynamically suppresses halide demixing under illumination. Compared to solution processing, vacuum-deposited monolayers ensure conformal coverage on textured sub-cells, eliminating localized strain concentrations caused by solvent accumulation.[202,203]

Although direct studies on substrate engineering for WBG PSCs remain limited, this section employs logical extrapolation from NBG interfacial dynamics[89] to bridge the knowledge gap in WBG vapor-phase design. Such cross-system inspiration is pivotal for guiding the development of high-efficiency, stable all-vacuum PSCs.

Bulk composition engineering

Pre-alloying

Incongruent sublimation kinetics of precursors presents a fundamental obstacle in the vapor-phase deposition of WBG perovskites. The vapor pressure of lead bromide is significantly higher than that of lead iodide, which leads to stochastic fluctuations in deposition rates during co-evaporation. Such kinetic disparity inevitably results in vertical phase segregation within the film. Therefore, establishing a pre-alloying strategy to lock stoichiometry at the precursor level has become a critical research frontier.

Initial approaches to address multi-source instability involved simplifying evaporation sources. However, Igual-Muñoz et al. critically noted that simple physical mixing of single-source precursors is insufficient. Their comparative study revealed that direct evaporation of physical mixtures leads to severe stoichiometric deviation in deposited films due to volatility differences.[132] To overcome this, Guesnay et al. proposed a transition to mechanochemical synthesis. They demonstrated that high-energy ball milling induces a solid-state halide-exchange reaction between cesium bromide and lead iodide, which creates a pre-alloyed precursor phase that evaporates more congruently.[145]

Building on this concept, Gil-Escrig et al. advanced the strategy by utilizing a chemically synthesized mixed-halide source such as $Pb(I_{1-x}Br_x)_2$ rather than a mechanical mixture. This chemically locked source effectively eliminated rate competition between dual lead sources. The resulting device achieved efficiencies exceeding 19% with superior thermal stability.[204]

Solid-state pre-alloying addresses chemical composition but fails to resolve heat transfer limitations. Poor thermal conductivity of powders causes internal temperature gradients, leading to rate drift over extended deposition periods. Li et al. developed a molten salt strategy to fundamentally alter the heat transfer mechanism by introducing components to pre-melt precursors into a liquid state. This phase-state engineering utilized the high thermal conductivity of liquids to homogenize the temperature field, and single-junction WBG PSC efficiencies approached 22%.[205]

Shi et al. recently integrated concepts of alloying and liquid-phase homogenization by proposing a halogen anion pre-homogenization strategy. They identified the formation of a eutectic system between lead iodide and lead bromide as key. In this eutectic state, iodine and bromine are locked at the molecular level within a single thermodynamic phase, forcing them to evaporate at a coupled rate. This approach successfully eliminated vertical phase segregation and enabled an efficiency of 30.83% for perovskite/silicon TSCs.[143]

Mainstream consensus has shifted to recognize that controlling the thermodynamic state of the source is as crucial as controlling vacuum parameters. However, a potential trade-off exists: the use of pre-fixed stoichiometric sources sacrifices the flexibility of online band-gap tuning. Future research should focus on developing versatile low-temperature eutectic solvents capable of accommodating a wider range of organic cations without compromising the stoichiometry-locking effect. Furthermore, precise stoichiometric delivery constitutes only the first half of the equation. Once these pre-locked components reach the substrate, rapid crystallization kinetics often lead to small grains and high defect densities, necessitating the introduction of a kinetic chaperone to regulate nucleation and growth.

Cl-mediated growth

While pre-alloying strategies successfully lock precursor stoichiometry, the crystallization kinetics of WBG perovskites on substrates remain a fundamental challenge. In vacuum environments, the absence of solvent coordination creates a high-supersaturation regime, leading to rapid nucleation and uncontrolled grain growth. This kinetic regime inevitably results in small grain sizes and a high density of grain boundaries, which act as non-radiative recombination centers. Therefore, chloride incorporation has evolved from a simple additive to a critical kinetic chaperone that separates nucleation and growth stages.

In hybrid sequential deposition, the primary role of chloride is to modulate inorganic framework density. Traditional evaporated lead iodide films are often too dense to react completely with organic salts. To address this, Xu et al. proposed a diffusible perovskite capping layer strategy by co-evaporating lead iodide and cesium chloride. Incorporation of cesium chloride creates a metastable porous inorganic framework that provides rapid diffusion channels for subsequent penetration of organic salts, ensuring homogeneous component distribution and complete conversion throughout the film thickness.[206]

Similarly, Luo et al. employed triple-source co-evaporation of lead iodide, lead chloride, and cesium bromide. They demonstrated that the chloride-rich intermediate phase expands the lattice spacing of the inorganic framework. This expansion lowers steric hindrance for organic cation intercalation, effectively solving the incomplete reaction issue in thick films and enabling scalable fabrication of perovskite/silicon TSCs.[151]

Beyond functioning as a kinetic sacrificial agent, trace chloride incorporation is also crucial for phase stabilization. Lattice strain at the buried interface is a critical issue in perovskite/silicon TSCs, as highlighted by Liu et al., who reported that strain accumulation accelerates degradation. Chloride incorporation serves as a powerful strain-relaxation tool to mitigate this.[28]

Selected area electron diffraction (SAED) patterns reveal distinct superlattice reflection spots (Figures 12A, 12B, and 12D). These spots indicate symmetry breaking where chloride incorporation induces minor octahedral tilting in the perovskite lattice. This structural insight is further corroborated by the X-ray diffraction (XRD) patterns shown in Figure 12C, which exhibit specific peak shifts and splitting behaviors corresponding to lattice strain relaxation rather than merely showing phase purity. This chloride-induced octahedral tilting thermodynamically stabilizes the photoactive black phase against the formation of the photo-inactive yellow phase and fundamentally suppresses phase segregation. Driven by this structural stabilization, WBG devices achieved a record efficiency of 27.43% in tandem configurations.[207]

In addition to phase stability, chloride additives are instrumental in directing crystal orientation. Wang et al. introduced n-propylamine hydrochloride (PACl) into the hybrid deposition process and found that chloride-containing intermediates favor face-on stacking of the (100) planes. This preferred orientation minimizes grain-boundary exposure to charge transport layers, thereby reducing non-radiative recombination pathways.[209] Liu et al. further demonstrated that using cesium chloride as a bulk additive in co-evaporation significantly retards crystallization rates. This effect promotes grain coarsening, reducing the total grain boundary area and enhancing V_{OC} for indoor photovoltaic applications.[210]

Chloride acts simultaneously as a transient pore former, facilitating reaction kinetics, and a permanent lattice dopant, enhancing thermodynamic stability. The conflict between requiring expulsion for the former and retention for the latter demands precise process control. While chloride-mediated growth effectively regulates grain size and phase purity, it does not fully resolve the intrinsic entropic instability caused by mixing iodine and bromine in WBG perovskites. Fundamentally suppressing light-induced phase segregation necessitates moving beyond anion engineering to explore cation-alloying strategies.

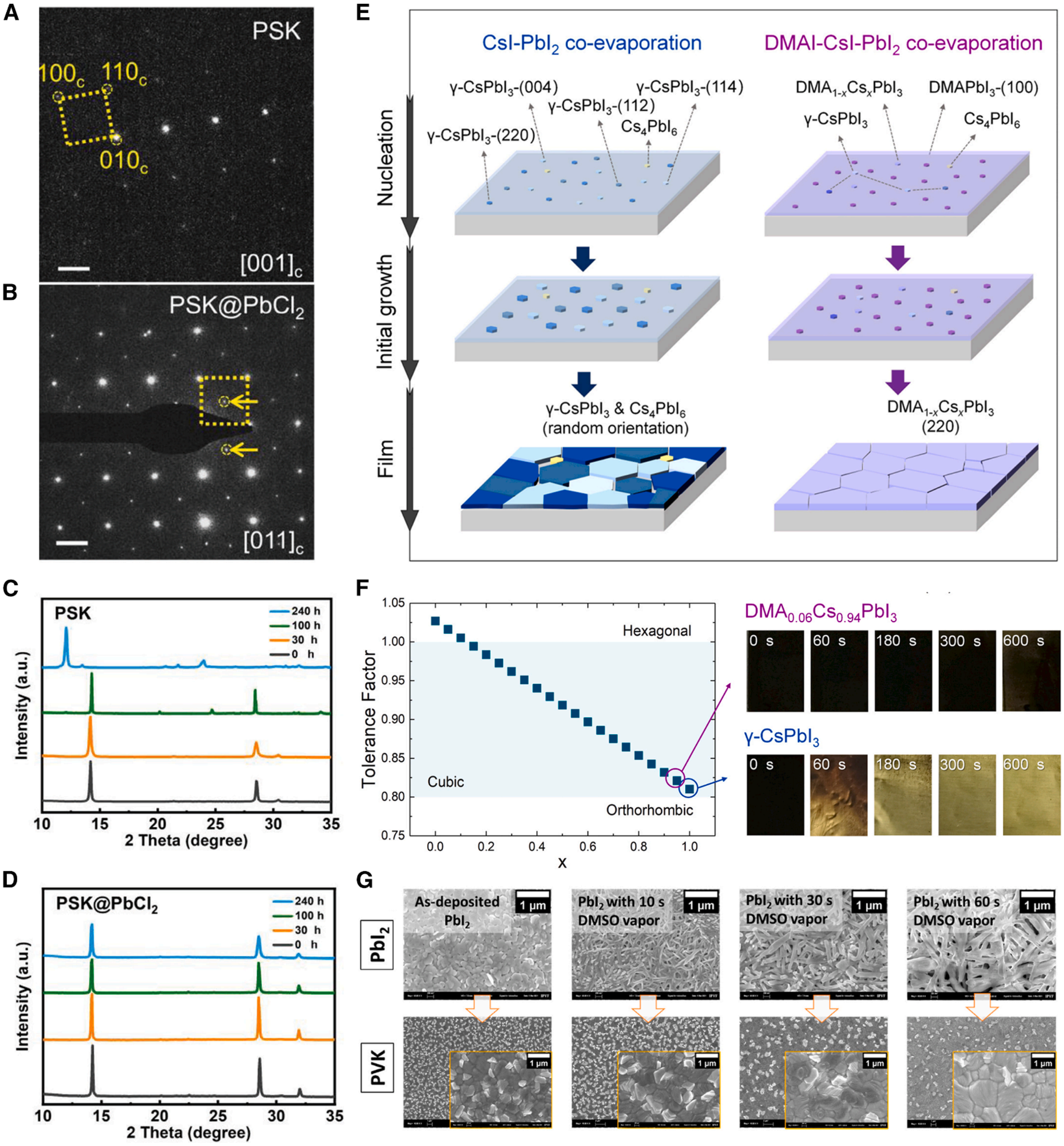

Figure 12. Additive engineering

(A) SAED patterns of perovskite thin films prepared without $PbCl_2$.

(B) SAED patterns of perovskite thin films prepared with $PbCl_2$.

(C) XRD patterns of control films over 240 h in ambient air (≈50% relative humidity [RH]).

(D) XRD patterns of perovskite@$PbCl_2$ films over 240 h in ambient air (≈50% RH).

(A–D) Reproduced with permission.[207] Copyright 2023, Wiley-VCH.

(E) The schematic diagram of nucleation and crystal growth processes for the $CsI-PbI_2$ and $DMAI-CsI-PbI_2$ co-evaporation system.

(F) The Goldschmidt tolerance factor curve for the $DMA_{1-x}CsxPbI_3$ perovskite varied with x ranging from 0 to 1, and photographs of the co-evaporated γ-$CsPbI_3$ and $DMA_{0.06}Cs_{0.94}PbI_3$ perovskite films kept in the ambiance of ~52% RH.

(E and F) Reproduced with permission.[208] Copyright 2023, Elsevier.

(G) Surface morphologies of the evaporated PbI_2 and the resulting PVK as a function of the DMSO vapor exposure time (0, 10, 30, and 60 s). Reproduced with permission.[153] Copyright 2023, Elsevier.

Multi-cation alloying

Although chloride optimizes grain size, it cannot alter the intrinsic thermodynamic instability of the perovskite lattice. WBG perovskites, particularly inorganic-rich compositions, suffer from a distorted tolerance factor t below 0.8. This geometric mismatch drives spontaneous degradation into photo-inactive δ-phases. Vapor-phase strategies must transition from binary systems to multi-cation alloying to fundamentally correct this. This approach leverages the Gibbs free energy equation, where introducing large organic cations increases mixing entropy and optimizes the tolerance factor, thereby lowering the free energy of the cubic black phase.

The first frontier lies in stabilizing the fragile inorganic $CsPbI_3$ lattice. Dong et al. introduced dimethylammonium (DMA) into the co-evaporation system, where the large DMA cation acts as a steric anchor within lattice voids. Figure 12E illustrates the fundamental alteration in the crystallization pathway. In the reference cesium iodide-lead iodide system, nucleation is random and prone to forming the yellow phase. In contrast, the DMAI-CsI-PbI_2 system exhibits a regulated nucleation process where DMA molecules act as surfactants during initial adsorption, promoting preferred orientation and suppressing non-perovskite nuclei formation. As shown in Figure 12F, the Goldschmidt tolerance factor curve indicates that increasing DMA content shifts the tolerance factor toward the ideal cubic range of 0.9–1.0. While the reference γ-$CsPbI_3$ film rapidly degrades to a yellow phase under 52% relative humidity, the alloyed film maintains its black phase, confirming that entropic stabilization effectively shields the lattice from moisture-induced degradation and enables a device efficiency of 16.10%.[208]

While doping stabilizes the lattice statically, constructing complex quaternary alloys containing cesium, formamidinium, iodine, and bromine requires dynamic control over the reaction pathway. Simply mixing four precursors in vapor deposition often leads to local phase segregation. Dong et al. recently advanced this approach by shifting focus from compositional mixing to intermediate-phase evolution. They identified that controlling stoichiometry in the vapor phase can induce the formation of a specific CsI_2Br intermediate. This phase serves as a crystallographic template rather than forming randomly and directs the subsequent reaction with FAI, enabling a self-guided crystal growth mode. This templated mechanism ensures uniform atomic-scale cation distribution, eliminating microscopic heterogeneity that typically triggers the Hoke effect. Consequently, this strategy yielded WBG PSCs with a record efficiency of 21.37%, proving that vapor deposition can achieve complex alloy synthesis previously considered exclusive to solution processing.[134]

However, even with a thermodynamically stable bulk, the polycrystalline nature of these films inevitably results in grain boundaries, which act as the final refuge for defects. Addressing remaining non-radiative recombination centers through *in situ* passivation strategies is required to fully realize the potential of entropy-stabilized lattices.

In situ grain-boundary passivation

While multi-cation alloying lowers the thermodynamic free energy of the bulk lattice, the polycrystalline nature of perovskite films inevitably introduces grain boundaries. In contrast to solution processing, where solvents often leave behind passivating species, the high-vacuum environment creates naked grain boundaries rich in undercoordinated lead and halide vacancies. These defects act as non-radiative recombination centers. Therefore, developing an *in situ* passivation strategy by introducing ligands directly into the vapor stream represents the final step for bulk optimization.

The most direct approach involves co-evaporating bulky organic ammonium salts with perovskite precursors. Due to steric hindrance, these large molecules are spontaneously expelled from the 3D lattice and self-assemble at grain boundaries. Zhang et al. demonstrated this using phenylethylammonium iodide (PEAI) in a co-evaporation process. PEAI molecules did not form a 2D phase but effectively coated the grain boundaries of the γ-$CsPbI_3$ film. This *in situ* passivation significantly reduced trap density and enhanced PL lifetime, pushing device efficiency to 15%.[211]

Furthermore, this strategy is critical for morphological control in extreme geometries. In a subsequent study, Zhang et al. applied PEAI co-evaporation to fabricate ultra-thin 10-nm perovskite films. The surfactant nature of PEAI promoted continuous wetting on the substrate, eliminating pinholes that typically compromise ultra-thin vapor-deposited films. This enabled semitransparent devices with high average visible transmittance (AVT), highlighting the dual role of ligands in defect passivation and film continuity.[212]

Beyond long-chain ligands, small functional cations can also passivate boundaries. Susic et al. introduced guanidinium into the vacuum deposition of mixed-cation perovskites. Unlike cesium or formamidinium, which occupy the A-site, the slightly larger guanidinium cation tends to accumulate at grain boundaries, creating a hydrogen-bonding network that reinforces film structural integrity. Resulting quadruple-cation films exhibited superior thermal stability compared to varying counterparts, proving that boundary engineering is essential for long-term reliability.[213]

In hybrid deposition routes, vapor-phase molecules can be used to fundamentally reconstruct the grain boundaries of the inorganic precursor. Nguyen et al. reported a solvent-vapor assisted conversion strategy by exposing evaporated compact lead iodide films to dimethyl sulfoxide vapor. Figure 12G presents SEM images, with the left side showing pristine evaporated lead iodide exhibiting highly compact and smooth morphology. This dense structure hinders organic salt infiltration. In sharp contrast, the right side reveals that after vapor treatment, the film transforms into a porous nanowire-like network of complexes. This vapor-induced porosity effectively dilates grain boundaries, creating percolation pathways that allow organic cations to penetrate deeply and react completely to passivate internal defects. This process yielded uniform WBG films with an efficiency of 19.8%.[153]

Progress has shifted from simply depositing materials to actively engineering defect landscapes during growth. Whether through steric exclusion of bulky ligands, boundary accumulation of functional cations, or vapor-induced reconstruction of precursors, the goal of neutralizing grain boundaries left vulnerable by vacuum processing remains identical. With bulk composition locked, kinetics regulated, lattice stabilized, and grain boundaries passivated, a high-quality absorber is achieved. However, device performance is ultimately gated by charge extraction. The next section addresses the critical interface between this optimized absorber and transport layers.

Interface and heterostructure engineering

Buried interface optimization

Following bulk optimization, as discussed in bulk composition engineering, carrier extraction efficiency at interfaces becomes the limiting factor for device performance. The buried interface where the perovskite nucleates on the charge transport layer presents a fundamental paradox because it determines initial crystallization and charge extraction yet remains inaccessible to post-deposition treatments. Furthermore, solution-processed interlayers on textured silicon substrates, essential for TSCs, often suffer from dewetting and thickness inhomogeneity. Vapor-phase deposition offers the ability to deposit ultra-thin and solvent-free functional layers that precisely modify energy alignment, lattice strain, and defect density without chemically eroding underlying sensitive charge transport layers.

Energetic misalignment at the heterojunction constitutes the primary barrier to efficient charge extraction. Constructing a graded homojunction via vapor deposition is a potent strategy to reshape the potential landscape. Li et al. demonstrated this by thermally evaporating an ultra-thin cesium bromide layer prior to perovskite deposition. Ultraviolet photoelectron spectroscopy (UPS) spectra in the high-binding-energy cutoff region reveal a significant shift (Figure 13A). The secondary electron cutoff for the cesium-bromide-modified perovskite moves toward higher binding energy compared to the pristine film on Spiro-TTB. This shift corresponds to a reduction in work function and indicates the formation of an interface dipole pointing away from the perovskite. The cesium bromide interlayer does not merely act as a passive buffer but diffuses to create a cesium-rich gradient that bends the valence band maximum downward, as illustrated in Figure 13B. This band bending minimizes the injection barrier for holes, effectively suppressing interfacial recombination and boosting tandem efficiency to 27.48%.[149]

Critically, the choice of evaporated salt dictates the trade-off between nucleation thermodynamics and electronic energetics. Škorjanc et al. systematically compared various seed layers, including lead iodide, lead chloride, cesium iodide, and cesium chloride, and found that while cesium bromide excels in energetic alignment, cesium chloride is superior in regulating nucleation density and preventing band-gap widening. This suggests that future optimizations must move toward mixed-halide seed layers to decouple crystallization control from band alignment.[112]

Beyond electronic barriers, physical lattice mismatch at the buried interface generates tensile strain upon cooling, which represents a significant obstacle to long-term stability. Liu et al. introduced a distinct approach: shifting from 2D interlayers to a vertically 3D/3D strained heterojunction by evaporating a lattice-mismatched cesium lead chloride buffer. The buried 3D buffer possesses a smaller lattice constant than the overlying active layer, as depicted in Figure 13C. During epitaxial growth, this mismatch pre-imposes compressive strain on the perovskite, effectively counteracting detrimental tensile strain that typically arises from thermal expansion coefficient mismatch with the silicon substrate. Time-resolved absorption spectroscopy reveals that the strain-free interface facilitates significantly faster hole extraction kinetics, as shown in Figure 13D. This strategy propelled the steady-state efficiency of fully textured TSCs to 31.5%.[28]

Even with optimized energetics and strain, atomic-scale defects such as oxygen vacancies in metal oxide transport layers remain prevalent. Vapor-phase deposition allows for a unique vapor-solid reaction to chemically repair these defects without solvent interference. Wu et al. utilized evaporated lead sulfide to passivate atomic-layer-deposited tin oxide surfaces. The lead sulfide layer executes a dual-site passivation mechanism, as illustrated in Figure 14F, where sulfur atoms fill oxygen vacancies in tin oxide while lead atoms coordinate with undercoordinated halides on the perovskite side. Dark current-voltage curves of electron-only devices demonstrate a dramatic reduction in trap-filled limit voltage for lead sulfide-treated films, indicating lower trap density (Figure 13G). This chemical passivation reduced the voltage deficit and validated the compatibility of evaporation with oxide interfaces.[214]

The evolution of buried interface engineering has transitioned from passive buffer layers to active, multifunctional heterostructures. Integration of energetic gradient construction, mechanical strain compensation, and chemical defect repair demonstrates the versatility of vapor-phase techniques. Crucially, these strategies are achieved without solvent-compatibility constraints typical of solution processing. With the buried interface optimized for extraction and stability, the degradation front shifts to the exposed top surface. The next section explores how vapor-solid reactions can be employed to functionalize this vulnerable boundary against environmental stressors.

Surface functionalization

While the buried interface dictates charge extraction, the top surface of the perovskite film represents a thermodynamic fragility point. It serves as both the initiation site for moisture-induced degradation and a reservoir of halide vacancies that accelerate non-radiative recombination. Conventional solution-based passivation faces an intrinsic dilemma where the solvent required to dissolve the passivator often erodes the underlying perovskite lattice, creating a disordered intermixed interface rather than an abrupt junction. Vapor-phase surface functionalization offers a distinct advantage by relying on vapor-solid reactions to exploit the intrinsic solvent orthogonality of gas-phase precursors. This allows the construction of atomically precise passivation layers and heterostructures without compromising the structural integrity of the absorber.

The most kinetically favorable strategy involves exposing the perovskite surface to reactive organic amine vapors. Unlike bulky molecules in solution that merely coat the surface, small gas-phase molecules can diffuse into the lattice surface and chemically neutralize defects. Chiang et al. demonstrated a vacuum-based healing strategy using ethylenediammonium diiodide ($EDAI_2$) vapor. PL quantum efficiency of the treated film exhibits substantial enhancement compared to pristine controls. Crucially, the addition of a C_{60} contact layer further boosts PL quantum efficiency, implying that vapor treatment optimizes band alignment for extraction in addition to passivating traps (Figure 14A). V_{OC} distribution for both pure-iodide and mixed-halide devices narrows significantly and shifts toward higher values after passivation, as depicted in Figure 14B. This confirms that vapor permeation provides a uniform, large-area healing effect unattainable with spin coating, enabling 17.8% efficiency in 1.76 eV cells.[215]

While organic molecules heal defects, they often lack the physical density to block ion migration. Constructing a robust barrier requires thermally evaporated inorganic salts or atomic-layer-deposited oxides. Wang et al. utilized evaporated cesium

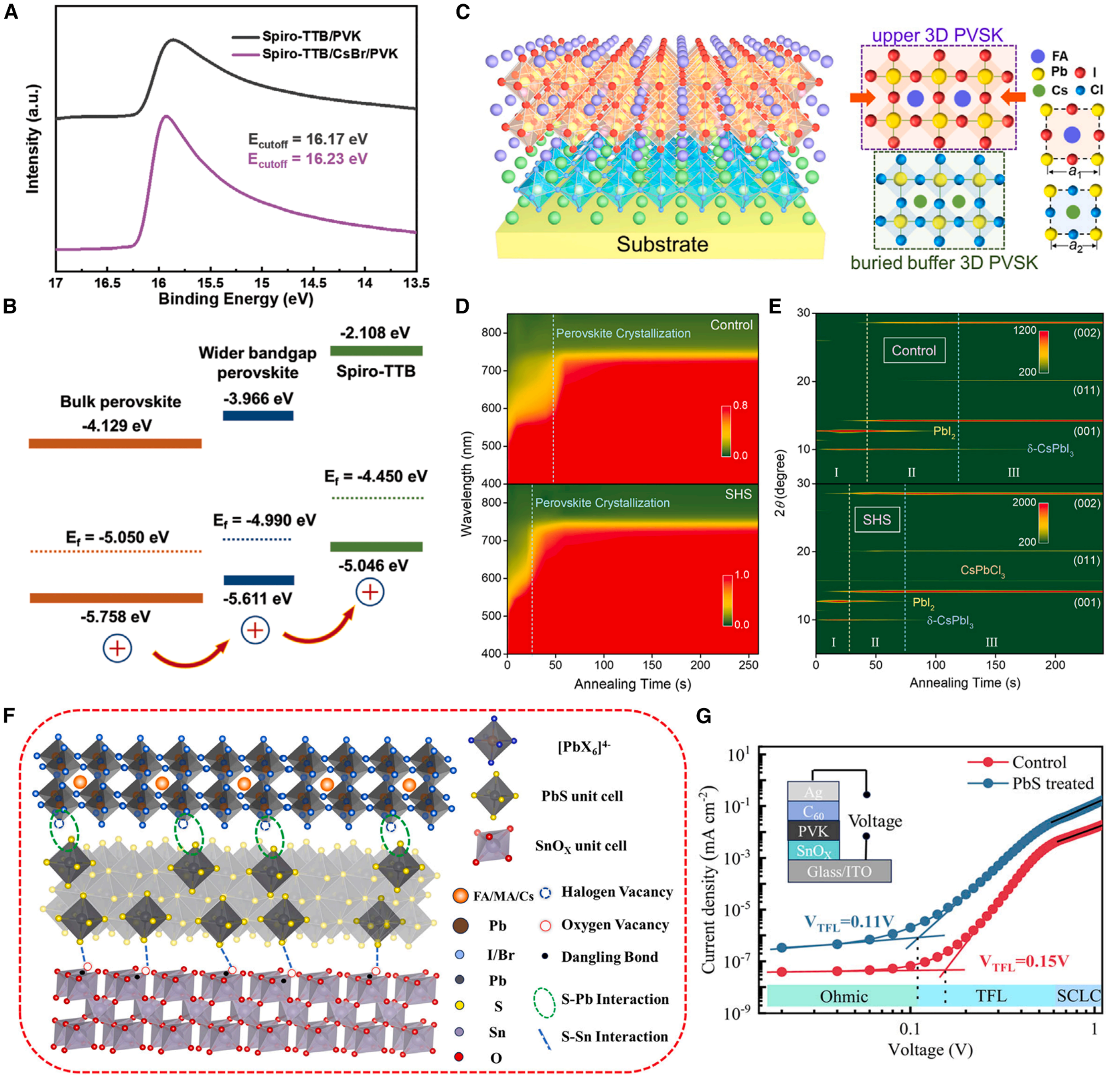

Figure 13. Buried interface optimization

(A) UPS spectra in the cutoff regions of perovskite films on Spiro-TTB with and without CsBr.

(B) Schematic diagram of the energy level of perovskite and HTL after introducing the CsBr interface layer.

(A and B) Reproduced with permission.[149] Copyright 2021, Wiley-VCH.

(C) Schematic illustration of compressive strain applied to upper 3D perovskite films by tailoring lattice parameters of buried buffer 3D perovskites.

(D) Time-resolved absorption of the CsFA perovskite films deposited on bare (control) and $CsPbCl_3$-modified (strained heterostructure, SHS) glass under different annealing times at 150°C.

(E) XRD measurements of the CsFA perovskite films deposited on bare (control) and $CsPbCl_3$-modified (SHS) glass under different annealing times at 150°C.

(C–E) Reproduced with permission.[28] Copyright 2024, Elsevier.

(F) Schematic diagram of PbS mechanism, including PbS passives, oxygen vacancies, and uncoordinated lead (Pb^{2+}). ALD, atomic layer deposition.

(G) Dark I-V curves of space-charge-limited current (SCLC) measurement for the electron-only devices with SnO_x or PbS-treated SnO_x films.

(F and G) Reproduced with permission.[214] Copyright 2025, Wiley-VCH.

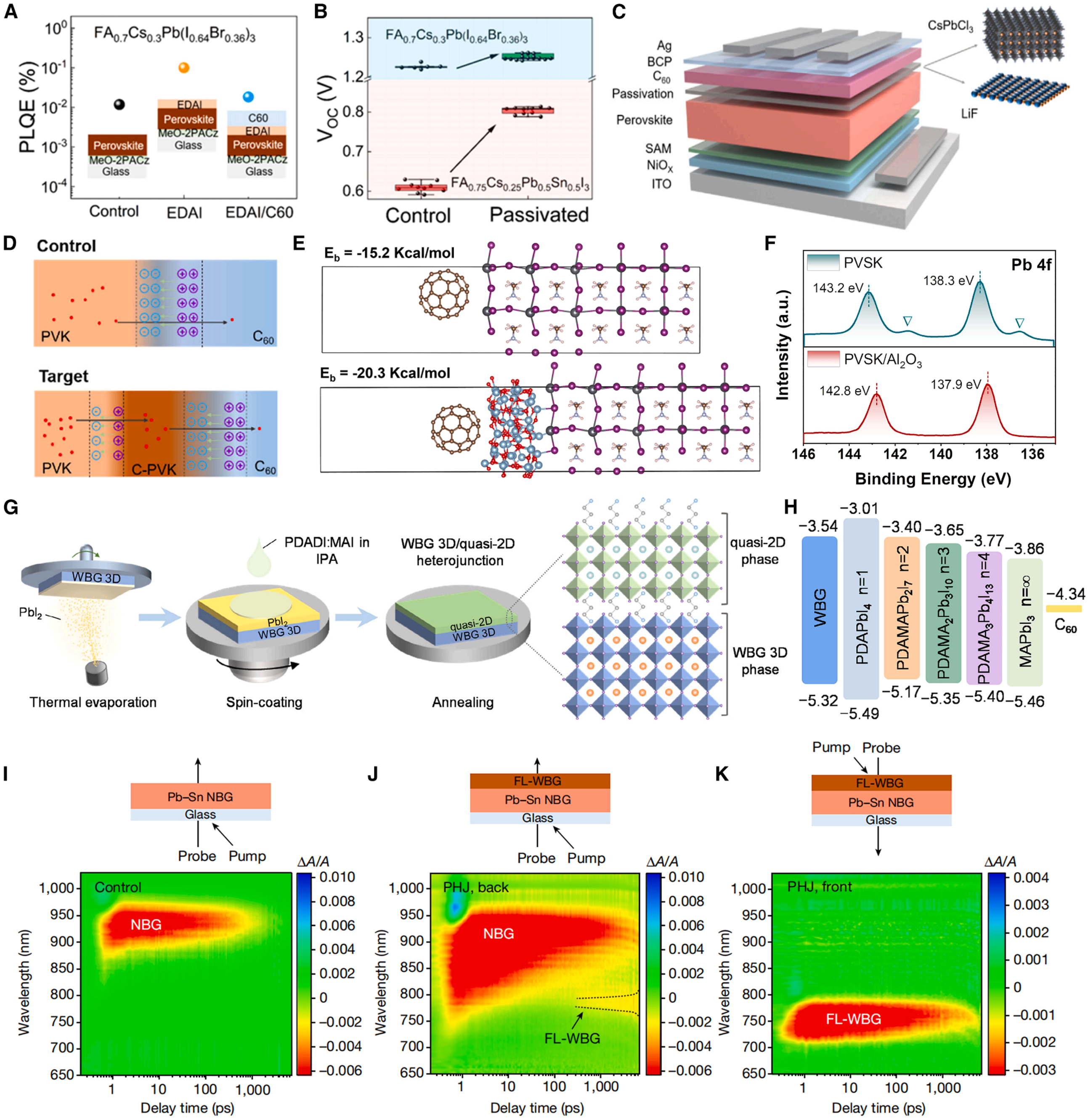

Figure 14. Surface optimization

(A) Photoluminescence quantum efficiency (PLQE) values for a $FA_{0.7}Cs_{0.3}Pb(I_{0.64}Br_{0.36})_3$ (1.77 eV) evaporated perovskite film, with $EDAI_2$ treatment and with $EDAI_2$ treatment plus C_{60} contact layer.

(B) V_{OC} statistics for devices based on $FA_{0.7}Cs_{0.3}Pb(I_{0.64}Br_{0.36})_3$ and $FA_{0.75}Cs_{0.25}Pb_{0.5}Sn_{0.5}I_3$ with and without $EDAI_2$ passivation.

(A and B) Reproduced with permission.[215] Copyright 2023, American Chemical Society.

(C) Device structure of PSC.

(D) Schematic diagram of the internal electric field at the control and the target interface.

(C and D) Reproduced with permission.[216] Copyright 2025, Wiley-VCH.

(E) The calculated binding energy of PVK/C_{60} and PVK/AlO_x.

(F) X-ray photoelectron spectroscopy (XPS) spectra of Pb *4f* pristine PVK and PVK/AlO_x films.

(E and F) Reproduced with permission.[217] Copyright 2024, Wiley-VCH.

(G) Schematic of the solution/evaporation process to form WBG 3D/DJ perovskite heterojunctions.

(H) Energy-level scheme of WBG 3D perovskite, $PDAMA_{n-1}Pb_nI_{3n+1}$ (n = 1–4), and C_{60} extracted from UPS data.

(legend continued on next page)

lead chloride to modify the surface, creating a purely inorganic tunneling junction. The evaporated cesium lead chloride forms an ultra-thin dense layer between the perovskite and the electron transport layer (ETL) (Figure 14C). WBG cesium lead chloride induces a strong internal electric field at the interface, which bends bands to repel holes from surface recombination centers while permitting electron tunneling (Figure 14D). This mechanism decouples surface passivation from carrier transport, pushing module efficiency over 21%.[216]

Similarly, Ji et al. employed atomic layer deposition to grow an aluminum oxide layer, exploiting the high reactivity of precursors. Aluminum oxide forms a much stronger chemical anchor to the perovskite surface than physical adsorption of C_{60}, as shown in Figure 14E. Binding energy shifts in Pb *4f* spectra indicate that aluminum species passivate undercoordinated surface leads, as evidenced in Figure 14F. This dense oxide barrier effectively blocks volatile species, achieving a PCE of 21.80%.[217]

Surface functionalization frontiers lie in constructing type II heterojunctions with distinct dimensionalities, such as 2D/3D, or band gaps. Vapor deposition is uniquely suited for this, as it can stack materials that are chemically incompatible in solution. Liu et al. developed a hybrid evaporation/solution approach to form phase-pure Dion-Jacobson (DJ) 2D perovskite capping layers on WBG 3D perovskite substrates. The organic spacer reacts with surface-excess lead iodide to form uniform quasi-2D perovskites with controllable *n* values, as depicted in Figure 14G. By tuning the *n* values of the DJ phase perovskites, a series of quasi-2D layers with gradually increasing band gaps are formed. These quasi-2D layers, together with the C_{60} electron transport layer, create a stepwise conduction band potential that efficiently funnels electrons from the WBG 3D perovskite to C_{60} while blocking holes, as shown in Figure 14H. This minimizes the voltage deficit typically associated with WBG cells.[218]

Furthermore, Lin et al. demonstrated the concept of an immiscible 3D/3D heterojunction, which represents an ideal scenario for surface passivation. Figures 14I–14K provide ultrafast kinetic evidence via transient absorption spectroscopy. While the control film in Figure 14I shows uniform decay, the heterojunction exhibits distinct bleaching signals when pumped selectively from the NBG side in Figure 14J vs. the functional layer side in Figure 14K. This indicates rapid unidirectional charge transfer driven by the heterojunction field. Although demonstrated via solution processing, this ideal architecture validates the design target for all-vapor processes to create atomically sharp interfaces acting as semi-permeable membranes for specific carriers.[219]

Vapor-phase strategies have proven superior for creating inorganic and heterojunction interfaces that solution methods struggle to achieve due to solvent redissolution issues. By strictly decoupling functional layer deposition from absorber formation, vapor-solid reactions enable independent optimization of stability and transport. Having secured both the bottom contact and top surface, the final challenge lies in healing residual crystallographic strain and defects deep within the lattice, which will be addressed in the subsequent section on post-deposition treatments.

Fundamental divergence in passivation mechanisms between vacuum deposition and solution processes

In solution processing, passivators reside in a solvent environment at ambient temperature with a stable saturated vapor pressure, ensuring the perfect preservation of molecular structural integrity. However, during vacuum thermal evaporation, organic halides face severe thermal stability challenges.

Traditional large-molecule organic salts, such as aromatic ammonium salts, typically exhibit low thermal decomposition temperatures. Before reaching the critical temperature required for sublimation, weak internal chemical bonds, such as C–N bonds, often undergo thermal pyrolysis.[220] Research indicates that these molecules exhibit non-constant sublimation behavior under vacuum, frequently dissociating into volatile amine fragments and hydrohalic acid gases.[84] This phenomenon makes evaporation rates difficult to monitor precisely, and the components reaching the substrate lose their intended passivation activity.[221,222] In contrast, solution methods ensure that molecules with intact functional groups act directly on defect sites.

During film formation in solution methods, the presence of solvents allows long-range diffusion of solute molecules and utilizes capillary forces to effectively transport passivators deep into grain boundaries.[223] Conversely, in the vacuum process of room temperature deposition and subsequent annealing, passivators encounter severe kinetic barriers.[224]

Due to the absence of a liquid medium, passivator diffusion within the solid matrix is restricted by extremely small lattice diffusion coefficients.[225] Consequently, passivators are often stochastically trapped within perovskite grains as inactive inclusions rather than effectively segregating at grain boundaries or surfaces, as seen in solution methods.[226] This randomness in spatial distribution is essentially a limitation of solid-state kinetics on the effective utilization of passivators, preventing vacuum processes from achieving the interfacial self-healing effects common in solution processing.[227]

WBG perovskites prepared by solution and vacuum methods exhibit an inversion in the spatial distribution of their defect chemistry.[228] Solution-processed films, influenced by solvation effects, tend to form an iodine-deficient/lead-rich environment at the surface, creating shallow-level iodine vacancies (V_I).[229]

However, vacuum co-evaporation processes often result in iodine-rich surface characteristics due to the instantaneous nature of precursor flux, inducing high densities of deep-level iodine antisite defects (I_{Pb}).[228] Traditional cationic passivators designed for solution methods are largely ineffective at repairing these deep-level defects specific to vacuum processes.[230] This disconnect between the nature of the defects and the passivation strategy is the profound physical root cause of why

---

(G and H) Reproduced with permission.[218] Copyright 2025, Wiley-VCH.
(I) The ultrafast TA spectra of control Pb-Sn perovskite films.
(J) The ultrafast TA spectra of perovskite heterojunction (PHJ) perovskite with 405-nm pump light, pumped from the NBG side.
(K) The ultrafast TA spectra of the full-lead wide-band-gap (FL-WBG) side.
(I–K) Reproduced with permission.[219] Copyright 2023, Springer Nature.

vacuum-processed WBG cells lag behind solution-processed ones in V_{OC}.[26,137]

In a vacuum environment, molecular transport follows the laws of line-of-sight propagation.[84] This quasi-ballistic transport mode creates severe shadowing effects on the rough microscopic morphology of polycrystalline films.[73] Passivation molecules cannot utilize liquid wettability to enter narrow and deep grain-boundary crevices as they do in solution-based methods. Since atomic migration rates are limited by lattice diffusion during the solid-state transformation stage, point defects encapsulated within the film are difficult to eliminate through simple surface post-treatments.[103,225] The incomplete coverage caused by shadowing effects, combined with the limitations of solid-state diffusion, constitutes the technical bottleneck of vacuum passivation.

Evolution of all-vacuum-compatible passivation strategies

tTo achieve all-vacuum compatibility, passivation molecules must possess high thermal stability and robust coordination capabilities to replace the easily dissociable traditional ammonium salts. Compared with easily deprotonated ammonium groups, amidinium ligands enhance N–H bonds via resonance effects, exhibiting superior thermal and photostability. This prevents the failure of the passivation layer during high-temperature deposition processes.[231] Organometallic molecules with large π-conjugated systems, such as copper phthalocyanine (CuPc) and zinc phthalocyanine (ZnPc), exhibit excellent sublimation characteristics. Their highly ordered stacking structures facilitate interfacial charge extraction while effectively passivating surface defects.[73] Pyridine-carbazole (Py-Cz) molecules bind to uncoordinated Pb^{2+} on the perovskite surface through specific coordination bonding. These molecules remain chemically stable under vacuum, enabling efficient defect remediation.[232]

For all evaporation processes, several promising technical strategies have been explored to eliminate reliance on solution-assisted methods.[103,116] To address the instability of organic salts, researchers have proposed passivation schemes using rigid aromatic molecules with high thermal stability. Copper phthalocyanine and triphenylamine derivatives are typical representative materials.[73] These molecules possess large conjugated systems and high decomposition temperatures. Copper phthalocyanine has a sublimation temperature exceeding 300°C in vacuum. This type of molecule maintains chemical structural integrity even at high temperatures.

Rigid molecules passivate uncoordinated lead ions on the surface through Lewis acid-base interactions. The nitrogen atoms in triphenylamine molecules have strong electron-donating capabilities. They can form stable coordination bonds with lead atoms on the perovskite surface.[233] This interfacial layer not only reduces charge trap density but also tunes the interfacial electric field. Research shows that the V_{OC} of WBG cells increases significantly after introducing rigid aromatic modification layers. This method effectively narrows the voltage loss gap between vacuum-prepared and solution-processed devices.

Inorganic salts are ideal passivation components for vacuum processes due to their outstanding thermal stability. Partially replacing lead iodide with lead chloride in WBG perovskite fabrication has proven extremely effective.[234] The introduction of chloride ions significantly improves crystal growth kinetics. Chloride atoms reduce point-defect formation by filling lattice vacancies. Experimental results show that introducing lead chloride extends carrier lifetimes from 5.6 to over 100 ns. This massive lifetime gain directly enhances the photovoltaic performance of WBG cells.

Alkali metal salts, such as potassium thiocyanate, also exhibit excellent passivation potential.[235] Potassium ions tend to enrich at grain boundaries and occupy interstitial sites. This distribution effectively suppresses the long-range migration of halide ions. Thiocyanate ions passivate lead defects through Lewis coordination. This multifunctional inorganic additive strategy optimizes both crystallization quality and interfacial stability.

Acid modulation strategies offer new approaches to addressing the thermal decomposition of organic salts such as MAI. Introducing more acidic cations can inhibit deprotonation reactions.[231] The addition of methylammonium chloride stabilizes the chemical environment of methylammonium cations. This synergy reduces the formation of harmful byproducts.[222]

This method establishes a stable sublimation kinetic window. Mixing precursors of different acidities via pre-pelletizing processes reduces the non-uniform escape of volatiles.[222] This technique significantly enhances the vertical uniformity and crystallinity of co-evaporated films. The efficiency of WBG cells optimized by acid modulation has exceeded 20%.[222]

Interface field effects can be utilized to address common voltage losses in WBG cells. Introducing molecules with strong dipole moments, such as isopropylammonium iodide, can form a dual-field passivation mechanism.[236] These molecules can establish a stable molecular dipole field on the perovskite surface. Simultaneously, they interact with charge transport layers to form interfacial electric fields.

This dual electric field can repel minority carriers. This repulsion reduces their chances of contacting interface defects. The voltage deficit of WBG cells treated with i-PAI was reduced to 0.39 V.[236] These molecules exhibit good thermal robustness under vacuum conditions. This characteristic makes them very suitable as a final passivation step in vacuum evaporation processes. It not only improves cell efficiency but also significantly suppresses light-induced phase separation.

Utilizing vacuum methods to deposit 2D perovskite capping layers on the surface of WBG perovskites is an excellent physical repair method.[164] This can be achieved by precisely controlling the evaporation rates of molecules such as n-hexylammonium bromide. Vacuum-deposited 2D layers can uniformly fill microscopic pinholes on the surface of 3D perovskites. This repair effect is difficult to achieve with solution post-treatments.

The vacuum process avoids damage to the underlying 3D perovskite by solvents. It ensures a steep chemical potential distribution at the interface. Research shows that this 2D/3D structure exhibits excellent uniformity on large-area submodules. This structure effectively isolates the erosion of WBG components due to external moisture. This scheme provides a practical passivation path for large-scale industrial production.

Table 10 summarizes the comparative analysis of vacuum-compatible passivation strategies.

Table 10. Analysis of vacuum-compatible passivation strategies

Specific methods/materials	Passivation mechanism and physical essence	Sublimation stability	Core gains for WBG perovskites
Rigid aromatic molecules: CuPc, TPA, SAMs	utilizing π-π stacking and heteroatom lone pairs to form stable Lewis acid-base coordination with uncoordinated surface Pb^{2+}	extremely high (>300°C); maintains molecular structural integrity	significantly reduces interface traps, tunes dipole fields, and narrows V_{OC} deficit
Cl-alloy mediated: $PbCl_2$	chloride segregation induces grain-boundary self-passivation and promotes organic salt diffusion via lattice modulation	extremely high (>400°C); outstanding thermal stability of inorganic salts	achieves micron-scale grains, extends lifetime from 5 to >100 ns, and suppresses non-radiative recombination
Acid modulation: MACl + FAI/MAI	inhibits deprotonation of organic salts via strong acidic environments to stabilize the sublimation window	moderate (100°C–150°C); achieves controlled co-sublimation	ensures stoichiometric precision of WBG components and enhances vertical uniformity
Polar molecules: i-PAI, isopropylammonium	establishes molecular dipole fields to form dual-electric field passivation, repelling minority carriers	good (150°C–250°C); strong thermal robustness	specifically suppresses light-induced phase segregation and reduces voltage deficit to 0.39 V
In situ 2D capping: PEABr, HABr	constructs 2D/3D heterojunctions via sequential evaporation, forming physical shields and repairing surface pinholes	good (150°C–250°C); *in situ* growth without solvent damage	establishes steep interface chemical potential gradients and enhances submodule reproducibility and lifetime

Annealing engineering

Even with precise nucleation control and interface functionalization, vapor-deposited WBG perovskite films exist in a kinetically trapped metastable state immediately after deposition. Unlike solution processing, where solvent evaporation drives crystallization, vapor-deposited films often suffer from distinct vulnerabilities, including volatile component deficiency due to high-vacuum promoting organic cation desorption, residual tensile strain generated by thermal expansion mismatch with the substrate during cooling, and under-coalesced grain boundaries resulting in nanoscale voids. Therefore, post-deposition annealing represents a critical lattice healing process rather than merely a thermal activation step. This section critically evaluates three advanced strategies, including vapor-assisted, atmosphere-controlled, and pressure-assisted annealing, that transcend conventional thermal treatment to reconstruct the lattice and release strain.

Vapor-assisted annealing

Incongruent sublimation of organic vs. inorganic precursors constitutes the fundamental thermodynamic challenge in vacuum deposition. Annealing in an inert atmosphere often exacerbates the loss of volatile A-site cations such as methylammonium or formamidinium, which leads to surface decomposition. Vapor-assisted annealing addresses this by introducing a compensatory vapor atmosphere to establish a solid-vapor equilibrium that suppresses decomposition and drives grain-boundary reconstruction.

Dou et al. developed a vapor-assisted, pressure-controlled annealing strategy specifically for WBG perovskites. Recognizing that simple vapor exposure is insufficient for deep healing, they utilized a high-pressure mixed vapor of 4-fluorophenylmethylammonium bromide and ammonium fluoride. Unlike conventional thermal annealing, in which vapors primarily interact with the surface, the pressure-controlled process creates a high-pressure gradient that forces reactive molecules to permeate the entire film thickness (Figure 15A). Organic vapors compensate for A-site vacancies while simultaneously forming a robust 2D/3D heterostructure at grain boundaries (Figure 15B). While control and thermally annealed films display heterogeneous and short carrier lifetimes, represented by blue and green regions, respectively, the pressure-controlled film exhibits a uniform and extended lifetime distribution, as indicated by the red and orange regions in Figure 15C. This confirms that manipulating the chemical potential of the annealing atmosphere effectively heals deep-level traps inherent to vacuum-processed films, enabling an V_{OC} of 1.28 V.[237]

This principle extends beyond organic cations. Putland et al. demonstrated that for complex quaternary absorbers such as Cu_2AgBiI_6, annealing in iodine vapor is mandatory to prevent segregation of metallic bismuth and binary phases.[239] Similarly, Zia et al. proved that methylammonium chloride vapor drives the recrystallization of $MAPbCl_3$ to reduce surface energy.[240] These findings collectively establish vapor-assisted annealing as a universal tool for stoichiometry correction.

Atmosphere-controlled annealing

While vapor-assisted annealing balances stoichiometry, regulating crystallization kinetics requires a catalytic agent. In vacuum deposition, the transition from amorphous or nanocrystalline intermediate phases to the crystalline perovskite phase often involves a high energy barrier. Moisture is usually considered detrimental, yet it lowers the activation energy for grain-boundary migration and lattice expansion.

Wu et al. systematically exploited this effect in a humidity-controlled annealing strategy for WBG perovskites on textured silicon. The rigid texture of silicon typically imposes severe compressive strain on the growing perovskite. Figure 15D reveals that under an optimized relative humidity of 40%, perovskite characteristic peaks intensify rapidly within 30 min. This

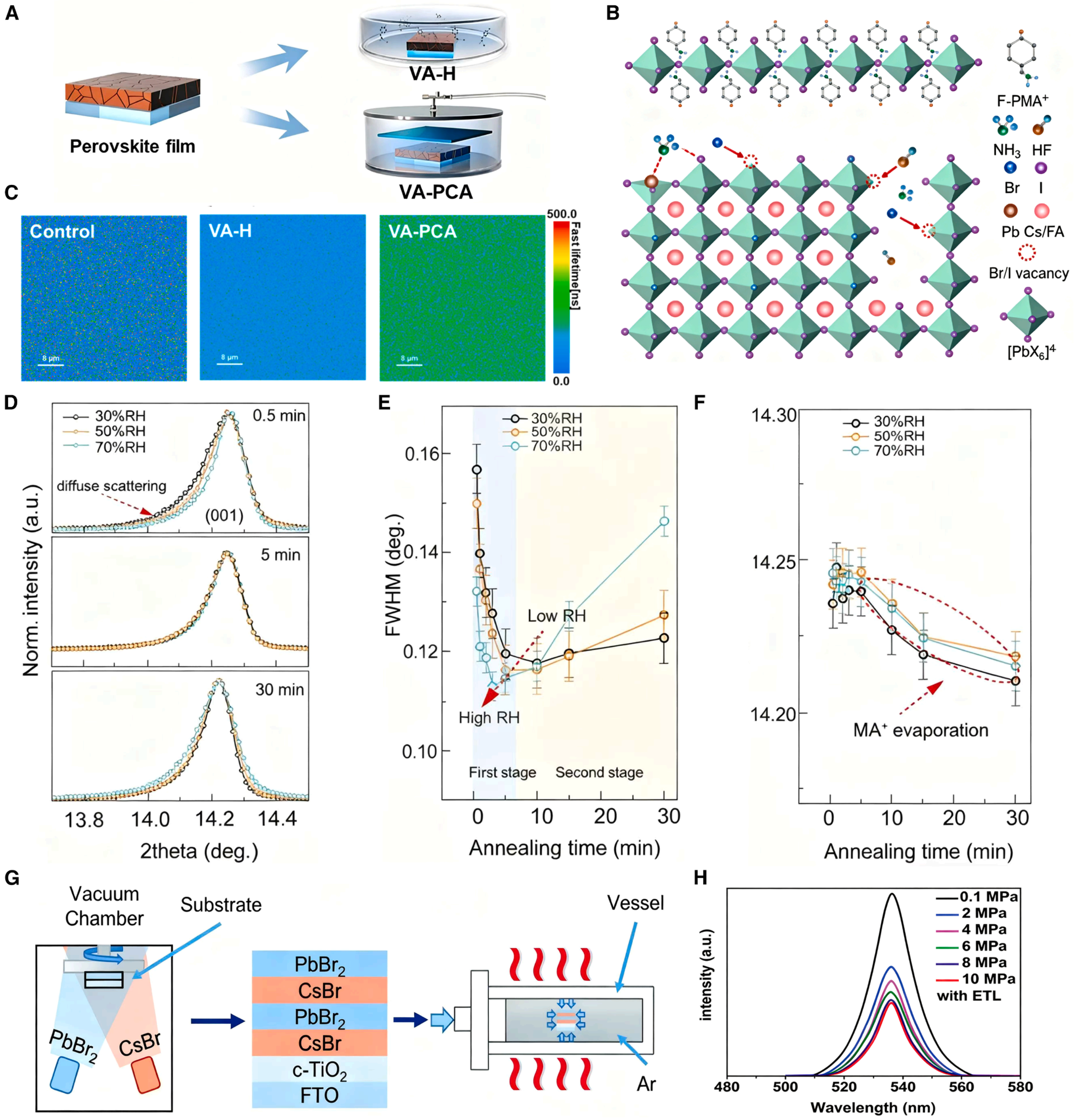

Figure 15. Vapor-assisted annealing

(A) Schematic diagram of the vapor-assisted healing (VA-H) and vapor-assisted pressure-controlled annealing (VA-PCA) post-treatment processes.

(B) Schematic diagram of the interaction between perovskite film and F-PMABr/NH_4F mixed vapor.

(C) Fluorescence lifetime imaging (FLIM) of control and VA-H- and VA-PCA-treated perovskite films. (A–C) Reproduced with permission.[237] Copyright 2025, Elsevier.

(D) Enlarged diffraction profiles of perovskite films after annealing for 0.5, 5, and 30 min.

(E) The FWHM of the (001) diffraction peak of the perovskite phase during the annealing process.

(F) Peak position evolution of the (001) diffraction peak of the perovskite phase during the annealing process.

(D–F) Reproduced with permission.[238] Copyright 2025, American Chemical Society.

(G) Schematic illustration for the deposition of $CsPbBr_3$ films by multi-step sequential dual-source vacuum deposition (MS-DSVD) method and the pressure-assisted annealing process.

(H) Steady-state PL of the $CsPbBr_3$ films deposited on the substrate with ETL.

(G and H) Reproduced with permission.[126] Copyright 2020, The Royal Society of Chemistry.

Table 11. Mapping of challenges, techniques, and strategies

Core challenges	Relevant techniques	Key strategies
Intrinsic thermodynamic fragilities	co-evaporation; combinatorial vacuum deposition; vapor-phase epitaxy; pulsed laser deposition	multi-cation alloying; pre-alloying; Cl-mediated growth
The halide segregation dilemma in vacuum	co-evaporation; combinatorial vacuum deposition; innovation of equipment and monitoring technology	multi-cation alloying; *in situ* grain-boundary passivation
The challenge of organic precursor volatility	continuous flash sublimation; close-space sublimation; innovation of equipment and monitoring technology	vapor-assisted annealing; atmosphere-controlled annealing; pressure-assisted annealing
The solid-state growth constraints in solvent-free environments	sequential evaporation; solution-vapor hybrid processes; chemical vapor deposition	substrate surface energy engineering; buried interface optimization; surface functionalization

indicates that trace water vapor accelerates the mass transport required for phase conversion. The full width at half-maximum (FWHM) of the (001) peak decreases significantly, signifying grain coarsening and defect annihilation (Figure 15E). Critically, the (001) diffraction peak shifts toward lower angles during humidity-controlled annealing (Figure 15F). This shift corresponds to the release of compressive strain accumulated during heteroepitaxial growth on textured silicon. By leveraging moisture to decouple nucleation from growth, a high FF of 82.6% was achieved in tandem devices.[238]

Zhang et al. corroborated this in all-inorganic $CsPbBr_3$, showing that moisture-assisted annealing promotes ion diffusion in kinetically sluggish inorganic films.[241] However, Huang et al. warned that while oxidative annealing in dry air can passivate vacancies, the window of operation is narrow because prolonged exposure leads to degradation.[242] Thus, precise atmospheric control presents a trade-off that requires rigorous optimization.

Pressure-assisted annealing

A unique morphological defect of vapor deposition is the tendency to form fluffy or porous films due to the non-directional nature of gas-phase adsorption. To address this physical limitation, Hua et al. proposed a pressure-assisted annealing method that introduces an external mechanical field during the thermal process.

Physical pressure applied to the film during annealing serves a dual function, as illustrated in Figure 15G. Thermodynamically, it lowers the Gibbs free energy barrier for grain coalescence while mechanically compressing grains to eliminate nanoscale voids. Steady-state PL of pressure-annealed $CsPbBr_3$ films is significantly enhanced compared to pristine films, as shown in Figure 15H. This enhancement is attributed to the reduction of non-radiative recombination centers at grain boundaries, which are effectively annihilated by pressure-induced densification. This strategy demonstrates that physical fields effectively complement thermal fields in lattice reconstruction.[126]

The evolution from conventional passive thermal annealing to active vapor or pressure-assisted strategies marks a significant maturation in vapor-phase technology. Throughout vapor-phase optimization strategies for WBG perovskite thin films, a comprehensive bottom-up roadmap for the vapor-phase optimization of WBG perovskites is presented: originating from source chemistry to lock stoichiometry at the molecular level, leveraging kinetic and entropic engineering to construct a robust lattice skeleton, employing interface engineering to ensure selective charge extraction and surface protection, and finally, utilizing annealing engineering to provide thermodynamic healing of strain and defects.

This holistic strategy underscores that the high quality of vapor-deposited films is not solely determined within the vacuum chamber but is meticulously engineered through post-deposition evolution. Such a blueprint is essential for approaching the theoretical limits of perovskite-based tandem photovoltaics. To visualize the practical efficacy of these strategies, Table 11 systematically summarizes photovoltaic performance parameters of representative small-area WBG PSCs, highlighting the suppression of V_{OC} deficits and efficiency breakthroughs achieved under varying band gaps.

The industrialization of WBG perovskites is constrained by the interplay between thermodynamic instability and kinetic retardation in solvent-free vacuum environments.

To address intrinsic thermodynamic fragilities and halide segregation, the quintessential approach involves achieving atomic-level mixing through co-evaporation or combinatorial vacuum deposition. These techniques are synergistically coupled with multi-cation alloying and pre-alloying to enhance mixing entropy and mitigate lattice strain.

To address the challenges posed by organic precursor volatility and subsequent stoichiometric drift, the technical focus shifts to CFS and innovations in monitoring technology to maintain precise partial pressures. These advancements support post-processing strategies, such as atmosphere-controlled annealing and pressure-assisted annealing, to safeguard chemical integrity.

Regarding solid-state growth constraints without solvent assistance, the solution lies in utilizing hybrid solution-vapor processes to introduce chemical mediators. Concurrently, substrate surface energy engineering and buried interface optimization are implemented to modulate heterogeneous nucleation barriers, ultimately enabling high-quality crystallization through surface functionalization.

Table 12 maps the core challenges, corresponding techniques, and key strategies for vapor-phase perovskite growth.

Table 12. Summary and comparison of champion efficiency and open-circuit voltage values for small-area, single-junction wide-band-gap solar cells based on different material systems, vapor-phase fabrication methods, and optimization strategies

Material system	Preparation method	Further strategy	Configuration	Band gap (eV)	Active area (cm^2)	PCE (%)	V_{OC} (V)	Reference
Single A, single X	sequential evaporation	–	FTO/SnO_2/$CsPbI_3$/Spiro-OMeTAD/Ag	~1.70	0.09200	8.80	1.000	Hutter et al.[129]
			ITO/PTAA/$CsPbI_3$/PCBM/Al	1.74	–	10.20	1.000	Kottokkaran et al.[243]
			FTO/TiO_2/$CsPbI_3$/P3HT/Ag	~1.65	0.04000	5.71	0.710	Yonezawa et al.[244]
			FTO/TiO_2/$CsPbBr_3$/Spiro-OMeTAD/Ag	~2.36	–	10.91	1.498	Tong et al.[128]
			FTO/TiO_2/$CsPbBr_3$/C	2.33	0.14750	9.35	1.545	Xiang et al.[125]
		annealing engineering	FTO/TiO_2/$CsPbBr_3$/C	2.20	–	8.86	1.520	Zhang et al.[241]
			FTO/TiO_2/$CsPbBr_3$/C	~2.36	0.16000	7.22	1.420	Hua et al.[126]
	co-evaporation	–	ITO/Ca/C_{60}/$CsPbI_3$/TAPC/TAPC:MoO_3/Ag	1.72	0.05100	9.40	0.980	Chen et al.[131]
			ITO/c-TiO_2/$CsPbI_3$/P3HT/Au	1.67	–	10.50	1.063	Frolova et al.[136]
			FTO/c-TiO_2/$CsPbBr_3$/Spiro-MeOTAD/Au	2.35	0.09000	6.95	1.270	Lei et al.[245]
		additive engineering	ITO/PTAA/γ-$CsPbI_3$/PCBM/BCP/Ag	~1.75	0.04500	15.00	1.090	Zhang et al.[211]
		interface engineering	ITO/Me-4PACz/$MAPbI_3$/C_{60}/SnO_x/Ag	~1.63	0.05000	23.10	1.140	Alvianto et al.[246]
		annealing engineering	FTO/c-TiO_2/γ-$CsPbI_3$/Spiro-OMeTAD/Au	1.73	0.09000	16.30	1.100	Huang et al.[242]
	other evaporation	additive engineering	FTO/TiO_2/Sn:$CsPbBr_3$/C	~2.20	0.09000	8.95	1.360	Abib et al.[247]
	solution-assisted evaporation	–	FTO/c-TiO_2/m-TiO_2/$CsPbBr_3$/MnS/C	2.30	–	10.45	1.520	Li et al.[140]
Single A, mixed X	sequential evaporation	–	ITO/Ca/C_{60}/$CsPbI_2Br$/TAPC/TAPC:MoO_3/MoO_3/Ag	~1.85	0.05100	13.00	1.130	Lin et al.[127]
	co-evaporation	–	FTO/TiO_2/$CsPbIBr_2$/Au	2.05	0.15900	4.70	0.959	Ma et al.[130]
			FTO/TiO_2/$CsPbI_2Br$/Spiro-OMeTAD/Au	1.97	0.09000	5.70	1.100	Park et al.[248]
			ITO/MoO_3/TaTm/$CsPbI_2Br$/C_{60}/BCP/Ag	1.90	0.02640	10.00	0.940	Igual-Muñoz et al.[132]
			ITO/Ca/C_{60}/$CsPbI_2Br$/TAPC/TAPC:MoO_3/Ag	1.82	0.05100	11.80	1.130	Chen et al.[131]
			ITO/C_{60}:PhIm/C_{60}/$MAPb(Br_xI_{1-x})_3$/TaTm/TaTm: F6-TCNNQ/Au	1.72	–	15.90	1.120	Longo et al.[133]
			ITO/Spiro-TTB/$MAPb(I_{1-x}Br_x)_3$/C_{60}/BCP/Ag	1.64	0.16000	19.40	1.180	Gil-Escrig et al.[204]
		interface engineering	ITO/NiO_x/MeO-2PACz/$CsPbI_2Br$/PEACl/PCBM/BCP/Cu	1.91	0.09000	13.21	1.148	Ghavidel et al.[249]
		additive engineering	FTO/ITO/PTAA/Al_2O_3/$MAPbBrI_2$:CsCl/PCBM/BCP/Ag	1.77	–	13.80	1.140	Liu et al.[210]
	other evaporation	–	ITO/MoO_3/TaTm/$CsPbI_2Br$/C_{60}/BCP/Ag	1.90	0.02640	8.30	0.970	Igual-Muñoz et al.[132]
		interface engineering	FTO/SnO_2/$FA_{0.9}Cs_{0.1}Pb(I_{0.58}Cl_{0.15}Br_{0.27)2.1}$/Spiro-OMeTAD/Au	1.65	0.10000	21.92	1.200	Li et al.[205]
	solution-assisted evaporation	–	FTO/c-TiO_2/$CsPbIBr_2$/CuPc/C	2.05	0.07100	8.76	1.289	Liu et al.[141]

(*Continued on next page*)

Table 12. *Continued*

Material system	Preparation method	Further strategy	Configuration	Band gap (eV)	Active area (cm^2)	PCE (%)	V_{OC} (V)	Reference
			ITO/SnO_2/PCBM/$MAPb(Br_{0.18}I_{0.82})_3$/Spiro-OMeTAD or PTAA/Au	1.66	0.08600	14.50	1.120	Dewi et al.[147]
mixed A, single X	other evaporation	–	FTO/TiO_2/$MA_{1-x}Cs_xPbI_3$/Spiro-OMeTAD/Au	1.65	0.09000	17.13	1.080	Zhu et al.[250]
	co-evaporation	additive engineering	ITO/PTAA/$DMA_{1-x}Cs_xPbI_3$/LiF/C_{60}/Ag	1.73	0.09000	16.10	1.003	Dong et al.[208]
mixed A, mixed X	co-evaporation	–	ITO/C_{60}:PhIm/C_{60}/$Cs_{0.5}FA_{0.4}MA_{0.1}Pb(I_{0.83}Br_{0.17})_3$/TaTm/TaTm:F6-TCNNQ/Au	1.70	–	16.00	1.140	Gil-Escrig et al.[135]
			ITO/NiO_x/Me-2PACz/$Cs_{0.45}FA_{0.55}Pb(I_{0.85}Br_{0.15})_3$/$C_{60}$/$SnO_2$/Ag	1.69	0.05500	21.37	1.195	Dong et al.[134]
			ITO/MoO_3/TaTm/$(FA_{1-n}Cs_n)Pb(I_{1-x}Br_x)_3$/$C_{60}$/BCP/Ag	1.70–1.76	0.08250	~15	1.200	Susic et al.[182]
			ITO/MoO_3/TaTm/$FA_{0.65}Cs_{0.35}Pb(I_{0.73}Br_{0.27})_3$/$C_{60}$/BCP/Ag	1.75	–	16.80	1.183	Gil-Escrig et al.[78]
		additive engineering	ITO/NiO_x/Spiro-TTB/(Cs, FA)Pb(I, $Br)_3$/LiF/C_{60}/BCP/Ag	1.67	0.14750	17.80	1.160	Xu et al.[207]
			ITO/PTAA/$Cs_{0.5}FA_{0.4}MA_{0.1}Pb(I_{0.83}Br_{0.17})_3$/$C_{60}$/BCP/Ag	1.73	–	16.40	1.148	Susic et al.[213]
			ITO/Me-4PACz/$Cs_{0.66}FA_{0.34}Pb(Cl_{0.01}Br_{0.22}I_{0.77})_3$/$C_{60}$/$SnO_x$/Ag	1.75	0.05	18.17	1.270	Guo et al.[251]
		interface engineering	ITO/MeO-2PACz/$FA_{0.7}Cs_{0.3}Pb(I_{0.64}Br_{0.36})_3$/$C_{60}$/BCP/Cu	1.77	0.13800	17.80	1.260	Chiang et al.[215]
			ITO/MeO-2PACz/$(FA_xCs_{1-x})Pb(I_xBr_{1-x})_3$/$C_{60}$/BCP/Ag	1.69	0.16000	19.60	1.200	Škorjanc et al.[112]
			ITO/MeO-2PACz/$FA_{0.8}Cs_{0.2}PbI_{2.7}Br_{0.3}$/$C_{60}$/BCP/Ag	1.65	0.16000	18.00	1.140	Leyden et al.[252]
	other evaporation	annealing engineering	FTO/Me-4PACz/$Cs_{0.24}FA_{0.76}Pb(I_{0.8}Br_{0.2})_3$/$C_{60}$/BCP/Ag	1.66	0.14800	20.10	1.201	Dou et al.[237]
	solution-assisted evaporation	–	ITO/NiO_x/(Cs,FA)Pb(I,$Br)_3$/LiF/C_{60}/BCP/Cu	1.67	0.12500	20.34	1.140	Afshord et al.[146]
			ITO/Me-4PACZ/CsFAPb(I,$Br)_3$/LiF/C_{60}/BCP/Ag	1.68	–	22.21	1.247	Shi et al.[143]
			ITO/2PACz/$FA_{0.85}Cs_{0.15}Pb(I_{0.78}Br_{0.22})_3$/$C_{60}$/$SnO_x$/Au	1.66	0.25000	14.30	1.050	Er-raji et al.[148]
			ITO/MeO-2PACz/(FA,Cs)Pb(I,$Br)_3$/C_{60}/BCP/Ag	1.70	0.10000	15.10	1.170	Guesnay et al.[145]
		additive engineering	ITO/Me-4PACz/(FA,MA,Cs)Pb(I,$Br)_3$/C_{60}/SnO_x/Ag	1.84	0.05000	17.48	1.315	Wang et al.[209]

(*Continued on next page*)

Table 12. ***Continued***

Material system	Preparation method	Further strategy	Configuration	Band gap (eV)	Active area (cm^2)	PCE (%)	V_{OC} (V)	Reference
			ITO/Spiro-TTB/CsCl/$CsFAMAPb(I,Br)_3$/C_{60}/BCP/Ag	1.60	0.08875	22.74	1.150	Liu et al.[110]
			ITO/NiOx/2PACz:MeO-2PACz/$Cs_{0.2}FA_{0.8}Pb(I,Br,Cl)_3$/$C_{60}$/BCP/Cu	1.68	–	20.30	1.207	Luo et al.[151]
			FTO/SnO_2/$Cs_xFA_{1-x}Pb(I_xBr_{1-x})_3$/Spiro-OMeTAD/Au	1.68	0.15000	19.42	1.170	Chen et al.[155]
			FTO/SnO_2/$Cs_xFA_{1-x}Pb(I_xBr_{1-x})_3$/Spiro-OMeTAD/Au	1.66	0.14800	19.46	1.154	Liang et al.[253]
			FTO/SnO_2/$Cs_xFA_{1-x}Pb(I_xBr_{1-x})_3$/Spiro-OMeTAD/Au	1.68	0.14800	19.91	1.126	Zhang et al.[152]
			FTO/SnO_2/$MA_{0.30}FA_{0.70}Pb(I_{0.84}Br_{0.16})_3$/Spiro-OMeTAD/Au	1.64	0.09000	19.80	1.140	Nguyen et al.[153]
			ITO/NiO_x/$(FA,MA,Cs)Pb(I,Br,Cl)_3$/C_{60}/BCP/Ag	1.68	0.09000	20.00	1.180	Li et al.[156]
		interface engineering	ITO/Me-4PACz/$Cs_{0.15}FA_{0.85}PbI_{1.8}Br_{1.2}$/$EDAI_2$/PCBM/$C_{60}$/BCP/Ag	1.68	0.05000	22.62	1.217	Zhou et al.[142]
			ITO/Spiro-TTB/CsBr/$FA_{0.9}Cs_{0.1}PbI_{2.87}Br_{0.13}$/$C_{60}$/ZnO/Al	1.68	0.08900	17.04	1.100	Li et al.[149]
			ITO/Spiro-TTB/$Cs_xFA_yMA_{1-x-y}Pb(I,Br,Cl)_3$/TEABr/$C_{60}$/BCP/Ag	1.63	0.08875	20.74	1.188	Xu et al.[206]
			ITO/PTAA/$(Cs:FA:MA)Pb(I,Br,Cl)_3$/PCBM/BCP/Ag	1.68	–	19.24	1.100	Zhang et al.[144]
			ITO/4PADCB/$FA_{0.8}Cs_{0.2}Pb(I_{0.6}Br_{0.4})_3$/$PDAMA_{n-1}Pb_nI_{3n+1}$/$C_{60}$/BCP/Ag	1.78	0.08000	20.71	1.337	Liu et al.[218]
			ITO/NiO_x/Me-4PACz/$Cs_xFA_{1-x}Pb(I_xBr_{1-x})_3$/$CsPbCl_3$/$C_{60}$/BCP/Ag	1.68	0.08875	21.84	1.204	Wang et al.[216]
			ITO/2PACz/$Cs_{0.16}FA_{0.65}MA_{0.19}Pb(I_{0.77}Br_{0.17}Cl_{0.06})_3$/$PDAI_2$:BAI/$C_{60}$/BCP/Ag	1.66	0.10500	19.84	1.140	Pesch et al.[154]
			ITO/Me-4PACz/$FA_{0.78}Cs_{0.22}Pb(I_{0.77}Br_{0.23})_3$/PDAI/$C_{60}$/$SnO_x$/IZO/Ag/$MgF_x$	1.68	1.04000	17.00	1.230	Er-raji et al.[150]
			ITO/NiO_x/2PACz:MeO-2PACz/$FA_{0.8}Cs_{0.15}MA_{0.05}Pb(I_{0.82}Br_{0.18})_3$/$C_{60}$/$SnO_x$/Cu	1.68	0.04900	20.80	1.220	Zheng et al.[254]
			ITO/NiO_x/Me-4PACz/$FA_{0.8}Cs_{0.2}Pb(Br_{0.6}I_{2.4})$/4-PBA/$C_{60}$/BCP/Ag	1.68	0.08875	22.53	1.253	Gao et al.[255]

Physical mechanisms of stability enhancement via vapor-phase optimization strategies

Interfacial chemical anchoring and halide migration suppression

Substrate surface energy engineering is the first line of defense in establishing the initial stability of the film. In a vacuum environment, the film nucleation process is not disturbed by solvent coordination, making interfacial molecular design more efficient.[221,256] Vapor-deposited SAMs such as Me-4PACz form strong chemical coordination with lead ions on the perovskite surface through their phosphonic acid groups.[215] This chemical anchoring effect holds special significance in WBG systems. Since phase segregation in mixed-halide perovskites often originates at defect-dense interfaces, powerful chemical bonding can significantly increase the activation energy for ion migration.[99,215]

Experimental data demonstrate that vapor-deposited interfaces possess a higher ion-locking capability.[228] The work of Feeney et al. indicates that this anchoring effect can fix halide ions at the buried interface, preventing their diffusion under illumination.[138] Raising the barrier for halide demixing is the fundamental means to suppress the Hoke effect.[257,258] In contrast, interfaces fabricated by solution methods often become channels for ion leakage due to incomplete wetting and solvent residue.[259,260] The V_{OC} decay of vapor-deposited WBG films under continuous illumination is significantly lower than that of solution-processed films, directly validating the effectiveness of interfacial chemical locking.[161,261]

Compositional pre-alloying and construction of thermodynamic steady states

The pre-alloying strategy in bulk composition engineering is another core support for the stability of vapor-phase methods. A severe challenge faced by WBG perovskites is the microscopic non-uniformity arising from compositional randomness.[262] When mixing multiple precursor salts in solution methods, local bromine-rich or iodine-rich phases easily emerge within the film due to solubility differences and crystallization rate mismatches.[261] Such microscopic compositional deviations serve as seeds that trigger thermodynamic instability.

The vapor-phase method forcibly locks the stoichiometry through physical means, enabling pinhole-free films with complete surface coverage.[250] Utilizing chemically synthesized mixed-halide sources such as $Pb(I_{1-x}Br_x)_2$ or eutectic systems ensures the uniformity of anion ratios at the molecular scale.[221] Research by Shi et al. confirmed that eutectic systems force iodine and bromine to evaporate at a completely coupled rate, thereby eliminating compositional segregation in the vertical direction.[143]

Recent studies further reveal that by regulating the intermediate-phase evolution during evaporation, such as the CsI_2Br phase, crystal growth can be guided to construct textured films with enhanced thermodynamic resistance.[134] Additionally, introducing bulky molecules to create a 3D hollow structure can further erect barriers against ion migration.[257] This high degree of atomic-level mixing and oriented growth provides WBG films with a broader thermodynamic stability window.[215] WBG devices optimized through such pre-alloying and structural engineering show no diffraction peak splitting or shifting even after long-term storage at 85°C, proving that their lattice structures possess extreme resistance to thermal degradation.[73,261]

Chloride-mediated lattice strain-relaxation mechanism

The introduction of chloride ions acts as a lattice regulator during vapor-phase growth. Traditional WBG perovskites often exhibit severe lattice distortion due to high Cs content, leading to a low Goldschmidt tolerance factor. This geometric mismatch is the driving force for the spontaneous transformation of perovskite into the non-photoactive yellow phase.[263]

Co-evaporating lead chloride in the vapor phase not only regulates crystallization kinetics but also induces minor tilting of the perovskite octahedra.[264] SAED results show that chloride incorporation generates superlattice reflection spots, marking the release of internal lattice strain.[265] Experimental evidence from Xu et al. shows that chloride-mediated WBG films maintain phase purity even after being stored in ambient air at 50% relative humidity for over 240 h.[207] This strain-relaxation effect structurally stabilizes the black phase, addressing the long-standing environmental instability issues in WBG systems.[250]

Synergistic effects of in situ *passivation and vacuum environment*

In situ grain-boundary passivation (*in situ* grain-boundary passivation) represents another breakthrough for the vapor-phase method in terms of stability. During solution processing, the presence of solvents hinders the effective migration of bulky ligands to grain boundaries.[259] In a high-vacuum environment, long-chain molecules such as PEAI are expelled to grain boundaries due to steric hindrance.[264]

This self-assembly process is more orderly and compact in vapor deposition.[191] Vapor-phase passivating molecules can uniformly cover undercoordinated lead ions on grain-boundary surfaces, cutting off the infiltration paths for moisture and oxygen at the source.[266] Research data indicate that $CsPbI_3$ films with *in situ* PEAI vapor passivation maintain morphological continuity even under extreme geometries, significantly reducing the number of pinholes. Reducing pinholes means reducing the initiation sites for electrochemical corrosion, providing excellent long-term operational stability for WBG devices.[263,264,267]

APPLICATIONS OF VAPOR-PHASE-OPTIMIZED WBG PEROVSKITE FILMS IN SEMITRANSPARENT, LARGE-AREA, AND TANDEM SCs

Semitransparent solar cells

Integrating photovoltaics into building skins or building-integrated photovoltaics requires balancing photon harvesting and visual transparency. This compromise is quantified by light utilization efficiency (LUE), which is the product of PCE and AVT weighted by the photopic response of the human eye, as defined in Equation 4[268,269]:

$$AVT = \frac{\int T(\lambda)P(\lambda)S(\lambda)d\lambda}{\int P(\lambda)S(\lambda)d\lambda}. \qquad \text{(Equation 4)}$$

Here, $T(\lambda)$ represents spectral transmittance, $P(\lambda)$ denotes the photopic luminous efficiency function, and $S(\lambda)$ is the AM 1.5G solar spectrum. While solution-processed semitransparent PSCs frequently surpass the commercial LUE benchmark of

5%, vapor-deposited counterparts currently exhibit lower performance, with most single-junction devices remaining below 10% efficiency at comparable transparencies.[269]

Despite this efficiency deficit, vapor deposition offers independent regulation of film thickness and morphological continuity, which is difficult in liquid processing. In solution processing, thinning the absorber layer to below 50 nm typically induces dewetting driven by Rayleigh-Plateau instability, which results in island formation via Volmer-Weber growth and electrical shunting. In contrast, vapor deposition operates via adatom accumulation and enables the growth of continuous pinhole-free films at an ultra-thin limit below 20 nm.

Zhang et al. demonstrated this capability by co-evaporating $CsPbI_3$ with PEAI additives. PEAI modulated nucleation density and induced a columnar growth mode that preserved film continuity even at a thickness of 10 nm. Resulting ultra-thin films demonstrate exceptional clarity for background text without haze or scattering artifacts common in thicker porous films, as shown in Figure 16A. Crucially, the 10 nm thickness suppresses parasitic absorption in the blue region. CIE 1931 chromaticity coordinates remain clustered near the white point, effectively eliminating the reddish-brown tint inherent to thicker perovskite layers, as depicted in Figure 16B. Although the PCE was 3.6%, this work validates vapor deposition as a precise tool for engineering neutral-colored windows, which remains challenging for solution methods.[212]

Thermal and environmental stability is paramount for building-integrated applications, necessitating the use of all-inorganic WBG perovskites such as $CsPbBr_3$ with a band gap of approximately 2.3 eV. However, solution processing of $CsPbBr_3$ is hindered by low precursor solubility, especially for cesium bromide, and rapid crystallization, which leads to high trap densities. Vapor deposition avoids solubility limits and enables precise compositional doping. Jiang et al. employed a sequential alternating evaporation strategy to introduce potassium bromide dopants into $CsPbBr_3$. Unlike solution mixing, in which segregation often occurs, vapor-phase introduction of potassium ions facilitated uniform lattice integration and surface passivation. Improved energy-level alignment and reduced defect density resulted in a V_{OC} increase to 1.55 V and a PCE of 7.28%, as shown in Figure 16D. Notably, unencapsulated doped devices retained 87% of initial efficiency after 1,300 h at 60% relative humidity, as illustrated in Figure 16E. This indicates that vapor-phase passivation can impart necessary moisture resilience for building-integrated applications without complex encapsulation.[268]

Despite these advances, vapor-deposited single-junction building-integrated devices have not yet reached parity with solution-processed analogs. Most reported vapor-deposited semitransparent cells exhibit LUE values well below the 5% threshold, and lead-free alternatives such as $AgBiI_4$ yield low LUEs around 0.45 due to low photovoltages.[270]

This disparity stems from a passivation deficit. High-efficiency solution-processed cells rely on complex multi-component synergistic formulations that incorporate bulk heterojunctions and solvent-coordinated additives, such as ionic liquids and polymers, to suppress non-radiative recombination. Replicating this synergistic chemical environment in a high-vacuum chamber remains challenging. Vapor-deposited films often suffer from higher grain-boundary defect densities despite physical uniformity, which limits V_{OC} and FF.

The application of semitransparent solar cells is typically restricted to a band-gap range of 1.60–1.68 eV to ensure an optimal balance between PCE and AVT. Within this specific range, the primary technical challenge lies in the trade-off between absorber thickness and charge-collection efficiency. As the band gap shifts toward the higher end of this window, reliance on high bromine content heightens the risk of halogen migration, which compromises the color stability of the device under long-term operation. Consequently, achieving a high LUE necessitates the implementation of ultra-thin and pinhole-free films that can only be reliably processed via vapor-phase techniques to prevent the morphological instabilities common in solution-processed equivalents.

Currently, vapor deposition serves as a high-precision tool for optical geometry control regarding thickness and band gap rather than defect minimization in single-junction building-integrated photovoltaics. While offering the ability to fabricate continuous neutral-colored ultra-thin films, electronic quality lags behind solution processing due to the absence of mature *in situ* passivation strategies. Consequently, the primary application of these vapor-deposited WBG films is as top cells in tandem architectures, where conformal coverage on textured substrates provides a decisive advantage over solution methods.[27,146,204,246,271,272]

Large-area solar cells

Expanding the device area from square millimeters to square decimeters, exceeding 100 cm^2, shifts the primary challenge from defect passivation to spatial homogeneity. In contrast to solution processing, which is hindered by fluid dynamics issues such as coffee-ring effects and solvent-drying gradients on large substrates, vapor deposition operates via a flux-driven mechanism. This section examines the scalability of vapor-phase WBG perovskites through the distinct lenses of non-module scaling and module integration.

Maintaining compositional consistency across large substrates constitutes the primary obstacle for scaling WBG perovskites. In mixed-halide systems involving iodine and bromine mixtures, slight thermodynamic fluctuations can lead to localized phase segregation, creating low-voltage hotspots. Vapor deposition addresses this issue via precise mass flow control, ensuring that every point on the substrate receives an identical stoichiometric flux regardless of substrate size.

Soufiani et al. demonstrated this capability on semi-M6 wafers measuring 166 × 166 mm using a three-step sequential evaporation process. Optimizing crystallization kinetics through gradient thermal control achieved exceptional spatial uniformity across the entire wafer.[185] PL mapping, shown in Figure 16F, reveals that the annealed film exhibits uniform emission intensity over a large area, indicating a homogeneous distribution of trap states and suppression of non-radiative recombination centers at the edges. The implied V_{OC} (iV_{OC}) map in Figure 16G reveals a tight distribution around 1,230 mV across the sample holder. High voltage uniformity is critical, as it prevents current-matching loss in monolithic TSCs caused by weak local sub-cells. A statistical scatterplot of FF vs. V_{OC} for 108

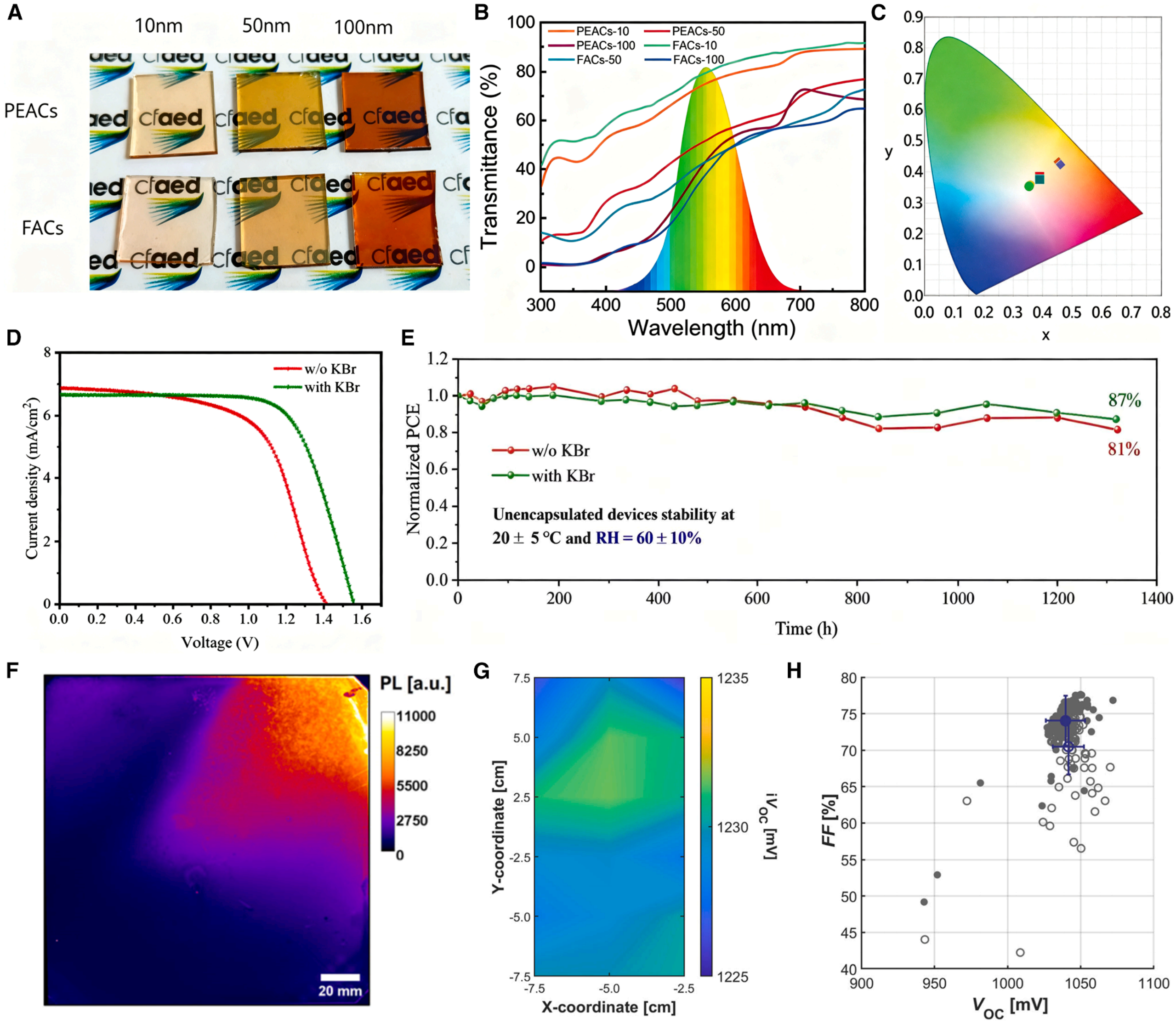

Figure 16. Semitransparent solar cells and large-area solar cells

(A) Corresponding photos of semitransparent PEACs and FACs perovskite films with different thicknesses.

(B) The human luminosity curve and transmittance spectra of PEAC and FAC perovskite films with different thicknesses.

(C) Color coordinates plotted on the CIE 1932 chromaticity diagram.

(A–C) Reproduced with permission.[212] Copyright 2023, Wiley-VCH.

(D) J-V curves of the 5 × 5 cm semitransparent module.

(E) Long-term stability of the control and KBr-doped PSCs under 60% RH. Both devices are unencapsulated.

(D and E) Reproduced with permission.[268] Copyright 2024, American Chemical Society.

(F) PL image of an evaporated (dynamic FAI and static inorganics) and subsequently annealed film acquired using BP740-10 filter at the detection side. Light-emitting diodes with a central wavelength of 525 nm were used as the illumination source.

(G) Implied V_{OC} map, measured under approximately 0.5-suns equiv photon flux from the glass side, plotted as a function of the location on the sample holder.

(H) Scatterplot of device FF vs. V_{OC} measured on 108 small-area cells. Filled (hollow) symbols represent the reverse (forward) scan measurement results.

(F–H) Reproduced with permission.[185] Copyright 2025, Wiley-VCH.

small-area cells, shown in Figure 16H, displays narrow clustering. This confirms that the vapor process eliminates the stochasticity inherent in spin coating and offers batch-to-batch reproducibility required for industrial yield.

Uniformity of passivation layers is equally critical beyond the absorber itself. Wang et al. demonstrated that evaporated cesium lead chloride creates a more continuous passivation layer on large-area 10 × 10 cm substrates compared to solution processing, boosting the efficiency of 1.68 eV cells to 21.84%. This finding supports the premise that an all-vapor or vapor-dominant workflow is essential to maintain homogeneity as dimensions scale.[216]

Transitioning from films to interconnected modules introduces constraints on geometric FF (GFF) and series resistance R_s. While vapor deposition excels at the former, it faces challenges with the latter. Vapor-deposited films possess superior mechanical integrity and surface smoothness compared to solution-processed ones, making them highly compatible with high-resolution laser scribing. Afshord et al. utilized a hybrid evaporation-solution method to fabricate WBG mini-modules. Co-evaporating a robust, porous lead iodide and cesium bromide framework forms a uniform, pinhole-free inorganic template across the entire substrate. This exceptional film quality enables precision laser scribing with extremely narrow line widths and minimal safety margins, achieving a remarkably high GFF of 96% on a 16 cm^2 aperture area module. This minimizes dead area in P1-P2-P3 scribing zones to only 4%, resulting in an exceptional <2% absolute PCE loss when upscaling from small-area cells, representing a critical advantage for commercial viability.[146]

However, the performance of all-vapor modules drops significantly compared to small-area cells. Vapor-deposited WBG films, particularly all-inorganic compositions such as cesium lead bromide, often exhibit smaller grain sizes and higher grain-boundary densities than solution-grown counterparts. In a module in which current travels laterally through the transparent conductive oxide and vertically through the perovskite, increased bulk resistivity leads to ohmic losses. Jiang et al. reported a potassium-bromide-doped cesium lead bromide module of 5 × 5 cm that yielded only 5.35% efficiency despite small cells achieving much higher performance. This disparity indicates that defect passivation alone cannot compensate for transport losses inherent to the polycrystalline nature of large-area vapor films.[268]

Hybrid approaches have emerged to mitigate transport limitations. Nguyen et al. introduced dimethyl sulfoxide vapor treatment to slot-die-coated modules, achieving 17.7% efficiency on 25 cm^2. Solvent vapor promotes grain enlargement to improve carrier mobility.[153] Alternatively, for applications where current density is naturally low, such as indoor photovoltaics, the resistance penalty is negligible. Liu et al. demonstrated a 10 × 10 cm vapor-deposited module with 13.25% efficiency under LED light. Here, the pinhole-free nature of the vapor method, leading to high shunt resistance (Rsh), becomes the dominant advantage over mobility.[210]

For large-area modules, a band-gap range of 1.65–1.75 eV is preferred to meet the performance requirements of building-integrated photovoltaics. The critical hurdle in this scenario is the spatial homogeneity of the chemical composition across decimeter-scale substrates. Vapor-phase deposition demonstrates a significant advantage over blade coating by mitigating the drying-induced stoichiometric gradients that typically occur during solvent evaporation. However, maintaining a consistent WBG phase over large areas requires precise control over the precursor flux to prevent localized phase impurities that act as recombination centers and limit the overall module efficiency.

Vapor deposition has evolved from a tool for material optimization to a viable manufacturing route for system-level integration. It definitively solves the spatial uniformity problem, enabling high GFF and consistent voltage potentials across large wafers. However, the conductivity-scalability trade-off remains the central bottleneck because maximizing module efficiency requires not just uniform films but also films with transport properties comparable to solution-grown crystals. Future advancements lie in cross-process integration to enhance interface quality.

Perovskite/silicon TSCs

While large-area modules represent a significant step toward commercialization, the thermodynamic objective of photovoltaics is to surpass the Shockley-Queisser limit of single-junction devices. In this context, perovskite/silicon TSCs have emerged as the primary vehicle for market entry. Here, vapor deposition ceases to be merely an option and becomes a geometric necessity. Unlike planar substrates used in lab-scale research, industrial silicon solar cells feature micrometer-sized pyramidal textures ranging from 2 to 5 μm to minimize reflection. Solution processing on such rough terrain inevitably leads to planarization effects, resulting in shunt paths at pyramid tips and thick resistive layers in valleys. Vapor-phase deposition with its line-of-sight propagation or mean-free-path dominance offers the only scalable pathway to achieve conformal coverage on fully textured wafers without polishing, thereby preserving the light-trapping advantage of the silicon bottom cell.

Design rules and process guidance for perovskite/silicon TSCs

Vapor-phase techniques offer inherent conformality advantages for industrially textured silicon. However, the primary challenge lies in the profound modulation of vapor flux distribution by the micron-sized pyramids. Designing high-performance perovskite/silicon TSCs must adhere to the following four refined criteria.

In industrial textures, the pyramid facet inclination, typically 54.7°, leads to severe line-of-sight shadowing. Design rules dictate that the source-to-substrate distance (d_{ss}) must be co-optimized with the mean free path (λ). In the molecular flow regime ($\lambda \gg d_{ss}$), planetary rotation is mandatory. Literature indicates that the ratio of rotation frequency to deposition rate determines atomic-layer stacking quality; to eliminate leeward thinning, process guidance suggests biasing the rotation axis to dynamically cycle the vapor incidence angle between 0° and 60°, ensuring that the time-averaged flux received by all four pyramid facets is strictly equivalent.[221,273]

For WBG perovskites, the stoichiometry of organic components is severely constrained by the re-evaporation effect in vacuum. Since the saturated vapor pressure of FAI is much higher than that of PbI_2, design rules require a linked control system based on QCM and vacuum feedback. Process-wise, the total working pressure must be stabilized around 10^{-4} mbar, adjusting shutter apertures and heating power to compensate for thermal desorption of organic salts. Evidence shows that excessive vacuum leads to organic cation loss, inducing PbI_2 residues in pyramid valleys, whereas precise pressure window regulation ensures vertical chemical homogeneity of the WBG layers.[78,274]

Recent research reveals a partitioning adsorption bottleneck: surface energy heterogeneity between pyramid ridges and valleys causes vapor molecules to nucleate preferentially in valleys, resulting in severe thickness non-uniformity.[104] The core design rule introduces surface chemical programming using fluorinated silanes. These electronegative molecules modulate the substrate surface potential, equalizing adsorption probabilities via enhanced molecular anchoring of organic cations. The process guidance goal is to achieve a ridge-to-valley thickness ratio approaching unity, avoiding optical losses from thick valleys and shunting from thin ridges.

The high Br content in WBG perovskites makes them prone to I/Br phase segregation under thermodynamic equilibrium. Design rules emphasize non-equilibrium growth, requiring the substrate temperature (T_{sub}) to be strictly locked between 40°C and 80°C. This range provides sufficient kinetic energy for precursor diffusion into dense films while freezing the composition in a uniformly distributed metastable phase via kinetic quenching. Furthermore, introducing CsCl or CsBr seed layers as nucleation sites effectively lowers the activation energy for homogeneous growth, ensuring band-gap stability of the WBG top cell under continuous illumination.[78]

Unlike vapor deposition, solution processing is governed by fluid dynamics and strict capillary constraints on textured silicon. On 2–5 μm pyramids, liquid inks are driven by Laplace pressure gradients, naturally flowing from high-curvature tips to low-curvature valleys, causing valley accumulation and tip exposure. Design rules require modulating ink rheology via solvent engineering. The literature suggests that high-viscosity solvents or non-polar additives increase fluid resistance to capillary flow, maintaining a dynamic conformal liquid film before drying. This is the core physical path to preventing severe shunting at pyramid tips.[275,276]

Slower solvent evaporation in valleys leads to compositional gradients. To address this challenge, latest process guidance suggests a hybrid vacuum deposition strategy: first depositing an ultra-thin CsCl or CsBr seed layer via single-source evaporation, then growing the wide-bandgap perovskite film via multi-source co-evaporation on top. This seed layer provides uniform surface energy, eliminates intrinsic nucleation heterogeneity, and acts as heterogeneous nucleation centers to induce synchronized crystallization across the entire substrate. This approach drastically reduces bandgap fluctuations and process variability, resolving the fundamental conflict between high crystallinity and reproducibility in large-area co-evaporated perovskite fabrication for tandem applications.[112]

In summary, the core processes of solution methods involve fluid control and gradient suppression, whereas the design rules for vapor deposition focus on flux equalization and surface dynamic equilibrium. As a topography-dominant process, vapor deposition offers the advantage of precisely preserving the silicon bottom cell's light-trapping structures without parasitic shunting.

All-vapor-phase deposition perovskite/silicon TSCs

The all-vapor approach, where all functional layers are deposited under vacuum, represents an ideal manufacturing protocol, as it is solvent-free, highly reproducible, and intrinsically compatible with rough textures. However, recent breakthroughs have revealed that conformality is not automatic and requires sophisticated kinetic management. Ideally, vapor deposition yields a uniform film thickness perpendicular to the substrate.

However, Li et al. challenged this assumption by revealing a critical bottleneck known as facet-dependent vapor partitioning. They found that on random pyramids, the adsorption probability of organic precursors differs significantly between ridges and valleys due to surface energy heterogeneity, leading to thickness variations and local stoichiometry mismatches.[104]

To counter this, 3,3,3-trifluoropropyl-trimethoxysilane was incorporated to chemically modify the textured substrate. This specific silane enhances the interaction between the substrate and organic vapor molecules. By homogenizing surface adsorption energy, it balances vapor flux partitioning across complex pyramid geometry, effectively eliminating the ridge-valley thickness gradient without altering the physical evaporation source. The resulting device achieved consistent J-V characteristics under forward and reverse scans, as shown in Figures 17A and 17B, and, remarkably, maintained a tight performance distribution across a large 18 × 18 cm^2 substrate holder, as depicted in Figure 17C. This proves that surface chemical programming, rather than just line-of-sight geometry, is a prerequisite for scaling all-vapor TSCs on industrial textures.

Even with conformal growth, the sharp tips of silicon pyramids remain stress concentration points prone to electrical shunting. Chozas-Barrientos et al. introduced a fully evaporated molecular recombination junction to replace the traditional sputtered indium tin oxide interlayer. Low lateral conductivity of the evaporated organic layer comprising C_{60} and doped HTLs effectively isolates localized shunts caused by surface roughness, boosting the V_{OC} to 1.84 V. This highlights a distinct advantage of vapor deposition: the ability to deposit delicate organic layers without sputtering damage associated with transparent conductive oxide deposition.[27]

To address the thermodynamic instability of WBG perovskites in vacuum, Xu et al. utilized lead chloride as a co-evaporated additive. Unlike solution methods in which chloride regulates crystallization in vacuum, chloride incorporation induces minor octahedral tilting, thereby relaxing lattice strain and stabilizing the photoactive black phase. This all-evaporated strategy achieved a certified efficiency of 27.43% with matched currents, confirming that microstructure regulation is possible even without solvents.[207]

Hybrid deposition perovskite/silicon TSCs

While all-vapor methods excel in geometry, they historically lag in defect passivation compared to solution processing. The hybrid deposition route, evaporating an inorganic framework followed by solution infiltration, has thus emerged as a pragmatic dominant path that combines the conformal template of evaporation with the chemical flexibility of solution chemistry.

The hybrid route allows for precise chemical modification of interfaces. Er-raji et al. demonstrated the efficacy of this approach by treating the hybrid-deposited WBG perovskite surface with 1,3-propanediammonium iodide (PDAI). PDAI treatment created a positive surface dipole that reduced the conduction band offset from 180 to 70 meV, as illustrated in Figure 17D. This favorable alignment induced electron accumulation at the ETL interface, significantly enhancing electron extraction and reducing surface recombination. The tandem device achieved a remarkable efficiency of 33.1% (Figure 17E) and demonstrated superior outdoor stability in a harsh Red Sea environment, maintaining performance over 1,500 h (Figure 17F). This work definitively proves that hybrid routes can achieve world-record efficiencies by leveraging solution-based surface chemistry on vapor-framed worked films.[29]

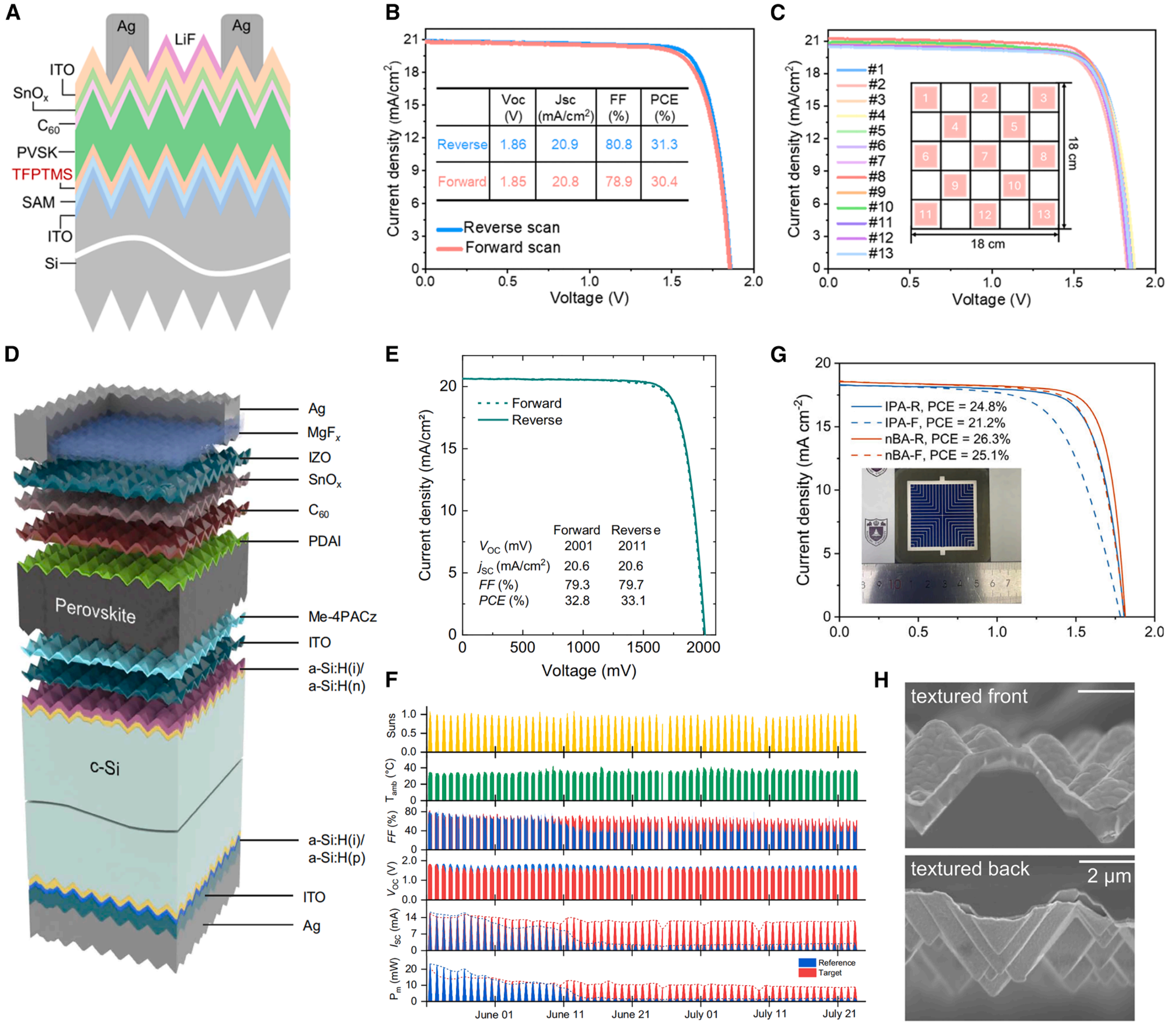

	Voc (V)	Jsc (mA/cm^2)	FF (%)	PCE (%)
Reverse	1.86	20.9	80.8	31.3
Forward	1.85	20.8	78.9	30.4

	Forward	Reverse
V_{OC} (mV)	2001	2011
j_{SC} (mA/cm^2)	20.6	20.6
FF (%)	79.3	79.7
PCE (%)	32.8	33.1

Figure 17. Perovskite/silicon tandem solar cells

(A) Schematic architecture of the perovskite/silicon tandem solar cells.

(B) J-V curves under reverse (2.2 to −0.2 V) and forward (−0.2 to 2.2 V) scans of target perovskite/silicon tandem solar cells (aperture area of 1 cm^2).

(C) J-V curves of one batch of perovskite/silicon tandem solar cells with different locations on the 18 × 18 cm holder during perovskite thermal evaporation (aperture area of 1 cm^2).

(A–C) Reproduced with permission.[104] Copyright 2025, The American Association for the Advancement of Science.

(D) Sketch of the tandem solar cell structure.

(E) J-V curves of the champion tandem solar cell with an adapted band gap.

(F) Maximum power point (MPP) stability tracking of encapsulated devices outdoors (in the Red Sea region) with evolution of PV parameters, illumination intensity, and ambient temperature over the testing period (1,500 h).

(D–F) Reproduced with permission.[29] Copyright 2025, The American Association for the Advancement of Science.

(G) J-V curves of the tandem device (16 cm^2 aperture area); a digital photo of the device is shown in the inset.

(H) Cross-sectional SEM images of perovskite/silicon heterojunction (SHJ) (average pyramid size is 2–3 μm) tandem for nBA devices.

(G and H) Reproduced with permission.[254] Copyright 2024, Springer Nature.

For hybrid methods to be industrially relevant, the solution step must transition from spin coating to scalable techniques such as blade or slot-die coating. Zheng et al. addressed the kinetic mismatch between evaporation and blade coating using n-butanol as the organic salt solvent. Unlike traditional alcohols, the moderate volatility and viscosity of n-butanol enabled uniform infiltration into the evaporated lead iodide framework on textured silicon, preventing rapid drying that leads to non-uniformities. The resulting 16 cm^2 blade-coated tandem module achieved 29.4% efficiency, as shown in Figures 17G and 17H, bridging the gap between lab cells and modules.[254] Similarly, Li et al. utilized slot-die coating with a 2,5-NaDPA additive. The additive modulated the nucleation energy barrier on convex pyramids, delaying crystallization to ensure large grain growth during the slot-die process, yielding 28.28% efficiency in large-area devices.[156]

The hybrid interface is also a locus for stress management. Liu et al. constructed a 3D/3D bilayer heterojunction at the buried interface. By evaporating a specific precursor ratio followed by solution conversion, they created a graded lattice that effectively released the tensile strain inherent in coating silicon pyramids, boosting certified efficiency to 31.5%.[28] Furthermore, Shi et al. addressed the halogen heterogeneity problem by co-evaporating a pre-synthesized lead iodine bromide eutectic with cesium chloride. This pre-homogenization strategy ensured that iodine and bromine were uniformly distributed throughout the film, eliminating vertical segregation often observed in sequential deposition.[150]

Comparison between all-evaporation and hybrid deposition

The geometric incompatibility between industrial random pyramids (2–5 μm) and thin-film perovskites (~500 nm) necessitates a rigorous evaluation of thickness uniformity, as local deviations directly dictate the optoelectronic parity of WBG top cells.[277] While vapor-phase techniques are inherently superior to pure solution processing, a critical distinction exists between all-evaporated and hybrid routes regarding their conformality index.

The all-vapor approach represents an ideal manufacturing protocol for tandem architectures, as it facilitates the deposition of all functional layers within a solvent-free vacuum environment, ensuring high reproducibility and intrinsic compatibility with rough textures. Ideally, vapor deposition should yield a conformal film with uniform thickness perpendicular to the substrate facets. However, recent breakthroughs by Li et al. have revealed that such conformality is not automatically achieved due to a critical bottleneck known as facet-dependent vapor partitioning.[104] In this process, film growth is governed by the surface residence time and adsorption probability of precursors rather than mere line-of-sight geometry.

Quantitatively, unmodified thermal evaporation on micrometer-scale pyramids often exhibits a ridge-to-valley thickness ratio ranging from 1.2:1 to 1.3:1. This non-uniformity arises from shadowing effects and surface energy heterogeneity across silicon facets, which causes organic salts to preferentially accumulate in the valleys. This phenomenon leads to a localized stoichiometric gradient and thickness variation, which significantly destabilizes the photoactive α-phase of WBG perovskites, particularly at the pyramid tips, where the film is thinnest.

To counter this, researchers incorporated 3,3,3-trifluoropropyl-trimethoxysilane to chemically modify the textured substrate.[104] By homogenizing the surface adsorption energy, this specific silane strengthens the interaction between the substrate and organic vapor molecules, effectively balancing the vapor flux partitioning across complex geometries. Consequently, the ridge-to-valley ratio can be narrowed to near unity (<1.05:1), eliminating the structural gradient. Nanobeam diffraction has confirmed that the perovskite cubic phase formed via this surface chemical programming possesses extremely high structural consistency across different pyramid regions. This kinetic precision is pivotal for WBG perovskites; it ensures that the halide ratio (Br/I) remains spatially uniform, preventing the formation of localized low-band-gap wells that typically trigger halide segregation and V_{OC} loss in tandem devices. Such modified all-evaporation strategies not only achieve vertically uniform films but also ensure performance consistency across large-area (18 × 18 cm^2) industrial substrates.

The hybrid deposition route comprising the evaporation of an inorganic framework followed by solution infiltration of organic salts is recognized for combining the conformal structural template of vapor deposition with the superior chemical passivation flexibility of solution processing.[29] However, this pragmatic path introduces significant fluid dynamic complexities that compromise film thickness uniformity on micrometer-scale textures. Unlike the curtain-like coverage of all evaporation, the hybrid approach inherently suffers from a planarization effect in which the solution step tends to smooth the underlying pyramidal topography.[162]

Quantitative cross-sectional SEM analysis of 3–5 μm random pyramids reveals that hybrid-deposited perovskite films often exhibit a pronounced rounding effect in the valleys. In these regions, the local thickness can exceed 800 nm, whereas the pyramid tips remain covered by a mere 300–400 nm of perovskite.[162,277] This 2:1 thickness variation represents a critical optoelectronic bottleneck where the excessive material in the valleys increases resistive losses and carrier recombination, while the insufficient coverage at the tips creates shunting paths that severely limit the V_{OC} of the tandem device. Farag et al. demonstrated that even with optimized Lewis base additives, the capillary forces generated during solution drying inherently drive mass transport toward the valleys, reinforcing this nonconformal distribution.[277]

Furthermore, this thickness heterogeneity manifests as localized energetic disorder. Quantitative PL studies and simulations indicate that material accumulation in valleys leads to a spectral redshift of approximately 6 meV due to increased reabsorption and local stoichiometry shifts, while thinning at the tips causes a 2–3 meV blueshift.[162] To mitigate these risks, solvent engineering has emerged as a primary strategy. Zheng et al. utilized n-butanol as a low-polarity organic salt solvent, whose moderate volatilization rate and viscosity enable uniform infiltration into the evaporated lead iodide framework, preventing the rapid uncontrolled drying that typically triggers planarization.[254] This approach enabled a 16 cm^2 blade-coated tandem module to achieve a 29.4% efficiency, bridging the gap between lab-scale cells and industrial modules. Improving performance via molecular doping and interfacial energy alignment further bridges the gap for such blade-coated devices.[278]

The 1.65–1.72 eV band-gap regime represents the thermodynamic sweet spot for monolithic perovskite/silicon TSCs to achieve ideal current matching with crystalline silicon bottom cells. In this configuration, the technical focus is on suppressing photoinduced phase segregation at the perovskite/silicon interface. The use of vapor-phase techniques allows for the formation of highly conformal films on industrially textured silicon, yet the mismatch in thermal expansion coefficients remains a potential source of lattice strain. Stabilizing the WBG phase requires interfacial engineering to minimize non-radiative recombination and ensure that the top cell can sustain the high voltages required to surpass the Shockley-Queisser limit of single-junction silicon.

The current landscape of perovskite/silicon TSCs presents a dichotomy. All-vapor deposition is the choice for future industrialization, offering superior conformality and process simplicity via a single vacuum line. However, it currently faces challenges regarding facet-dependent kinetics and lacks the chemical diversity for deep passivation that solution methods possess. Conversely, hybrid deposition dominates efficiency charts by combining the conformal vapor framework with solution-based passivation. Yet reliance on a solution step introduces solvent handling and drying complexities at the gigawatt scale. Ultimately, the future likely belongs to vapor-based passivation strategies such as vapor transport of bulky ligands that can replicate the success of hybrid routes within an all-vacuum environment, thereby eliminating the solution step while retaining high efficiency.

Other perovskite TSCs

While perovskite/silicon TSCs lead in efficiency, the versatility of vapor deposition extends to other multi-junction architectures that offer unique functionalities, including flexibility, lightweight properties, and semitransparency. This section evaluates three emerging tandem classes comprising all-perovskite, perovskite-organic, and perovskite-copper indium gallium selenide (CIGS) architectures, in which vapor-phase techniques solve specific integration bottlenecks that solution processing cannot address.

All-perovskite TSCs

Monolithic all-perovskite TSCs comprising a WBG top cell and an NBG bottom cell offer a pathway to flexible high-specific-power photovoltaics. However, depositing the top cell without dissolving the underlying bottom cell represents a major bottleneck. Vapor deposition inherently bypasses this issue. Chiang et al. demonstrated a robust four-source co-evaporation strategy for depositing formamidinium-cesium lead iodine bromide top cells. $EDAI_2$ was introduced via vapor-phase surface treatment. This dry passivation reduced non-radiative recombination at the perovskite-fullerene interface without exposing underlying layers to hazardous solvents, yielding a tandem efficiency of 24.1% with a high V_{OC} of 2.06 V. This validates vacuum deposition as an effective approach for constructing multi-junction stacks.[215]

Hybrid routes are also evolving to optimize band alignment. Liu et al. utilized a hybrid evaporation-solution method to construct a DJ phase quasi-2D/3D heterojunction. Converting an evaporated framework into a uniform $n = 3$ quasi-2D layer atop the WBG perovskite optimized carrier extraction, as shown in Figure 18A. The resulting all-perovskite tandem achieved 28.99% efficiency, with excellent current matching verified by external quantum efficiency (EQE), as depicted in Figure 18B. This proves that hybrid methods can precisely engineer the buried interface of the top cell, which is a region typically inaccessible to solution post-treatments in monolithic stacks.[218]

All perovskite tandem devices require a significantly wider band gap, ranging from 1.75 to 1.85 eV, for the top cell to effectively complement low-band-gap tin-lead perovskite bottom cells. This regime faces the most severe voltage deficit due to the high bromine concentration, which leads to a massive energetic mismatch at the charge transport interfaces. The primary challenge is managing the excessive lattice strain and defect density inherent in such WBG compositions. Sequential vapor deposition strategies have emerged as a pivotal tool to create functional gradients that facilitate charge extraction while maintaining structural integrity under environmental stresses that typically trigger the formation of the non-perovskite yellow phase.

Perovskite/organic TSCs

Perovskite-organic TSCs combine the tunable near-infrared absorption of organics with the high voltage of perovskites. Here, the WBG perovskite top cell serves a dual function of power generation and ultraviolet filtration to protect the ultraviolet-sensitive organic bottom cell.

Chen et al. utilized dual-source co-evaporation to fabricate all-inorganic $CsPbBr_3$ top cells. The vapor process yielded pinhole-free films with high transmittance exceeding 90% in the 530–800 nm range. When integrated with an organic bottom cell, the inorganic perovskite effectively filtered ultraviolet light, significantly enhancing the photostability of the organic sub-cell while contributing to a 14.03% tandem efficiency.[271]

To further boost efficiency, Wang et al. introduced PACl into the hybrid deposition process. The PACl additive promoted face-on stacking of the (100) perovskite planes, reducing roughness and defect density, as shown in Figure 18D. This crystallographic tuning enabled a perovskite-organic tandem with 26.46% efficiency, as illustrated in Figure 18E, retaining over 90% performance after 500 h. This highlights that vapor-based hybrid routes can achieve the high crystallinity required to match the current of NBG organic absorbers.[209]

In perovskite-organic tandem architectures, the top cell band gap is typically tuned within 1.70–1.80 eV to maximize the utilization of the solar spectrum in conjunction with organic acceptors. The fundamental challenge involves aligning the perovskite conduction band with the lowest unoccupied molecular orbital of the organic sub-cell. As the band gap widens, the upward shift of the conduction band minimum often necessitates the inclusion of specialized interlayer materials to prevent interfacial charge accumulation. Vapor-deposited WBG films provide the necessary morphological control to integrate with delicate organic layers without risking solvent damage, which is a prerequisite for achieving stable and efficient hybrid TSCs.

Perovskite/CIGS TSCs

CIGS solar cells possess rough surfaces similar to silicon, which challenge solution processing. CIGS is also temperature sensitive, making low-temperature vapor deposition ideal. Fu et al. demonstrated the feasibility of this approach using a hybrid evaporation-spin coating method for low-temperature processing and achieved 20.5% efficiency in a mechanically stacked configuration.[279]

Scalable integration represents a significant advancement. Alvianto et al. developed a co-evaporation strategy depositing a bilayer $MAPbI_3$ structure. Accelerating the lead iodide rate for the top layer smoothed the perovskite surface and reduced the contact potential difference. Using this optimized film in a

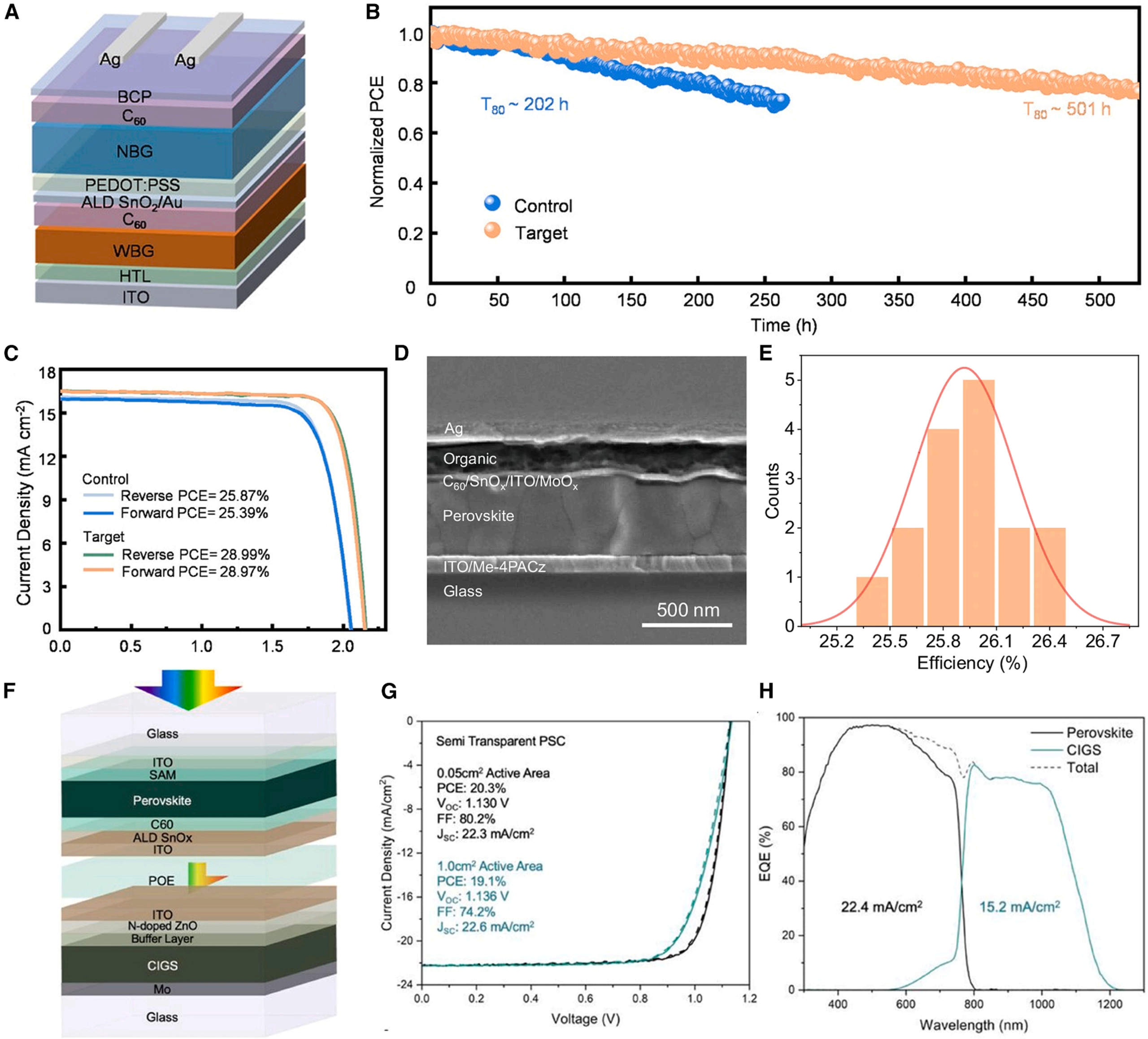

Figure 18. Other tandem solar cells

(A) The structural diagram of an all-perovskite tandem device.

(B) The MPP test of encapsulated tandem devices under continuous simulated AM 1.5 G illumination.

(C) J-V curves of all-perovskite tandem devices; the aperture area is 0.11 cm^2.

(A–C) Reproduced with permission.[218] Copyright 2025, Wiley-VCH.

(D) Cross-sectional SEM image of perovskite/organic tandem solar cells.

(E) statistical distributions of efficiency of perovskite/organic tandem solar cells with 16 devices. (D and E) Reproduced with permission.[209] Copyright 2025, Springer Nature.

(F) Schematic structure of perovskite-CIGS 4T tandem solar cells integrated using POE.

(G) J-V scan of semitransparent PSCs using bilayer $MAPbI_3$ with active area of 0.05 and 1.0 cm^2.

(H) EQE spectra of the perovskite and CIGS sub-cells from the laminated tandem solar cells (1.0 cm^2). (F–H) Reproduced with permission.[246] Copyright 2025, Wiley-VCH.

4-terminal mechanically stacked configuration, as shown in Figure 18F, a tandem efficiency of 26.1% was achieved by laminating with a CIGS bottom cell using polyolefin elastomer (POE). EQE spectra in Figure 18G confirm efficient photon harvesting across the spectrum. This demonstrates that vapor deposition is key to integrating perovskites with rough thin-film bottom cells such as CIGS or cadmium telluride, where polishing is not an option.[246]

Perovskite-CIGS TSCs utilize a band-gap range of 1.68–1.75 eV to accommodate the variable band gap of the CIGS bottom cell, which typically ranges from 1.0 to 1.2 eV. The integration of perovskites with the inherently rough and chemically complex CIGS surface demands superior conformality and chemical robustness. The primary technical hurdle is controlling interfacial recombination at the heterojunction where the WBG perovskite meets the CIGS layer. Achieving high efficiency in this 4-terminal or 2-terminal configuration depends on the ability of the vapor-phase process to deposit a uniform buffer layer that minimizes shunting paths while facilitating efficient hole extraction from the WBG absorber.

Vapor deposition technology, leveraging excellent compositional controllability, interface modification capability, and crystallization kinetics regulation, has achieved significant progress in various types of TSCs. Champion efficiencies have exceeded 33%, and V_{OC}s have surpassed 2.1 V, demonstrating core advantages in band-gap engineering, spectral management, and stability optimization.

Stability advantages in tandem and large-area applications

Moisture resistance and long lifetime of all-inorganic WBG films

The application of all-inorganic perovskites demonstrates the survival capability of the vapor-phase method in harsh environments. For all-inorganic WBG materials such as $CsPbBr_3$, solution processing is often limited by the low solubility of precursors in organic solvents, leading to numerous unreacted voids in the film.

Vapor deposition completely solves the solubility issue, making dense, pinhole-free crystalline structures possible.[250] Research by Jiang et al. provides powerful evidence that unencapsulated devices with KBr vapor doping retained 87% of their efficiency after 1,300 h in air at 60% relative humidity. These data far exceed the performance of similar solution-processed devices, fully demonstrating the advantage of vapor deposition in enhancing the density of inorganic lattice structures.[268] High-density films effectively resist moisture infiltration, which is key to achieving long-term durability for WBG devices.[256,267]

Spatial uniformity and statistical stability of large-area modules

Solution methods lead to severe compositional segregation and morphological defects on large substrates due to non-uniform fluid dynamics.[161] Local small-area defects can trigger cascade current-matching failures in large modules.

Vapor deposition possesses extreme spatial uniformity because its flux distribution follows strict physical laws. The highly uniform PL emission map achieved by Soufiani et al. on 166-mm silicon wafers demonstrates the capability of the vapor-phase method to eliminate local degradation kernels.[185] The statistically tight V_{OC} distribution means every sub-cell within the module is under identical electrical stress.[191] This global consistency reduces early degradation caused by localized overheating, significantly enhancing the statistical lifetime of the entire system.[275,280]

Superior performance of TSCs under real-world conditions

The stability advantages of vapor deposition in TSCs are supported by the latest 2025 research. The study by Er-raji et al., published in *Science*, demonstrated the stability of fully textured perovskite/silicon TSCs under extreme environments along the Red Sea coast.[29]

The vapor-phase framework, via solution-based surface treatments such as PDAI, successfully achieved 1,500 h of continuous outdoor testing. This achievement is a milestone, as it proves that WBG devices can withstand severe diurnal temperature fluctuations and intense light impact.[263] Li et al. utilized silane modification to balance vapor-partitioning kinetics, achieving conformal growth on industrial-grade pyramid textures, with devices retaining over 90% efficiency after 1,400 h of continuous operation at 85°C.[104] This evidence firmly establishes that vapor deposition is a reliable path to resolve the stability issues of WBG top cells in tandem devices.[134,215]

Scientific attribution of superior stability in vapor methods

A fundamental challenge faced by solution methods is the residue left by high-boiling-point solvents such as DMF and DMSO.[259] Due to the strong coordination between these solvent molecules and lead ions, they remain trapped in grain gaps even after high-temperature annealing.[260] Residual solvents act as low-energy channels for phase segregation in WBG perovskites.[259] They absorb moisture to form unstable intermediate complexes and lower the diffusion barrier for halide ions.[262] Since vapor deposition is performed under ultra-high vacuum, the film formation process involves no liquid media at all.[73] This process ensures the chemical purity within the layers, fundamentally removing the catalytic media that induce chemical degradation.[228] This is the primary reason vapor-deposited devices perform far better than solution-processed ones in long-term thermal stress tests at 85°C.

Ion migration is the main kinetic process for performance decay in PSCs.[281] Photoinduced phase segregation in WBG perovskites is essentially the rearrangement of halide ions under chemical potential gradients.[258] Films prepared by vapor-phase methods possess smaller average lattice constants and higher lattice density. As vapor deposition involves the atom-by-atom accumulation of molecules, it can form a more compact 3D framework than solution methods.[264] This compactness significantly increases the spatial and energy overhead required for ions to undergo hopping migration.[267] Research shows that the ion migration activation energy E_a for vapor-deposited WBG perovskites can reach 0.94 eV, far higher than the 0.58 eV typical of solution methods.[99] This nearly double increase in E_a ensures halide ions are firmly fixed at lattice sites under operating voltages, thereby completely suppressing the voltage loss caused by the Hoke effect.[257]

During solution processing, solvent evaporation is accompanied by drastic volume contraction, which generates non-uniform residual tensile strain between grains. These local high-strain regions are zones where chemical bonds are stretched and weakened, making them highly susceptible to photochemical degradation.[265] The vapor deposition process utilizes its quasi-static equilibrium growth characteristics to more uniformly distribute thermal expansion stress.[256] Through precise modulation of the deposition rate, strain accumulation at interfaces can be eliminated *in situ* during crystal growth.[134] Latest research confirms that vapor-deposited WBG films exhibit narrower

Table 13. Summary comparison of stability advantages in vapor methods

Key parameters	Vapor phase	Solution processed	Physical mechanism
Volatile impurity	zero residue	significant solvent retention	vacuum excludes volatiles
E_a	high	low	lattice density and locking
Phase segregation	low	severe and prone	coupled evaporation locks ratio
Residual strain	uniform and small	large local tensile stress	atom-by-atom relaxation
T_{90}/T_{80}	3,000–70,000 h[134]	<1,000 h	structural and purity gains

XRD peak widths, physically corresponding to a lower microscopic strain distribution. This structural robustness provides mechanical assurance for devices during thousands of hours of continuous operation.

Table 13 systematically summarizes the key differences in WBG perovskite stability between vapor and solution methods.

Table 14 systematically summarizes key PCE and V_{OC} parameters of multi-junction PSCs achieved based on vapor-phase techniques and provides a comprehensive assessment of their technological development level and application potential.

CONCLUSIONS AND PERSPECTIVES

The intrinsic limitations of WBG perovskites, as dissected in the intrinsic challenges of vapor-deposited WBG perovskites, represent a delicate balance between entropy-driven mixing and enthalpy-driven segregation. While halide segregation and phase instability are well known, vapor-phase deposition itself faces unique intrinsic challenges in a vacuum, such as volatility mismatches of organic precursors and the constraints of solid-state growth in the absence of solvent-mediated relaxation. However, the core advantage of vapor deposition lies in its ability to decouple film formation from the solubility limits that plague wet chemistry. By moving beyond the solvent-mediated intermediate complexes, vapor-phase strategies suppress the initial formation of non-perovskite yellow phases, offering a cleaner crystallization energy landscape.

The transition from empirical trial and error to rigorous kinetic control is facilitated by the diverse methodologies reviewed in vapor-phase methodologies for WBG perovskite thin films and applicability assessment. Beyond standard co-evaporation, techniques such as sequential evaporation, solution-assisted vapor deposition, and flash evaporation provide unique pathways to manage the ballistic transport of adatoms. The introduction of innovative monitoring technologies, such as *in situ* QCM and optical spectroscopy, allows for real-time compensation of precursor flux fluctuations. This level of precision ensures that even for complex multi-cation systems, the stoichiometry remains locked at the optimal point, preventing the thermodynamic relaxation into segregated phases that typically occurs during the slow drying stages of solution processing.

Vapor-phase optimization strategies for WBG perovskite thin films details a comprehensive suite of optimization strategies that collectively fortify the WBG lattice. Substrate surface energy engineering and buried interface optimization address the initial nucleation barrier, while pre-alloying and multi-cation alloying minimize local lattice strain. Chlorine-mediated growth and annealing engineering further promote grain coarsening and crystallinity. Crucially, *in situ* grain-boundary passivation and surface functionalization eliminate the vacancy defects that serve as shunts for ion migration. These strategies work in concert to achieve strain-relaxed and defect-minimized films, effectively raising the activation energy for halide segregation and ensuring the long-term stability of the photoactive phase.

As explored in applications of vapor-phase-optimized WBG perovskite films in semitransparent, large-area, and tandem SCs, the true value of vapor-deposited WBG films is realized in semitransparent, large-area, and tandem SCs. The geometric fidelity of vacuum transport enables conformal coverage on the micron-scale pyramids of silicon bottom cells, a feat nearly impossible for liquid-phase methods, which suffer from shunting and planarization issues. This capability, combined with the independent regulation of thickness and morphological continuity, makes vapor deposition the only viable pathway for high-throughput, industry-standard tandem manufacturing. By resolving the fundamental physicochemical contradictions of WBG materials, vapor technology bridges the gap between lab-scale research and commercial-scale photovoltaic modules.

Based on current research progress, vapor deposition technology has been proven to effectively inhibit segregation and phase transformation of WBG perovskites throughout the entire process, from nucleation and growth to final film formation. It stands as the definitive methodological foundation for the next generation of high-efficiency, stable multi-junction photovoltaics.

However, a technical contradiction persists: current methodologies often attempt to directly transplant solution-based chemistries into vacuum environments despite the intrinsic solvent-free scalability of the technology. This mismatch engenders four fundamental physicochemical challenges, which are detailed below. Resolving these issues requires a transition from empirical parameter tuning to rational and vacuum-specialized process engineering.

Remaining challenges

The chemical space limitation regarding passivation-agent incompatibility

The fundamental divergence in film-forming environments between solution processing and vacuum deposition necessitates a radical paradigm shift in passivation chemistry. A critical challenge lies in the thermal instability and fragmented sublimation of traditional passivators.

Unlike solution methods where molecular integrity is preserved by solvation at ambient temperatures, traditional bulky organic ammonium salts, such as PEAI or BAI, frequently undergo thermal pyrolysis via C–N bond scission before reaching their sublimation points. This non-congruent evaporation results

Table 14. Summary of PCE and V_{OC} for multi-junction PSCs fabricated by vapor-phase deposition

Types	Preparation methods of perovskite layers	Bandgap (eV)	active area (cm^2)	V_{OC} (V)	PCE (%)	Reference
Perovskite-organic	co-evaporation	2.36	0.1	–	14.03	Chen et al.[271]
		1.75	0.05	1.813	24.86	Guo et al.[251]
	solution-assisted evaporation	1.84	0.05	2.125	26.46	Wang et al.[209]
Perovskite-CIGS	co-evaporation	~1.63	1	–	26.1	Alvianto et al.[246]
		1.65	1	1.784	25.72	Li et al.[282]
	solution-assisted evaporation	1.55	0.213	–	20.50	Fu et al.[279]
All-perovskite	co-evaporation	1.77	0.138	2.06	24.1	Chiang et al.[215]
	solution-assisted evaporation	1.78	0.11	2.16	28.99	Liu et al.[218]
		1.63	0.049	2.112	28.50	Lin et al.[219]
Perovskite-silicon	co-evaporation	1.66	–	1.84	>22	Chozas-Barrientos et al.[27]
		1.67	0.25	1.817	27.43	Xu et al.[207]
		1.69	1	–	29.43	Dong et al.[134]
		1.65	1	1.860	31.40	Li et al.[104]
	other evaporation	~1.6	1	1.71	26.9	Zhang et al.[272]
		1.70	1	1.62	24.00	Mahboubi et al.[185]
	solution-assisted evaporation	1.68	0.5091	1.808	27.48	Er-raji et al.[148]
		1.67	3.84	–	30.61	Afshord et al.[146]
		1.63	0.5003	1.871	29.61	Xu et al.[206]
		1.68	1.05	1.849	30.83	Shi et al.[143]
		1.60	0.5003	1.81	30.05	Liu et al.[110]
		1.65	1.015	1.87	32.13	Liu et al.[28]
		1.73	–	1.918	31.58	Wu et al.[238]
		1.68	1.05	1.85	28.80	Luo et al.[151]
		1.69	1.04	1.85	27.43	Pesch et al.[154]
		1.66	1	1.775	26.50	Er-raji et al.[148]
		1.68	1.04	1.903	27.80	Er-raji et al.[150]
		1.68	1.044	1.83	29.40	Zheng et al.[254]
		1.68	16	1.815	26.30	Zheng et al.[254]
		1.70	1.04	2.01	33.10	Er-raji et al.[29]

in the deposition of inactive amine fragments and hydrohalic acid, rather than the intended intact functional ligands, leading to precise stoichiometric deviation and passivation failure. Consequently, the "chemical space" for vapor-compatible passivators remains severely constrained, primarily limited to thermally robust, rigid aromatic systems or inorganic salts, which often lack the molecular flexibility to conform to complex surface defect topologies.

Beyond thermal stability, a more profound physical bottleneck is the inversion of defect chemistry and the kinetic limitation imposed by solid-state diffusion. While solution-processed WBG perovskites typically exhibit iodine-deficient surfaces, vacuum co-evaporation often induces a high density of deep-level iodine antisites (I_{Pb}) due to the instantaneous precursor flux. Traditional cationic passivators, optimized to repair iodine vacancies (V_I), are fundamentally mismatched with the electronic nature of these deep-level defects.

Furthermore, the quasi-ballistic transport inherent to vacuum deposition creates a shadowing effect on the micro-textured surfaces of polycrystalline WBG films. In the absence of liquid capillary forces to facilitate grain-boundary infiltration, passivation molecules are stochastically trapped as inactive inclusions or localized on surface peaks, leaving the deep grain-boundary crevices unpassivated.

Metrological failure and equipment bottlenecks in stoichiometric control

The synthesis of high-quality WBG perovskite thin films necessitates precise maintenance of complex multi-component stoichiometry. However, current deposition equipment and monitoring frameworks exhibit profound limitations when managing precursors with vast vapor-pressure disparities. Conventional processes rely heavily on QCM for rate monitoring, yet their underlying physical mechanisms possess inherent flaws. During co-evaporation, the sticking coefficients of organic halides are highly susceptible to fluctuations in substrate temperature and residual chamber pressure, resulting in severe linear deviations between sensor readings and actual deposition rates. This metrological blind spot renders the critical cation ratios in WBG perovskites nearly impossible to lock precisely, directly inducing micro-scale stoichiometric heterogeneity.

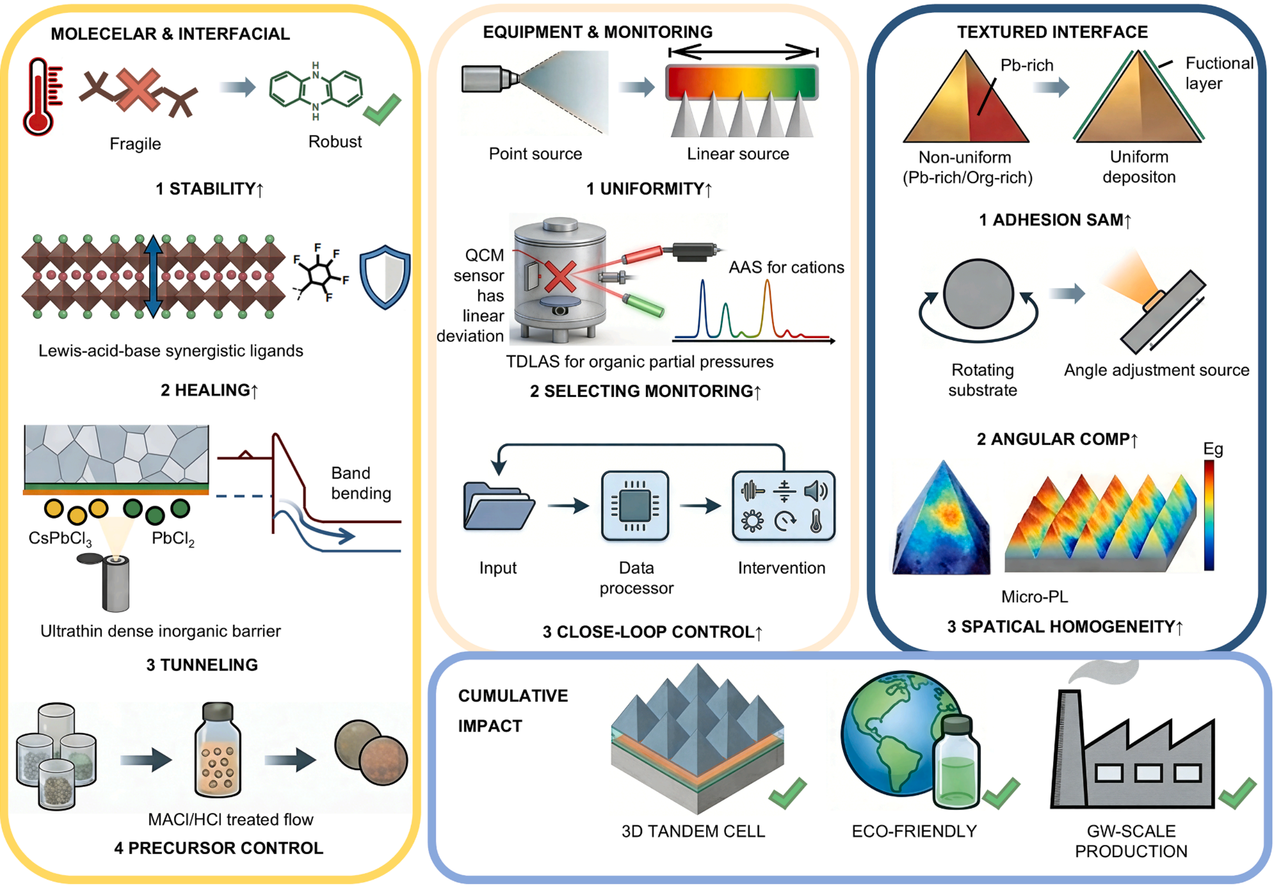

Figure 19. Future prospects

Furthermore, existing evaporation source designs fail to account for the competitive reaction kinetics between bromine and iodine species in WBG compositions. When employing linear scanning sources for large-area fabrication, the spatial intersection of multiple molecular beams exhibits thermal field gradients, which not only constrain material utilization but also lead to macro-scale band-gap gradients. For TSCs, such equipment-level control failures result in catastrophic current mismatch.

Synergetic misalignment of geometric shadowing and chemical adsorption on textured interfaces

Integrating WBG perovskites onto industrial-grade random-pyramid silicon substrates represents the most formidable engineering challenge in vapor-phase processing. The core conflict arises from the mismatch between the line-of-sight transport of vapor molecules under high vacuum and the disparate adsorption kinetics of multi-component precursors on anisotropic surfaces. This challenge has transcended traditional geometric shadowing, evolving into a sophisticated physical-chemical coupled failure mechanism.

Firstly, the geometric barriers created by micron-scale textures result in an extreme spatial maldistribution of vapor flux. In high-Knudsen-number environments, the mean free path of vapor molecules far exceeds the pyramid feature size, leading to severe starvation of direct incident flux on leeward facets. More critically, however, is the stoichiometric drift induced by the vapor-partitioning effect. Given that the sticking coefficients of different precursors (e.g., PbI$_2$ vs. FAI) on varying silicon facets (e.g., (111) vs. (100)) differ by orders of magnitude, inorganic species tend to be captured upon first impact, whereas volatile organic species undergo multiple secondary scatterings between pyramids. This imbalance in chemical adsorption energy results in a profound stoichiometric gradient between pyramid sidewalls and valleys, typically manifesting as organic enrichment in valleys and lead residues on sidewalls, directly inducing non-radiative recombination centers and spatial band-gap heterogeneity.

Future prospects

Designing vacuum-specialized passivators

To conclude, we outline critical bottlenecks and promising pathways for industrialization, as illustrated in Figure 19.

To achieve the theoretical PCE of WBG perovskites, the research community must move beyond empirical screening and adopt a problem-centric engineering approach. We propose the following four priority research tasks to overcome the intrinsic bottlenecks of vacuum deposition.

The primary chemical limitation stems from the thermal fragility of traditional soft aliphatic ligands. Therefore, research must prioritize the transition from flexible aliphatic chains to thermally robust, rigid-conjugated molecular architectures. Specifically, the design of π-extended aromatic systems, such as carbazole or phthalocyanine derivatives, can significantly elevate bond dissociation energy through delocalized resonance, ensuring molecular integrity at temperatures exceeding 300°C. These rigid systems not only survive vacuum thermal stress but also enable highly ordered face-on-orientation stacking, which facilitates vertical charge extraction while maintaining a dense physical barrier against ion migration.

While solution processing typically yields iodine-deficient surfaces (V_I), vacuum co-evaporated WBG films often exhibit iodine-rich characteristics dominated by deep-level iodine antisite (I_{Pb}) defects. We suggest developing Lewis acid-base synergistic ligands incorporating strong electron-withdrawing groups, such as perfluorinated phenylammonium salts. In this configuration, the fluorine-induced inductive effect enhances the positive charge density on the ammonium head, strengthening the electrostatic interaction with I_{Pb} sites. Concurrently, the lone pairs on the fluorine atoms can coordinate with undercoordinated Pb^{2+} centers, providing a dual-site healing mechanism that suppresses non-radiative recombination at the WBG interface.

The line-of-sight shadowing effects and restricted solid-state diffusion in vacuum deposition leave deep grain-boundary crevices unpassivated. To overcome these geometric barriers, the community should prioritize the *in situ* construction of graded 2D/3D heterojunctions or inorganic tunneling layers via precise flux control. By sequentially evaporating $CsPbCl_3$ or $PbCl_2$ at ultra-low rates immediately following absorber formation, an ultrathin, dense inorganic barrier can be formed. This layer serves as a semi-permeable membrane that bends the energy bands to repel minority carriers from the interface while allowing majority carriers to extract via quantum tunneling. This approach bypasses the inability of vapor molecules to infiltrate grain boundaries by instead sealing the top surface with an atomically sharp, solvent-free junction.

A final actionable direction is shifting from post-deposition healing to precursor-level acid modulation. To address the instability of organic salts during co-evaporation, we propose using pre-pelletized mixed precursors with controlled acidity, such as incorporating MACl- or HCl-treated additives. The introduced chloride-rich acidic environment suppresses the deprotonation of organic cations during the heating stage, thereby widening the stable sublimation kinetic window. This proactive chemical stabilization ensures a more uniform vertical distribution of A-site cations throughout the film thickness, minimizing the initial formation of deep-level traps and serving as a pivotal strategy to narrow the V_{OC} deficit toward its theoretical limit.

Equipment evolution and monitoring paradigm shift

Although vapor-phase deposition of WBG perovskites faces severe metrological and equipment challenges, drawing lessons from mature technologies in molecular beam epitaxy (MBE) and aerospace gas detection provides a clear physical pathway. However, these technologies have not yet been implemented at scale in the perovskite field, and the underlying engineering barriers and transfer rationales require in-depth discussion.

Currently, spectroscopy-based monitoring technologies such as atomic absorption spectroscopy (AAS) and TDLAS remain a vacuum in the perovskite field, primarily because the vapor compositions of perovskite precursors—especially thermally unstable organic salts—are far more complex than simple atomic species in conventional semiconductors. Nevertheless, the physical foundation for transferring these technologies is robust. AAS has demonstrated flux-control precision superior to 0.1% in complex oxide epitaxy. This non-contact, highly selective monitoring of cations such as Cs and Pb can perfectly bypass the inherent deficiencies of QCM related to sticking coefficient dependence.

For the most challenging organic components (FAI/MAI), the rationale for transferring TDLAS lies in its precise locking of vibrational energy levels in the molecular fingerprint region. The ppb-level sensitivity demonstrated by TDLAS in hydrocarbon monitoring proves its feasibility for resolving complex organic partial pressures in vacuum. The lack of current applications stems from the perovskite field's long-standing prioritization of low-cost laboratory scaling, which overlooks the spectral interference shielding caused by decomposition byproducts such as ammonia and hydroiodic acid. Future research must focus on calibrating the absolute absorption cross-sections of organic precursors within perovskite-specific vacuum environments to establish quantitative models linking optical attenuation to molecular flux density.

At the equipment level, WBG perovskites urgently need to adopt large-area linear scanning source technologies from the organic light-emitting diode (OLED) industry. Current perovskite vapor-phase fabrication remains largely stuck at the point-source stage, causing thickness uniformity and stoichiometric distribution to deteriorate rapidly on substrates larger than 10 cm. Linear source designs, by optimizing the geometric topology of nozzle arrays, can achieve molecular beam homogenization across spans exceeding 1 m.

The necessity of this transfer stems from the zero tolerance of WBG perovskites toward band-gap gradients. Since these films typically serve as the top cell in TSCs, minor stoichiometric shifts trigger phase segregation and subsequent current mismatch. The critical future task is to integrate OLED linear evaporation technology with temperature-graded showerhead manifolds to resolve spatial mixing uniformity during multi-source co-evaporation. This cross-industry equipment transfer from the display industry to the photovoltaics industry represents the only viable path to semiconductor-grade mass production of WBG perovskites.

Finally, regarding control logic, *in situ* feedback mechanisms from CVD should be adopted. Currently, perovskite fabrication generally lacks real-time intervention capabilities, remaining an open-loop process. Drawing on the application of biased QCM techniques in CVD surface chemistry studies, we can intervene in the film formation process via electric fields or thermal feedback. The ultimate future goal is to construct an intelligent control system that integrates spectroscopic monitoring (input) with *in situ* performance evaluation (output). This data-driven control paradigm will decouple WBG perovskite fabrication from reliance on researcher experience, achieving true industrial-scale precision manufacturing.

Synergistic control on textured interfaces

Achieving conformal growth of WBG perovskites on industrial random pyramids is essentially a synergistic process of overcoming the non-uniformity of line-of-sight flux and the disparities in facet-dependent adsorption energies. Current process optimizations are largely confined to macroscopic rotation or empirical flux compensation, lacking fundamental intervention in micro-kinetic mismatch. To achieve semiconductor-grade interfacial quality, future research must prioritize the following three core tasks.

In existing vapor processes, inorganic components (PbI_2) exhibit strong chemisorption ($S \approx 1.0$), whereas organic species (FAI) are constrained by weak hydrogen bonding ($S < 0.25$), resulting in drastic stoichiometric gradients between pyramidal facets and valleys. The primary future task is to chemically program the textured interface using functional molecules, such as fluorinated silanes or specific SAMs. Specifically, electronegative interfacial layers must be developed to enhance the anchoring of organic cations by increasing intermolecular electrostatic interactions, thereby artificially elevating the effective sticking coefficient of organic components on pyramidal sidewalls. The goal is to constrain the adsorption energy variance across different facets within the range of thermal fluctuations (kBT), fundamentally eliminating the valley enrichment phenomenon caused by secondary scattering.

Simple planetary rotation no longer meets the stringent requirements of WBG perovskites for stoichiometric precision within 1%. Future equipment innovation should focus on dynamic oblique compensation evaporation, which involves real-time adjustment of the relative incidence angle between the evaporation source and the textured substrate (cycling between 0° and 60°) to compensate for flux deficits caused by the pyramidal geometric inclination (54.7°). Building on this, there is an urgent need to develop multi-physics models that integrate Knudsen diffusion and surface adsorption kinetics. Such models should predict the mean collision frequency and capture the probability of vapor molecules within microscopic cavities under varying vacuum levels. By precisely locking the substrate temperature between 40°C and 80°C, the kinetic quenching effect can be utilized to freeze uniform quasi-metastable compositions onto the textured surface, preventing the I/Br phase segregation common in WBG systems.

In *in situ* performance evaluation, a critical future research direction is the development of *in situ* monitoring tools with micron-scale spatial resolution. Traditional QCM provides only average rates and fails to reflect localized dynamics on textured interfaces. *In situ* micro-PL and spatially resolved spectroscopic ellipsometry (SRE) should be implemented to monitor the bandgap evolution at pyramidal tips and valleys in real time during film growth. By capturing spatial shifts in PL peak positions, the system can automatically identify early signals of stoichiometric mismatch and trigger partial pressure control feedback loops, such as adjusting pulse valves or heating power. This *in situ* diagnosis-instantaneous feedback control chain is the technical core for mitigating V_{OC} deficits in WBG TSCs and achieving consistency in large-area production.

Ultimately, the strategic significance of vapor deposition extends beyond the laboratory metrics of efficiency and stability. It represents a paradigm convergence between emerging photovoltaics and the mature semiconductor industry. By adopting vacuum-based manufacturing, the perovskite community can leverage decades of established infrastructure, ranging from precision tooling to automated process control, accelerating the transition from pilot lines to terawatt-scale foundries.

Furthermore, this technology offers a profound environmental dividend. In an era where sustainability is paramount, the ability to fabricate high-performance modules without relying on millions of liters of toxic solvents fundamentally de-risks the environmental footprint of solar energy deployment. As we approach net-zero targets in the future, vapor-deposited perovskites stand not only as a scientific curiosity but as a cornerstone technology for a clean, scalable, and sustainable energy future.

DATA AND CODE AVAILABILITY

All relevant data supporting this review are contained within the manuscript.

ACKNOWLEDGMENTS

The authors thank the National Natural Science Foundation of China (52502171), the State Key Laboratory of Photovoltaic Science and Technology (202401030303), and the National Key Research and Development Program of China (2023YFC2505900) for the financial support.

AUTHOR CONTRIBUTIONS

Conceptualization, X.M., Q.Z., Z.H., S.Z., and H.Z.; supervision, X.M. and Q.Z.; writing – original draft, Z.H., S.Z., H.Z., and Q.Z.; writing – review & editing, Z.H. and Q.Z.; formal analysis, all authors; investigation, all authors; validation, all authors. All authors have read and agreed to the published version of the manuscript.

DECLARATION OF INTERESTS

The authors declare no conflicts of interest.

REFERENCES

1. Green, M.A., Dunlop, E.D., Yoshita, M., Kopidakis, N., Bothe, K., Siefer, G., Hao, X., and Jiang, J. (2025). Solar Cell Efficiency Tables (Version 66). Progress in Photovoltaics. *33*, 795–810. https://doi.org/10.1002/pip.3919.
2. Li, G., Zhang, Z., Agyei-Tuffour, B., Wu, L., Gries, T.W., Prashanthan, K., Musiienko, A., Li, J., Zhu, R., Hart, L.J.F., et al. (2026). Stabilizing high-efficiency perovskite solar cells via strategic interfacial contact engineering. Nat. Photonics *20*, 55–62. https://doi.org/10.1038/s41566-025-01791-1.
3. Xiong, Z., Zhang, Q., Cai, K., Zhou, H., Song, Q., Han, Z., Kang, S., Li, Y., Jiang, Q., Zhang, X., and You, J. (2025). Homogenized chlorine distribution for> 27% power conversion efficiency in perovskite solar cells. Science *390*, 638–642.
4. Luo, C., Gu, H., Zhang, B., Park, S.M., Wei, M., and Hou, Y. (2025). Perovskite Tandems: the Next Big Leap in Photovoltaic Technology. Adv. Mater. *37*, e08331. https://doi.org/10.1002/adma.202508331.
5. Wen, J., Hu, H., Chen, C., McMeekin, D.P., Xiao, K., Lin, R., Liu, Y., Snaith, H.J., Tang, J., Paetzold, U.W., and Tan, H. (2025). Present status of and future opportunities for all-perovskite tandem photovoltaics. Nat. Energy *10*, 681–696. https://doi.org/10.1038/s41560-025-01782-0.
6. Yang, G., Deng, C., Li, C., Zhu, T., Liu, D., Bai, Y., Chen, Q., Huang, J., and Li, G. (2025). Towards efficient, scalable and stable perovskite/silicon tandem solar cells. Nat. Photonics *19*, 913–924. https://doi.org/10.1038/s41566-025-01732-y.
7. Jia, L., Xia, S., Li, J., Qin, Y., Pei, B., Ding, L., Yin, J., Du, T., Fang, Z., Yin, Y., et al. (2025). Efficient perovskite/silicon tandem with asymmetric

self-assembly molecule. Nature *644*, 912–919. https://doi.org/10.1038/s41586-025-09333-z.

8. Fang, Z., Ding, L., Yang, Y., Gu, X., Li, H., Chen, H., Yin, Y., Wang, W., Wu, X., Rao, Z., et al. (2026). Flexible perovskite/silicon tandem solar cell with a dual buffer layer. Nature *649*, 65–72. https://doi.org/10.1038/s41586-025-09835-w.
9. Mei, J., and Yan, F. (2025). Recent Advances in Wide-Bandgap Perovskite Solar Cells. Adv. Mater. *37*, e2418622. https://doi.org/10.1002/adma.202418622.
10. Guo, Y., Tan, H., and Xu, B. (2025). Deciphering halide ion migration and performance loss in wide-bandgap perovskite solar cells: connection, mechanism, and solutions. Energy Environ. Sci. *18*, 8744–8755. https://doi.org/10.1039/d5ee03136b.
11. Draguta, S., Sharia, O., Yoon, S.J., Brennan, M.C., Morozov, Y.V., Manser, J.S., Kamat, P.V., Schneider, W.F., and Kuno, M. (2017). Rationalizing the light-induced phase separation of mixed halide organic–inorganic perovskites. Nat. Commun. *8*, 200. https://doi.org/10.1038/s41467-017-00284-2.
12. Cui, Z., Zhang, Q., Bai, Y., and Chen, Q. (2023). Issues of phase segregation in wide-bandgap perovskites. Mater. Chem. Front. *7*, 1896–1911. https://doi.org/10.1039/d2qm01341j.
13. Guo, Y., Zhang, C., Wang, L., Yin, X., Sun, B., Wei, C., Luo, X., Yang, S., Sun, L., and Xu, B. (2025). Unveiling the impact of photoinduced halide segregation on performance degradation in wide-bandgap perovskite solar cells. Energy Environ. Sci. *18*, 2308–2317. https://doi.org/10.1039/d4ee05604c.
14. Chen, Z., Brocks, G., Tao, S., and Bobbert, P.A. (2021). Unified theory for light-induced halide segregation in mixed halide perovskites. Nat. Commun. *12*, 2687. https://doi.org/10.1038/s41467-021-23008-z.
15. Li, N., Pratap, S., Guo, R., He, Z., Liang, S., Jia, X., Gholipoor, M., Babbe, F., Barchi, N.S., Slack, J.L., et al. (2025). Unveiling the role of halide mixing on crystallization kinetics and charge transfer mechanisms in wide-bandgap organic-inorganic halide perovskites. Energy Environ. Sci. *18*, 10460–10472. https://doi.org/10.1039/d5ee05540g.
16. Huang, J., Wang, H., Jia, C., Tang, Y., Yang, H., Chen, C., Gou, K., Zhou, Y., Zhang, D., and Liu, S. (2024). Advances in Crystallization Regulation and Defect Suppression Strategies for All-inorganic CsPbX3 Perovskite Solar Sells. Prog. Mater. Sci. *141*, 101223. https://doi.org/10.1016/j.pmatsci.2023.101223.
17. Dastidar, S., Hawley, C.J., Dillon, A.D., Gutierrez-Perez, A.D., Spanier, J.E., and Fafarman, A.T. (2017). Quantitative Phase-Change Thermodynamics and Metastability of Perovskite-Phase Cesium Lead Iodide. J. Phys. Chem. Lett. *8*, 1278–1282. https://doi.org/10.1021/acs.jpclett.7b00134.
18. Marronnier, A., Roma, G., Boyer-Richard, S., Pedesseau, L., Jancu, J.-M., Bonnassieux, Y., Katan, C., Stoumpos, C.C., Kanatzidis, M.G., and Even, J. (2018). Anharmonicity and Disorder in the Black Phases of Cesium Lead Iodide Used for Stable Inorganic Perovskite Solar Cells. ACS Nano *12*, 3477–3486. https://doi.org/10.1021/acsnano.8b00267.
19. Li, Z., Wei, Z., Sun, X., Zhang, Y., Wang, Q., Guan, Z., Qiu, M., Zhang, Y., Yue, Y., Liu, F., et al. (2025). Nanocrystal-Nucleus Template Strategy for Efficient Wide-Bandgap Perovskite Solar Cells with Enhanced Homogeneity and Energy-Level Alignment. Adv. Mater. *37*, e2509202. https://doi.org/10.1002/adma.202509202.
20. Yan, J., Zhao, X., Li, M., Ma, T., Luo, D., Wang, H., Yang, X., Hsu, H.Y., Zhou, Y., Chen, C., et al. (2025). Sulfonic Surfactant Promises Uniform Wide-Bandgap Perovskite Solar Modules for All-Perovskite Tandem Photovoltaics. Adv. Energy Mater. *15*, 2501871. https://doi.org/10.1002/aenm.202501871.
21. Qi, Y., and Liang, J. (2026). Facets as the key to stable perovskites. Nat. Mater. *25*, 549–550. https://doi.org/10.1038/s41563-025-02406-4.
22. Li, W., Hao, M., Baktash, A., Wang, L., and Etheridge, J. (2023). The role of ion migration, octahedral tilt, and the A-site cation on the instability of Cs1-xFAxPbI3. Nat. Commun. *14*, 8523. https://doi.org/10.1038/s41467-023-44235-6.
23. Gao, Y., Wang, Y., Yang, P., Shi, B., Liu, Z., Liu, S., Li, S., Liu, Y., Ge, X., Liu, P., et al. (2025). Shear flow strategy for coating homogeneity of organic materials in perovskite solar cells and modules. Joule *9*, 102098. https://doi.org/10.1016/j.joule.2025.102098.
24. Sun, K., Wang, Z., Li, N., Liu, L., Xiong, W., Xu, Z., Geng, Z., Guo, X., Jiang, Y., Feng, S.P., et al. (2025). Dynamic Reconstruction of Fluid Interface Manipulated by Fluid Balancing Agent for Scalable Efficient Perovskite Solar Cells. Adv. Mater. *37*, e2419419. https://doi.org/10.1002/adma.202419419.
25. Aydin, E., Allen, T.G., De Bastiani, M., Razzaq, A., Xu, L., Ugur, E., Liu, J., and De Wolf, S. (2024). Pathways toward commercial perovskite/silicon tandem photovoltaics. Science *383*, eadh3849. https://doi.org/10.1126/science.adh3849.
26. Xu, Y., Xu, K., Pan, T., Ke, X., Li, Y., Meng, N., Shi, X., Liu, J., Cui, Y., Wang, Z., et al. (2025). Fully thermally evaporated perovskite solar cells based on reverse layer-by-layer deposition. Nat. Photonics *19*, 1345–1352. https://doi.org/10.1038/s41566-025-01768-0.
27. Chozas-Barrientos, S., Paliwal, A., Ventosinos, F., Roldán-Carmona, C., Gil-Escrig, L., Held, V., Carroy, P., Muñoz, D., and Bolink, H.J. (2025). Molecular Recombination Junction for Vacuum-Deposited Perovskite/Silicon Two-Terminal Tandem Solar Cells. ACS Energy Lett. *10*, 1733–1740. https://doi.org/10.1021/acsenergylett.5c00155.
28. Liu, Z., Xiong, Z., Yang, S., Fan, K., Jiang, L., Mao, Y., Qin, C., Li, S., Qiu, L., Zhang, J., et al. (2024). Strained heterojunction enables high-performance, fully textured perovskite/silicon tandem solar cells. Joule *8*, 2834–2850. https://doi.org/10.1016/j.joule.2024.06.015.
29. Er-Raji, O., Messmer, C., Pradhan, R.R., Fischer, O., Hnapovskyi, V., Kosar, S., Marengo, M., List, M., Faisst, J., Jurado, J.P., et al. (2025). Electron accumulation across the perovskite layer enhances tandem solar cells with textured silicon. Science *390*, eadx1745. https://doi.org/10.1126/science.adx1745.
30. Dunlap-Shohl, W.A., Zhou, Y., Padture, N.P., and Mitzi, D.B. (2019). Synthetic Approaches for Halide Perovskite Thin Films. Chem. Rev. *119*, 3193–3295. https://doi.org/10.1021/acs.chemrev.8b00318.
31. Yin, W.-J., Shi, T., and Yan, Y. (2014). Unusual defect physics in CH3NH3PbI3 perovskite solar cell absorber. Appl. Phys. Lett. *104*, 063903. https://doi.org/10.1063/1.4864778.
32. Wang, Y., Wang, Y., Doherty, T.A.S., Stranks, S.D., Gao, F., and Yang, D. (2025). Octahedral units in halide perovskites. Nat. Rev. Chem *9*, 261–277. https://doi.org/10.1038/s41570-025-00687-6.
33. Gao, Q., Qi, J., Chen, K., Xia, M., Hu, Y., Mei, A., and Han, H. (2022). Halide Perovskite Crystallization Processes and Methods in Nanocrystals, Single Crystals, and Thin Films. Adv. Mater. *34*, e2200720. https://doi.org/10.1002/adma.202200720.
34. Han, J., Park, K., Tan, S., Vaynzof, Y., Xue, J., Diau, E.W.-G., Bawendi, M.G., Lee, J.-W., and Jeon, I. (2025). Perovskite solar cells. Nat. Rev. Methods Primers *5*, 3. https://doi.org/10.1038/s43586-024-00373-9.
35. Brivio, F., Caetano, C., and Walsh, A. (2016). Thermodynamic Origin of Photoinstability in the CH3NH3Pb(I1-xBrx)3 Hybrid Halide Perovskite Alloy. J. Phys. Chem. Lett. *7*, 1083–1087. https://doi.org/10.1021/acs.jpclett.6b00226.
36. McGovern, L., Grimaldi, G., Futscher, M.H., Hutter, E.M., Muscarella, L.A., Schmidt, M.C., and Ehrler, B. (2021). Reduced Barrier for Ion Migration in Mixed-Halide Perovskites. ACS Appl. Energy Mater. *4*, 13431–13437. https://doi.org/10.1021/acsaem.1c03095.
37. Hoke, E.T., Slotcavage, D.J., Dohner, E.R., Bowring, A.R., Karunadasa, H.I., and McGehee, M.D. (2015). Reversible photo-induced trap formation in mixed-halide hybrid perovskites for photovoltaics. Chem. Sci. *6*, 613–617. https://doi.org/10.1039/c4sc03141e.
38. Bischak, C.G., Hetherington, C.L., Wu, H., Aloni, S., Ogletree, D.F., Limmer, D.T., and Ginsberg, N.S. (2017). Origin of Reversible

Photoinduced Phase Separation in Hybrid Perovskites. Nano Lett. *17*, 1028–1033. https://doi.org/10.1021/acs.nanolett.6b04453.

39. Zhao, Y., Miao, P., Elia, J., Hu, H., Wang, X., Heumueller, T., Hou, Y., Matt, G.J., Osvet, A., Chen, Y.T., et al. (2020). Strain-activated light-induced halide segregation in mixed-halide perovskite solids. Nat. Commun. *11*, 6328. https://doi.org/10.1038/s41467-020-20066-7.
40. Limmer, D.T., and Ginsberg, N.S. (2020). Photoinduced phase separation in the lead halides is a polaronic effect. J. Chem. Phys. *152*, 230901. https://doi.org/10.1063/1.5144291.
41. Eames, C., Frost, J.M., Barnes, P.R.F., O'Regan, B.C., Walsh, A., and Islam, M.S. (2015). Ionic transport in hybrid lead iodide perovskite solar cells. Nat. Commun. *6*, 7497. https://doi.org/10.1038/ncomms8497.
42. Sabino, F.P., Dalpian, G.M., and Zunger, A. (2023). Light-Induced Frenkel Defect Pair Formation Can Lead to Phase-Segregation of Otherwise Miscible Halide Perovskite Alloys. Adv. Energy Mater. *13*, 2301539. https://doi.org/10.1002/aenm.202301539.
43. Zhang, X., Ma, Q., Wang, Y., Zheng, J., Liu, Q., Liu, L., Yang, P., He, W., Cao, Y., Duan, W., et al. (2024). Ligand Homogenized Br-I Wide-Bandgap Perovskites for Efficient NiO(x)-Based Inverted Semitransparent and Tandem Solar Cells. ACS Nano *18*, 15991–16001. https://doi.org/10.1021/acsnano.4c04341.
44. Ruth, A., Okrepka, H., Kamat, P., and Kuno, M. (2023). Thermodynamic Band Gap Model for Photoinduced Phase Segregation in Mixed-Halide Perovskites. J. Phys. Chem. C *127*, 18547–18559. https://doi.org/10.1021/acs.jpcc.3c04708.
45. Belisle, R.A., Bush, K.A., Bertoluzzi, L., Gold-Parker, A., Toney, M.F., and McGehee, M.D. (2018). Impact of Surfaces on Photoinduced Halide Segregation in Mixed-Halide Perovskites. ACS Energy Lett. *3*, 2694–2700. https://doi.org/10.1021/acsenergylett.8b01562.
46. Kerner, R.A., Xu, Z., Larson, B.W., and Rand, B.P. (2021). The role of halide oxidation in perovskite halide phase separation. Joule *5*, 2273–2295. https://doi.org/10.1016/j.joule.2021.07.011.
47. Yoon, S.J., Kuno, M., and Kamat, P.V. (2017). Shift Happens. How Halide Ion Defects Influence Photoinduced Segregation in Mixed Halide Perovskites. ACS Energy Lett. *2*, 1507–1514. https://doi.org/10.1021/acsenergylett.7b00357.
48. Ren, X., Wang, J., Lin, Y., Wang, Y., Xie, H., Huang, H., Yang, B., Yan, Y., Gao, Y., He, J., et al. (2024). Mobile iodides capture for highly photolysis- and reverse-bias-stable perovskite solar cells. Nat. Mater. *23*, 810–817. https://doi.org/10.1038/s41563-024-01876-2.
49. Zhang, Z., Chen, W., Jiang, X., Cao, J., Yang, H., Chen, H., Yang, F., Shen, Y., Yang, H., Cheng, Q., et al. (2024). Suppression of phase segregation in wide-bandgap perovskites with thiocyanate ions for perovskite/organic tandems with 25.06% efficiency. Nat. Energy *9*, 592–601. https://doi.org/10.1038/s41560-024-01491-0.
50. Cho, J., and Kamat, P.V. (2020). How Chloride Suppresses Photoinduced Phase Segregation in Mixed Halide Perovskites. Chem. Mater. *32*, 6206–6212. https://doi.org/10.1021/acs.chemmater.0c02100.
51. Muscarella, L.A., Hutter, E.M., Wittmann, F., Woo, Y.W., Jung, Y.K., McGovern, L., Versluis, J., Walsh, A., Bakker, H.J., and Ehrler, B. (2020). Lattice Compression Increases the Activation Barrier for Phase Segregation in Mixed-Halide Perovskites. ACS Energy Lett. *5*, 3152–3158. https://doi.org/10.1021/acsenergylett.0c01474.
52. Yang, B., Bogachuk, D., Suo, J., Wagner, L., Kim, H., Lim, J., Hinsch, A., Boschloo, G., Nazeeruddin, M.K., and Hagfeldt, A. (2022). Strain effects on halide perovskite solar cells. Chem. Soc. Rev. *51*, 7509–7530. https://doi.org/10.1039/d2cs00278g.
53. Li, C., Chen, C., Gao, W., Dong, H., Zhou, Y., Wu, Z., and Ran, C. (2024). Wide-Bandgap Lead Halide Perovskites for Next-Generation Optoelectronics: Current Status and Future Prospects. ACS Nano *18*, 35130–35163. https://doi.org/10.1021/acsnano.4c12107.
54. Hu, L., Guan, X., Chen, W., Yao, Y., Wan, T., Lin, C.-H., Pham, N.D., Yuan, L., Geng, X., Wang, F., et al. (2021). Linking Phase Segregation and Photovoltaic Performance of Mixed-Halide Perovskite Films through Grain Size Engineering. ACS Energy Lett. *6*, 1649–1658. https://doi.org/10.1021/acsenergylett.1c00213.
55. Yin, J., Xu, Z., Hu, Q., Teobaldi, G., Liu, L.M., and Prezhdo, O.V. (2023). Tuning Octahedral Tilting by Doping to Prevent Detrimental Phase Transition and Extend Carrier Lifetime in Organometallic Perovskites. J. Am. Chem. Soc. *145*, 5393–5399. https://doi.org/10.1021/jacs.2c13593.
56. Zhang, X., Liu, Y., Chen, X., Zhang, C., Wang, J., Cheng, J., and Li, J. (2024). Improved perovskite crystallization by antisolvent engineering in tin-perovskite photovoltaics. Phys. Chem. Chem. Phys. *26*, 28715–28723. https://doi.org/10.1039/d4cp02655a.
57. Lee, B.I., Gupta, R.K., and Whang, C.M. (2008). Effects of solvent and chelating agent on synthesis of solid oxide fuel cell perovskite, La0.8Sr0.2CrO3−δ. Mater. Res. Bull. *43*, 207–221. https://doi.org/10.1016/j.materresbull.2007.10.007.
58. Smecca, E., Valenzano, V., Valastro, S., Deretzis, I., Mannino, G., Malandrino, G., Accorsi, G., Colella, S., Rizzo, A., La Magna, A., et al. (2021). Two-step MAPbI3 deposition by low-vacuum proximity-space-effusion for high-efficiency inverted semitransparent perovskite solar cells. J. Mater. Chem. A Mater. *9*, 16456–16469. https://doi.org/10.1039/d1ta02535j.
59. Li, H., Liu, M., Li, M., Park, H., Mathews, N., Qi, Y., Zhang, X., Bolink, H.J., Leo, K., Graetzel, M., and Yi, C. (2022). Applications of vacuum vapor deposition for perovskite solar cells: A progress review. iEnergy *1*, 434–452. https://doi.org/10.23919/ien.2022.0053.
60. Iizuka, A., Shibata, E., Sato, M., and Nakamura, T. (2015). Vapor pressure measurements of PbBr2 by the Knudsen effusion method and identification of its vapor species. Thermochim. Acta *622*, 103–106. https://doi.org/10.1016/j.tca.2015.10.014.
61. Sheikh, M.A.K., Singh, S., Abdur, R., Lee, S.M., Kim, J.H., Nam, H.S., Lee, H., and Lee, J. (2022). Effects of the PbBr(2):PbI(2) Molar Ratio on the Formation of Lead Halide Thin Films, and the Ratio's Application for High Performance and Wide Bandgap Solar Cells. Materials *15*, 837. https://doi.org/10.3390/ma15030837.
62. Zhidkov, I.S., Akbulatov, A.F., Poteryaev, A.I., Kukharenko, A.I., Rasmetyeva, A.V., Frolova, L.A., Troshin, P.A., and Kurmaev, E.Z. (2023). The Photochemical Stability of PbI2 and PbBr2: Optical and XPS and DFT Studies. Coatings *13*, 784. https://doi.org/10.3390/coatings13040784.
63. Gil-Escrig, L., Nespoli, J., Elhorst, F.D., Ventosinos, F., Roldán-Carmona, C., Koster, L.J.A., Savenije, T.J., Sessolo, M., and Bolink, H.J. (2025). Tuning substrate temperature for enhanced vacuum-deposited wide-bandgap perovskite solar cells: insights from morphology, charge transport, and drift-diffusion simulations. EES Solar *1*, 391–403. https://doi.org/10.1039/d5el00021a.
64. Rodkey, N., Gomar-Fernández, I., Ventosinos, F., Roldan-Carmona, C., Koster, L.J.A., and Bolink, H.J. (2024). Close-Space Sublimation as a Scalable Method for Perovskite Solar Cells. ACS Energy Lett. *9*, 927–933. https://doi.org/10.1021/acsenergylett.3c02794.
65. Gualdrón-Reyes, A.F., Yoon, S.J., Barea, E.M., Agouram, S., Muñoz-Sanjosé, V., Meléndez, Á.M., Niño-Gómez, M.E., and Mora-Seró, I. (2019). Controlling the Phase Segregation in Mixed Halide Perovskites through Nanocrystal Size. ACS Energy Lett. *4*, 54–62. https://doi.org/10.1021/acsenergylett.8b02207.
66. Barker, A.J., Sadhanala, A., Deschler, F., Gandini, M., Senanayak, S.P., Pearce, P.M., Mosconi, E., Pearson, A.J., Wu, Y., Srimath Kandada, A.R., et al. (2017). Defect-Assisted Photoinduced Halide Segregation in Mixed-Halide Perovskite Thin Films. ACS Energy Lett. *2*, 1416–1424. https://doi.org/10.1021/acsenergylett.7b00282.
67. Funk, H., Binyamin, T., Etgar, L., Shargaieva, O., Unold, T., Eljarrat, A., Koch, C.T., and Abou-Ras, D. (2023). Phase Segregation Mechanisms in Mixed-Halide CsPb(Br(x)I(1-x))(3) Nanocrystals in Dependence of Their Sizes and Their Initial [Br]:[I] Ratios. ACS Mater. Au *3*, 687–698. https://doi.org/10.1021/acsmaterialsau.3c00056.

68. Nasi, L., Calestani, D., Mezzadri, F., Mariano, F., Listorti, A., Ferro, P., Mazzeo, M., and Mosca, R. (2020). All-Inorganic CsPbBr(3) Perovskite Films Prepared by Single Source Thermal Ablation. Front. Chem. *8*, 313. https://doi.org/10.3389/fchem.2020.00313.
69. Ghosh, P., Spencer, B.F., and Krishnan Jagadamma, L. (2024). Vertical Compositional Heterogeneity Induces Instability in All-Inorganic CsPbIBr(2) Perovskites. ACS Appl. Energy Mater. *7*, 9045–9051. https://doi.org/10.1021/acsaem.4c01898.
70. Mahmoud, M.A.A., Gupta, Y., Fischer, O., Landgraf, J.B., Bivour, M., and Borchert, J. (2025). Unveiling the complexity of co-evaporation of perovskite: Why co-evaporation might not be the optimal choice. J. Mater. Chem. A Mater. *13*, 42281–42288. https://doi.org/10.1039/d5ta08316h.
71. Yang, L., Zheng, F., Wu, J., Hou, Y., Qi, X., Miao, Y., Wang, X., Huang, L., Liu, X., Zhang, J., et al. (2024). Unveiling Local Current Behavior and Manipulating Grain Homogenization of Perovskite Films for Efficient Solar Cells. ACS Nano *18*, 17547–17556. https://doi.org/10.1021/acsnano.4c00911.
72. Abzieher, T., Feeney, T., Schackmar, F., Donie, Y.J., Hossain, I.M., Schwenzer, J.A., Hellmann, T., Mayer, T., Powalla, M., and Paetzold, U.W. (2021). From Groundwork to Efficient Solar Cells: On the Importance of the Substrate Material in Co-Evaporated Perovskite Solar Cells. Adv. Funct. Mater. *31*, 2104482. https://doi.org/10.1002/adfm.202104482.
73. Yuan, Q., Lohmann, K.B., Oliver, R.D.J., Ramadan, A.J., Yan, S., Ball, J.M., Christoforo, M.G., Noel, N.K., Snaith, H.J., Herz, L.M., and Johnston, M.B. (2023). Thermally Stable Perovskite Solar Cells by All-Vacuum Deposition. ACS Appl. Mater. Interfaces *15*, 772–781. https://doi.org/10.1021/acsami.2c14658.
74. Roß, M., Gil-Escrig, L., Al-Ashouri, A., Tockhorn, P., Jošt, M., Rech, B., and Albrecht, S. (2020). Co-Evaporated p-i-n Perovskite Solar Cells beyond 20% Efficiency: Impact of Substrate Temperature and Hole-Transport Layer. ACS Appl. Mater. Interfaces *12*, 39261–39272. https://doi.org/10.1021/acsami.0c10898.
75. Jagadamma, L.K., Edwards, P.R., Martin, R.W., Ruseckas, A., and Samuel, I.D.W. (2021). Nanoscale Heterogeneity in CsPbBr3 and CsPbBr3:KI Perovskite Films Revealed by Cathodoluminescence Hyperspectral Imaging. ACS Appl. Energy Mater. *4*, 2707–2715. https://doi.org/10.1021/acsaem.0c03154.
76. Yu, L., Xing, C., Bao, Q., Zhang, L., Lu, F., He, M., Tai, Q., Zhang, T., and Wang, D. (2024). Inhomogeneous Halide Anions Distribution along Out-of-Plane Direction in Wide-Bandgap Perovskite Solar Cells and Its Effect on Open Circuit Voltage Loss and Phase Segregation. ACS Appl. Mater. Interfaces *16*, 33360–33370. https://doi.org/10.1021/acsami.4c03285.
77. Li, X., Jiang, Z., Chen, S., Tang, Y., Xue, B., Wu, T., Lu, Y., Moya, X., Rao, A., Yu, Z., and Ducati, C. (2026). Visualizing Strain-Coupled Cryogenic Phase Transitions and Defect Dynamics in Perovskite Quantum Dots Using In Situ STEM. Adv. Sci. *13*, e16496. https://doi.org/10.1002/advs.202516496.
78. Gil-Escrig, L., Dreessen, C., Palazon, F., Hawash, Z., Moons, E., Albrecht, S., Sessolo, M., and Bolink, H.J. (2021). Efficient Wide-Bandgap Mixed-Cation and Mixed-Halide Perovskite Solar Cells by Vacuum Deposition. ACS Energy Lett. *6*, 827–836. https://doi.org/10.1021/acsenergylett.0c02445.
79. Stoumpos, C.C., Malliakas, C.D., and Kanatzidis, M.G. (2013). Semiconducting tin and lead iodide perovskites with organic cations: phase transitions, high mobilities, and near-infrared photoluminescent properties. Inorg. Chem. *52*, 9019–9038. https://doi.org/10.1021/ic401215x.
80. Juarez-Perez, E.J., Ono, L.K., and Qi, Y. (2019). Thermal degradation of formamidinium based lead halide perovskites into sym-triazine and hydrogen cyanide observed by coupled thermogravimetry-mass spectrometry analysis. J. Mater. Chem. A Mater. *7*, 16912–16919. https://doi.org/10.1039/c9ta06058h.
81. Kuba, A.G., Sahli, F., Othman, M., Artuk, K., Jeangros, Q., Hessler-Wyser, A., Ballif, C., and Wolff, C.M. (2025). Making from Breaking: Degradation Inversion Enables Vapor-Phase Synthesis of Halide Perovskites in Ambient Conditions. ACS Energy Lett. *10*, 2710–2717. https://doi.org/10.1021/acsenergylett.4c03395.
82. Bækbo, M.J., Hansen, O., Chorkendorff, I., and Vesborg, P.C.K. (2018). Deposition of methylammonium iodide via evaporation - combined kinetic and mass spectrometric study. RSC Adv. *8*, 29899–29908. https://doi.org/10.1039/c8ra04851g.
83. Roß, M., Stutz, M.B., and Albrecht, S. (2022). Revealing the Role of Methylammonium Iodide Purity on the Vapor-Phase Deposition Process of Perovskites. Sol. RRL *6*, 2200500. https://doi.org/10.1002/solr.202200500.
84. Diercks, A., Petry, J., Feeney, T., Thelen, R., Fassl, P., and Paetzold, U.W. (2025). Particle Size Matters – Impact of Particle Size and Crucible Geometry on Sublimation Behavior of Formamidinium Iodide. Adv. Mater. Technol. *11*, e01549. https://doi.org/10.1002/admt.202501549.
85. Thampy, S., Zhang, B., Park, J.-G., Hong, K.-H., and Hsu, J.W.P. (2020). Bulk and interfacial decomposition of formamidinium iodide (HC(NH2)2I) in contact with metal oxide. Mater. Adv. *1*, 3349–3357. https://doi.org/10.1039/d0ma00624f.
86. Sahli, F., Guesnay, Q., Salsi, N., Duchêne, L., Ballif, C., and Jeangros, Q. (2021). Ammonia-assisted vapour transport deposition of formamidinium salts for perovskite thin films.
87. Borchert, J., Levchuk, I., Snoek, L.C., Rothmann, M.U., Haver, R., Snaith, H.J., Brabec, C.J., Herz, L.M., and Johnston, M.B. (2019). Impurity Tracking Enables Enhanced Control and Reproducibility of Hybrid Perovskite Vapor Deposition. ACS Appl. Mater. Interfaces *11*, 28851–28857. https://doi.org/10.1021/acsami.9b07619.
88. Kroll, M., Öz, S.D., Zhang, Z., Ji, R., Schramm, T., Antrack, T., Vaynzof, Y., Olthof, S., and Leo, K. (2022). Insights into the evaporation behaviour of FAI: material degradation and consequences for perovskite solar cells. Sustain. Energy Fuels *6*, 3230–3239.
89. Kim, B.S., Han, Y., and Kim, J.J. (2020). Growth mechanism of CH(3)NH(3)I in a vacuum processed perovskite. Nanoscale Adv. *2*, 3906–3911. https://doi.org/10.1039/d0na00466a.
90. Bhowmik, K.K., Ma, D., Topper, B., Koehler, K., Foulger, S.H., Xiao, H., Zhu, L., and Zhao, L. (2025). Thermal Evaporation of Overlayers Induces Degradation of Metal Halide Perovskites. ACS Nano *19*, 38428–38439. https://doi.org/10.1021/acsnano.5c11297.
91. Zanoni, K.P.S., Martínez-Goyeneche, L., Dreessen, C., Sessolo, M., and Bolink, H.J. (2023). Photovoltaic Devices Using Sublimed Methylammonium Lead Iodide Perovskites: Long-Term Reproducible Processing. Sol. RRL *7*, 2201073. https://doi.org/10.1002/solr.202201073.
92. Coppeta, R., Ceric, H., Karunamurthy, B., and Grasser, T. (2013). Epitaxial Volmer-Weber Growth Modelling (IEEE), pp. 45–48.
93. Parrott, E.S., Patel, J.B., Haghighirad, A.A., Snaith, H.J., Johnston, M.B., and Herz, L.M. (2019). Growth modes and quantum confinement in ultrathin vapour-deposited MAPbI(3) films. Nanoscale *11*, 14276–14284. https://doi.org/10.1039/c9nr04104d.
94. Wang, Z., He, D., Steele, J.A., Xu, H., Zhang, B., Cheng, H., Han, E.Q., Ding, S., Zhang, C., Lyu, M., and Wang, L. (2026). Frank-van der Merwe-Mediated Sequential Thermal Evaporation for Stable FASnI(3) Perovskite Solar Cells. ACS Nano *20*, 1159–1169. https://doi.org/10.1021/acsnano.5c16992.
95. Gil-Escrig, L., Dreessen, C., Kaya, I.C., Kim, B.-S., Palazon, F., Sessolo, M., and Bolink, H.J. (2020). Efficient Vacuum-Deposited Perovskite Solar Cells with Stable Cubic FA1–xMAxPbI3. ACS Energy Lett. *5*, 3053–3061. https://doi.org/10.1021/acsenergylett.0c01473.
96. Zhao, J., Deng, Y., Wei, H., Zheng, X., Yu, Z., Shao, Y., Shield, J.E., and Huang, J. (2017). Strained hybrid perovskite thin films and their impact on the intrinsic stability of perovskite solar cells. Sci. Adv. *3*, eaao5616.
97. Kong, W., Zhao, C., Huang, T., Li, X., Xing, J., Yu, Z., Yang, P., Li, W., and Yu, W. (2022). Accurate Adjusting the Lattice Strain of Triple-Cation and Mixed-Halide Perovskites for High-Performance Photodetector. ACS

Appl. Mater. Interfaces *14*, 28154–28162. https://doi.org/10.1021/acsami.2c02427.

98. Wang, Y., Li, J., Cao, H., Huang, T., Qian, Y., Qiu, Y., Yang, L., and Yin, S. (2022). Strain Relaxation on Perovskite Surface via Light-Enhanced Ionic Homogeneity. J. Phys. Chem. Lett. *13*, 10447–10454. https://doi.org/10.1021/acs.jpclett.2c02449.
99. Rijal, B., Alzoubi, K.M., Chen, Z., Latif Khammash, A., Lu, S., and Dhakal, T.P. (2025). Understanding the Long-Term Instability in Perovskite Solar Cells: Mechanisms and Mitigation Strategies. Electronics *14*, 4428. https://doi.org/10.3390/electronics14224428.
100. Yang, G., Zhang, J., Sun, B., Feng, W., Jiao, J., Yang, Z., Liu, X., Ning, T., Shan, Y., Li, W., et al. (2025). Tensile Strain Release by Surface Modulation with Amylamine Hydrochloride toward Improved Efficiency and Stability of Perovskite Solar Cells. ACS Appl. Mater. Interfaces *17*, 66744–66752. https://doi.org/10.1021/acsami.5c19724.
101. Kapil, G., Bessho, T., Ng, C.H., Hamada, K., Pandey, M., Kamarudin, M.A., Hirotani, D., Kinoshita, T., Minemoto, T., Shen, Q., et al. (2019). Strain Relaxation and Light Management in Tin–Lead Perovskite Solar Cells to Achieve High Efficiencies. ACS Energy Lett. *4*, 1991–1998. https://doi.org/10.1021/acsenergylett.9b01237.
102. Pandey, P., and Kang, D.-W. (2025). Vapor-Deposited Inorganic Perovskite Solar Cells from Fundamentals to Scalable Commercial Pathways. Electronics *14*, 3171. https://doi.org/10.3390/electronics14163171.
103. Abzieher, T., Moore, D.T., Roß, M., Albrecht, S., Silvia, J., Tan, H., Jeangros, Q., Ballif, C., Hoerantner, M.T., Kim, B.-S., et al. (2024). Vapor phase deposition of perovskite photovoltaics: short track to commercialization? Energy Environ. Sci. *17*, 1645–1663. https://doi.org/10.1039/d3ee03273f.
104. Li, N., Niu, X., Dong, Z., Hu, J., Luo, R., Yang, S., Zhou, Q., Shi, Z., Chen, J., Du, X., et al. (2025). Optimal perovskite vapor partitioning on textured silicon for high-stability tandem solar cells. Science *390*, eadz3698. https://doi.org/10.1126/science.adz3698.
105. Öz, S.D., and Olthof, S. (2025). Effect of Hole Extraction Layer on the Composition of Thermally Evaporated Formamidinium-Based Mixed Halide Perovskites. ACS Appl. Mater. Interfaces *17*, 24535–24546. https://doi.org/10.1021/acsami.4c21701.
106. Kralj, S., Artuk, K., Nales, M., Hnapovskyi, V., Minguez-Avellan, M., Vishal, B., Said, A.A., Boix, P.P., De Wolf, S., Wolff, C.M., and Morales-Masis, M. (2026). Rapid Laser-Based Deposition of PbI2/CsBr Inorganic Scaffolds for Hybrid Fabrication of Perovskite/Silicon Tandem Solar Cells. ACS Energy Lett. *11*, 2798–2809. https://doi.org/10.1021/acsenergylett.5c04010.
107. Chen, Y., Yang, N., Zheng, G., Pei, F., Zhou, W., Zhang, Y., Li, L., Huang, Z., Liu, G., Yin, R., et al. (2024). Nuclei engineering for even halide distribution in stable perovskite/silicon tandem solar cells. Science *385*, 554–560.
108. Sukow, C.A., and Nemanich, R.J. (1994). Morphology of TiSi2 and ZrSi2 on Si (100) and (111) surfaces. J. Mater. Res. *9*, 1214–1227.
109. Gao, F., Zhao, P., Qin, X., and Zhao, Z. (2025). Crystal facet engineering in perovskite photovoltaics: the rise of (111)-oriented structures. Front. Chem. *13*, 1692350. https://doi.org/10.3389/fchem.2025.1692350.
110. Liu, J., Shi, B., Xu, Q., Li, Y., Li, Y., Liu, P., SunLi, Z., Wang, X., Sun, C., Han, W., et al. (2024). Textured Perovskite/Silicon Tandem Solar Cells Achieving Over 30% Efficiency Promoted by 4-Fluorobenzylamine Hydroiodide. Nano-Micro Lett. *16*, 189. https://doi.org/10.1007/s40820-024-01406-4.
111. Wang, Y., Nie, Z., Guo, Q., Song, Y., and Liu, L. (2022). Adsorption Behaviors of Chlorosilanes, HCl, and H(2) on the Si(100) Surface: A First-Principles Study. ACS Omega *7*, 42105–42114. https://doi.org/10.1021/acsomega.2c04502.
112. Škorjanc, V., Miaskiewicz, A., Roß, M., Maniyarasu, S., Severin, S., Leyden, M.R., Holzhey, P., Ruske, F., Korte, L., and Albrecht, S. (2024). Seed Layers for Wide-Band Gap Coevaporated Perovskite Solar Cells: CsCl Regulates Band Gap and Reduces Process Variability. ACS Energy Lett. *9*, 5639–5646. https://doi.org/10.1021/acsenergylett.4c02173.
113. Li, Y., Shi, B., Xu, Q., Yan, L., Ren, N., Li, Y., Han, W., Zhu, Z., Zhang, Y., Liu, J., et al. (2024). CsCl induced efficient fully-textured perovskite/crystalline silicon tandem solar cell. Nano Energy *122*, 109285. https://doi.org/10.1016/j.nanoen.2024.109285.
114. Castro-Méndez, A.F., Jahanbakhshi, F., LaFollette, D.K., Lawrie, B.J., Li, R., Perini, C.A.R., Rappe, A.M., and Correa-Baena, J.P. (2024). Tailoring Interface Energies via Phosphonic Acids to Grow and Stabilize Cubic FAPbI(3) Deposited by Thermal Evaporation. J. Am. Chem. Soc. *146*, 18459–18469. https://doi.org/10.1021/jacs.4c03911.
115. Fang, Z., Deng, B., Jin, Y., Yang, L., Chen, L., Zhong, Y., Feng, H., Yin, Y., Liu, K., Li, Y., et al. (2024). Surface reconstruction of wide-bandgap perovskites enables efficient perovskite/silicon tandem solar cells. Nat. Commun. *15*, 10554. https://doi.org/10.1038/s41467-024-54925-4.
116. Susic, I., Gil-Escrig, L., Zanoni, K.P.S., Roldán-Carmona, C., Sessolo, M., and Bolink, H.J. (2023). Pure Iodide Multication Wide Bandgap Perovskites by Vacuum Deposition. ACS Mater. Lett. *5*, 3299–3305. https://doi.org/10.1021/acsmaterialslett.3c01094.
117. Zhang, T., Yang, M., Zhao, Y., and Zhu, K. (2015). Controllable Sequential Deposition of Planar CH(3)NH(3)PbI(3) Perovskite Films via Adjustable Volume Expansion. Nano Lett. *15*, 3959–3963. https://doi.org/10.1021/acs.nanolett.5b00843.
118. Kim, S.-Y., Jo, H.J., Sung, S.-J., and Kim, D.-H. (2016). Perspective: Understanding of ripening growth model for minimum residual PbI2 and its limitation in the planar perovskite solar cells. APL Mater. *4*, 100901. https://doi.org/10.1063/1.4963841.
119. Lin, D., Fang, J., Yang, X., Wang, X., Li, S., Wang, D., Xie, G., Li, H., Wang, X., and Qiu, L. (2024). Modulating the Distribution of Formamidinium Iodide by Ultrahigh Humidity Treatment Strategy for High-Quality Sequential Vapor Deposited Perovskite. Small *20*, e2307960. https://doi.org/10.1002/smll.202307960.
120. Du, T., Burgess, C.H., Kim, J., Zhang, J., Durrant, J.R., and McLachlan, M.A. (2017). Formation, location and beneficial role of PbI2 in lead halide perovskite solar cells. Sustain. Energy Fuels *1*, 119–126. https://doi.org/10.1039/c6se00029k.
121. Liu, K., Wang, Z., Qu, S., and Ding, L. (2023). Stress and Strain in Perovskite/Silicon Tandem Solar Cells. Nano-Micro Lett. *15*, 59. https://doi.org/10.1007/s40820-023-01019-3.
122. Bush, K.A., Rolston, N., Gold-Parker, A., Manzoor, S., Hausele, J., Yu, Z.J., Raiford, J.A., Cheacharoen, R., Holman, Z.C., Toney, M.F., et al. (2018). Controlling Thin-Film Stress and Wrinkling during Perovskite Film Formation. ACS Energy Lett. *3*, 1225–1232. https://doi.org/10.1021/acsenergylett.8b00544.
123. Wu, J., Liu, S.C., Li, Z., Wang, S., Xue, D.J., Lin, Y., and Hu, J.S. (2021). Strain in perovskite solar cells: origins, impacts and regulation. Natl. Sci. Rev. *8*, nwab047. https://doi.org/10.1093/nsr/nwab047.
124. Nath, B., Panchal, A., Kumar, J., Singh, B., C K, S., Rondiya, S.R., and Ramamurthy, P.C. (2025). Low-Temperature-Processed Flexible Perovskite Solar Cells: Performance Analysis and Stability Dynamics. ACS Appl. Energy Mater. *8*, 17297–17310. https://doi.org/10.1021/acsaem.5c02466.
125. Xiang, T., Zhang, Y., Wu, H., Li, J., Yang, L., Wang, K., Xia, J., Deng, Z., Xiao, J., Li, W., et al. (2020). Universal defects elimination for high performance thermally evaporated CsPbBr3 perovskite solar cells. Sol. Energy Mater. Sol. Cell. *206*, 110317. https://doi.org/10.1016/j.solmat.2019.110317.
126. Hua, J., Deng, X., Niu, C., Huang, F., Peng, Y., Li, W., Ku, Z., and Cheng, Y.-b. (2020). A pressure-assisted annealing method for high quality CsPbBr3 film deposited by sequential thermal evaporation. RSC Adv. *10*, 8905–8909. https://doi.org/10.1039/d0ra00446d.
127. Lin, H.Y., Chen, C.Y., Hsu, B.W., Cheng, Y.L., Tsai, W.L., Huang, Y.C., Tsao, C.S., and Lin, H.W. (2019). Efficient Cesium Lead Halide Perovskite

Solar Cells through Alternative Thousand-Layer Rapid Deposition. Adv. Funct. Mater. *29*, 1905163. https://doi.org/10.1002/adfm.201905163.

128. Tong, G., Chen, T., Li, H., Qiu, L., Liu, Z., Dang, Y., Song, W., Ono, L.K., Jiang, Y., and Qi, Y. (2019). Phase transition induced recrystallization and low surface potential barrier leading to 10.91%-efficient CsPbBr3 perovskite solar cells. Nano Energy *65*, 104015. https://doi.org/10.1016/j.nanoen.2019.104015.

129. Hutter, E.M., Sutton, R.J., Chandrashekar, S., Abdi-Jalebi, M., Stranks, S.D., Snaith, H.J., and Savenije, T.J. (2017). Vapour-Deposited Cesium Lead Iodide Perovskites: Microsecond Charge Carrier Lifetimes and Enhanced Photovoltaic Performance. ACS Energy Lett. *2*, 1901–1908. https://doi.org/10.1021/acsenergylett.7b00591.

130. Ma, Q., Huang, S., Wen, X., Green, M.A., and Ho-Baillie, A.W.Y. (2016). Hole Transport Layer Free Inorganic CsPbIBr2 Perovskite Solar Cell by Dual Source Thermal Evaporation. Adv. Energy Mater. *6*, 1502202. https://doi.org/10.1002/aenm.201502202.

131. Chen, C.Y., Lin, H.Y., Chiang, K.M., Tsai, W.L., Huang, Y.C., Tsao, C.S., and Lin, H.W. (2017). All-Vacuum-Deposited Stoichiometrically Balanced Inorganic Cesium Lead Halide Perovskite Solar Cells with Stabilized Efficiency Exceeding 11%. Adv. Mater. *29*. https://doi.org/10.1002/adma.201605290.

132. Igual-Muñoz, A.M., Navarro-Alapont, J., Dreessen, C., Palazon, F., Sessolo, M., and Bolink, H.J. (2020). Room-Temperature Vacuum Deposition of CsPbI2Br Perovskite Films from Multiple Sources and Mixed Halide Precursors. Chem. Mater. *32*, 8641–8652. https://doi.org/10.1021/acs.chemmater.0c03038.

133. Longo, G., Momblona, C., La-Placa, M.-G., Gil-Escrig, L., Sessolo, M., and Bolink, H.J. (2017). Fully Vacuum-Processed Wide Band Gap Mixed-Halide Perovskite Solar Cells. ACS Energy Lett. *3*, 214–219. https://doi.org/10.1021/acsenergylett.7b01217.

134. Dong, Z., Hu, J., Guo, X., Shi, Z., Chen, H., Wang, Y., Luo, R., Steele, J.A., Degnan, Z., Solano, E., et al. (2026). Intermediate phase evolution for stable and oriented evaporated wide-bandgap perovskite solar cells. Nat. Mater. *25*, 635–642. https://doi.org/10.1038/s41563-025-02375-8.

135. Gil-Escrig, L., Momblona, C., La-Placa, M.G., Boix, P.P., Sessolo, M., and Bolink, H.J. (2018). Vacuum Deposited Triple-Cation Mixed-Halide Perovskite Solar Cells. Adv. Energy Mater. *8*, 1703506. https://doi.org/10.1002/aenm.201703506.

136. Frolova, L.A., Anokhin, D.V., Piryazev, A.A., Luchkin, S.Y., Dremova, N.N., Stevenson, K.J., and Troshin, P.A. (2017). Highly Efficient All-Inorganic Planar Heterojunction Perovskite Solar Cells Produced by Thermal Coevaporation of CsI and PbI2. J. Phys. Chem. Lett. *8*, 67–72. https://doi.org/10.1021/acs.jpclett.6b02594.

137. Li, H., Zhou, J., Tan, L., Li, M., Jiang, C., Wang, S., Zhao, X., Liu, Y., Zhang, Y., Ye, Y., et al. (2022). Sequential vacuum-evaporated perovskite solar cells with more than 24% efficiency. Sci. Adv. *8*, eabo7422.

138. Feeney, T., Fassl, P., Petry, J., Laufer, F., Singh, R., Severin, S., Škorjanc, V., Miaskiewicz, A., Maniyarasu, S., Korte, L., et al. (2025). Deposition rate limitations for FA-based co-evaporated perovskites and how to overcome them. In Proceedings of the International Conference on Perovskite Thin Film Photovoltaics and Perovskite Photonics and Optoelectronics.

139. Gordillo, G., Pena, J., Otalora, C., and Torres, O. (2021). Inorganic perovskite solar cells based on CsPbBr3 films grown by different thermal evaporation routes. J. Eng. Sci. Technol. *16*, 3234–3249.

140. Li, X., Tan, Y., Lai, H., Li, S., Chen, Y., Li, S., Xu, P., and Yang, J. (2019). All-Inorganic CsPbBr3 Perovskite Solar Cells with 10.45% Efficiency by Evaporation-Assisted Deposition and Setting Intermediate Energy Levels. ACS Appl. Mater. Interfaces *11*, 29746–29752. https://doi.org/10.1021/acsami.9b06356.

141. Liu, X., Li, J., Liu, Z., Tan, X., Sun, B., Xi, S., Shi, T., Tang, Z., and Liao, G. (2020). Vapor-assisted deposition of CsPbIBr2 films for highly efficient and stable carbon-based planar perovskite solar cells with superior Voc. Electrochim. Acta *330*, 135266. https://doi.org/10.1016/j.electacta.2019.135266.

142. Zhou, Y.-P., Wang, L.-X., Hui, S.-C., Song, L., Ran, C., Wu, Z., and Huang, W. (2025). Controlled Nucleation and Targeted Interface Modification in Wide-Bandgap Perovskite Solar Cells Based on Evaporation/Solution Two-Step Deposition. ACS Nano *19*, 15820–15830. https://doi.org/10.1021/acsnano.5c00458.

143. Shi, B., Liu, P., Sunli, Z., Han, W., Sun, C., Liu, Y., Luo, Y., Si, J., Du, P., Zhang, F., et al. (2025). Halogen anion pre-homogenization of sequentially deposited wide bandgap perovskites for commercial textured perovskite/silicon tandem solar cells. Energy Environ. Sci. *18*, 6297–6306. https://doi.org/10.1039/d5ee00563a.

144. Zhang, Z., Liu, Z., Zhi, M., Zhao, J., Lian, J., Yu, Z., Guo, Y., Liang, X., and Li, Z. (2025). Insights into the hybrid evaporation-spin coating method: process optimization and consequences for wide band gap perovskite solar cells. J. Mater. Chem. A Mater. *13*, 20697–20705. https://doi.org/10.1039/d5ta02535d.

145. Guesnay, Q., McMonagle, C.J., Chernyshov, D., Zia, W., Wieczorek, A., Siol, S., Saliba, M., Ballif, C., and Wolff, C.M. (2023). Substoichiometric Mixing of Metal Halide Powders and Their Single-Source Evaporation for Perovskite Photovoltaics. ACS Photonics *10*, 3087–3094. https://doi.org/10.1021/acsphotonics.3c00438.

146. Afshord, A.Z., Uzuner, B.E., Soltanpoor, W., Sedani, S.H., Aernouts, T., Gunbas, G., Kuang, Y., and Yerci, S. (2023). Efficient and Stable Inverted Wide-Bandgap Perovskite Solar Cells and Modules Enabled by Hybrid Evaporation-Solution Method. Adv. Funct. Mater. *33*, 2301695. https://doi.org/10.1002/adfm.202301695.

147. Dewi, H.A., Li, J., Erdenebileg, E., Wang, H., De Bastiani, M., De Wolf, S., Mathews, N., Mhaisalkar, S., and Bruno, A. (2022). Efficient bandgap widening in co-evaporated MAPbI3 perovskite. Sustain. Energy Fuels *6*, 2428–2438. https://doi.org/10.1039/d1se01692j.

148. Er-raji, O., Bett, A.J., Lange, S., Nagel, H., Bivour, M., Schultz-Wittmann, O., Hagendorf, C., Hermle, M., Borchert, J., Glunz, S.W., and Schulze, P.S.C. (2023). Toward efficient and industrially compatible fully textured perovskite silicon tandem solar cells: Controlled process parameters for reliable perovskite formation. Prog. Photovoltaics Res. Appl. *33*, 86–99. https://doi.org/10.1002/pip.3770.

149. Li, Y., Shi, B., Xu, Q., Yan, L., Ren, N., Chen, Y., Han, W., Huang, Q., Zhao, Y., and Zhang, X. (2021). Wide Bandgap Interface Layer Induced Stabilized Perovskite/Silicon Tandem Solar Cells with Stability over Ten Thousand Hours. Adv. Energy Mater. *11*, 2102046. https://doi.org/10.1002/aenm.202102046.

150. Er-raji, O., Said, A.A., Subbiah, A.S., Hnapovskyi, V., Vishal, B., Pininti, A.R., Marengo, M., Bivour, M., Kohlstädt, M., Borchert, J., et al. (2025). Coating dynamics in two-step hybrid evaporated/blade-coated perovskites for scalable fully-textured perovskite/silicon tandem solar cells. EES Solar *1*, 419–430. https://doi.org/10.1039/d5el00073d.

151. Luo, H., Zheng, X., Kong, W., Liu, Z., Li, H., Wen, J., Xia, R., Sun, H., Wu, P., Wang, Y., et al. (2023). Inorganic Framework Composition Engineering for Scalable Fabrication of Perovskite/Silicon Tandem Solar Cells. ACS Energy Lett. *8*, 4993–5002. https://doi.org/10.1021/acsenergylett.3c02002.

152. Zhang, Y., Geng, C., Zheng, C., Zheng, H., Zhao, X., Zhu, M., Peng, Y., and Cheng, Y.-B. (2025). Additive passivation strategies to improve properties of evaporation-spray coating perovskite solar cells. Sustain. Energy Fuels *9*, 2670–2677. https://doi.org/10.1039/d5se00143a.

153. Nguyen, V.S., Zimmermann, I., Grépin, E., Medjoubi, K., Jutteau, S., Donsanti, F., Bruhat, E., Duchatelet, A., Berson, S., and Rousset, J. (2023). Solvent-vapor assisted conversion process for hybrid perovskites coupling thermal evaporation and slot-die coating. Mater. Sci. Semicond. Process. *158*, 107358. https://doi.org/10.1016/j.mssp.2023.107358.

154. Pesch, R., Petry, J., Petermann, J., Pappenberger, R., Kuechle, T., Schenck, J., Rothbauer, L.P., Fang, L., Liu, X., Rafizadeh, S., et al.

(2025). Efficient Perovskite/Silicon Tandem Solar Cells Using Hybrid Two-Step Inkjet Printing with Edge Isolation Precision. Small Sci. *5*, 2500362. https://doi.org/10.1002/smsc.202500362.

155. Chen, X., Geng, C., Yu, X., Feng, Y., Liang, C., Peng, Y., and Cheng, Y.-b. (2023). Additive engineering in spray enables efficient methylammonium-free wide-bandgap perovskite solar cells. Mater. Today Energy *34*, 101316. https://doi.org/10.1016/j.mtener.2023.101316.

156. Li, H., Zhang, Z., Wei, Y., An, B., Liao, J., Lv, X., Lv, W., Yang, J., Li, H., Zeng, C., et al. (2025). Nucleation Modification in Two-Step Slot-Die Coating Toward Efficient Large Scale Perovskite/Silicon Tandems Based on Commercial Silicon Cells. Adv. Mater. *37*, e2501961. https://doi.org/10.1002/adma.202501961.

157. Xu, X., Li, M., Xie, Y.M., Ma, Y., Ma, C., Cheng, Y., Lee, C.S., and Tsang, S.W. (2019). Porous and Intercrossed PbI(2)-CsI Nanorod Scaffold for Inverted Planar FA-Cs Mixed-Cation Perovskite Solar Cells. ACS Appl. Mater. Interfaces *11*, 6126–6135. https://doi.org/10.1021/acsami.8b20933.

158. Huang, N., and Qiu, L. (2025). Toward stable wide-bandgap perovskite solar cells: Comprehensive review of degradation mechanisms and mitigation strategies. Mater. Today Energy *53*, 102010. https://doi.org/10.1016/j.mtener.2025.102010.

159. Sutter-Fella, C.M., Li, Y., Amani, M., Ager, J.W., Toma, F.M., Yablonovitch, E., Sharp, I.D., and Javey, A. (2016). High Photoluminescence Quantum Yield in Band Gap Tunable Bromide Containing Mixed Halide Perovskites. Nano Lett. *16*, 800–806. https://doi.org/10.1021/acs.nanolett.5b04884.

160. Zhou, H., Chen, Q., and Yang, Y. (2015). Vapor-assisted solution process for perovskite materials and solar cells. MRS Bull. *40*, 667–673. https://doi.org/10.1557/mrs.2015.171.

161. Kim, S., Kim, T., Lee, J., Cho, S.H., Kim, T.E., and Lee, Y.S. (2026). Vacuum-Controlled Solvent Evaporation for Morphological Engineering of Wide-Bandgap Perovskite Films. ACS Appl. Mater. Interfaces *18*, 3863–3871. https://doi.org/10.1021/acsami.5c21734.

162. Er-raji, O., Rustam, L., Kore, B.P., Glunz, S.W., and Schulze, P.S.C. (2023). Insights into Perovskite Film Formation Using the Hybrid Evaporation/Spin-Coating Route: An In Situ XRD Study. ACS Appl. Energy Mater. *6*, 6183–6193. https://doi.org/10.1021/acsaem.3c00698.

163. Pesch, R., Diercks, A., Petry, J., Welle, A., Pappenberger, R., Schackmar, F., Eggers, H., Sutter, J., Lemmer, U., and Paetzold, U.W. (2024). Hybrid Two-Step Inkjet-Printed Perovskite Solar Cells. Sol. RRL *8*, 2400165. https://doi.org/10.1002/solr.202400165.

164. Fan, Y., Qin, Z., Lu, L., Zhang, N., Liang, Y., Wang, S., Zhan, W., Guo, J., Wang, H., Chen, Y., et al. (2025). An efficient and precise solution-vacuum hybrid batch fabrication of 2D/3D perovskite submodules. Nat. Commun. *16*, 7019. https://doi.org/10.1038/s41467-025-62392-8.

165. Longo, G., Gil-Escrig, L., Degen, M.J., Sessolo, M., and Bolink, H.J. (2015). Perovskite solar cells prepared by flash evaporation. Chem. Commun. *51*, 7376–7378. https://doi.org/10.1039/c5cc01103e.

166. Abzieher, T., Muzzillo, C.P., Mirzokarimov, M., Lahti, G., Kau, W.F., Kroupa, D.M., Cira, S.G., Hillhouse, H.W., Kirmani, A.R., Schall, J., et al. (2024). Continuous flash sublimation of inorganic halide perovskites: overcoming rate and continuity limitations of vapor deposition. J. Mater. Chem. A Mater. *12*, 8405–8419. https://doi.org/10.1039/d3ta05881f.

167. Leyden, M.R., Ono, L.K., Raga, S.R., Kato, Y., Wang, S., and Qi, Y. (2014). High performance perovskite solar cells by hybrid chemical vapor deposition. J. Mater. Chem. A *2*, 18742–18745. https://doi.org/10.1039/c4ta04385e.

168. Tavakoli, M.M., Gu, L., Gao, Y., Reckmeier, C., He, J., Rogach, A.L., Yao, Y., and Fan, Z. (2015). Fabrication of efficient planar perovskite solar cells using a one-step chemical vapor deposition method. Sci. Rep. *5*, 14083. https://doi.org/10.1038/srep14083.

169. Qiu, L., He, S., Jiang, Y., Son, D.-Y., Ono, L.K., Liu, Z., Kim, T., Bouloumis, T., Kazaoui, S., and Qi, Y. (2019). Hybrid chemical vapor deposition enables scalable and stable Cs-FA mixed cation perovskite solar modules with a designated area of 91.8 cm 2 approaching 10% efficiency. J. Mater. Chem. A Mater. *7*, 6920–6929.

170. Ke, C.-R., Lewis, D.J., Walton, A.S., Chen, Q., Spencer, B.F., Mokhtar, M.Z., Compean-Gonzalez, C.L., O'Brien, P., Thomas, A.G., and Flavell, W.R. (2019). Air-Stable Methylammonium Lead Iodide Perovskite Thin Films Fabricated via Aerosol-Assisted Chemical Vapor Deposition from a Pseudohalide Pb(SCN)2 Precursor. ACS Appl. Energy Mater. *2*, 6012–6022. https://doi.org/10.1021/acsaem.9b01124.

171. Guo, Q., Li, C., Qiao, W., Ma, S., Wang, F., Zhang, B., Hu, L., Dai, S., and Tan, Z. (2016). The growth of a CH3NH3PbI3thin film using simplified close space sublimation for efficient and large dimensional perovskite solar cells. Energy Environ. Sci. *9*, 1486–1494. https://doi.org/10.1039/c5ee03620h.

172. Liu, J., Zhang, M., Sun, X., Xiang, L., Yang, X., Hu, X., Wang, Z., Hou, T., Qin, J., Huang, Y., et al. (2025). Scalable fFabrication of methylammonium-free wide-bandgap perovskite solar cells by blade coating in ambient air. Nanomicro Lett *17*, 318. https://doi.org/10.1007/s40820-025-01838-6.

173. Mali, S.S., Patil, J.V., and Hong, C.K. (2019). Hot-Air-Assisted Fully Air-Processed Barium Incorporated CsPbI(2)Br Perovskite Thin Films for Highly Efficient and Stable All-Inorganic Perovskite Solar Cells. Nano Lett. *19*, 6213–6220. https://doi.org/10.1021/acs.nanolett.9b02277.

174. Leyden, M.R., Jiang, Y., and Qi, Y. (2016). Chemical vapor deposition grown formamidinium perovskite solar modules with high steady state power and thermal stability. J. Mater. Chem. A Mater. *4*, 13125–13132.

175. Qiu, L., He, S., Liu, Z., Ono, L.K., Son, D.-Y., Liu, Y., Tong, G., and Qi, Y. (2020). Rapid hybrid chemical vapor deposition for efficient and hysteresis-free perovskite solar modules with an operation lifetime exceeding 800 hours. J. Mater. Chem. A Mater. *8*, 23404–23412. https://doi.org/10.1039/d0ta09007g.

176. Kim, J. (2024). Parametric dependence of CsPbI2Br perovskite film growth using a mist chemical vapor deposition method. Curr. Appl. Phys. *60*, 1–8. https://doi.org/10.1016/j.cap.2024.01.005.

177. Zhang, G., Luo, W., Dai, H., Li, N., Li, Y., Peng, Y., Huang, F., Ku, Z., and Cheng, Y.-B. (2022). Ultrafast Growth of High-Quality Cs0.14FA0.86Pb(BrxI1–x)3 Thin Films Achieved Using Super-Close-Space Sublimation. ACS Appl. Energy Mater. *5*, 5797–5803. https://doi.org/10.1021/acsaem.2c00132.

178. Gomar-Fernández, I., Gil-Escrig, L., Rodkey, N., Ventosinos, F., Senno, M., Roldán-Carmona, C., Held, V., Sessolo, M., and Bolink, H.J. (2025). Large-area close-space sublimation enables the fabrication of efficient and stable perovskite solar cells. EES Solar *1*, 1126–1134. https://doi.org/10.1039/d5el00145e.

179. Ihrenberger, J., Roux, F., Lédée, F., Emieux, F., Anglade, C., Lemercier, T., Lorin, G., Gros-Daillon, E., and Grenet, L. (2024). Solution-Free Growth of CsPbBr3 Perovskite Films Using a Fast and Scalable Close Space Sublimation Method. Cryst. Growth Des. *24*, 5542–5548. https://doi.org/10.1021/acs.cgd.4c00249.

180. Lee, S.W., Bae, S., Hwang, J.K., Lee, W., Lee, S., Hyun, J.Y., Cho, K., Kim, S., Heinz, F.D., Bin Choi, S., et al. (2020). Perovskites fabricated on textured silicon surfaces for tandem solar cells. Commun. Chem. *3*, 37. https://doi.org/10.1038/s42004-020-0283-4.

181. Du, T., Macdonald, T.J., Yang, R.X., Li, M., Jiang, Z., Mohan, L., Xu, W., Su, Z., Gao, X., Whiteley, R., et al. (2022). Additive-Free, Low-Temperature Crystallization of Stable alpha-FAPbI(3) Perovskite. Adv. Mater. *34*, e2107850. https://doi.org/10.1002/adma.202107850.

182. Susic, I., Kama, A., Gil-Escrig, L., Dreessen, C., Palazon, F., Cahen, D., Sessolo, M., and Bolink, H.J. (2022). Combinatorial Vacuum-Deposition of Wide Bandgap Perovskite Films and Solar Cells. Adv. Mater. Interfac. *10*, 2202271. https://doi.org/10.1002/admi.202202271.

183. Lu, Y., Jung, Y.-K., Dubajic, M., Li, X., Maqbool, S., Gu, Q., Bai, X., Boeije, Y., Chua, X.W., Mirabelli, A.J., et al. (2025). Layer-by-layer epitaxial growth of perovskite heterostructures with tunable band offsets. Science *390*, 716–721.

184. Soto-Montero, T., and Morales-Masis, M. (2024). Laser Deposition of Metal Halide Perovskites. ACS Energy Lett. *9*, 4199–4208. https://doi.org/10.1021/acsenergylett.4c01466.

185. Mahboubi Soufiani, A., Moumine, H., Wutke, E., Farias Basulto, G.A., de Araujo, W.M.B., Leyden, M., Szot, M., Bertram, T., Škorjanc, V., Harter, A., et al. (2025). Sequentially Evaporated Wide Bandgap Perovskite Absorber for Large-Area and Reproducible Fabrication of Solar Cells. Sol. RRL *9*, 2500412. https://doi.org/10.1002/solr.202500412.

186. Wang, Y., Sun, X., Chen, Z., Sun, Y.Y., Zhang, S., Lu, T.M., Wertz, E., and Shi, J. (2017). High-Temperature Ionic Epitaxy of Halide Perovskite Thin Film and the Hidden Carrier Dynamics. Adv. Mater. *29*, 1702643. https://doi.org/10.1002/adma.201702643.

187. Sun, H., van de Ven, L.M., Duncan, B., Stein, E., Methorst, D., Mohammadi, M., Rigter, S.A., Schall, P., and Garnett, E.C. (2025). Contact Transfer Epitaxy of Halide Perovskites. Adv. Mater. *37*, e2308892. https://doi.org/10.1002/adma.202308892.

188. Soto-Montero, T., Kralj, S., Azmi, R., Reus, M.A., Solomon, J.S., Cunha, D.M., Soltanpoor, W., Utomo, D.S., Ugur, E., Vishal, B., et al. (2024). Single-source pulsed laser-deposited perovskite solar cells with enhanced performance via bulk and 2D passivation. Joule *8*, 3412–3425. https://doi.org/10.1016/j.joule.2024.09.001.

189. Kliner, V., Soto-Montero, T., Nespoli, J., Savenije, T.J., Ledinský, M., and Morales-Masis, M. (2025). Pulsed Laser Deposition of Halide Perovskites with over 10-Fold Enhanced Deposition Rates. J. Phys. Chem. Lett. *16*, 1453–1460. https://doi.org/10.1021/acs.jpclett.5c00047.

190. Chuang, T.H., Chen, Y.H., Sakalley, S., Cheng, W.C., Chan, C.K., Chen, C.P., and Chen, S.C. (2023). Highly Stable and Enhanced Performance of p-i-n Perovskite Solar Cells via Cuprous Oxide Hole-Transport Layers. Nanomaterials *13*, 1363. https://doi.org/10.3390/nano13081363.

191. Petry, J., Škorjanc, V., Diercks, A., Feeney, T., Morsa, A., Kimmig, S.R., Baumann, J., Löffler, F., Auschill, S., Damm, J., et al. (2025). Industrialization of perovskite solar cell fabrication: strategies to achieve high-throughput vapor deposition processes. EES Solar *1*, 404–418. https://doi.org/10.1039/d5el00069f.

192. Sanders, S., Stümmler, D., Gerber, J.D., Seidel, J.H., Simkus, G., Heuken, M., Vescan, A., and Kalisch, H. (2020). Showerhead-assisted chemical vapor deposition of Perovskite films for solar cell application. MRS Adv. 5, 385–393.

193. Sahli, F., Miaz, N., Salsi, N., Bucher, C., Schafflützel, A., Guesnay, Q., Duchêne, L., Niesen, B., Ballif, C., and Jeangros, Q. (2021). Vapor Transport Deposition of Methylammonium Iodide for Perovskite Solar Cells. ACS Appl. Energy Mater. *4*, 4333–4343. https://doi.org/10.1021/acsaem.0c02999.

194. Werner, J., Nogay, G., Sahli, F., Yang, T.C.-J., Bräuninger, M., Christmann, G., Walter, A., Kamino, B.A., Fiala, P., Löper, P., et al. (2018). Complex Refractive Indices of Cesium–Formamidinium-Based Mixed-Halide Perovskites with Optical Band Gaps from 1.5 to 1.8 eV. ACS Energy Lett. *3*, 742–747. https://doi.org/10.1021/acsenergylett.8b00089.

195. Wang, X., Gong, J., Shan, X., Zhang, M., Xu, Z., Dai, R., Wang, Z., Wang, S., Fang, X., and Zhang, Z. (2018). In Situ Monitoring of Thermal Degradation of CH3NH3PbI3 Films by Spectroscopic Ellipsometry. J. Phys. Chem. C *123*, 1362–1369. https://doi.org/10.1021/acs.jpcc.8b12275.

196. Ermolaev, G., Pushkarev, A.P., Zhizhchenko, A., Kuchmizhak, A.A., Iorsh, I., Kruglov, I., Mazitov, A., Ishteev, A., Konstantinova, K., Saranin, D., et al. (2023). Giant and Tunable Excitonic Optical Anisotropy in Single-Crystal Halide Perovskites. Nano Lett. *23*, 2570–2577. https://doi.org/10.1021/acs.nanolett.2c04792.

197. Roß, M., Severin, S., Hildebrandt, J., Erdmann, K., Miaskiewicz, A., Škorjanc, V., Bernardes de Araujo, W.M., Leyden, M., Korte, L., Seeger, S., et al. (2026). Compositional Analysis of Metal Halide Perovskites: Insight into the Coevaporation Process via Nuclear Magnetic Resonance and X-ray Fluorescence Spectroscopy. ACS Energy Lett. *11*, 1935–1943. https://doi.org/10.1021/acsenergylett.5c03689.

198. Kim, B.S., Gil-Escrig, L., Sessolo, M., and Bolink, H.J. (2020). Deposition Kinetics and Compositional Control of Vacuum-Processed CH(3)NH(3)PbI(3) Perovskite. J. Phys. Chem. Lett. *11*, 6852–6859. https://doi.org/10.1021/acs.jpclett.0c01995.

199. Choi, Y., Ma, H., Jung, S., Jang, Y., Kim, Y., Kim, J., Jeong, M., Lee, S., Yang, S., Hong, K.K., et al. (2025). Scalable All-Vacuum-Processed Perovskite Solar Cells Enabled by Low Energy-Disorder Hole-Transport Layer. Adv. Energy Mater. *15*, 2404797. https://doi.org/10.1002/aenm.202404797.

200. Diercks, A., Petry, J., Feeney, T., Singh, R., Zhao, T., Hu, H., Li, Y., Paetzold, U.W., and Fassl, P. (2025). Sequential Evaporation of Inverted FAPbI3 Perovskite Solar Cells – Impact of Substrate on Crystallization and Film Formation. ACS Energy Lett. *10*, 1165–1173. https://doi.org/10.1021/acsenergylett.4c03315.

201. Yan, J., Stickel, L.S., van den Hengel, L., Wang, H., Anusuyadevi, P.R., Kooijman, A., Liu, X., Ibrahim, B., Mol, A., Taheri, P., et al. (2023). Vacuum Deposited Perovskites with a Controllable Crystal Orientation. J. Phys. Chem. Lett. *14*, 8787–8795. https://doi.org/10.1021/acs.jpclett.3c01920.

202. Roß, M., Severin, S., Stutz, M.B., Wagner, P., Köbler, H., Favin-Lévêque, M., Al-Ashouri, A., Korb, P., Tockhorn, P., Abate, A., et al. (2021). Co-Evaporated Formamidinium Lead Iodide Based Perovskites with 1000 h Constant Stability for Fully Textured Monolithic Perovskite/Silicon Tandem Solar Cells. Adv. Energy Mater. *11*, 2101460. https://doi.org/10.1002/aenm.202101460.

203. Han, H., Yun, S., Irshad, Z., Lee, W., Kim, M., Lim, J., and Kim, J. (2025). Vacuum Processability of Self-Assembled Monolayers and Their Chemical Interaction with Perovskite Interfaces. Energies *18*, 1782. https://doi.org/10.3390/en18071782.

204. Gil-Escrig, L., Susic, I., Doğan, İ., Zardetto, V., Najafi, M., Zhang, D., Veenstra, S., Sedani, S., Arikan, B., Yerci, S., et al. (2023). Efficient and Thermally Stable Wide Bandgap Perovskite Solar Cells by Dual-Source Vacuum Deposition. Adv. Funct. Mater. *33*, 2214357. https://doi.org/10.1002/adfm.202214357.

205. Li, H., Tan, L., Jiang, C., Li, M., Zhou, J., Ye, Y., Liu, Y., and Yi, C. (2022). Molten Salt Strategy for Reproducible Evaporation of Efficient Perovskite Solar Cells. Adv. Funct. Mater. *33*, 2211232. https://doi.org/10.1002/adfm.202211232.

206. Xu, Q., Shi, B., Li, Y., Liu, J., Li, Y., SunLi, Z., Liu, P., Zhang, Y., Sun, C., Han, W., et al. (2024). Diffusible Capping Layer Enabled Homogeneous Crystallization and Component Distribution of Hybrid Sequential Deposited Perovskite. Adv. Mater. *36*, e2308692. https://doi.org/10.1002/adma.202308692.

207. Xu, Y.Y., Jiang, Y., Du, H.Q., Gao, X., Qiang, Z.Y., Wang, C.X., Tao, Z.W., Yang, L.H., Zhi, R., Liang, G.J., et al. (2023). Octahedral Tilt Enables Efficient and Stable Fully Vapor-Deposited Perovskite/Silicon Tandem Cells. Adv. Funct. Mater. *34*, 2312037. https://doi.org/10.1002/adfm.202312037.

208. Dong, C., Liu, D., Zhang, A., Yang, X., Song, H., Hu, L., Li, X., Xu, L., Wang, L., Chen, C., and Tang, J. (2024). Co-evaporated oriented DMA1-Cs PbI3 perovskite films for photovoltaics. Nano Energy *120*, 109159. https://doi.org/10.1016/j.nanoen.2023.109159.

209. Wang, Y.-D., Jia, Z., Liu, S., Luo, R., Zhang, Y., Steele, J.A., Degnan, Z., Bilal Faheem, M., Solano, E., Qiao, Q., et al. (2025). Regulating wide-bandgap perovskite face-on stacking in hybrid-deposited perovskite/organic tandem solar cells. Nat. Commun. *16*, 6142. https://doi.org/10.1038/s41467-025-61404-x.

210. Liu, Y., Yang, J., Luo, Q., He, M., Zhang, C., Liu, C., Yang, H., Wu, S., and Mai, Y. (2023). Vacuum co-evaporated wide-bandgap perovskite films for highly-efficient indoor photovoltaic cells and modules. Surf. Interfaces *36*, 102648. https://doi.org/10.1016/j.surfin.2023.102648.

211. Zhang, Z., Ji, R., Kroll, M., Hofstetter, Y.J., Jia, X., Becker-Koch, D., Paulus, F., Löffler, M., Nehm, F., Leo, K., and Vaynzof, Y. (2021). Efficient Thermally Evaporated γ-CsPbI3 Perovskite Solar Cells. Adv. Energy Mater. *11*, 2100299. https://doi.org/10.1002/aenm.202100299.

212. Zhang, Z., Ji, R., Jia, X., Wang, S.J., Deconinck, M., Siliavka, E., and Vaynzof, Y. (2023). Semitransparent Perovskite Solar Cells with an Evaporated Ultra-Thin Perovskite Absorber. Adv. Funct. Mater. *34*, 2307471. https://doi.org/10.1002/adfm.202307471.

213. Susic, I., Gil-Escrig, L., Palazon, F., Sessolo, M., and Bolink, H.J. (2022). Quadruple-Cation Wide-Bandgap Perovskite Solar Cells with Enhanced Thermal Stability Enabled by Vacuum Deposition. ACS Energy Lett. *7*, 1355–1363. https://doi.org/10.1021/acsenergylett.2c00304.

214. Wu, J., Ying, Z., Li, X., Zhang, M., Guo, X., Liu, L., Sun, Y., Ma, H., Yu, Y., He, Z., et al. (2025). Surface Sulfuration of Atomic Layer Deposited Snox for Enhanced Performance of n–i–P Perovskite Solar Cells. Sol. RRL *9*, 2400879. https://doi.org/10.1002/solr.202400879.

215. Chiang, Y.H., Frohna, K., Salway, H., Abfalterer, A., Pan, L., Roose, B., Anaya, M., and Stranks, S.D. (2023). Vacuum-Deposited Wide-Bandgap Perovskite for All-Perovskite Tandem Solar Cells. ACS Energy Lett. *8*, 2728–2737. https://doi.org/10.1021/acsenergylett.3c00564.

216. Wang, Y., Gao, Y., Liu, P., Jia, C., Si, J., Wen, J., Sunli, Z., Du, X., Zhao, Y., Zhang, X., and Shi, B. (2025). Scalable Passivation of Perovskite Solar Cells Using Evaporated CsPbCl3. Sol. RRL *9*, 2500042. https://doi.org/10.1002/solr.202500042.

217. Ji, X., Ding, Y., Bi, L., Yang, X., Wang, J., Wang, X., Liu, Y., Yan, Y., Zhu, X., Huang, J., et al. (2024). Multifunctional Buffer Layer Engineering for Efficient and Stable Wide-Bandgap Perovskite and Perovskite/Silicon Tandem Solar Cells. Angew. Chem. Int. Ed. Engl. *63*, e202407766. https://doi.org/10.1002/anie.202407766.

218. Liu, R., Lan, C., Zeng, M., Zheng, Z., Zheng, X., Guo, R., Guo, J., Yang, S., Wang, Z., and Li, X. (2025). Precisely Tuning 3D/Quasi-2D Perovskite Heterojunctions in Wide-Bandgap Perovskites for High-Performance Tandem Solar Cells. Adv. Mater. *37*, e2504321. https://doi.org/10.1002/adma.202504321.

219. Lin, R., Wang, Y., Lu, Q., Tang, B., Li, J., Gao, H., Gao, Y., Li, H., Ding, C., Wen, J., et al. (2023). All-perovskite tandem solar cells with 3D/3D bilayer perovskite heterojunction. Nature *620*, 994–1000. https://doi.org/10.1038/s41586-023-06278-z.

220. Ma, L., Guo, D., Li, M., Wang, C., Zhou, Z., Zhao, X., Zhang, F., Ao, Z., and Nie, Z. (2019). Temperature-Dependent Thermal Decomposition Pathway of Organic–Inorganic Halide Perovskite Materials. Chem. Mater. *31*, 8515–8522. https://doi.org/10.1021/acs.chemmater.9b03190.

221. Guesnay, Q., Sahli, F., Ballif, C., and Jeangros, Q. (2021). Vapor deposition of metal halide perovskite thin films: Process control strategies to shape layer properties. APL Mater. *9*, 100703. https://doi.org/10.1063/5.0060642.

222. Piot, M., Gil-Escrig, L., Ventosinos, F., Roldán-Carmona, C., Robinson, A., Schmidt, J.A., Sessolo, M., and Bolink, H.J. (2025). Vacuum Deposition of Triple-Halide Wide-Bandgap Perovskites Enabled by Sublimation of Mixed Organic-Halide Pellets. ACS Mater. Lett. *7*, 3692–3698. https://doi.org/10.1021/acsmaterialslett.5c01161.

223. Ren, Z., Tuo, B., Wang, N., Ma, J., Li, P., Zhang, Y., and Song, Y. (2024). Advances in Intermediates for the Solution-Processing of Perovskite Films. CCS Chem. *6*, 585–603. https://doi.org/10.31635/ccschem.023.202302989.

224. Held, V., Mrkyvkova, N., Halahovets, Y., Nádaždy, P., Vegso, K., Vlk, A., Ledinský, M., Jergel, M., Bernstorff, S., Keckes, J., et al. (2024). Evolution of Defects, Morphology, and Strain during FAMAPbI(3) Perovskite Vacuum Deposition: Insights from In Situ Photoluminescence and X-ray Scattering. ACS Appl. Mater. Interfaces *16*, 35723–35731. https://doi.org/10.1021/acsami.4c04095.

225. Ahmad, B., Limon, M.S.R., and Ahmad, Z. (2024). Modulation of point defect properties near surfaces in metal halide perovskites. Phys. Rev. Mater. *8*, 125402. https://doi.org/10.1103/PhysRevMaterials.8.125402.

226. Mariyappan, T., Dewi, H.A., Chakar, J., Puel, J.-B., De Luca, D., Ahmad, R., Tang, Y., Degani, M., Grancini, G., Bonnassieux, Y., et al. (2025). Enhancing Wide-Bandgap Perovskite Solar Cells with Synergistic Surface and Bulk Passivation. ACS Energy Lett. *10*, 5304–5313. https://doi.org/10.1021/acsenergylett.5c02406.

227. Wang, J., Bi, L., Fu, Q., and Jen, A.K.Y. (2024). Methods for Passivating Defects of Perovskite for Inverted Perovskite Solar Cells and Modules. Adv. Energy Mater. *14*, 2401414. https://doi.org/10.1002/aenm.202401414.

228. Wu, X., Jin, X., Yang, Y., Huang, Z., Niu, X., Zhang, Y., Tang, Z., Zhu, S., Han, M., Xiao, Y., et al. (2023). Insight into the Defect Chemistry and Ion Migration in Perovskite Fabricated by Hybrid Chemical Vapor Deposition. ACS Appl. Energy Mater. *6*, 12198–12205. https://doi.org/10.1021/acsaem.3c01705.

229. Zhang, Y., Wang, Y., Zhao, L., Yang, X., Hou, C.-H., Wu, J., Su, R., Jia, S., Shyue, J.-J., Luo, D., et al. (2021). Depth-dependent defect manipulation in perovskites for high-performance solar cells. Energy Environ. Sci. *14*, 6526–6535. https://doi.org/10.1039/d1ee02287c.

230. Jo, B., Zhu, J., Han, G.S., Vu, T.K.O., Mularso, K.T., Ahn, T.K., Kim, E.K., and Jung, H.S. (2026). Ionic Defect Analysis and Suppression for Highly Efficient and Stable Perovskite Solar Cells and Mini-Modules. ACS Appl. Mater. Interfaces *18*, 1434–1444. https://doi.org/10.1021/acsami.5c19582.

231. Yang, Y., Chen, H., Liu, C., Xu, J., Huang, C., Malliakas, C.D., Wan, H., Bati, A.S.R., Wang, Z., Reynolds, R.P., et al. (2024). Amidination of ligands for chemical and field-effect passivation stabilizes perovskite solar cells. Science *386*, 898–902.

232. Tumen-Ulzii, G., Auffray, M., Klotz, D., Harrington, G.F., Chen, X.-K., Balijapalli, U., Vediyappan, V., Nakamura, N., Feng, Z., Takekuma, K., et al. (2022). Defect Passivation by Pyridine-Carbazole Molecules for Efficient and Stable Perovskite Solar Cells. ACS Appl. Energy Mater. *5*, 15819–15827. https://doi.org/10.1021/acsaem.2c03364.

233. Long, Y., Wang, G., Xiao, L., Xu, H., Li, W., Jiang, Z., Li, Z., Wang, C., Zhang, Z., and Li, C. (2026). Enhanced Efficiency and Moisture Stability of Dopant-Free P3HT Perovskite Solar Cells via a Tricarboxytriphenylamine Molecular Lock. ACS Appl. Mater. Interfaces *18*, 18475–18484. https://doi.org/10.1021/acsami.5c25402.

234. Lohmann, K.B., Motti, S.G., Oliver, R.D.J., Ramadan, A.J., Sansom, H.C., Yuan, Q., Elmestekawy, K.A., Patel, J.B., Ball, J.M., Herz, L.M., et al. (2022). Solvent-Free Method for Defect Reduction and Improved Performance of p-i-n Vapor-Deposited Perovskite Solar Cells. ACS Energy Lett. *7*, 1903–1911. https://doi.org/10.1021/acsenergylett.2c00865.

235. Li, M., Peng, Z., Yao, X., Huang, J., and Zhang, D. (2025). Study on the Passivation of Defect States in Wide-Bandgap Perovskite Solar Cells by the Dual Addition of KSCN and KCl. Nanomaterials *15*, 1602. https://doi.org/10.3390/nano15201602.

236. Feng, X., Li, X., Li, Z., Xue, Y., Chen, X., Sun, X., Tang, J., Liu, S., Wang, Z., Xie, Y., et al. (2025). Dual Field Passivation Strategy for High-Performance Wide-Bandgap Perovskite Solar Cells. ACS Appl. Mater. Interfaces *17*, 25883–25893. https://doi.org/10.1021/acsami.4c20406.

237. Dou, Y., Geng, C., Duan, C., Hu, S., Deng, X., Chen, Y., Kong, A., Peng, Y., Qiang, Z., and Ku, Z. (2025). A vapor-assisted annealing strategy towards high-quality perovskite absorbers enabling efficient wide bandgap perovskite solar cells. Nano Energy *139*, 110914. https://doi.org/10.1016/j.nanoen.2025.110914.

238. Wu, L., Zhang, J., Guo, Y., Yang, B., Hao, L., Li, J., Zhang, Z., Ma, C., Wang, L., Xu, Y., et al. (2025). Crystallization Modulation of Wide-Bandgap Perovskites on Textured Silicon for Tandem Solar Cells. ACS Energy Lett. *10*, 4296–4303. https://doi.org/10.1021/acsenergylett.5c01244.

239. Putland, B.W.J., Righetto, M., Jin, H., Fischer, M., Ramadan, A.J., Zaininger, K.A., Herz, L.M., Sansom, H.C., and Snaith, H.J. (2024). Compositional Transformation and Impurity-Mediated Optical Transitions in Co-Evaporated Cu2AgBiI6 Thin Films for Photovoltaic Applications.

Adv. Energy Mater. *14*, 2303313. https://doi.org/10.1002/aenm.202303313.

240. Zia, W., Malekshahi Byranvand, M., Rudolph, T., Rai, M., Kot, M., Das, C., Kedia, M., Zohdi, M., Zuo, W., Yeddu, V., et al. (2024). MAPbCl3 Light Absorber for Highest Voltage Perovskite Solar Cells. ACS Energy Lett. *9*, 1017–1024. https://doi.org/10.1021/acsenergylett.3c02777.

241. Zhang, Y., Luo, L., Hua, J., Wang, C., Huang, F., Zhong, J., Peng, Y., Ku, Z., and Cheng, Y.-b. (2019). Moisture assisted CsPbBr3 film growth for high-efficiency, all-inorganic solar cells prepared by a multiple sequential vacuum deposition method. Mater. Sci. Semicond. Process. *98*, 39–43. https://doi.org/10.1016/j.mssp.2019.03.021.

242. Huang, Q., Li, F., Wang, M., Xiang, Y., Ding, L., and Liu, M. (2021). Vapor-deposited CsPbI3 solar cells demonstrate an efficiency of 16%. Sci. Bull. *66*, 757–760. https://doi.org/10.1016/j.scib.2020.12.024.

243. Kottokkaran, R., Gaonkar, H.A., Bagheri, B., and Dalal, V.L. (2018). Efficient p-i-n inorganic CsPbI3 perovskite solar cell deposited using layer-by-layer vacuum deposition. J. Vac. Sci. Technol. A: Vacuum, Surfaces, and Films *36*, 041201. https://doi.org/10.1116/1.5029253.

244. Yonezawa, K., Yamamoto, K., Shahiduzzaman, M., Furumoto, Y., Hamada, K., Ripolles, T.S., Karakawa, M., Kuwabara, T., Takahashi, K., Hayase, S., and Taima, T. (2017). Annealing effects on CsPbI3-based planar heterojunction perovskite solar cells formed by vacuum deposition method. Jpn. J. Appl. Phys. *56*, 04CS11. https://doi.org/10.7567/jjap.56.04cs11.

245. Lei, J., Gao, F., Wang, H., Li, J., Jiang, J., Wu, X., Gao, R., Yang, Z., and Liu, S.F. (2018). Efficient planar CsPbBr3 perovskite solar cells by dual-source vacuum evaporation. Sol. Energy Mater. Sol. Cell. *187*, 1–8. https://doi.org/10.1016/j.solmat.2018.07.009.

246. Alvianto, E., Wang, Y., Lin, S., Liang, H., Li, J., Lee, L.K., Dong, Z., Guo, X., Chen, J., Sun, Y., et al. (2025). Industry-Compatible Fully Laminated Perovskite-CIGS Tandem Solar Cells with Co-Evaporated Perovskite. Adv. Mater. *37*, e2505571. https://doi.org/10.1002/adma.202505571.

247. Abib, M.H., Li, J., Yang, H., Wang, M., Chen, T., Jiang, Y., and Jiang, Y. (2021). Direct deposition of Sn-doped CsPbBr3 perovskite for efficient solar cell application. RSC Adv. *11*, 3380–3389. https://doi.org/10.1039/d0ra09202a.

248. Park, C.-G., Choi, W.-G., Na, S., and Moon, T. (2018). All-Inorganic Perovskite CsPbI2Br Through Co-evaporation for Planar Heterojunction Solar Cells. Electron. Mater. Lett. *15*, 56–60. https://doi.org/10.1007/s13391-018-0095-1.

249. Ghavidel, E., Raoui, Y., JoverArrate, Ó., Ammirati, G., Zarotti, F., Magliano, E., Di Giacomo, F., Di Giovannantonio, M., Catone, D., Mariani, P., and Di Carlo, A. (2025). Low-Temperature Processing of Co-Evaporated CsPbI2Br for High-Efficiency, Wide-Bandgap Inverted Perovskite Solar Cells. Adv. Funct. Mater. *35*, e02970. https://doi.org/10.1002/adfm.202502970.

250. Zhu, X., Yang, D., Yang, R., Yang, B., Yang, Z., Ren, X., Zhang, J., Niu, J., Feng, J., and Liu, S.F. (2017). Superior stability for perovskite solar cells with 20% efficiency using vacuum co-evaporation. Nanoscale *9*, 12316–12323. https://doi.org/10.1039/c7nr04501h.

251. Guo, X., Jia, Z., Dong, Z., Kalasariya, N., Hu, J., Shi, Z., Steele, J.A., Chen, Y.-H., Ochsner, G., Chen, J., et al. (2026). Stable perovskite–organic tandem solar cells enabled by chloride-doped evaporated wide-bandgap perovskites. Energy Environ. Sci. *19*, 2679–2689. https://doi.org/10.1039/d5ee04477d.

252. Leyden, M.R., Škorjanc, V., Miaskiewicz, A., Severin, S., Maniyarasu, S., Gries, T., Beckedahl, J., Scheler, F., Simmonds, M., Holzhey, P., et al. (2024). Loading Precursors into Self-Assembling Contacts for Improved Performance and Process Control in Evaporated Perovskite Solar Cells. Sol. RRL *8*, 2400575. https://doi.org/10.1002/solr.202400575.

253. Liang, C., Du, H.-Q., Geng, C., Yu, X., Jiang, X., Huang, S., Long, F., Han, L., Li, W., Liang, G., et al. (2024). Low temperature method-based evaporation/spray-coating technology for wide bandgap perovskite solar cells. Mater. Today Energy *44*, 101612. https://doi.org/10.1016/j.mtener.2024.101612.

254. Zheng, X., Kong, W., Wen, J., Hong, J., Luo, H., Xia, R., Huang, Z., Luo, X., Liu, Z., Li, H., et al. (2024). Solvent engineering for scalable fabrication of perovskite/silicon tandem solar cells in air. Nat. Commun. *15*, 4907. https://doi.org/10.1038/s41467-024-49351-5.

255. Gao, Y., Wang, Y., Liu, Z., Ge, X., Li, B., Guo, H., He, H., Chang, J., Liu, Y., Li, S., et al. (2026). Molten Phosphonoalkanoic Acid-Driven Grain Boundary Passivation in Evaporated/Blade-Coated 1.68-eV Perovskite Solar Cells. Adv. Energy Mater. *16*, e05854. https://doi.org/10.1002/aenm.202505854.

256. Jiang, Y., He, S., Qiu, L., Zhao, Y., and Qi, Y. (2022). Perovskite solar cells by vapor deposition based and assisted methods. Appl. Phys. Rev. *9*, 021305. https://doi.org/10.1063/5.0085221.

257. Grater, L., Wang, M., Teale, S., Mahesh, S., Maxwell, A., Liu, Y., Park, S.M., Chen, B., Laquai, F., Kanatzidis, M.G., and Sargent, E.H. (2023). Sterically Suppressed Phase Segregation in 3D Hollow Mixed-Halide Wide Band Gap Perovskites. J. Phys. Chem. Lett. *14*, 6157–6162. https://doi.org/10.1021/acs.jpclett.3c01156.

258. Loukeris, G., Baretzky, C., Bogachuk, D., Gillen, A.E., Yang, B., Suo, J., Kaiser, W., Mosconi, E., De Angelis, F., Boschloo, G., et al. (2025). Suppressing Halide Segregation in Wide-Bandgap Perovskite Absorbers by Transamination of Formamidinium. ChemPhysChem *26*, e202500022. https://doi.org/10.1002/cphc.202500022.

259. Lin, Z., Wang, Q., Mei, A., Zhou, Y., and Han, H. (2025). Solvent residue management: A key factor for achieving high efficiency and stability in printable mesoscopic perovskite solar cells. APL Energy *3*, 030902. https://doi.org/10.1063/5.0282875.

260. Zhou, Y., Najar, A., Zhang, J., Feng, J., Cao, Y., Li, Z., Zhu, X., Yang, D., and Liu, S.F. (2022). Effect of Solvent Residue in the Thin-Film Fabrication on Perovskite Solar Cell Performance. ACS Appl. Mater. Interfaces *14*, 28729–28737. https://doi.org/10.1021/acsami.2c02525.

261. Yang, X., Yan, Z., Wang, S., Fu, P., Deng, C., Yang, G., Lou, Y., Wang, Z., Zeng, M., Chen, Y., et al. (2026). Thermodynamic inhibition of bromine-rich phase nucleation in wide-bandgap perovskites for operationally stable tandem solar cells. Energy Environ. Sci. *19*, 2273–2288. https://doi.org/10.1039/d5ee06815k.

262. Pei, F., Chen, Q., and Jiang, Y. (2025). Stability of Wide-Bandgap Perovskites for Tandem Applications: A Review. Energy Mater. Adv. *6*, 0172. https://doi.org/10.34133/energymatadv.0172.

263. Miah, M.H., Rahman, M.B., Nur-E-Alam, M., Islam, M.A., Shahinuzzaman, M., Rahman, M.R., Ullah, M.H., and Khandaker, M.U. (2025). Key degradation mechanisms of perovskite solar cells and strategies for enhanced stability: issues and prospects. RSC Adv. *15*, 628–654. https://doi.org/10.1039/d4ra07942f.

264. Hu, S., Hou, P., Dou, Y., Duan, C., Deng, X., Peng, Y., Cheng, Y.B., Liang, G., Li, X., and Ku, Z. (2026). Precursor Stabilization Strategies via Vapor-Solid Reaction for Reproducible and High-Efficiency Vapor-Deposited Perovskite Solar Cells. ACS Nano *20*, 5007–5020. https://doi.org/10.1021/acsnano.5c18423.

265. He, S., Li, S., Zhang, A., Xie, G., Wang, X., Fang, J., Qi, Y., and Qiu, L. (2022). Residual strain reduction leads to efficiency and operational stability improvements in flexible perovskite solar cells. Mater. Adv. *3*, 6316–6323. https://doi.org/10.1039/d2ma00431c.

266. Zhu, H., Teale, S., Lintangpradipto, M.N., Mahesh, S., Chen, B., McGehee, M.D., Sargent, E.H., and Bakr, O.M. (2023). Long-term operating stability in perovskite photovoltaics. Nat. Rev. Mater. *8*, 569–586. https://doi.org/10.1038/s41578-023-00582-w.

267. Lin, Y., Bai, Y., Fang, Y., Wang, Q., Deng, Y., and Huang, J. (2017). Suppressed Ion Migration in Low-Dimensional Perovskites. ACS Energy Lett. *2*, 1571–1572. https://doi.org/10.1021/acsenergylett.7b00442.

268. Jiang, X., Geng, C., Yu, X., Pan, J., Zheng, H., Liang, C., Li, B., Long, F., Han, L., Cheng, Y.-B., and Peng, Y. (2024). Doping with KBr to Achieve

High-Performance CsPbBr3 Semitransparent Perovskite Solar Cells. ACS Appl. Mater. Interfaces *16*, 19039–19047. https://doi.org/10.1021/acsami.4c02402.

269. Traverse, C.J., Pandey, R., Barr, M.C., and Lunt, R.R. (2017). Emergence of highly transparent photovoltaics for distributed applications. Nat. Energy *2*, 849–860. https://doi.org/10.1038/s41560-017-0016-9.
270. Lim, S., Back, J.-Y., Jeon, B.-C., Park, J., Lee, J., Kim, E.-J., Kim, E., Park, H.J., Kim, J., and Moon, T. (2024). Evaporated, Semitransparent Rudorffite AgBiI4 Films for Pb-Free Indoor Photovoltaics. Energy Fuels *38*, 23741–23745. https://doi.org/10.1021/acs.energyfuels.4c04215.
271. Chen, W., Zhang, J., Xu, G., Xue, R., Li, Y., Zhou, Y., Hou, J., and Li, Y. (2018). A Semitransparent Inorganic Perovskite Film for Overcoming Ultraviolet Light Instability of Organic Solar Cells and Achieving 14.03% Efficiency. Adv. Mater. *30*, e1800855. https://doi.org/10.1002/adma.201800855.
272. Zhang, Y., Zhu, Y., Sun, J., Hu, M., Chen, J., Duan, B., Hu, S., Hou, P., Tan, W.L., Ku, Z., et al. (2025). Low Pressure Chemical Vapor Deposited Perovskite Enables all Vacuum-Processed Monolithic Perovskite-Silicon Tandem Solar Cells. Adv. Energy Mater. *15*, 2405377. https://doi.org/10.1002/aenm.202405377.
273. Wang, Z., Lyu, M., Zhang, B.W., Xiao, M., Zhang, C., Han, E.Q., and Wang, L. (2025). Thermally Evaporated Metal Halide Perovskites and Their Analogues: Film Fabrication, Applications and Beyond. Small Methods *9*, e2301633. https://doi.org/10.1002/smtd.202301633.
274. Ávila, J., Momblona, C., Boix, P.P., Sessolo, M., and Bolink, H.J. (2017). Vapor-Deposited Perovskites: The Route to High-Performance Solar Cell Production? Joule *1*, 431–442. https://doi.org/10.1016/j.joule.2017.07.014.
275. Kan, C., Luo, C., and Hou, Y. (2026). Scalable deposition and drying methods toward large-area monolithic perovskite/silicon tandem solar cells. Energy Environ. Sci. *19*, 1101–1123. https://doi.org/10.1039/d5ee06772c.
276. Subbiah, A.S., Isikgor, F.H., Howells, C.T., De Bastiani, M., Liu, J., Aydin, E., Furlan, F., Allen, T.G., Xu, F., Zhumagali, S., et al. (2020). High-Performance Perovskite Single-Junction and Textured Perovskite/Silicon Tandem Solar Cells via Slot-Die-Coating. ACS Energy Lett. *5*, 3034–3040. https://doi.org/10.1021/acsenergylett.0c01297.
277. Farag, A., Schmager, R., Fassl, P., Noack, P., Wattenberg, B., Dippell, T., and Paetzold, U.W. (2022). Efficient Light Harvesting in Thick Perovskite Solar Cells Processed on Industry-Applicable Random Pyramidal Textures. ACS Appl. Energy Mater. *5*, 6700–6708. https://doi.org/10.1021/acsaem.1c04028.
278. Subbiah, A.S., Torres Merino, L.V., Pininti, A.R., Hnapovskyi, V., Mannar, S., Aydin, E., Razzaq, A., Allen, T.G., and De Wolf, S. (2024). Enhancing the Performance of Blade-Coated Perovskite/Silicon Tandems via Molecular Doping and Interfacial Energy Alignment. ACS Energy Lett. *9*, 727–731. https://doi.org/10.1021/acsenergylett.4c00070.
279. Fu, F., Feurer, T., Jäger, T., Avancini, E., Bissig, B., Yoon, S., Buecheler, S., and Tiwari, A.N. (2015). Low-temperature-processed efficient semitransparent planar perovskite solar cells for bifacial and tandem applications. Nat. Commun. *6*, 8932. https://doi.org/10.1038/ncomms9932.
280. Shen, X., Lin, X., Su, H., Zhang, Z., Wu, T., Zhang, J., Peng, Y., Zhang, Y., Zhang, S., Zhou, Z., et al. (2026). Key Advancements and Emerging Trends of Perovskite Solar Cells in 2024-2025. Nano-Micro Lett. *18*, 209. https://doi.org/10.1007/s40820-025-02022-6.
281. Miyano, K., Yanagida, M., Tripathi, N., and Shirai, Y. (2016). Hysteresis, Stability, and Ion Migration in Lead Halide Perovskite Photovoltaics. J. Phys. Chem. Lett. *7*, 2240–2245. https://doi.org/10.1021/acs.jpclett.6b00579.
282. Li, N., Lin, S., Niu, X., Jia, Z., Zhao, M., Zhao, Y., Sun, Y., Zhong, D., and Hou, Y. (2026). Efficient Perovskite–Cu(In,Ga)Se2 Tandem Solar Cells Enabled by Coevaporation. ACS Energy Lett. *11*, 1605–1608. https://doi.org/10.1021/acsenergylett.5c04203.